8-7-2018

Development of Novel Collagen-targeted Protein-based MRI Contrast Agent for Imaging of Chronic Liver and Heart Diseases

Mani Salarian

DEVELOPMENT OF NOVEL COLLAGEN-TARGETED PROTEIN-BASED MRI CONTRAST AGENT FOR IMAGING OF CHRONIC LIVER AND HEART DISEASES

by

MANI SALARIAN

Under the Direction of Jenny J. Yang, Ph.D.

ABSTRACT

Chronic diseases and conditions such as liver and heart diseases are among the most common, costly, and preventable of all health problems. As of 2012 in the U.S., about half of all adults—117 million people—had one or more chronic health conditions. Aortic aneurysm and liver fibrosis are among the most common chronic diseases which are generated by the formation and deposition of excess extracellular matrix proteins (largely type I collagen) as a result of a reparative process, represents one of the most major global health problems. Collagen type I is one of the major diagnostic biomarkers and therapeutic targets for many chronic diseases including heart and liver diseases. Early diagnosis, noninvasive detection and staging of these diseases,

remain as one of the major clinical barriers which can lead to effective treatment and stop further progression toward major clinical consequences. MRI as one the popular imaging modalities has several unique advantages for monitoring slow progression and detection of disease with high resolution without using radiation, however, there is an unmet medical need to develop MRI contrast agents with desired sensitivity and collagen specificity. In this dissertation, the successful design of a protein-based contrast agent with collagen type I targeting capability (ProCA32.collagen1) is reported to diagnose and stage liver and heart diseases in many mouse models of caner, fibrosis and aortic aneurysm. ProCA32.collagen1 exhibits the highest relaxivity values for r_1 (34 ± 0.12 $mM^{-1}.s^{-1}$) and r_2 (50 ± 0.16 $mM^{-1}.s^{-1}$) per Gd^{3+} at 1.4 T and r_1 (21.3 ± 0.5 $mM^{-1}.s^{-1}$) and r_2 (108.5 ± 1.2 $mM^{-1}.s^{-1}$) at 7.0 T. ProCA32.collagen1 can detect both early (Ishak 3 of 6) and late stage mouse liver fibrosis as well as early stage nonalcoholic steatohepatitis (Ishak 1 of 6) in different models with strong metal binding affinity and selectivity. The targeted contrast agent is also capable of detecting disease heterogeneity with high collagen type I binding affinity with dissociation constant of $K_d=1.42 \pm 0.2$ μM. ProCA32.collagen1 has largely reduced dose and strong resistance against transmetallation (10^4-10^{12}-fold higher metal selectivity for Gd^{3+} over Ca^{2+} and Zn^{2+}) compared to existing contrast agents. ProCA32.collagen1 is expected to have strong translational potential to improve detection of different diseases at early stages with high confidence, and subsequently monitor disease progression and patient response to treatment.

INDEX WORDS: MRI Contrast Agent, Protein Design, Gadolinium, Collagen Type I, Chronic Diseases, Liver Fibrosis, Aortic Aneurysm, Early Diagnosis,

DEVELOPMENT OF NOVEL COLLAGEN-TARGETED PROTEIN-BASED MRI CONTRAST AGENT FOR IMAGING OF CHRONIC LIVER AND HEART DISEASES

by

MANI SALARIAN

A Dissertation Submitted in Partial Fulfillment of the Requirements for the Degree of

Doctor of Philosophy

in the College of Arts and Sciences

Georgia State University

2018

DEVELOPMENT OF NOVEL COLLAGEN-TARGETED PROTEIN-BASED MRI CONTRAST AGENT FOR IMAGING OF CHRONIC LIVER AND HEART DISEASES

by

MANI SALARIAN

Committee Chair: Jenny J. Yang

Committee: Markus Germann

Ming Luo

Zhi-Ren Liu

Shella Keilholz

Phillip Zhe Sun

Electronic Version Approved:

Office of Graduate Studies

College of Arts and Sciences

Georgia State University

August 2018

DEDICATION

I would like to dedicate my dissertation to my father; Firooz, my mother; Mahshid and my brother; Khosro for their tremendous unconditional love, moral and financial support. They have been the source of my strength throughout these years. I am extremely thankful to my parents for all their sacrifices and hard work for providing me the best environment and bright future throughout my education and showing me the right path. They taught me to never give up and always fight for my goals and that hard work will eventually pay off. I would also like to thank my brother who was always encouraging and supportive with his kind words during all these years, he is the best brother anyone could ever have.

ACKNOWLEDGEMENTS

My deepest and sincerest gratitude goes to Dr. Jenny J. Yang, my Ph.D. advisor. She has been one of the best role models that any graduate student could ever have. I am extremely thankful to her for providing me the best environment for any graduate student ever needs to shine and bloom. Her knowledge, experience, fighting spirit and passion in science have been such an inspiration for me throughout these years. She has certainly played an essential role in developing my career. I am grateful for her guidance and advice during my research and providing both moral and financial support for moving my research forward and playing a crucial role in my research progression. Because of her trainings, I have learnt a variety of valuable lab skills that I extremely cherish. Because of her, I am a better problem solver, better in communication skills, team work and in general better researcher and scientist.

I would also like to thank my previous mentors in the lab, Dr. Yanyi Chen and Xueyun (Snow) Liu who were my first mentors when I joined Dr. Yang's lab for their guidance and patience. They were part of Gap Junction projects and I learned some of the basic techniques such as PCR, expression and purification of proteins from them.

My highest gratitude goes to Dr. Shenghui Xue for his excellent mentorship and patience in teaching me all the important techniques and skills required for conducting research in MRI projects. His continued help, guidance, and support during my research has been valuable for my project advancement. Dr. Jingjuan Qiao has also been one of my important mentors providing detailed suggestions and teaching me some of the *in vivo* skills during all these years. Without Dr. Shenghui Xue's and Dr. Jingjuan Qiao's help, this dissertation could not have been finished.

I am very thankful to other current and previous members of MRI group, first of all Anvi Patel for also teaching me some of the important skills. Shanshan Tan for her helpful guidance and

discussions regarding my research. I would also like to thank Dr. Fan Pu for her suggestions and Oluwatosin Y. Ibhagui for her kind help during my research in the lab.

I am very thankful to Dr. Chen Zhang and Dr. Juan Zou as well for their suggestions and help during some tough times in Gap Junction project. I would appreciate all our collaborators help in these multi-disciplinary projects, my dear friend and collaborator Dr. Maysam Nezafati for image processing, Drs. Ravi Chakra Turaga, Yinwei Zhang, Hua Yang and Ganesh Satyanarayana for histology analysis and animal models' development, Dr. Khan Hekmatyar for image processing and operating the MRI instrument and providing helpful suggestions, Dr. Alton Brad Farris for his pathology analysis in liver fibrosis project, Drs. Hans E. Grossniklaus and David H. Lawson for their helpful discussions in Uveal Melanoma project, Drs. Xiaoping Hu, Jason Langley and Qun Zhao for their guidance on MRI image analysis, and Dr. Pardeep Mittal for his suggestions on clinical contrast agent field. I greatly appreciate Dr. Jibiao Li and Dr. Liqing Yu for their contribution in generating nonalcoholic fatty liver disease animal models. I would also thank Dr. Rao Mukkavilli for his tremendous help in analyzing pharmacokinetics data. I am very thankful to Dr. Ming-Hui Zou and Dr. Ramprasath Tharmarajan for their contribution in generating the heart disease animal models.

At the end, I would like to express my heartfelt gratitude to all my committee members, Drs. Ming Luo, Markus Germann, Shella Keilholz, Phillip Zhe Sun and Zhi-Ren Liu for accepting my invitation to be part of my dissertation committee, and their detailed analysis and assistance for supporting my research.

TABLE OF CONTENTS

LIST OF TABLES

LIST OF FIGURES

LIST OF ABBREVIATION

3D: three-dimensional

3DGE: 3D gradient echo

AAA: abdominal aortic aneurysm

AIF: arterial input function

ALD: alcoholic liver disease

ALP: alkaline phosphatase

ALT: alanine transaminase

APRI: aspartate-to-platelet ratio index

AST: aspartate transaminase

BSA: bovine serum albumin

CCMV: cowpea chlorotic mottle virus

CD2: cluster of differentiation

CDC: center for disease control and prevention

CLD: chronic liver disease

CNR: contrast-to-noise ratio

CNS: central nervous system

CT: computed tomography

CV: column volume

Cys: cystein

DD: dipole-dipole

DEC-MRI: dynamic contrast enhanced-MRI

DTPA: diethylene-triamine-pentaacetic acid

ECM; extracellular matrix

EDTA: ethylenediaminetetraacetic acid

EGFR: epidermal growth factor receptor

EGTA: ethylene glycol tetraacetic acid

EnDOR: Electron-nuclear double resonance spectroscopy

FDA: U S Food and Drug Administration

FOV: field of view

FPLC: fast protein liquid chromatography

FRET: Förster resonance energy transfer

FSE: fast spin echo

FSEMS: fast spin echo multi-slices

Gd^{3+}: Gadolinium

Gd-DTPA: gadolinium-diethylene-triamine-pentaacetic acid

GRF: glomerular filtration rate

GRP: gastrin-releasing peptide

GRPR: gastric-releasing peptide receptor

HCC: hepatocellular carcinoma

HER2 or HER2/Neu: human epidermal growth factor receptor 2

HSC: hepatic stellate cell

ICP-OES: inductively coupled plasma atomic emission spectroscopy

IF: immunofluorescence

IHC: immunohistochemistry

IPTG: isopropyl β-D-1-thiogalactopyranoside

Kd: dissociation constant

LRET: luminescence resonance energy transfer

MEMS: multi-echo-multi-slices

Mn-DPDP: manganese dipyridoxal diphosphate

MRE: magnetic resonance elastography

MRI: magnetic resonance imaging

MVD: mean vascular density

NAFL: nonalcoholic fatty liver

NAFLD: nonalcoholic fatty liver disease

NASH: nonalcoholic steatohepatitis

NHS: N-hydroxysuccinimide

NIR: near infared

NMRD: Nuclear Magnetic Relaxation Dispersion

NSF: nephrogenic systemic fibrosis

NTA: nitrilotriacetic acid

OD: optical density

OI: optical imaging

PAI: photo acoustic imaging

PCR: polymerase chain reaction

PEG: polyethylene glycol

PET: positron emission tomography

PMSF: phenylmethylsulfonyl fluoride

ProCA: protein-based MRI contrast agent

ProCA32.collagen1: ProCA32 linked with collagen I peptide

PV: parvalbumin

R1: longitudinal relaxation rate

r_1: longitudinal relaxivity

R2: transverse relaxation rate

r_2: transverse relaxivity

RGD: Arg-Gly-Asp

SBM: Solomon-Bloembergen-Morgan

SC: scalar or contact

SDS-PAGE: sodium dodecyl sulfate polyacrylamide gel electrophoresis

SE: spin echo

SLE: systemic lupus erythematous

SPECT: single-photon emission computed tomography

SWE: shear wave elastography

TAA: thoracic aortic aneurysm

T1: longitudinal relaxation time

T2: transverse relaxation time

T1W: T1-weighted

T2W: T2-weighted

TBST: Tris-buffered saline with Tween 20

TE: echo time

TR: repetition time

US: ultrasound

UM: uveal melanoma

Vc: initial volume distribution

Vdss: steady state phase

VEGF: vascular endothelial growth factor

WT: wild type

ZFS: zero field splitting

ΔKobs: Difference in decay rates of Tb^{3+} in H_2O and D_2O

τ: life time

Γ: the radiative decay

1 INTRODUCTION

1.1 Magnetic resonance imaging (MRI) and contrast agents

Magnetic resonance imaging (MRI) is an imaging modality and diagnostic technique in current clinical medicine. MRI as a diagnostic imaging modality has so many advantages such as its noninvasiveness, using no radiation, excellent spatial resolution, and soft tissue contrast. MRI is one of the premiere techniques resulting in important anatomical information. In addition, combination of MRI with other techniques leads to contrast in MRI which can provide noticeable images from the same anatomical region. As can example, MRI pulse sequences can be applied to create contrast between different tissues based on their proton density difference, T1 or T2 relaxation times, water diffusion rates, and chemical shifts based on difference between water and lipids [2-6].

One of the major challenges associated with MRI is the lack of adequate sensitivity. In clinical imaging field, the primary importance is observing hydrogen atoms from water that are present in tissue at the concertation of approximately 90 M. In order to create more contrast to aid the MRI modality, usually a compound is necessary to affect properties of the 90 M water protons and this effect should be in a level that a noticeable change is reached. These compounds are called MRI contrast agents [6]. They can be categorized into three general subgroups of paramagnetic, superparamagnetic, or ferromagnetic compounds that will shorten the relaxation times of water protons. All contrast agents can shorten both T1 and T2 relaxation times, however based on whether the agent increases the transverse relaxation rate (1/T2) by roughly the same amount that it increases the longitudinal relaxation rate (1/T1) or whether 1/T2 is altered to a much greater extent, they can be classified into two groups of T1 agents and T2 agents, respectively [6, 7].

In T1 agents, T1 lowering effect is dominant which increases the signal intensity; these are positive contrast agents. The T2 agents mainly increase the 1/T2 property and results in reduction in signal intensity, therefore, they are called negative contrast agents [6, 8]. One of the examples of paramagnetic agents with T1 effect are gadolinium-based contrast agents. Ferromagnetic iron oxide particles can be named as contrast agents with high T2 effect. The majority of contrast agents being used in clinical field are based on gadolinium complexes, however there are some instances of manganese- and iron-based contrast agents approved for clinical use. It has been reported that there are more than 10 million MRI studies being performed with gadolinium every year [6].

The interaction of contrast agent with the water hydrogen will affect relaxation properties of nuclei that creates the contrast which is different from contrast in other imaging modalities such as X-ray and nuclear imaging agents where the effect observed is more related to the concentration of the imaging agent. The concentration of water is much higher than the contrast agent, therefore, the agent must act as a catalyst to relax the water protons for the effect to be observed. The relaxivity is one of most important properties of a contrast agent which can be defined as the ability of an agent to change relaxation rate, and it is represented as r_1 or r_2, where r_1 refers to longitudinal relaxation (1/T1) and r_2 refers to transverse rate (1/T2). In other words, relaxivity is the change in relaxation rate after a contrast agent ($\Delta(1/T)_1$) is applied which is normalized to the concentration of contrast agent or metal ion (M), Eqn (1-1).

$$r_1 = \frac{\Delta(1/T_1)}{[\mathrm{M}]} \qquad (1\text{-}1)$$

Different contrast agents have different relaxivity values and therefore have different sensitivities. Commercial and clinical contrast agents usually lack enough sensitivity and are effective at high concentrations (> 0.1 mM), therefore there has been an unmet medical need to increase their sensitivity [6].

1.2 Clinical Gd^{3+}-based MRI contrast agents: Advantages and limitations

Gadolinium-based contrast agent (GBCA) are used in approximately 25–30% of all MRI scans [9, 10]. The contrast agent creates a brighter or darker image specifically in the area of diseased tissue. The first approved contrast agent was Gd-DTPA (gadopentetate dimeglumine, Magnevist®) introduced in 1988. The first generation of contrast agents produced were for different purposes such as extracellular fluid (ECF) agents, liver imaging and agent that were given orally for gastrointestinal imaging. Currently, several agents are in clinical trials and one has been recently approved for MR angiography [11]. In preclinical stage, there has been continues efforts to create gadolinium-based contrast agents in molecular imaging.

All GBCAs are used by intravenous (i.v.) administration. The route in which the contrast agent is being administered plays an indispensable role on biodistribution and safety. The majority of GBCAs are approved at a dose of ~ 0.1 mmol Gd/kg, however, for MR angiography two or three times higher dosage is required. Some newly developed agents such as gadofosveset and gadoxetic acid can be used at lower doses (0.03 mmol/kg and 0.025 mmol/kg, respectively). The injection dosage of contrast agent is also important since it affects the Gd^{3+} levels the subject receives. Furthermore, it can impact the exposure and how fast the compound is eliminated [11].
Since the first approval of clinical MRI contrast agent, gadopentetate dimeglumine (Magnevist), in 1987, they have been successful in MR imaging of different types of tissues, diagnostics, characterization of tumors and other diseased tissues. In different cases of diseases, the change in permeability of blood vessels is crucial for the function of these MRI contrast agents. For instance, stroke, liver fibrosis, neuron degenerative diseases and so on are all have change in permeability of blood vessels. These clinical contrast agents can function as probes for organs such as liver, kidney, and gall bladder [8].

Currently, all clinically approved MRI contrast agents based on Gd^{3+}, the primary structure has a Gd^{3+} encapsulated by organic chelators, such as diethylenetriaminepentaacetic acid (DTPA) and 1,4,7,10-tetraazacyclododecane-1,4,7,10-tetraacetic acid (DOTA) (Table 1.1). Usually, the coordination site of Gd^{3+} has up to 8 nitrogen and oxygen atoms contributed by the chelator to function as Gd^{3+} binding ligands. Furthermore, there is one water molecule exist in Gd^{3+} coordination site in clinical MRI contrast agent which interacts with Gd^{3+} through the Gd-O interactions. Charge and structure of chelators are important factors for Gd^{3+} coordination, therefore as a result, clinically approved Gd^{3+} MRI contrast agents are categorized into four groups: *ionic linear contrast agents* (examples: Magnevist, Multihance, Abalavar and Eovist), *non-ionic linear contrast agents* (examples: Ominiscan and Optimark), *ionic cyclic contrast agents* (examples: ProHance and Gadovist) and *non-ionic cyclic contrast agents* (example: Dotarem). Multihance and Eovist are organ (liver) specific agents, however, most of the clinical MRI contrast agents are extracellular contrast agents which are eliminated through kidney. Extracellular contrast agents can be successfully used for imaging of the whole body, structural changes in blood vessels and central nervous system (CNS). Since Eovist and Multihance are liver agents, hepatocytes in liver are responsible for their uptake (~50 %) and 5 % is eliminated by biliary excretion. These two contrast agents are widely used for liver imaging, such as primary liver cancer (hepatocellular carcinoma), liver metastases from other organs, and liver fibrosis [8, 12].

With the advent of MRI contrast agents, contrast enhanced MRI attracted great attention and became one of the most popular imaging modalities in the clinical field. For instance, the diagnosis of different liver diseases such as liver metastases and fibrosis heavily depends on imaging techniques, such as MRI, CT, ultrasound and PET, however, MRI is the best diagnostic tool among them. With the use of contrast agents, MRI is able to detect small lesions in liver

metastases with detection limit of ~ 2 cm or larger. Although other imaging modalities such as ultrasound may detect lesions as small as 2 mm, it faces important challenges such as surgery and limitations regarding the location of tumors since they need to be on the surface of the liver in order to be detected [13]. In addition, for detection of diseases such as liver fibrosis, MRI has the capacity to cover the whole liver in order to assess its heterogeneity [14]. Clinical MRI contrast agents can also play critical roles in MRI assisted surgery and biopsy and MRI guided therapy for different types of diseases, such as liver cancer [15].

Despite evolving the whole MRI field with their advantages, clinically approved contrast agents have their own limitations. Since they are small-molecule chelators with small molecular mass, clinical MRI contrast agents usually have a short half-life time (half-life of approximately 0.5-3 minutes in the blood of mice and elimination half-life of about 1.5 hours in humans [16, 17]. Optimization of MRI contrast agent's properties are extremely important since it would directly affect the time window of MRI data collection and eliminate repeated dose injections. In addition, the application of these contrast agents can be widened to potential biological targets for molecular imaging which would significantly increase and improve their detection limits. For instance, this number is ~30 μM in mouse skeletal muscle for the contrast agent, [Gd(HPDO3A)(H_2O)]. Overall, clinical MRI contrast agents have the following limitations: low relaxivity, low metal selectivity, high toxicity which causes Nephrogenic Systemic Fibrosis (NSF) due to high injection dosage, and they are non-specific and lack targeting capability with short half-life. All of these limitations have driven the need to develop contrast agents with significantly improved relaxivity, optimized retention time, and high targeting capabilities [16, 18, 19].

Other important characteristic of contrast agents are their toxicity and pharmacokinetics which have been well-studied in 1980s. Studies have shown that these contrast agents were proven

to be safer than iodinated contrast agents used in CT and X-ray. Despite their good safety profiles, clinical MRI contrast agents usually need high injection dosage of 0.025-0.3 mmol/kg and a concentration in mM range to be considered effective for contrast in tissues. In principal, the injection dosage and concentration can be lowered if the longitudinal relaxivity (r_1) is increased or optimized. Since high concentrations are being utilized, these agents are facing concerns regarding the renal toxicity due to release of free Gd^{3+} from the most commonly used contrast agent, gadolinium-diethylene-triaminepentaacetic acid (Gd-DTPA). There are increased reports of nephrogenic systemic fibrosis (NSF) associated with Gd-DTPA, as well as a complication found in patients with end-stage renal failure (GRF < 30 ml min-1) [20-23].

Table 1.1 Clinical MRI Contrast Agents Based on Gd^{3+} [1, 24-26].

Generic Name	Chemical Formula	Trade Name	r_1,Plasma Relaxivity 1.5T, 37°C ($mM^{-1}s^{-1}$)	r_2,Plasma Relaxivity 1.5T, 37°C ($mM^{-1}s^{-1}$)	Formulation Concentration	Standard dose (mmol/kg)
Gadopentetate dimeglumine	$[Gd(DTPA)(H_2O)]^{2-}$	Magnevist	4.1	4.6	0.5 M	0.1
Gadodiamide	$[Gd(DTPA\text{-}BMA)(H_2O)]$	Omniscan	4.3	5.2	0.5 M	0.1
Gadoversetamide	$[Gd(DTPA\text{-}BMEA)(H_2O)]$	Optimark	4.7	5.2	0.5 M	0.1
Gadoterate meglumine	$[Gd(DOTA)(H_2O)]^{-}$	Dotarem	3.6	4.3	0.5 M	0.1
Gadoteridol	$[Gd(HP\text{-}DO3A)(H_2O)]$	ProHance	4.1	5.0	0.5 M	0.1
Gdobutrol	$[Gd(HP\text{-}butrol)(H_2O)]$	Gadovist	5.2	6.1	1.0 M	0.1
Gadoxetic acid disodium	$[Gd(EOB\text{-}DTPA)(H_2O)]^{2-}$	Eovist (Primovist)	6.9	8.7	0.25 M	0.025
Gadobenate dimeglumine	$[Gd(BOPTA)(H_2O)]^{2-}$	Multihance	6.3	8.7	0.5 M	0.1
Gadofosveset trisodium	Diphenylcyclohexyl phosphodiester-Gd-DTPA	Ablavar	27.7	72.6	0.25 M	0.03

1.3 Important criteria of an MRI Contrast Agent

There are several criteria that need to be considered in order to have an ideal contrast agent. One of the most important requirements for a contrast agent is to have minimum toxicity. In addition, thermodynamic and kinetic properties should be taken into consideration to have good stability and reasonable elimination half-life. Another important characteristic is the metal binding affinity and selectivity to minimize the adverse effects of the release of free Gd^{3+} into the body. Since other physiological metals such as Ca^{2+} and Zn^{2+} are present in high concentrations in the body, they have the ability to compete with Gd^{3+} in the contrast agent and cause its release, therefore, a high metal selectivity for paramagnetic metal ions (e.g. Gd^{3+} and Mn^{3+}) against physiological metal ions is needed [27, 28]. High relaxivity, especially longitudinal relaxation (r_1), is another important criterion required to achieve images with high dose efficiency and high contrast-to-noise ratio (CNR). Proper vascular retention time, permeability and perfusion is also crucial to allow the contrast agent to penetrate tissues in order to have enhancement, and monitor capillary integrity changes.

Different methods have been used to improve the properties of MRI contrast agents based on small chelators. For instance, small chelators are being non-covalently bound to plasma proteins, such as albumin (MS-325), in order to greatly increase their relaxivity and blood retention time, however, these contrast agents can only be used in magnetic resonance angiography (MRA) [29, 30]. As it was mentioned previously, elimination or excretion time from the body is important for the contrast agent and needs to be optimized in order to have optimal imaging and reduced toxicity. Size of the contrast agent is therefore becoming important as molecules that are greater than ~ 7 nm or ~ 60 kDa in diameter can pass through the glomeruli. The circulation half-life of those molecules, compared to molecules with a diameter of less than 5 nm, can significantly

increase to over 78 minutes in mice, as the molecular weight is larger than 60 kDa [31-33]. Eventually, targeting specific molecules or biomarkers can dramatically increase the specificity and sensitivity of MRI contrast agents as powerful diagnostic and prognostic tools. Due to very low expression of biomarkers in the disease area, creating contrast agents with this capability will be beneficial. Moreover, high dose efficiency, low toxicity, optimal pharmacokinetics and thermodynamics and targeting capability and perfusion are indispensable for concreate molecular imaging. Understanding relaxivity as the most important criteria for designing an ideal contrast agent with the mentioned characteristics needs a thorough understanding of its theory to assist in development of MRI contrast agents [34]. In the next section, relaxivity and its theory and how it can assist the design of contrast agents will be discussed.

1.4 Strategies for the design of Gd^{3+}-based MRI contrast agents

In general, there are different approaches which will lead to increase in molecular relaxivity of contrast agents. First step can be optimization of the parameters that affect relaxivity and second, connecting multiple gadolinium complexes together. Linking multiple gadolinium complexes together for MR imaging have attracted great attention recently. The linking can occur either covalently (e.g. polymers, dendrimers) or non-covalently (e.g. liposomes). Many strategies have been used to optimize the relaxivity of these complexes and also designing them to target specific diseases.

As a summary, most important factors affecting relaxivity are external field, the electronic properties of the gadolinium, water exchange, rotational diffusion, first and second coordination sphere hydration, and the ion to water proton distance. Each factor will be discussed in the next sections as well as the physical methods for the estimation of these parameters [6].

Extracellular clinical MRI contrast agents like Magnevist ($[Gd(DTPA)(H_2O)]^{2-}$ are cheap to manufacture and have good safety profile. As it was mentioned earlier, doses as high as 0.3 mmol/kg are given clinically for applications such as angiography and cerebral perfusion. After injection of the contrast agent at this dose, T1 becomes much shorter than T1 in any other tissue without contrast agent, and provides good contrast. One approach to increase the relaxivity is to increase the sensitivity of MRI for molecular targets instead of increasing the sensitivity of the contrast agent itself or making a better Magnevist.

In order for a contrast agent to be effective in clinical exams with considerable and observable contrast, a relaxation rate change of at least ~ 0.5 s^{-1} is needed. For commercial contrast agents that are extracellular with a relaxivity of ~ 4 $mM.s^{-1}$, ~125 μM of the agent is needed. If a targeted contrast agent is developed with the assumption of 1:1 binding stoichiometry, a minimum of 125 μM of the target needs to be present in order to observe the contrast. In order to assess the sensitivity, a study was conducted and concluded that the limit of detection of $[Gd(HPDO3A)(H_2O)]$ is around 30 μM in mouse skeletal muscle [19, 35].

It can be concluded that the amount of potential biological targets detected by the contrast agent is limited. In order to have a reasonable and observable T1 change, relaxivity values and/or the number of Gd/molecule should be increased. Since molecular motion can affect relaxivity and the mobility will be dependent on molecular size, its rigidity, and possible tendency to bind other proteins, relaxivity must be optimized based on each molecule. As a matter of fact, no gadolinium complex exists which can be conjugated to a targeting molecule to necessarily create a targeted contrast agent with high relaxivity. Another important point is about the rotational dynamics of the final molecule which can be critical. With these parameters, there are several strategies to achieve an effective molecular targeted MRI contrast agent [36].

The interaction between Gd^{3+} and water proton which affects its relaxation happens through a dipolar mechanism depending on $1/r^6$ which is the distance between the ion and the nucleus, therefore, it is crucial to have at least one exchangeable water in the inner coordination sphere of Gd^{3+} binding site. The number of water in the inner coordination sphere is represented by q and is called hydration number, however if this hydration number is bigger than one then the complex should be stable since the water can be displaced by ligands inside the inner coordination sphere [37].

It is also very important for the complex to be stable and not reacting with any other molecules for in vivo applications since the gadolinium can be released because of these interactions. The rate in which the water is exchanging in and out of the first coordination sphere should be fast, therefore the solvent surrounding the contrast agent becomes important and the relaxation rate of bulk solvent should be increased. In order for that to happen, Gd^{3+} should relax the water that has interaction with it, and the relaxed water should exchange fast enough with the bulk water. For complexes like $[Gd(DTPA)(H_2O)]^{2-}$ which has fast tumbling rate, the relaxation rate of the bound water is the rate limiting process. When rotational motion is slow, then water exchange rate becomes an important factor [37].

The impact of both water exchange and rotational motion can be observed in an example where you compare the relaxivity of 0.1 mM MS-325 and MS-325-BMA in pH 7.4 phosphate buffer with saline (PBS) and 0.67 mM human serum albumin (HSA) solution at 37 °C and 0.47 T. In this example, there are two contrast agents, one is one of the Gd-DTPA analogs called MS-325 and the other one is its bis(N methyl)amido derivative along with their relaxivities at pH 7.4 phosphate buffered saline (PBS) or in a PBS solution with human serum albumin (HSA) present. Gd^{3+} complexes with amido oxygen donor atoms present in their structure usually have slower

water exchange rates [6]. The complex of the bis (N-methyl) amide with Gd^{3+} which is the analog of DTPA, [Gd(DTPA-BMA)(H_2O)], possesses a water exchange rate of about 10 times slower than [Gd(DTPA)(H2O)]$^{2-}$along which has similar water exchange rates to their parent complexes. In PBS buffer, the relaxivity is similar since the relaxation of the bound water is the rate-limiting step [6, 37].

This effect can determine how fast the molecules tumble in solutions and because of the similar size, their relaxivity values are similar. When there is serum albumin present in the solution, both of the Gd^{3+} complexes will bind to serum albumin and therefore as a result, their tumbling rate will be slower which will make the relaxation mechanism of the bound water more effective. In this example, it is evident that the water exchange rate is important and the slow water exchange in GdDTPA-BMA derivative complex affects its relaxivity. In some cases, increase in water exchange can improve relaxivity further and increase it, however, this will happen only if the process for relaxing the bound water is very efficient.

For imaging of the majority of biological targets, multiple Gd^{3+} ions are needed to provide the required relaxation rate change. One option is linking multiple Gd^{3+} complexes to increase the effective correlation time for motion, however, it is important to understand and control the rotational flexibility which has a large impact on the relaxivity. Based on the way Gd^{3+} complexes are linked together, they can have different rotational motions and therefore, a different relaxivity value. Some complexes are linked in a linear oligomer way with anisotropic rotation, in this fashion, the rotation along the short axis of the molecule is fast and limits relaxivity. Usually,

dendrimers consist of Gd^{3+} complexes have higher relaxivity since the dendritic structure creates a more isotropic rotational dynamic which in this situation the effect of the larger molecular weight

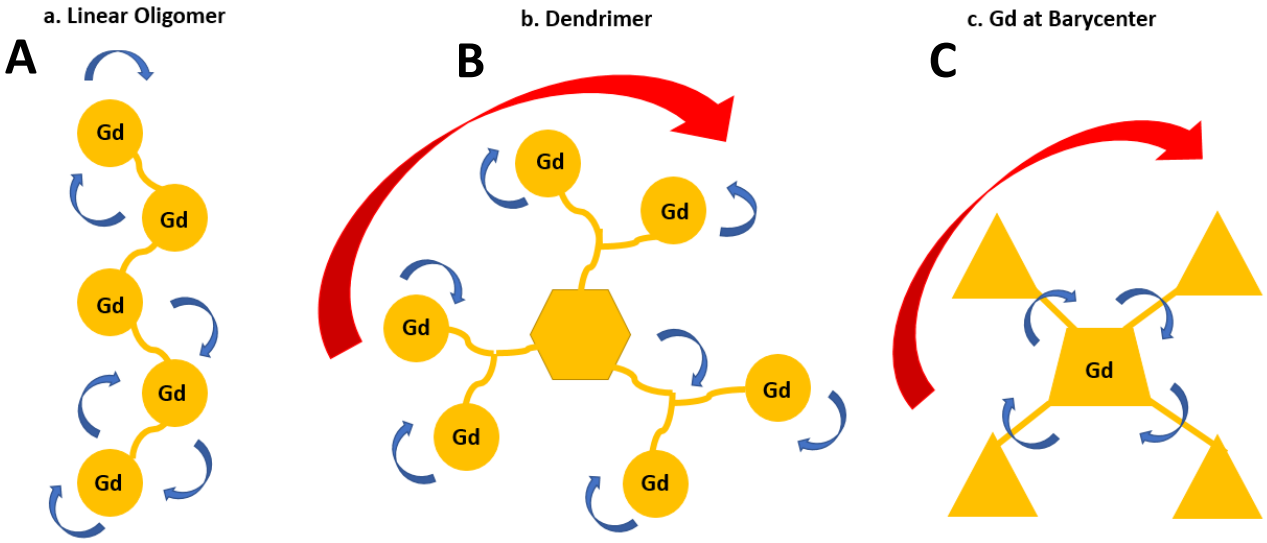

***Figure 1.1**. Different types of motions and linking strategies affecting relaxivity.*

and size on relaxivity is more effective (Fig 1.1 A).

An example of a linear polymer is based on a modified dextran polymer with DO3A-monoamide chelates with molecular weight of 52 kDa. The relaxivity of this molecule is about 10.6 $mM^{-1}.s^{-1}$ (37°C, 0.47 T) per Gd^{3+} [38]. Twenty-four of these Gd^{3+} chelates are linked together to create a polyamide dendrimer with the name of Gadomer-17. With similar conditions (40°C, 0.47 tesla), Gadomer has a relaxivity of 16.5 $mM^{-1}.s^{-1}$ per gadolinium [36]. The Gd^{3+} chelates in the dendrimer can also have internal motion within the connectors in the dendrimer core.

Another strategy to have the best effect of motion on relaxivity is to create a site for Gd^{3+} at the barycenter of a compound. For instance, Gadomelitol (also called P792 or Vistarem) which is a Gd-DOTA with large hydrophilic groups attached to each of the α-carbons on the acetate branch follows this strategy. In this molecule, the Gd-H water vector rotates with the entire molecule, however, there is some level of flexibility within the hydrophilic arms, (Fig. 1.1 B). This

limitation in rotation can cause a significantly high relaxivity which has r_1 of 39.0 $mM^{-1}s^{-1}$ (37°C, 0.47 T) for a molecule with the size of just 6.4 kDa. It has been reported that this rotational effect can be tuned by changing the size of the hydrophilic arms [39-41].

Another strategy for controlling rotational motion is called metal templated self-assembly approach [42, 43]. In this molecule, Gd^{3+} complexes are attached to rigid bidentate or tridentate ligands, and then a transition metal is used to connect the Gd^{3+} complexes in a compressed space. Another group has used this study with Gd^{3+} complexes with two water molecules [44]. In this structure, there are two complexes that are covalently linked to a bipyridyl ligand which coordinate Fe (II) in an octahedral structure leading to a high relaxivity per Gd^{3+} and per molecule. This specific compound has high Gd^{3+} content and low molecular weight which makes it more demanding as a contrast agent. The per Gd^{3+} relaxivity of the compound bipyridyl Gd^{3+} dimer is 12.5 $mM^{-1}s^{-1}$ at 40 MHz, 37°C compared to 3.8 $mM^{-1}s^{-1}$ for [Gd(DTPA)(H_2O)]. In conclusion, the high relaxivity can be attributed to two exchangeable water molecules and a large molecular weight. In the presence of Fe^{2+} and bipy ligands, the Gd^{3+} ions are part of the whole molecule with a longer correlation time which doubles the relaxivity to 26.5 $mM^{-1}s^{-1}$.

These were just a few examples to demonstrate how relaxivity can be tuned in contrast agents of stable gadolinium complexes by changing the number of water molecules in Gd^{3+} coordination site, water exchange rate, and dynamics of the molecules related to their rotations. In some cases, these parameters can be changed by introducing a new environment such as buffer in the presence of serum albumin. Specifically, in this case, both water exchange rate and rotational motion contributed to an increase in relaxivity, and only one of them could not change relaxivity significantly by itself. Therefore, it would be very informative to know exactly what molecular

parameters can contribute to relaxivity in more details and how can these specific parameters be tuned. In order to answer these questions, we need to study the relaxivity theory more in details.

1.5 **Relaxivity**

The deterioration of an MRI signal which is the decay of water relaxation is analyzed in terms of two separate processes: First, spin-lattice relaxation time (T1) and second, spin-spin relaxation time (T2). When a proton is placed in a magnetic field, the overall magnetization will be on the z axis. When an RF pulse is given, then the net magnetization will be oriented in different directions as long as the RF pulse is in place. Immediately after that RF pulse is ended, the protons will relax to their original position.

Spin–lattice relaxation is the mechanism by which the z component of the magnetization vector comes into thermodynamic equilibrium with its surroundings (the "lattice") in nuclear magnetic resonance and magnetic resonance imaging. It is characterized by the spin–lattice relaxation time, a time constant known as T1. T1 characterizes the rate at which the longitudinal M_z component of the magnetization vector recovers exponentially towards its thermodynamic equilibrium, according to equation:

$$M_z(t) = M_{z,eq} - [(M_{z,eq} - M_z(0)] e^{-t/T1} \quad (1\text{-}2)$$

Or, for the specific case that $M_z(0) = 0$

$$M_z(t) = M_{z,eq} (1 - e^{-t/T1}) \quad (1\text{-}3)$$

It is thus the time it takes for the longitudinal magnetization to recover approximately 63% [1-(1/e)] of its initial value after being flipped into the magnetic transverse plane by a 90° radiofrequency pulse.

The spin–spin relaxation is the mechanism by which M_{xy}, the transverse component of the magnetization vector, exponentially decays towards its equilibrium value in NMR and MRI. It

is characterized by the spin–spin relaxation time, known as T2, a time constant characterizing the signal decay. It is named in contrast to T1, the spin–lattice relaxation time. It is the time it takes for the magnetic resonance signal to irreversibly decay to 37% (1/e) of its initial value after its generation by tipping the longitudinal magnetization towards the magnetic transverse plane. Hence the relation:

$$M_{xy}(t) = M_{xy}(0)\, e^{-t/T2} \qquad (1\text{-}4)$$

T_2 relaxation generally proceeds more rapidly than T_1 recovery.

The MRI signal enhancement in tissues are determined by T1 and T2 relaxation time. MRI pulse sequences use different repetition time (TR) and echo time (TE) in order to observe the T1 and T2 effect on signal enhancement. Based on TR and TE parameters, different pulse sequences can be applied such as T1-weighted MRI, T2 (or T2*)-weighted MRI, proton density-weighted, T1 map and T2 map. Since T1 effect is being observed in T1-weighted MRI, it usually has a short TR and very short TE to minimize the T2 effect, For T2 (or T2*)-weighted MRI, TR is very long (usually more than 3 s) to minimize the T1 effect and TE is relatively long (at around 40 – 100 ms). Proton density imaging has both T1 and T2 effect which has long TR (more than 3 s) and short TE. T1 and T2 maps are generally more sensitive than T_1- and T_2-wieghted sequences as they reflect the actual T1 and T2 values rather than intensities. To generate T2 map, one single TR is used and multiple TEs are applied. For T1 map inversion recovery, multiple inversion times (TI) are being used. Using different TRs and TEs, MRI is able to show the differences of T1 or T2 (or T2*) of the tissue. As it was mentioned before, Gd^{3+}-based MRI contrast agents are mainly T1 agents because they can only shorten the T1 time of the water, however other contrast agents such as iron oxide nanoparticles are T2 agents because of their ability to shorten T2 time, therefore they are widely used in T2- or T2*-weighted MRI sequences. Generally, contrast agents have the ability

to shorten either T1 or T2 not both of them and these contrast agents cannot be used in both T1-weighted and T2-weighted MR imaging. Moreover, clinical Gd^{3+}-based MRI contrast agents have very low relaxivity and sensitivity which further limits their application in T1-weighted MRI.

An MRI contrast agent with both high r_1 and r_2 has the capability to change the MRI signal in both T1- and T2-weighted images, and both T1 and T2 maps can be used for imaging with such contrast agent. In addition, T1 inversion recovery with short TE which uses inversion time to suppress the signal can be combined with such contrast agent. ProCA32.collagen1 has both high r_1 and r_2 values and enables both T1 and T2 imaging. The application of a T1-T2 contrast agent has not been widely reported in the literature since the majority of contrast agent are either T1 or T2 agents and their relaxivity specially for small-molecule clinical contrast agents are low.

A gadolinium complex causes the relaxation of solvent water (bulk water) which is a phenomenon with multiple variables involved. When water molecule is close to Gd^{3+} or any other metal with similar properties, it will be relaxed and can be exchanged with water molecules in the solvent. Therefore, three types of water molecules will be involved. First, there is *inner-sphere* water. This type of water has directly coordinated Gd^{3+} in the binding site through its oxygen arms. Second, there is *2nd-sphere* water. In this type of water molecule, they have hydrated the Gd^{3+} complex, and they spend specific time with the complex which is longer than the translational diffusion time of pure water. Third is *outer-sphere* water. Outer-sphere water can interact with the waters that are with Gd^{3+} and they are guided only by translational diffusion and a distance of closest approach [6].

The water hydrogen has a T1 relaxation by Gd^{3+} which happens through dipolar mechanism. Generally, relaxation time will be affected by the number of water molecules, their distance to

Gd^{3+}, rate of exchange with bulk solvent, as well as rotational correlation time, τ_c which all of them will be discussed in more details.

Constant changes in magnetic field strength can cause spin transitions and relaxation. In order to quantify these changes, usually, a correlation time is defined as the time constant for characterizing these fluctuations and $1/\tau_c$ is the average rate constant to quantify the changes in dipoles of magnetic field. The phenomena resulting in to fluctuation of magnetic dipoles are: 1. Electronic relaxation ($1/T_{1e}$) at the Gd^{3+} ion creates. 2. Rotational diffusion ($1/\tau_R$) of the Gd^{3+} complex. 3. Water exchange in and outside of the first ($1/\tau_m$) or 2nd ($1/\tau_m'$) coordination spheres for the hydrogen nucleus. The shortest time constant or the fastest rate has the maximum effect on the extent of relaxation. The lifetime of water in the second sphere and its corresponding correlation time is usually ~ 10's of picoseconds, however, the water in the first coordination sphere has a much longer lifetime which is around 1 ns–10,000 ns, therefore, the correlation time is usually rotational diffusion or electronic relaxation [6].

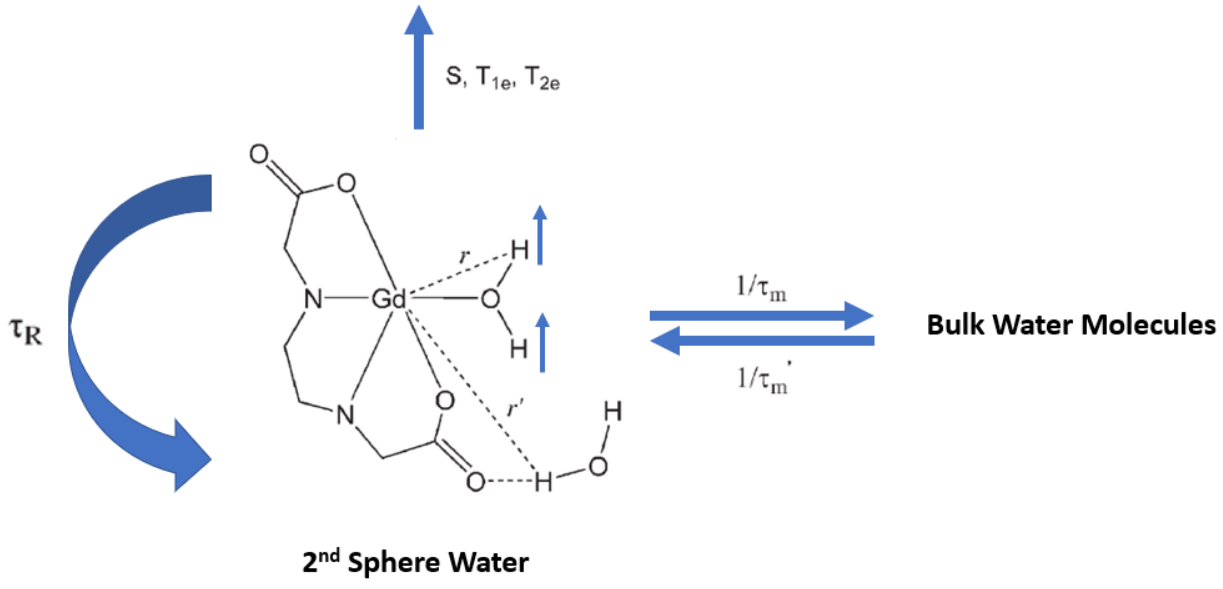

Figure 1.2 *Describing molecular parameters that are affecting inner- and 2nd-sphere relaxivity.*

Fig. 1.2 is demonstrating these effects. The hydrogen nuclei have magnetic dipoles shown by the vectors. The water number that is shown by q are the waters in the inner-sphere which has Gd–H distance of r and a residency time of τ_m, and q´ waters in the second-sphere at a Gd–H distance of r´ and residency time τ_m´. Besides hydrogen, Gd^{3+} also has magnetic dipole which is stronger and is shown by a large vector and quantified by spin S. The magnetic dipole can undergo relaxation which is defined by T_{1e} and T_{2e}. If the complex tumbles in a isotropical manner, the rotational motion resulting from this tumble is defined as rotational correlation time, τ_R.

Water in the outer-sphere is defined by a parameter called translational diffusion correlation time τ_D and a distance of closest approach called *a*. Therefore, there are a total of 11 parameters that can contribute to relaxation at a magnetic field of B_0. In addition, electronic relaxation also depends on magnetic field. It is important to mention that the simple measurement of relaxivity cannot represent the effect of all these parameters. Some of these parameters and their effect on relaxivity can be stimulated and some of these parameters can be determined independently. In conclusion, a more complete perception of the molecular basis of relaxivity evolved the contrast agent field and can result in improved agents with higher relaxivity [6].

1.5.1 Inner-Sphere Relaxivity

Relaxivity originating from the inner-sphere waters can be explained by equation (1-2). In this equation, there are two sites for exchange where T_{1m} is the T1 of the water hydrogen in the inner-sphere and $[H_2O]$ is the water concentration in mM. In order to increase relaxivity, water number q can be increased or T_{1m} or τ_m can be decreased.

$$r_1^{IS} = \frac{q/[H_2O]}{(T_{1m} + \tau_m)} \qquad (1\text{-}5)\ [6]$$

1.5.2 Hydration number, q

The safety of contrast agents used for human is the most important priority in developing them and they should be stable enough so that the complex that is holding the Gd^{3+} does not release it into the body, therefore due to safety concerns, the number of waters (q) that can be incorporated into the complex to increase the relaxivity of the contrast agent is limited. Theoretically, when there are more waters in Gd^{3+} coordination sites as ligands, the thermodynamic stability of the complex is compromised and the Gd^{3+} is likely to be released from the complex. Another disadvantage of increasing the water number is that other ligands such as endogenous phosphate or bicarbonate can replace and displace water and coordinate Gd^{3+} instead which results in reduced relaxivity. For instance, if an acetate group is removed from $[Gd(DOTA)(H_2O)]^-$ to produce $[Gd(DO3A)(H_2O)_2]$, this will increase the hydration number but still results in a stable complex[45]. The water molecules can be displaced by anion binding as well. A group of compounds called hydroxypyridinone (HOPO) described in the literature have shown stability with q = 2 and are resistant to anion coordination [46-48].

1.5.3 Inner-Sphere water relaxation

As it can be observed in eqn (1-5), both the relaxation time of the bound water (T_{1m}), and the water residency time (τ_m) should be as short as possible to increase the relaxivity. At the beginning of development of MR contrast agents, T_{1m} was larger than τ_m and therefore it was T_{1m} that was limiting the relaxivity of these agents. The compounds shown in Figure 1.1 followed the same rule for their relaxivity in buffer. Dipolar relaxation originating from electron–nuclear spin coupling can be described by Eqns (1-6) and (1-7):

$$\frac{1}{T_{1m}} = \frac{2}{15}\frac{\gamma_H^2 g_e^2 \mu_B^2 S(S+1)}{r_{GdH}^6}\left[\frac{7\tau_{c2}}{1+\omega_S^2\tau_{c2}^2} + \frac{3\tau_{c1}}{1+\omega_H^2\tau_{c1}^2}\right] \quad (1\text{-}6)\ [6]$$

$$\frac{1}{\tau_{ci}} = \frac{1}{\tau_{m}} + \frac{1}{\tau_{R}} + \frac{1}{T_{ie}}; i = 1,2 \qquad \text{(1-7) [6]}$$

With respect to these equations, relaxation depends on the Gd–H distance, r_{GdH}, Larmor frequency of the proton ω_H (in rad/s), the electron Larmor frequency ω_S ($\omega_S = 658\omega_H$), and correlation times τ_{c1} and τ_{c2}. The $\omega^2\tau_{c2}^2$ are referred to as dispersive terms since $\omega^2\ \tau_{c2}^2 > 1$, the relaxation rate decreases and disperses with increase in frequency or magnetic field. Since the Larmor frequency of the electron is 658 times bigger than the proton, the first term in square brackets disperses at a lower magnetic field compared to the second term, however, if the correlation time is independent of magnetic field, then the relaxation rate relies on proton Larmor frequency. Usually, at low fields the rate decreases to almost 70% and then the rest will disperse at higher fields. For Gd^{3+} complexes, the correlation time depends on magnetic field and the NMRD behavior is more complicated.

1.5.4 Gadolinium-water distance

In equation (1-6), the term outside the square brackets are physical constants. First, it is the spin quantum number of Gd^{3+} which is S = 7/2, and Gd–H distance, which is shown by r_{GdH}. Gd^{3+} is a suitable metal as a relaxation agent since it has large spin number and slow electronic relaxation. Furthermore, Gd–H distance is important and if this distance is reduced, then it would result in increase in relaxivity. The distance varies based on literature, however it ranges between 2.7 and 3.3 A° which is obtained indirectly. One of the direct determination methods of calculating the Gd–H ion–nuclear distance is to use neutron diffraction on single crystals or using isotopic exchange techniques. Electron–nuclear double resonance (ENDOR) spectroscopy is also possible to use for measurement of Gd-H distance directly. ^{1}H ENDOR studies make the determination of

the hyperfine interactions between the Gd^{3+} and the water proton possible. One and two dimensional ENDOR studies have illustrated that Gd-H distance is about 3.1 A° for 8- and 9-coordinate complexes of Gd^{3+} and it is independent of ligand type or total charge. It is nearly impossible to change this distance in order to have higher relaxivity values [49-51].

1.5.5 Rotational diffusion

Based on eqn (1-7), the correlation time can be most affected by the shortest correlation time which are either rotation, electronic relaxation, or chemical exchange times. At the magnetic field strength of 1.5 Tesla (64 MHz) which is the most commonly used magnetic field in clinical imaging, the most effective correlation time is rotational diffusion in most of the cases. For instance, in simple monomeric Gd^{3+} complexes, τ_R is in the range of 0.1 ns which have rotational rate constant in the range of few GHz leading to small relaxation. Slowing down rotation leads to higher relaxivity values at 1.5 tesla.

In higher fields, if a molecule's rotation is too slow, then based on $\omega^2\tau_{c2}^2 > 1$, the relaxivity decreases with increasing τ_R. Relaxivity can be simulated for three values of τ_R. For instance, r_1 can be simulated over a range of magnetic fields between 0-3 Tesla for correlation times of 0.1 ns (small molecule contrast agents, Gd-DTPA), 1 ns (intermediate motion), and 10 n (albumin bound contrast agents). It can be concluded that by increasing the rotational correlation time from 0.1 ns 10 ns, the relaxivity will also increase, however, this effect is maximized at lower magnetic field strengths. It is worth mentioning that r_1 cannot obtain the zero value since there is also an outer-sphere parameter exists that contribute to relaxivity which has its own correlation time which is very short.

Using various methods such as NMR relaxation, EPR, and fluorescence, rotational diffusion can be estimated. Furthermore, it can also be calculated from the Stokes–Einstein

equation as described in the literature. For larger molecules such as proteins, rotation may not be isotropic. Correlation time can be reduced with anisotropic rotation or internal motion within a molecule predicted by an isotropic model based on molecular weight. Anisotropy can be observed when relaxation is determined as a function of magnetic field. It has been reported that there are two types of motion in a complex molecule which the spectral density function can be simulated by two correlation times corresponding to these motions, one for the global motion (τ_g) of the molecule and another for the local motion (τ_1) of the Gd–H_{water} vector [6, 47, 48, 52].

$$\frac{1}{T_{1M}} = \frac{C}{r_{GdH}^6}\left[\left(\frac{7F\tau_{cgi}}{1+\omega_S^2\tau_{cgi}^2} + \frac{7(1-F)\tau_{cli}}{1+\omega_S^2\tau_{cli}^2}\right) + \left(\frac{3F\tau_{cgi}}{1+\omega_H^2\tau_{cgi}^2} + \frac{3(1-F)\tau_{cli}}{1+\omega_H^2\tau_{cli}^2}\right)\right] \quad (1\text{-}8)$$

$$\frac{1}{\tau_{cgi}} = \frac{1}{\tau_g} + \frac{1}{T_{ie}} + \frac{1}{\tau_m};\ \frac{1}{\tau_{cli}} = \frac{1}{\tau_{cgi}} + \frac{1}{\tau_1};\ i = 1,2 \quad (1\text{-}9)$$

Eqn (1-8) and (1-9) relates this parameter to dipolar relaxation of Gd^{3+} where C is a constant consists of terms from eqn (1-7). The degree of isotropic motion is described by the order parameter S^2 (also shown by F to avoid confusion with the spin quantum number). At higher fields, $\omega_S\tau >> 1$ and the spectral density is given by the second term in parentheses in eqn (1-8).

1.5.6 Electronic relaxation

Electronic relaxation for Gd^{3+} is a sophisticated process which relies on magnetic field. At lower magnetic fields usually below 0.1 T, the electronic relaxation is short or fast and therefore can dominate the correlation time, see eqn (1-8). With increase in magnetic fields, the electronic relaxation decreases and therefore becomes slower than rotational motion, see eqn (1-11). As a

result, the correlation time of nuclear relaxation depends on magnetic field and changes as a function of field.

$$1/T_{1e},\ 1/T_{2e} \gg 1/\tau_R;\ T_{1e} \approx \tau_{c1},\ T_{2e} \approx \tau_{c2} \quad \text{at low field } (B_0 < 0.1 \text{ T}) \tag{1-10}$$

$$1/T_{1e},\ 1/T_{2e} \ll 1/\tau_R;\ \tau_R \approx \tau_{c1} \approx \tau_{c2} \quad \text{at high field } (B_0 > 1.5 \text{ T}) \tag{1-11}$$

At lower magnetic fields, electronic relaxation is the dominant factor τ_c and as the relaxivity increases so as the magnetic field since electronic relaxation slows down and τ_c increases. In magnetic field strengths of about 0.7 T, relaxivity reaches its maximum and then starts to decrease since $\tau_c\omega_H$ becomes larger than 1, therefore, affecting eqn (1-8) and making it larger [47, 53].

1.5.7 Water exchange rate

Water exchange is another important factor affecting the relaxivity. The water molecule coordinating the Gd^{3+} in the complex must be exchanging rapidly with the bulk water in the solvent so that it can transfer the relaxation effect to the solvent. The water exchange parameter can be explained through ^{17}O NMR transverse relaxation rate measurements at different temperatures at high magnetic fields. There has been a significant body of data in the literature trying to address this effect. For instance, replacing an acetato oxygen donor with an amido oxygen donor will lead to a slower water exchange rate. In another case, for complexes experiencing dissociative water exchange, increase in the steric bulk can increase the water exchange rate. Replacing an acetato oxygen donor with the larger phosphonato oxygen donor can increase the exchange rate [54].

The water residency time τ_m ($k_{ex} = 1/\tau_m$) plays a direct role for relaxivity in the equation as well as through T_{1m}. If water exchange value is short or very fast, then the τ_m can is the correlation

time that dominates T_{1m}. In addition, if water exchange is very slow, relaxivity will be affected and decreased since the relaxation effect is not transferred to the bulk water sufficiently enough. The very fast water exchange can also have a negative impact on relaxivity since if the water is exchanging too fast then it does not have the ability to coordinate the Gd^{3+} and the time is not long enough for the water to be relaxed. The dependency of relaxivity on τ_m can be observed where inner-sphere relaxivity is simulated for a q = 1 in a 1.5 T system at different values of τ_R. The relaxivity can be affected with water exchange rate being too slow or too fast, however, this effect can observed if other important parameters such as τ_R are in their optimized conditions [55].

1.5.8 2nd-sphere and outer-sphere relaxivity

As it was mentioned before, 2nd-sphere and outer-sphere relaxivity can also contribute to relaxivity coming from the bulk water surrounding the Gd^{3+} complex. Using hard-sphere model of Hwang and Freed, the outer-sphere relaxivity can be simulated where relaxation is measured using the diffusion coefficient of water as well as distance of closest approach. The hydrogens of water that can be exchanged in the second coordination sphere of Gd^{3+} can also affect the relaxivity. These protons originate from water in the second coordination sphere or the sites being protonated on the molecule. As it was demonstrated, complexes even with q=0 can have high relaxivity. For instance in $[Gd(DTPA)(H_2O)]^{2-}$ approximately %50 of the effect originates from the inner-sphere water. In addition, according to outer-sphere prediction model, protein binding does not have any effect on relaxivity, however, the level and impact of 2nd-sphere on relaxivity is very difficult to predict. For complexes with q > 0, all the previously mentioned parameters will affect the relaxivity as well as the number of hydrogens in the 2nd sphere that can be exchanged. Moreover, the hydrogen distance from Gd^{3+}, and their lifetimes become important. When each of the single molecular parameters measured cannot contribute to the high relaxivity of a complex then the large

2nd-sphere effect is very well observed. Sometime by fitting NMRD data, additional parameters accounting for 2nd-sphere relaxivity can be modeled [56-58].

1.5.9 Effect of field strength and temperature

Relaxivity strongly depends on magnetic field strength. Moreover, since water exchange rate and rotational diffusion are affected by temperature, then as a result relaxivity will be affected by temperature as well. It is important to compare different relaxivity data at the same temperature and field strength. Usually the ideal temperature in which the data are compared is 37°C as it is the physiological temperature and all of the contrast agents are being applied in vivo at 37°C. Although most of the clinical MRI contrast agents function at 1.5 T (64 MHz), the clinical field is shifting towards higher magnetic fields as high as whole body 7.0 T (300 MHz) instruments. The reason is that the higher field strengths provide higher signal to noise ratio and increased resolution. At higher magnetic fields, the relaxivity is decreasing, therefore, clinical contrast agents should be less useful, however relaxation time of different tissues will increase with increase in magnetic field, therefore so less contrast agent with a fixed relaxivity is needed to produce the same level of contrast. Higher magnetic fields can reduce the acquisition time and the presence of a relaxation agent can make the acquisition time even shorter [59].

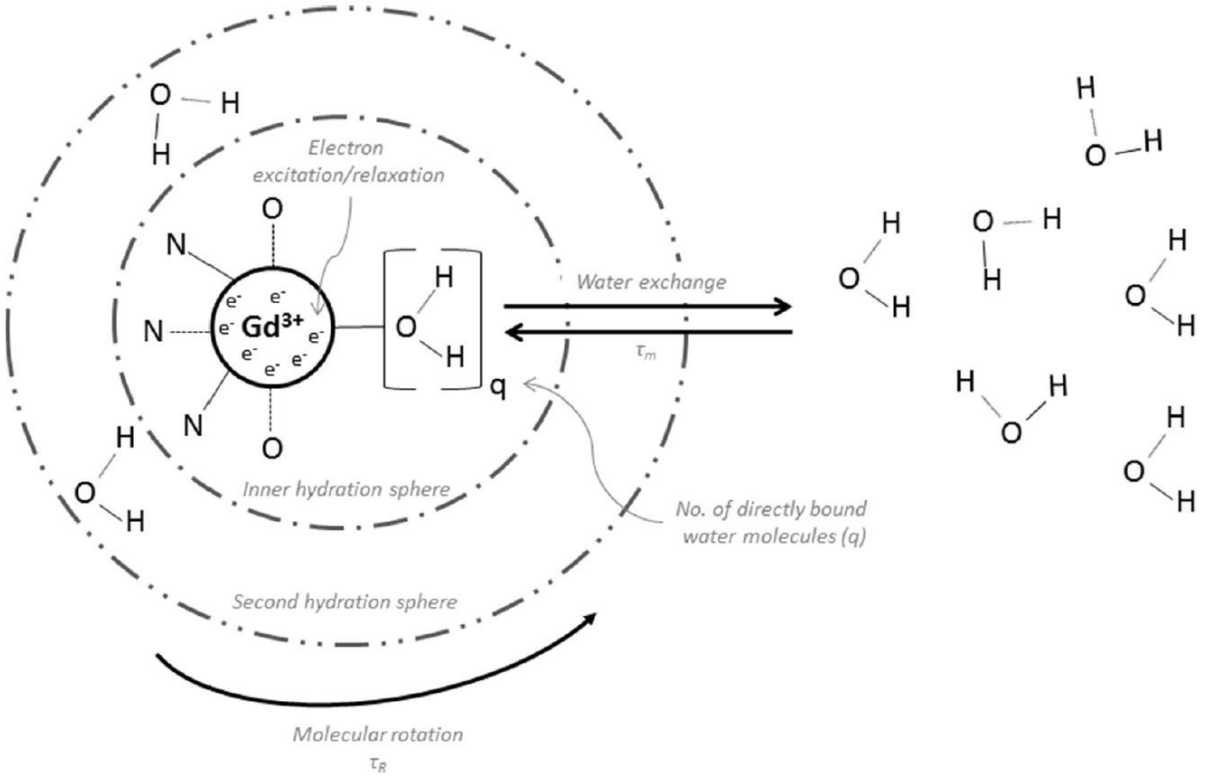

Figure 1.3 *A diagram demonstrating the parameters affecting relaxivity of a* Gd^{3+}*-based MRI contrast agent complex [6].*

In conclusion, there has been a tremendous effort to develop and design new MRI contrast agents with significant progress made. A more complete and thorough understanding of the parameters affecting relaxivity such as coordination chemistry and biophysics can result in improved contrast agents which will speed up the progress. among all of the parameters discussed, the most important one is the rotational motion since it depends on rotational dynamics. There are certain strategies being used to modulate the rotational dynamics in order to increase relaxivity. For instance, linking multiple gadolinium complexes is one of those approaches. Perception of how to modulate the water exchange rate at the Gd^{3+} coordination site and its complex can also benefit the current progress in the development contrast agents. At 1.5 T which is the most common

magnetic field for imaging with contrast agents, rotation, hydration, and water exchange rate are the key parameters.

1.6 Current advancements in improving the relaxvity of Gd^{3+}-based MRI Agents

Gadopentetate dimeglumine or Magnevist was the first gadolinium-based contrast agent (GBCA) which become available for clinical use worldwide in 1988. After that eight more gadolinium contrast agents based on chelates were introduced and approved in different countries across the world. Progress in the field of contrast media and the MRI instrument itself has increased the accuracy and application of contrast-enhanced-MRI (CE-MRI). Currently, CE-MRI as a diagnostic imaging tool covers approximately 30 million procedures annually. There is a close relationship between clinical diagnosis and the monitoring of specific therapies and research into new MRI contrast agents [60].

Significant progress has been made in improving the relaxivity of MRI contrast agents and there has been an ongoing effort. For instance, the relaxivity has been improved by covalently linking Gd^{3+}-chelates to nano-carriers, such as dendrimers, liposomes, nnanoparticle emulsions viral capsids, and nanotubes. Moreover, non-covalent binding between Gd^{3+} chelators and proteins, such as MS-325, have shown significant increase of relaxivity [61-66]. However, there are limited number of publications which reported the use of proteins to function as ligands to bind Gd^{3+} to improve the imaging capabilities.

Overall, there are two general approaches to use proteins Gd^{3+} ligands. First, Gd^{3+}-chelates will be covalently or non-covalently conjugated to proteins. Second, Gd^{3+} binding pockets are directly designed inside the proteins or basically the protein itself functions as a chelator. The first approach has been used numerously to create new class of MRI contrast agents. In these studies, Gd^{3+} chelates were designed to non-covalently interact with proteins, and as a result they

significantly increased the relaxivity of Gd^{3+} chelates [29, 30]. Furthermore, in a study proteins such as albumin directly used to interact with DTPA-dianhydride to produce a DTPA-protein complex loaded with Gd^{3+} [67]. Albumin labeled with Gd^{3+} has been extensively used in many preclinical procedures such as assessment of tumor permeability and angiogenesis by CE-MRI of cancer tissue, and monitoring vasculature changes of tumors [68, 69]. In another study, a class of biodegradable contrast agents were designed by conjugating evenly distributed lysine residues on protein polymers to Gd^{3+} chelates. Then the polymer length and lysine distribution were optimized to produce an r_1 of 14 $mM^{-1}s^{-1}$ per Gd^{3+} and 46.1 $mM^{-1}s^{-1}$ per particle at 1.5 T and 37 ˚C. These contrast agents can be excreted rapidly in vivo [70]. As creating a Gd^{3+} binding pocket inside a protein is challenging, the second approach has not been used frequently. When a protein is designed to be used as chelator for Gd^{3+}, several important parameters must be optimized for relaxivity which will be discussed later in this chapter.

1.7 Design of protein-based MRI contrast agent with improved relaxivity

1.7.1 MRI contrast agents based on proteins

One of the interesting approaches for the development of new MRI contrast agents is to use native or engineered proteins. Approximately one third of proteins have metal ions such as calcium, magnesium, zinc, copper, iron, and manganese in their structure and these proteins that exist naturally have Cu^{2+}, Fe^{2+}, Fe^{3+}, Mn^{2+}, and Mn^{3+} with spin quantum numbers ranging from 1/2 to 1/5. Some native proteins, such as hemoglobin, and engineered proteins like BM3h have been used to monitor brain activities in human and animals [71-73]. In addition, studies have shown that metalloproteins can be engineered to trap different metals such as manganese or iron in ferritin with significantly high T2 property per particle (r_2 = 5300 $mM^{-1}s^{-1}$) which can be applied as T2 MRI agents [74-76]. Other proteins such as human protamine-1 expressed by live cells have

been used as chemical exchange saturation transfer (CEST) MRI contrast agent. This protein is based on a small arginine-rich protein, which functions through CEST mechanism [77]. In the next section our protein design for development of MRI contrast agent will be discussed.

1.7.2 Choice of protein for designing Gd^{3+}-based MRI contrast agents

Instead of conjugating proteins with small Gd^{3+} chelators, a very different approach was chosen and used in which a Gd^{3+}-binding pocket was designed and engineered into a protein scaffold to change it to a protein chelator [78-80]. The design of protein-based contrast agent (ProCA) was based on the discussions mentioned about the factors affecting relaxivity as well as several other considerations. Proteins are in the category of biocompatible materials which will be beneficial for in vivo applications. Other protein drugs such as insulin have been successfully used in humans against different diseases [81, 82]. Moreover, there are some proteins that their well-folded structures and proper sizes allow god circulation and tissue penetration. For instance, a globular protein with molecular weight of 10–14 kDa has a size of 2–3 nm, therefore it can be excreted from kidney. Many computational and protein engineering strategies were applied to design Gd^{3+} binding sites in proteins with high coordination number and strong binding affinity. Some of these proteins have well-studied structural and dynamic profiles by high-resolution NMR which can be used for designing Gd^{3+} MRI contrast agents with improved metal binding and relaxation properties. Finally, when a protein-based contrast agent was developed with high relaxivity and metal-binding properties, its application can be extended to targeted contrast agents with the addition of different moieties to target various disease biomarkers by protein modification.

1.7.3 Design of MRI Contrast Agent based on α-Parvalbumin

Based on important parameters affecting relaxivity such as water number, rotational correlation time, water exchange rate, and etc as well as our strategy to design Gd^{3+} binding sites into a protein as an MRI contrast agent with high relaxivity, high dose efficiency and strong metal binding affinity, we have chosen α-parvalbumin as a scaffold protein to host Gd^{3+}-binding sites. Our lab had previously developed a protein contrast agent (ProCA32) [83] , which was designed and developed by creating one more negatively charged ligand S56D in the EF-hand motif 1 of rat or human α-parvalbumin to create Gd^{3+} binding affinity and selectivity. Parvalbumin protein was selected since it had strong calcium binding affinity (Kd = $8.35 \pm 0.29 \times 10^{-9}$ M; Fig. 1.4 a) and stability. Furthermore, F103W mutation was made to introduce luminescence resonance energy transfer (LRET) property to the protein to determine its metal binding affinity and water number by Tb^{3+} luminescence life time decay. The protein was further modified with PEGylation of ProCA32 by TMS(PEG)12 (named as ProCA32-P40) to increase blood retention time, liver preference, solubility, as well as stability of the designed protein [84].

There are some unique factors that make α-parvalbumin one of the best candidates for the design of a protein-based MRI contrast agent. Design of Gd^{3+} binding sites was based on our analysis of metal binding sites in different small chelators and metal proteins. It is important to mention that Gd^{3+}, Tb^{3+} and Ln^{3+} have similar coordination to Ca^{2+}. In addition, like Ca^{2+}, they prefer oxygen as ligands. Other small chelators used in generating contrast agents such as DTPA have both oxygen and nitrogen atoms as ligands, however, proteins like α-parvalbumin use oxygen as a ligand most of the times [85]. In α-parvalbumin, oxygen ligands from the side chain oxygens of Glu and Asp are used at different stretches of the protein sequence to coordinate Gd^{3+}. One position of metal geometry is left open to allow fast water exchange between solvent and metal

(Fig. 1.4 B). We have concluded that inserting a metal binding site without internal flexibility is crucial to achieve a high relaxivity contrast agent based on a protein. In the next section, different factors contributing to high relaxivity in ProCA32 will be discussed.

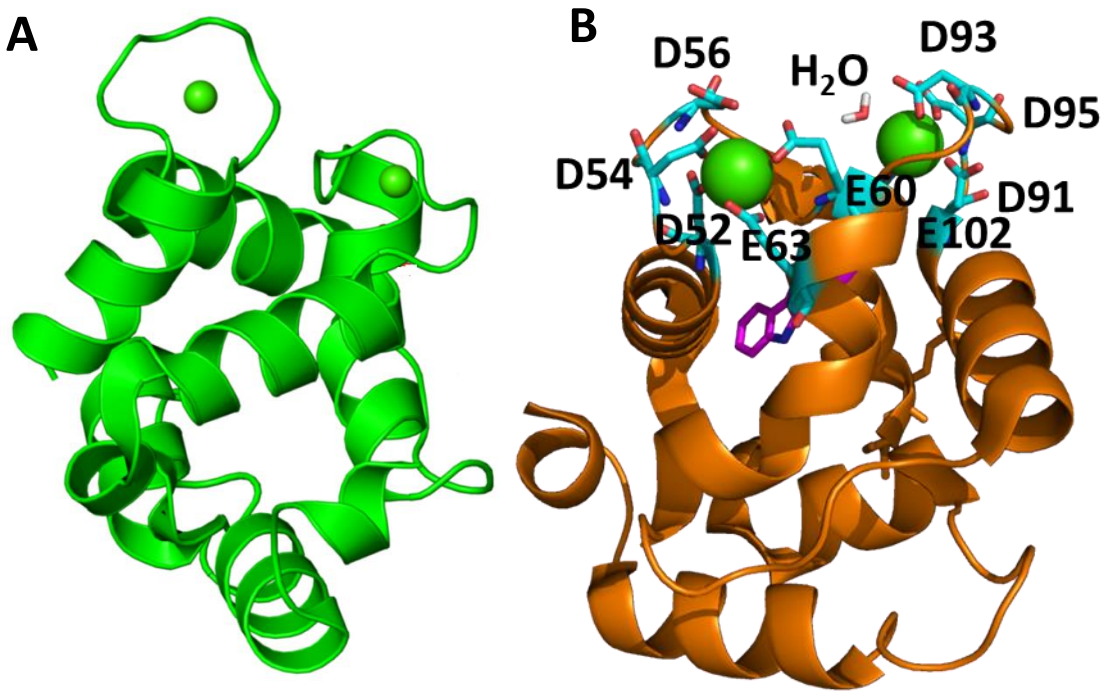

Figure 1.4 *Model structure of rat α-parvalbumin (a) and ProCA32 (b) with several mutations*

1.7.4 Factors Contributing to High Relaxivity in ProCA32

As it was mentioned before, there are different parameters such as correlation time and inner, second, and outer sphere water number that can affect the significantly high relaxivity in ProCAs compared to contrast agents based on small molecules. The first important parameter is the optimized *Correlation Time* which is one of factors contributing to the high relaxivity of ProCA32. As shown in previous equations, a protein contrast agent with τ_R of approximately 10 ns has a near optimized relaxivity at the most common magnetic field of 1.5 T. High-resolution

NMR was used to study the dynamic properties of our designed protein contrast agent [86, 87]. Based on other proteins with the similar, the τ_c of a protein MRI contrast agent is approximately 9.08 ns in the presence of metal and 9.20 nsec in the absence of metal. Furthermore, the dynamic NMR data demonstrate that the metal-binding pocket inside the protein contrast agent can rotate along with the scaffold protein as a rigid complex.

The second parameter contributing to the high relaxivity value is the *water number* which is also optimized in the protein-based MRI contrast agent. As shown in previous equations, the relaxivity of a contrast agent directly corresponds to q. One can increase the relaxivity of a contrast agent by increasing the water molecules coordinating the Gd^{3+} at the same time. In a study to develop an enzyme responsive contrast agent named Egad, water access to Gd^{3+} (q = 0) was denied by addition of a galactopyranose moiety to a Gd-DO3A chelate, however, after galactosidase activation, galactopyranose sugar was cleaved from Gd^{3+}, therefore exposing it to water molecules which subsequently increased water number from 0.7 to 1.2 [88] and the r_1 increased from 0.90 $mM^{-1}s^{-1}$ to 2.72 $mM^{-1}s^{-1}$ accordingly [89]. We have shown that ProCA32 has q=0.5 shared by the two binding sites of Gd^{3+} which can increase the relaxivity. Moreover, larger surface of proteins can also contribute to high relaxivity through second sphere relaxivity that could reach as high as 3.3 and 8.8 $mM^{-1}s^{-1}$ at 20 and 60 MHz, respectively (τ_R = 10 ns, τ_m = 10 ns, q = 4, r_{GdH} = 5 A°). According to all the parameters, it is highly likely that ProCA32 high relaxivity benefits from coordination water from the inner, second, and outer spheres of which cause the increase of relaxivity in ProCA32.

Table 1.2 *The relaxivity of some of the research-based Gd^{3+} MRI contrast agents [67, 84, 87, 89-106].*

Category of Contrast Agent	Contrast Agent	r_1 ($mM^{-1}s^{-1}$)	r_2 ($mM^{-1}s^{-1}$)	B_0 (T)
Paramagnetic Nanoparticles	$Gd@C82(OH)_{22\pm2}$	61.1		4.7
Nanodiamond	Nanodiamond	58.82		1.5
Trimetallic Nitride Metallofullerene CA	$Gd_3N@C_{80}$[DiPEG$(OH)_x$]	79		2.4
Dendrimer Nanoclusters	Dendrimer Nanoclusters	12.3		
Hydroxypyridonate Viral capsid conjugates	Gd-TREN-bis-HOPO-TAM-CO2H	41.7		0.7
Lipid Nanoparticles	$GdDOTA(GAC12)_2$	40		0.47
Gold Nanoparticles	Au@DTDTPA-Gdx	4.1		7.0
Nanoassembled Capsules	NACs	24		0.54
Ca^{2+}-Binding Proteins	α-lactalbumin	4.2	5	3
Nanoparticle emulsion	Gd-perfluorocarbon nanoparticles	34	50	1.5
Nanoglobular MRI CAs	G3 nanoglobular	10		3
Porous Polymersomes	porous polymersomes	7.2		1.5
Liposome	ACPL	12	11	1.5
Collagen peptide conjugated with Gd-DTPA	EP-3533	15.6	32.5	1.5
Multimeric CAs		12.2		1.5
Protein Carriers	Albumin	11.5	12.4	0.25
HOPO derivatives	Gd-TREN-1,2-HOPO	10.5		0.47
Cell-permeable CAs	Gd^{3+}-DTPA-Arg_8	7.8		1.5

Small Chelators	Gd-DTPA	5.4	8	1.5
Dendrimers	Gadomer-17	13		1.5

1.7.5 Design of a Targeted Contrast Agent for Imaging of Biomarkers

In order to image biomarkers with MRI, targeted contrast agents are needed to be developed with high specificity as well as sensitivity. Currently, many attempts have been made to design and develop targeted MR agents to obtain molecular imaging by MRI (Table 1.2). Different molecules such as antibody, peptide or small ligands, and small protein domains such as affibodies have been applied for targeting [61, 63, 107-117]. To have contrast agents with higher sensitivity, biomarker-targeting moieties are usually linked to these MRI contrast agents, such as nanoparticles. In a study, fibrin antibody was conjugated to emulsion nanoparticles and they were successfully used to image vulnerable plaques [62]. Furthermore, in a different study, arginine-glycineaspartic acid (RGD) peptide was conjugated to emulsion nanoparticles for successful application in imaging integrin, which is expressed in high levels in many diseases such as cancer and atherosclerosis [114, 115, 118], however, nanoparticles have limited applications to imaging biomarkers on the blood vessel due to the large size and low tissue penetration. Many approaches have been used to solve the issues with macromolecules in terms of extravasation and diffusion barriers. Caravan and coworkers used conjugation approaches with targeting and labeling strategies to create antibody-tagged magnetic particles as well as peptides targeting collagen type I conjugated with multiple Gd-DTPAs named EP-3533 [109, 119, 120]. In these studies, a small collagen targeting peptide was conjugated with Gd^{3+}-chelates and eventually was capable of targeting collagen type I in different diseases such as liver, lung and heart fibrosis [110, 121, 122]. In addition, small molecules such as peptoid-(Gd)8-dendron were synthesized and used for molecular imaging of vascular endothelial growth factor receptor 2 (VEGFR2) which is an

angiogenesis biomarker expressed in different tumors [113]. Although significant progress has been made in generating targeted MRI contrast agents, the development of these agents for molecular imaging by MRI is largely hampered by their low sensitivity compared to other agents in PET/SPECT. In addition, inadequate perfusion to diseased tissue, instability of the peptide-

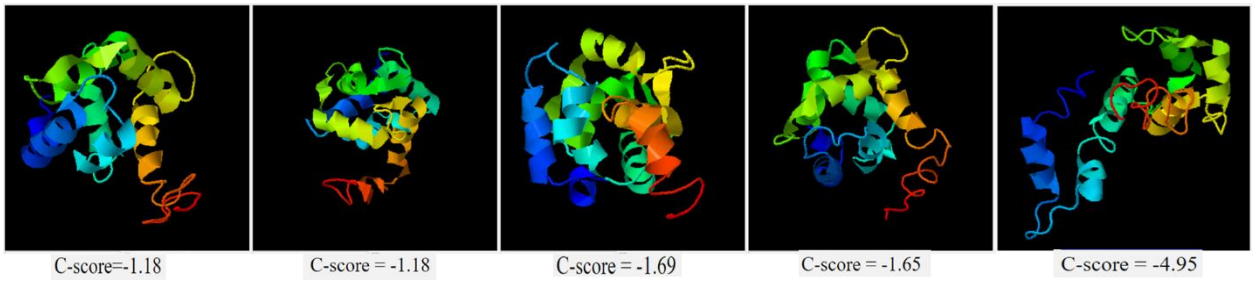

based targeting moieties, and targeting specificity and selectivity are other major limitations of the current MRI agents.

Figure 1.5 *Top 5 final modeled structures predicted by I-TASSER for ProCA32.collagen1*

Fig. 1.6 demonstrates the modeled structures generated by I-TASSER for ProCA32.collagen1. C-score is a confidence score for estimating the quality of predicted models by I-TASSER [123]. It is calculated based on the significance of threading template alignments and the convergence parameters of the structure assembly simulations. C-score is typically in the range of -5 to 2], where a C-score of higher value signifies a model with a high confidence and vice-versa. Therefore, model 1 with C score of -1.18 was chosen as our final model for ProCA32.collagen1.

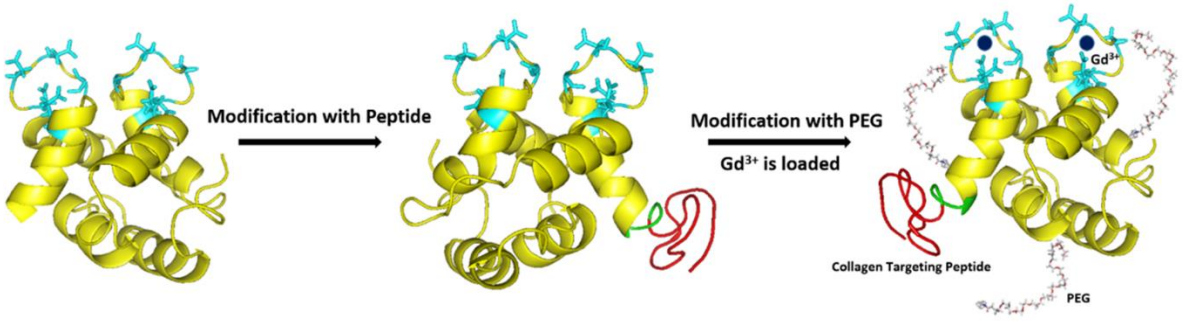

Figure 1.6 *The model structure and development of ProCA32.collagen1*

ProCA32 was generated from rat α-parvalbumin by incorporating the S56D and F103W mutations, then ProCA32 was further developed to ProCA32.collagen1 by linking collagen type I targeting moiety at its C-terminal, then ProCA32.collagen was further modified with covalently linking PEG by PEGylation. The model structures were generated based on the structure of α-parvalbumin (Protein Data Bank ID code 1RWY) and I-TASSER.

Based on our previous design of ProCA32 discussed in section 1.7.3 [83], ProCA32 was chosen to design a protein-based MRI contrast agent with biomarker targeting capacity, therefore, a collagen type I peptide targeting moiety was designed based on previous studies [120] and linked to the C-terminal of ProCA32 through a flexible linker. We have named this protein contrast agent *ProCA32.collagen1*. The protein was further modified with PEGylation, a representation of this process can be seen in Fig. 1.6. Collagen type I is an important biomarker in different diseases such as liver fibrosis and metastasis. It is an important target for molecular imaging of liver fibrosis and metastasis since its accumulation is a characteristic of most types of chronic liver diseases (CLD), further details will be discussed in the next chapters. In order to meet the requirements for MR imaging of different liver diseases, the targeting peptide was added to the C-terminal to avoid any alterations in the protein structure and its metal binding affinities which is very different from

other approaches. We have demonstrated that it is possible to increase relaxivity by addition of a targeting moiety to a protein MRI contrast agent without sacrificing relaxation and metal binding properties, such as affinity and metal specificity.

1.8 In vitro properties of MRI contrast agents

1.8.1 Optimizing peptide targeting capability of MRI contrast agents

The basis of biomaterial science and drug design is to have a good understanding and knowledge of the key protein–protein interactions occurring in cell–matrix, macromolecular organization of the extracellular matrix (ECM), and pathogen-induced and degenerative diseases [124]. The recognition of adhesion moieties used in biomaterials usually occurs via methods that are based on techniques such as phage display [125] or by using trial and error strategies such as screening different sequences from ECM components [126, 127]. In drug design, however, a more efficient strategy is applied which provides structural information from complexes of the binding partners. Furthermore, computational and experimental procedures can be extremely beneficial for the identification of binding epitopes [128]. Similar methods can be used to the rational design of collagen-binding peptides that have relevance to biomaterial applications. Although substantial progress has been made in medicinal chemistry, chemical biology, and biochemistry, biomaterial scientists largely dependent on a few peptide motifs in biomimetic design, such as RGD peptides or enzyme-sensitive peptide sequences [129]. In order to investigate an ideal targeting moiety for collagen type I, more diverse and specific motifs are required, similar to the ECM [130]. The ECM is a hydrogel based on reversible supramolecular interactions and its most abundant protein is collagen. [131-135]

Targeted Gd^{3+}-based contrast agents can become great diagnostic tools combined with MRI to positively enhance images with the contrast they provide since MR has an order of

magnitude better spatial resolution than nuclear imaging modalities such as positron emission tomography (PET) and single photon emission computerised tomography (SPECT), however the first challenge facing these targeted MR agents has always been sensitivity [6]. Usually, Gd^{3+} in μM levels are needed to be in the detectable range of MRI. One strategy can be generating a macromolecule which includes large numbers of metal complexes and targeting moiety (such as peptide or antibody). Different molecules such as polymers, dendrimers, liposomes and nanoparticles have been used successfully in animal models [63, 136-138], however nanoparticles have limitations for vascular targets as they have long half-life in blood leading to slow targeting capability as well as incomplete elimination from the body which usually leave Gd^{3+} behind. Another strategy is to use a chelate or multiple chelates of Gd^{3+} with a targeting moiety attached to them such as a peptide conjugated to one or more small molecule-chelates of Gd^{3+} such as Gd-DTPA [139-142].

Linking or conjugating short peptide fragments with affinity to biomarkers (peptide targeting) is a common approach used in molecular imaging because of its small size and advances in peptide synthesis [143], however application of peptides in targeting has some disadvantages such as their instability and degradation by enzymatic cleavage, having a short half-life in the body, and their undefined structure which could result in decreasing the binding specificity and affinity to the target biomarker. As discussed in previous section, we have used a protein chelate (ProCA32) to chelate two Gd^{3+} and conjugated a collagen type I targeting peptide to its C-terminal to produce ProCA32.collagen1 to overcome the mentioned challenges. Then, based on literature reviews and studying certain amino acid residues responsible for collagen binding, KKWHCYTYFPHHYCVYG sequence was chosen to be linked at the C-terminal via three glycine

linker so that the peptide can freely move for targeting. Using this approach, we have successfully imaged collagen type I with ProCA32.collagen1 in liver fibrosis and liver metastasis.

1.8.2 Thermodynamic stability of MRI contrast agents

Clinical contrast agents such as Gd-DTPA have long term toxic systemic effects (the LD_{50} of Gd^{3+} is 0.2-0.3 mmol/kg and the LD_{50} of Na_3Ca-DTPA is 5 mmol/kg) which is caused by free Gd^{3+} and the chelators. Since Gd^{3+} has an ionic radius (0.93 Å) very similar to Ca^{2+} (0.99), it is very likely that it can compete with Ca^{2+} in the biological systems and cause disruptions in the Ca^{2+} signaling pathways by interacting with calcium binding proteins such as calcium sensing receptor, and voltage-gated calcium channels. Therefore, it is crucial that contrast agents have enough stability in order to prevent Gd^{3+} from being released from their structure. Generally, the stability of contrast agents to Gd^{3+} is defined by thermodynamic, conditional, and kinetic stability. Since these contrast agents are used in medical diagnosis field, it is of great importance that Gd^{3+}-based chelators remain in the complex in vivo, and they need to have high metal binding stability and selectivity [144-147]. The chemical instability of the chelate can lead to exchanges with other metal ions (Zinc, copper, and calcium) which can, in turn, have biological consequences. Accumulation of Gd^{3+} in bones, interference with colorimetric serum determination of calcium and hence spurious hypocalcaemia, interaction with scintigraphic procedures, increased zincuria, interaction with metal-dependent biological systems such as metalloenzymes, are some these consequences, etc.

Basically, two structurally distinct categories of gadolinium chelates are currently used: a) The ‘macrocyclic’ chelates such as Gd-DOTA, where Gd^{3+} is ‘caged’ in the pre-organized cavity of the ligand. (b) The ‘linear’ chelates such as Gd-DTPA or Gd-DTPA-BMA. The toxicity of gadolinium complexes actually depends on their ability to release free Gd^{3+} ions. Transmetallation

is a type of organometallic reaction that involves the transfer of ligands from one metal to another. Several cations such as Fe^{3+}, Cu^{2+}, Zn^{2+} or Ca^{2+} compete with the Gd^{3+} cation and a number of other anions such as PO_4^{3-} , CO_3^{2-} , OH^- can compete with the ligand for the Gd^{3+}. Thermodynamic stability can be described by eqn 1-12.

$$GdL + [M]^{2+} \leftrightarrows Gd^{3+} + [ML]^{-} \quad (1\text{-}12)$$

where M is the endogenous bivalent cation which exchanges with Gd^{3+} in the chelate. Factors affecting the stability of contrast agents are their linear or cyclic structure and their overall charge of the molecule. The thermodynamic stability of contrast agents can be summarized as: Macrocyclic Ionic > Macrocyclic Non-ionic > Liner Di-ionic > Liner Non-ionic [148]. In addition, thermodynamic can be described by these following equations:

$$Gd + L \leftrightarrow GdL \quad (1\text{-}13)$$

$$K_{ML} = \frac{[GdL]}{[Gd] \times [L]} \quad (1\text{-}14)$$

where K_{ML} is thermodynamic stability constant, [GdL] is the concentration of metal ligand complex and [Gd] and [L] are the concentrations of free Gd^{3+} and ligand in the solution. Clinical MRI contrast agents have thermodynamic stability constants ranging from 16.6-25.8 (log K_{ML}).

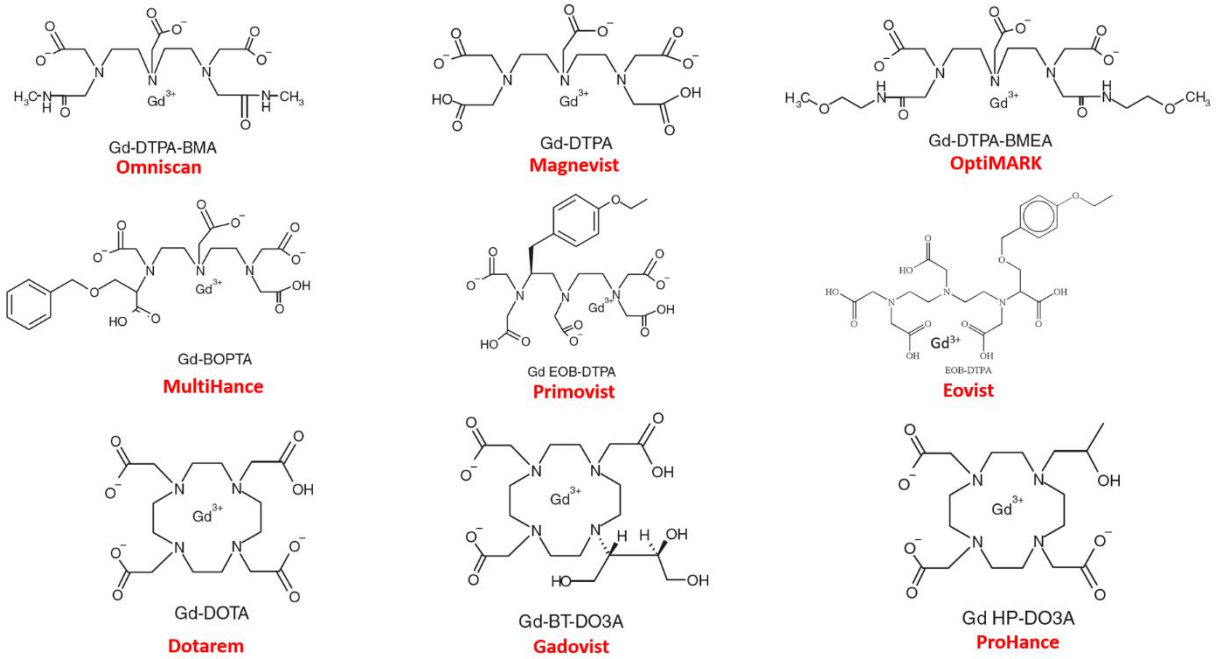

Figure 1.7 *Structure of some commonly used clinical contrast agents [149].*

ProCA32.collagen1, with two Gd^{3+} binding sites, has a thermodynamic stability constant of 22.3, which is greater than Gd-DTPA-BMA (log K_{ML}= 16.6). The conditional stability constant determines the stability of the metal-chelator complex at physiological pH, which is the protonation of the chelator at pH 7.4 [150]. To investigate the metal binding affinity and selectivity of ProCA32.collagen1, we have used different fluorescence spectroscopic methods such as dye competition and Tb^{3+} energy transfer. ProCA32.collagen1 has a metal selectivity for Gd^{3+} over physiological metal ions log (K_{Gd}/K_{Ca}) = 14.4 and log (K_{Gd}/K_{Zn}) = 16.2. Furthermore, the Gd^{3+} binding constant (log K_{Gd}) for ProCA32.collagen1 is comparable to DTPA and the metal selectivities of ProCA32.collagen1 for Gd^{3+} over Zn^{2+} and Ca^{2+} are much greater than other clinical contrast agents.

We also have investigated the stability of Gd^{3+} binding to ProCA32.collagen1 under the conditions of extracellular environment where there are other biological metal ions present and can compete with Gd^{3+} and subsequently affect the relaxivities of ProCA32.collagen1. The relaxivities (r_1 and r_2) of ProCA32.collagen1 were not significantly affected in the presence of Zn^{2+} and Ca^{2+}, more details will be discussed in Chapter 2 and 4.

Table 1.3 *Thermodynamic stability of some of clinical contrast agents compared to ProCA32.collagen1 and ProCA32-P40 [151].*

Contrast Agent	* Log (K_{Tb})	Log (K_{Gd})	Log (K_{Ca})	Log (K_{Zn})	Log(K_{Gd}) / Log (K_{Ca})	Log(K_{Gd}) / Log (K_{Zn})
Magnevist (DTPA)	22	22.46	10.75	18.6	12.24	4.13
Eovist (EOB-DTPA)	N/A	23.6	11.82	18.78	12.22	5.18
Dotarem (DOTA)	N/A	24.7	17.23	21.05	7.46	3.65
MultiHance (BOPTA)	N/A	21.91	N/A	17.04	N/A	4.87
ProHance (HP-DO3A)	N/A	23.8	14.83	19.37	10.07	4.37
ProCA32-P40	21.08	22.44	9.55	8.77	13.1	14.3
ProCA32.collagen1	22.80	22.30	8.70	6.12	14.4	16.2

*N/A, not available, * Values from NIST at pH 14*

Table 1.4 General data for all currently marketed Gd^{3+}-based MRI contrast agents [1].

Acronym	Gd-DTPA	Gd-DTPA-BMA	Gd-DTPA-BMEA	Gd-BOPTA	Gd-DOTA	Gd-HP-DO3A	Gd-BT-DO3A	Gd-EOB-DTPA
Generic name	Gadopentetate dimeglumine	Gadodiamide	Gadoversetamide	Gadobenate dimeglumine	Gadoterate meglumine	Gadoteridol	Gadobutrol	Gadoxetic acid disodium salt
Trade name	Magnevist®	Omniscan®	OptiMARK®	MultiHance®	Dotarem®	ProHance®	Gadovist®	Primovist®
Company	Schering AG	GE-Healthcare	Mallinckrodt	Bracco	Guerbet	Bracco	Schering AG	Schering AG
Chemical structure	Linear	Linear	Linear	Linear	Macrocyclic	Macrocyclic	Macrocyclic	Linear
Charge	Di-ionic	Non-ionic	Non-ionic	Di-ionic	Ionic	Non-ionic	Non-ionic	Di-ionic
Formulation	Free DTPA 0.2% (1 mmol/L)	Ca-DTPA-BMA (Na^+ salt) 5% (25 mmol/L)	Ca-DTPA-BMEA (Na^+ salt) (50 mmol/L)	No formulation	No formulation	$[Ca\text{-}HP\text{-}DO3A]_2$ (Ca^{2+} salt) 0.1% (0.5 mmol/L)	Ca-BT-DO3A (Na^+ salt) (1 mmol/L)	Ca-EOB-DTPA (trisodium salt) (concentration not disclosed)
Concentration (M)	0.5	0.5	0.5	0.5	0.5	0.5	1.0	0.25
Osmolality (mOsm/kg H_2O)	1960	789	1110	1970	1350	630	1603	688
Viscosity (mPa s) at 37 °C	2.9	1.4	2.0	5.3	2.0	1.3	4.96	1.19
log K_{therm}	22.1	16.9	16.6	22.6	25.8	23.8	21.8	23.5
log K'	17.7	14.9	15.0	16.9	18.8	17.1	N/A	N/A
Relaxivity (r_1/r_2) (s^{-1} mM^{-1}) at 37 °C, 20 MHz, in water	3.4/4.0	3.5/3.8	4.2/5.2	4.2/4.8	3.4/4.1	3.1/3.7	3.7/5.1	5.3/6.2

N/A, not available.

1.8.3 The kinetic stability and metal selectivity of MRI contrast agents

Metalloproteins such as Ca^{2+}-binding proteins are important in biological systems as they play a variety of roles in cell proliferation, migration, protein-protein interactions, protease activation, signal transduction, and immune-responses [152, 153]. These Ca^{2+}- and Zn^{2+}- binding proteins can potentially bind to free Gd^{3+} released from contrast agents in the body. Moreover, blood plasma and interstitial fluids in the body have multiple ions such as Ca^{2+} and Zn^{2+} and Fe^{3+} which can compete with Gd^{3+} in the contrast agent to release free Gd^{3+}. There are also certain anions in the body that can compete with contrast agent itself such as phosphate (0.6 M) and bicarbonate (0.36 M) in the biological systems form which in turn further drives the disassociation of Gd^{3+} from the metal contrast agent complex. Kinetic stability properties determine the rate of this dissociation in a contrast agent in which an agent with high kinetic stability will release less Gd^{3+} per unit time [154]. In order to assess the kinetic stability, the dissociation rate of Gd^{3+} from the complex can be measured at pH=1, at which the dissociation rate of a contrast agent is significantly increased compared with physiological pH. As it was mentioned previously, linear

contrast agents have higher dissociation rates or lower kinetic stability compared to cyclic contrast agents. As can be seen in Fig. 1.7, clinically approved contrast agents such as Gd-DTPA-BMA has the lowest kinetic stability, however Gd-DOTA has highest kinetic stability. It has been demonstrated that the dissociation rate of the Gd-chelator complex correlates with the Gd^{3+} retention in mouse 14 days after injection of these agents [35].

1.8.4 Size is essential for contrast agent distribution and excretion

Disease biomarkers have diverse locations based on the stage of the disease. For instance, Collagen type I is a biomarker expressed in higher levels in a variety of cancers such as liver and breast cancer as well as liver fibrosis and its progression to cirrhosis [155]. Collagen is also present in blood vessels and inside and on the surface of tumors, while other biomarkers such as HER-2 is deeply expressed in a tumor outside of the blood vessel. Therefore, it is important to have an ideal half-life for targeting different biomarkers. Theoretically, longer circulation times might provide more time for Gd^{3+} release and toxicity, therefore, the contrast agent should have a moderate and optimized blood circulation time tailored towards the specific targeted biomarker. For molecular imaging of a liver metastasis and fibrosis, the contrast agent should have sufficient blood half-life to allow the contrast agent to penetrate deeply into the tumor and then quickly be excreted out of the body to reduce the toxicity. The half-time of ProCA32.collagen1 in mouse is about 9 hours depending on the surface modification [84] and exhibits enhancement in various organs but mainly in the liver. Since the collagen concentration increases (μM levels) as fibrosis progresses and its extracellular location makes it readily accessible by the probe, therefore relatively longer half-life is needed.

The half-life of clinical contrast agents that are based on small chelators are very different from other agents such as nanoparticles that have uptake by macrophages and have accumulations

in the liver and spleen. In a study regarding the distribution of gold nanoparticles with a diameter ranging from 10, 50, 100, and 250 nm, after 24 h, the 10 nm gold nanoparticles distributed in different organs such as blood, liver, kidney, spleen, heart, lung, and brain, however the majority of 50 nm gold nanoparticles distributed in blood, lung, liver, and spleen [156]. Usually, the agents that are larger than 50 nm mainly distribute in blood, liver, and spleen. In addition to tumor penetration and organ distribution, the size of the contrast agents can also affect renal excretion. For instance, a molecule with a size of larger than 7 nm in diameter (approximately 60 kDa) is not readily able to pass through the glomeruli, and the blood half-live of these molecules in mouse is longer than 80 min [31]. Lysozyme with a molecular weight of 15 kDa and diameter of 3.4 nm, has the blood half-life of 12 min. On the other hand, IgG has the molecular weight of 152 kDa has the blood half-life of 330 min. The toxicity of nanoparticles with a size larger than 15 nm has grown concern since the renal excretion is prevented for these large macromolecules due to the risk of accumulation in the human body [31].

1.8.5 Transmetallation studies of MRI contrast agents

One of the important studies in MRI contrast agent field and their development is transmetallation of Gd^{3+} chelates by other physiological ions such as Fe^{3+}, Cu^{2+}, and Zn^{2+}. Protocols based on relaxivity have been used to compare the transmetallation of the approved clinical contrast agents (2.5 mM) in the presence of 2.5 mM Zn^{2+} in the phosphate buffer. In these studies, the highest kinetic stability was achieved for Gd-DOTA [35]. In addition, further studies demonstrated the kinetic profile of Gd^{3+} dissociation from Gd^{3+}-based MRI contrast agents in serum for the duration of 15 days using HPLC-ICP-MS. More unstable contrast agents such as nonionic linear ones like Gd-DTPA-BMA, demonstrated 10 times higher Gd^{3+} release than ionic linear contrast agents, such as Gd-DTPA. In contrast, macrocyclic contrast agents as the most

stable type of agents did not show any Gd^{3+} release such as Gd-DOTA. These studies demonstrate that cyclic contrast agents have good kinetic stability compared to linear contrast agents [157].

1.8.6 Toxicity studies of MRI contrast agents

The major organs in the body which have Gd^{3+} deposits are usually bone, lung, and liver. The dissociation rate in which Gd^{3+} is released from the contrast agents has direct effect on its deposition in bones. Studies have reported Gd^{3+} retention in mice 14 days after injection of different Gd^{3+}-based chelates with different dissociation rates. Results demonstrated that mice injected with Gd-DTPA-BMA or Gd-NP-DO3A had much higher Gd^{3+} deposition in the whole body, mainly in bone and liver, compared to mice injected with Gd-DOTA or Gd-HP-DO3A [35]. In another study, Gd^{3+} concentration in the bones of patients who had hip replacement was analyzed after injection of 0.1 mmol/kg Gd-HP-DO3A or Gd-DTPABMA. The analysis showed that Gd^{3+} retention was 1.77 and 0.447 μg per gram of bone for Gd-DTPA-BMA and Gd-HP-DO3A, respectively as revealed by ICP-AES [158]. Furthermore, the use of these contrast agents in patients with kidney problems is reported to cause NSF. Biopsy results of patients with NSF have confirmed the presence of insoluble Gd^{3+}-phosphate deposits in their skin [159, 160].

The acute toxicity of ProCA32.collagen1 was studied with clinical chemistry tests and different components of plasma samples were measured such as liver enzymes (ALT, ALP, AST, LDH), urea nitrogen, bilirubin, and total protein content from CD1 mice 5-7 days post tail veil injection of 0.0013 mmol/kg of ProCA32.collagen1. The results showed negligible toxicity compared to control subjects (CD-1 mice).

The serum stability experiment is another useful tool for monitoring unstable compounds in vitro. To test the stability of ProCA32.collagen1 in human serum, the protein was incubated in complex with an equal concentration of $GdCl_3$ in human serum at 37 ˚C. The degradation of the

protein was monitored by both SDS-PAGE. The results showed that the protein remained intact for at least 48 hours in the absence of serum as well as in the presence of 70% human serum up to 14 days of incubation. Long term Gd^{3+} retention and pharmacokinetics of ProCA32.collagen1 will be discussed in detail in the Chapter 4.

1.9 Molecular imaging by MRI using a biomarker-targeted contrast agent

Monitoring different disease biomarkers in patients with invasive methods such as biopsy has so many disadvantages such as its invasiveness, high costs and sampling error, intra/inter-observer variability, hospitalization in 1–5% of cases, mortality in 0.01–0.1% of cases, lack of accuracy due to substantial sampling error, cost associated morbidity, pain and bruising at the biopsy site, prolonged bleeding, infection of the biopsy site, and pneumothorax and hemothorax. For instance, there is a 33% error in diagnosis of liver cirrhosis which severely affect the patient outcomes [109, 161]. With its unique capacity to generate reproducible and non-invasive assessment of biological/disease processes of different organs at various time points, molecular imaging of disease biomarkers using MRI can be an important and ideal diagnostic tool to facilitate the understanding of the disease, monitoring disease progression and drug treatment and activity during preclinical and clinical application. Since MRI is cheaper compared to some other imaging modalities, its application for molecular imaging can dramatically lower the costs by reducing the number of animals required for a specific study. However, one of the major limitations of MRI to investigate specific disease biomarkers for diagnosis and drug treatment monitoring is the lack of sensitive contrast agents with high relaxivity, targeting capability, and tissue permeability.

The majority of disease biomarkers have very low expression levels. Approximately, 5×106 Gd^{3+} per cell are needed to acquire a good and sufficient contrast in MRI using current clinical contrast agents based on small chelators since they have low relaxivity of ~5 $mM^{-1}s^{-1}$[162].

Studies have shown that endocytosis is a useful process for contrast agents in tissues since it helps them to accumulate in a local area, however recent studies showed otherwise and that the relaxation enhancement is suppressed when the local concentration of Gd^{3+} is higher than 1010 Gd^{3+} per cell [163-165]. The decrease in relaxivity can be attributed to insufficient water exchange across the plasma membrane.

Targeted molecular imaging by MRI is now under development to increase sensitivity [109, 166]. The majority of these MRI contrast agents target biomarkers expressed on the surface of blood vessels and not so many have tried to target the biomarkers outside of the blood vessels. In order to improve the dose efficiency of MRI contrast agents, peptide fragments with high affinity to biomarkers are extensively applied for conjugation. For instance, two-component Gd^{3+}-based MRI contrast agents have been generated by binding of avidin-Gd^{3+} complexes to tumor cells which was labeled with a biotinlyated antibody [167, 168]. These contrast agents have the disadvantage of slow diffusion when targeting tumors *in vivo*. Moreover, antibodies demonstrate improper distribution and penetration in tumor blood vessel [80]. Peptides on the other hand have small size compared to the antibodies, therefore they have good tumor penetration [119, 169], however, these peptide-based MRI agents need further improvement in targeting capability and resistance to protease cleavage. Overall, the development of targeted MRI agents has long way to go despite the significant amounts of research. In conclusion, there is still unmet medical needs for the development of MRI contrast agents with higher relaxivity and improved targeting capability to image spatial distributions and patterns of biomarkers by MRI.

Magnetic resonance imaging (MRI) demonstrates several technical advantages such as deep tissue penetration, high spatial resolution, complete coverage of the entire liver, detailed structural and anatomical information, evaluation of organ morphology, and it is relatively inexpensive. Most importantly, MRI does not use ionizing radiation which makes it suitable for monitoring disease progression and treatment when repeated imaging is required for a long period of time [161]. More than 35% of MRI scans use MRI contrast agents, particularly paramagnetic gadolinium (Gd^{3+})-based contrast agents [83], which shorten T1 and increase MRI signal [7], however MRI lacks sensitive contrast agents. All clinically approved Gd^{3+}-based contrast agents are based on small chelators with relaxivity (r_1 and r_2) ranging from 4–6 $mM^{-1}{\cdot}s^{-1}$. Their low relaxivities severely limit their sensitivity to be applied in detection of early stages of chronic diseases, their progression and treatment monitoring. In addition, they do not have the targeting capability for any disease biomarker. For instance, gadolinium–ethoxybenzyl– diethylenetriamine pentaacetic acid (Gd-EOB-DTPA) (Eovist, United States; Primovist, Europe; Bayer) and gadobenate dimeglumine (Gd-BOPTA) (Multihance; Bracco) are among the most popular and common clinical contrast agent which are T1-weighted liver contrast agents, and have 50% and 5% hepatocyte uptake, respectively [8]. However, these contrast agents cannot detect early stages of many diseases where biomarkers expression play an important role in early diagnosis and progression. Therefore, development of targeted and sensitive MRI contrast agents with improved sensitivity, higher metal binding affinity and selectivity is needed to overcome MRI limitations and enable the earlier detection of different chronic diseases such as liver fibrosis, and monitor its progression as well as its treatment, which results in earlier diagnosis, treatment and subsequent reversion of the disease.

1.10 Collagen type I: An appealing target for many chronic diseases

Extracellular matrix (ECM) is a dynamic and complex environment characterized by biophysical, mechanical and biochemical properties specific for each tissue and able to regulate cell behavior. The ECM is composed of a large collection of biochemically and structurally diverse components. Biochemically, these components can be divided into proteins, proteoglycans, and glycoproteins, each of which has diverse sub-categories of components and varying physical and biochemical properties[170]. Collagen type I is the most abundant component of ECM. Collagen is abundant in humans accounting for one-third of total proteins. The fibrous, structural protein contains three polypeptide α-chains, displaying a polyproline-II conformation, a right-handed supercoil and a one-residue stagger between adjacent chains [171]. Each polypeptide chain has a repeating Gly–X–Y triplet, and the three polypeptide α-chains in the triple helix held together by inter-chain hydrogen bonds can be identical, but heterotrimeric triple helices are more prevalent than homotrimeric triple helices.

Recent studies have highlighted the role of the ECM and shown the importance of deregulated ECM dynamics in molecular etiology of disease development. Excess ECM production or reduced ECM turnover, for example, are a salient feature in tissue fibrosis of many organs and collagen type I as the most abundant component of EMC plays an indispensable role in these processes [170].

Collagen type I is an appealing target for molecular imaging of a variety of diseases such as liver fibrosis, liver metastasis, breast cancer, pancreatic cancer and aortic aneurysms. In organ fibrosis and different cancers, collagen accumulation as well as its concentration increases by the disease progression. In addition, collagen type I is an extracellular protein which makes it accessible for any agent.

Collagen targeted MR imaging contrast agent could act as an agent to image these diseases, and these agents may have higher efficacy for fibrosis and cancers assessment than the clinically available contrast agents. [30, 109]. Furthermore, MRI contrast agent providing a measure of collagen levels as well as its capability to bind cross-linked collagen would have utility in detection of early stages of diseases such as fibrosis, cirrhosis and drug treatment monitoring. Although other groups such as Caravan et al, conducted extensive research on developing contrast agents for detection of fibrosis, or pancreatic cancer, sensitivity and specificity is still a challenge in development of contrast agents for early detection [109, 110, 121, 122, 161, 172].

Using rational protein design, we have developed a protein-based MRI contrast agent ProCA32.collagen1 that targets collagen type I. ProCA32.collagen1 has high relaxivity values for r_1 and r_2 per Gd^{3+} at both 1.5 and 7.0 T. In addition, ProCA32.collagen1 is able to detect both early and late stage (Ishak score of 3 and 5) of mouse liver fibrosis in multiple mouse models which has not been achieved by any clinical contrast agent such as Eovist and non-targeted contrast agent, ProCA32 previously developed by S. Xue. et al [83]. Moreover, ProCA32.collagen1 is able to detect small tumor lesions in uveal melanoma liver metastasis.

1.11 Motivation and challenges to be addressed

Early diagnosis for many diseases has always been a challenge for scientists and clinicians. It can play an indispensable role in treatment efficiency and strategies. Development of MRI contrast agents is an evolving field, however clinical MRI contrast agents have faced major limitations in terms of application in early diagnosis for many chronic diseases due to lack of sufficient sensitivity and targeting capability. Our lab has been working on development of novel Gd^{3+} protein-based MRI contrast agents (ProCA) to overcome the challenges associated with current MRI contrast agents in clinics.

In order to apply our contrast agent in diagnosis of chronic diseases, there are several challenges the need to be addressed. First, can we develop a new MRI contrast agent with improved sensitivity to target a specific biomarker for early stage diagnosis of chronic diseases? Can we improve the safety of an MRI contrast agent by reducing its dose and toxicity? Third, can we develop a new MRI contrast agent capable of monitoring diseases progression and treatment? Forth, can we stage chronic diseases with the use of a noninvasive technique and absent of biopsy? Fifth, can we improve accuracy and specificity of chronic disease diagnostics by taking advantage of a T1-T2 dual mode contrast agent combined with imaging methodologies?

1.12 Overview of the dissertation

In this Ph.D. dissertation, in order to address these mentioned challenges and questions, I have developed a collagen type I targeted protein-based MRI contrast agent, ProCA32.collagen1 with improved sensitivity and targeting capability compared to other previously developed contrast agents in our lab and clinically available contrast agents.

Chapter 2 details experimental methods and protocols that we used for the dissertation.

Chapter 3 describes our rationales for design of a novel collagen type I targeted protein contrast agent (ProCA32.collagean1) and its expression, purification and characterization.

Chapter 4 describes the biophysical properties of ProCA32.collagen1 such as its metal binding affinities, relaxivities, pharmacokinetic, transmetallation, collagen type I affinity, serum stability and toxicity studies.

Chapter 5 details the successful application of ProCA32.collagen1 in early detection of liver fibrosis in TAA/alcohol induced mouse liver fibrosis using both r_1 and r_2 property. Moreover, ProCA32.collagen1 ability to map liver cirrhosis heterogeneity in DEN- and TAA/alcohol-induced

mouse models is elaborated as well as its capability in revealing vascular structural changes, intrahepatic angiogenesis and portal hypertension.

Chapter 6 reports the successful application of ProCA32.collagen1 for early detection of human uveal melanoma tumors metastasis to mouse liver. In addition, ProCA32.collagen1 capability in distinguishing different uveal melanoma growth patterns (Nodular vs Infiltrative) in liver is described.

Chapter 7 reports the studies of hepatocellular carcinoma (HCC) tumor detection in liver in DEN-induced mouse model using ProCA32.collagen1. ProCA32.collagen1 is able to distinguish cirrhotic regions in liver from HCC tumors.

Chapter 8 describes our attempt in extending the application of ProCA32.collagen1 in imaging collagen in mouse model of thoracic and abdominal aortic aneurysm (TAA/AAA) with subcutaneous infusion of angiotensin II (AngII) from implanted osmotic pump.

Chapter 9 provides our studies in application of ProCA32.collagen1 in early detection of Nonalcoholic steatohepatitis (NASH) in Nonalcoholic fatty liver disease (NAFLD) in mouse models on a NASH diet.

Chapter 10 describes and summarizes the major findings of this dissertation and future direction.

In Appendix, my studies on a different topic involving Connexin43 (Cx43) gap junction regulation by Ca^{2+}/Calmodulin will be discussed. We have identified several Calmodulin binding sites in Cx43, and fluorescence spectroscopy was used to study the interaction between Cx43 and calmodulin in the presence of Ca^{2+}.

2 MATERIALS AND EXPERIMENTAL METHODS

2.1 Molecular cloning, expression, purification and Lysine PEGylation.

In the contrast agent design, collagen type I-targeting peptide (KKWHCYTYFPHHYCVYG) for type I human collagen) was linked to the C-terminal of ProCA32 by a flexible linker (GGG). The protein contrast agent was named ProCA32.collagen and then it was purified according to Henzl's and Xue et al procedure with some modifications [83, 173]. First, ProCA32.collagen was expressed in Escherichia coli BL21 (DE3) cell strain, and then it was induced by 0.5 mM isopropyl β-D-1-thiogalactopyranoside (IPTG) when the optical density at 595 nm (OD595) reached 0.6. After induction, the culture temperature was reduced from 37 °C to 28 °C for expression overnight. The bacterial pellets were re-suspended and sonicated in 10 mM Tris.HCl buffer for 12 times at pH 7.2 with 1 μL of benzonuclease (Novagen). The supernatant of the cell lysate was incubated at 85 °C for 20 min, cooled to 4 °C in an ice-water bath, and centrifuged (41,100 × g, 20 min, 4 °C). Impurities including DNA, were then precipitated by addition of 3% (wt/vol) streptomycin sulfate and placed at 4 °C overnight. On the next day, the precipitate DNA was removed by centrifuge and the supernatant was dialyzed at least in 4 changes of buffer in 4 °C for 24 h against 10 mM Tris.HCl at pH 8.0 then the protein mixture was further purified using a HiTrap Q column (GE Healthcare) by fast protein liquid chromatography (FPLC) . After removing unbound proteins with 3 column volumes of 10 mM Tris at pH 8.0, the column was eluted with a 0–1 M NaCl gradient in 10 mM Tris·HCl at pH 8.0. Purified ProCA32.collagen was confirmed by SDS-PAGE and UV spectrum. Gd^{3+} was loaded to ProCA32.collagen at a 2 : 1 ratio. Other metals in ProCA32.collagen such as Ca^{2+} was removed by chelex-100 and the metal content in ProCA32.collagen was analyzed by ICP-OES. The protein was PEGylated by the following steps: First, it was dialyzed three times against 10 mM Hepes at pH 7.0–7.2. Second,

ProCA32.collagen was mixed with Methoxy Succinimidyl Carboxymethyl Ester (M-SCM-2000) reagent with molecular weight of 2 kDa (JenKem Technology), with a molar ratio of 1:5, and then incubated at room temperature for 4 h or 4 °C overnight. Third, unreacted free M-SCM-2000 was quenched by adding 100 mM Tris·HCl with a final concentration of 10 mM. Fourth, PEGylated ProCA32.collagen was further purified using HiTrap Q column and then concentrated about 4 times using concentrator with 3kDa membrane to remove the unreacted free PEG (MW 2 kDa). After removing unbound fractions with 3 bed volumes of 10 mM HEPES at pH 8.0, the proteins bound to the column were eluted with a 0–1 M NaCl gradient in 10 mM HEPES at pH 8.0. PEGylated products were analyzed by SDS/PAGE with protein staining by Coomassie Brilliant Blue and PEG staining by I_2.

2.2 Liver fibrosis and metastasis animal models

2.2.1 Thioacetamide (TAA)/alcohol induced fibrosis

Balb/c mice (6 - 7-week-old male) were I.P. injected with 100 mg/kg TAA and gradually increased to 200 mg/kg TAA in two weeks. 10% alcohol was also fed to mice along with the TAA treatment. For rPKM2 experiment, 5 mg/kg of rPKM2 was mixed with TAA for injection starting at two and a half weeks, and lasted for total of seven weeks. TAA mixed with buffer or rPKM1 was the control.

For the PKM2 antibody experiment, TAA was continuously treated for twelve weeks. After that, TAA and alcohol was stopped and 4mg/kg of PKM2 antibody was I.P. injected every other day for ten doses. Buffer and rabbit IgG were the control.

The body weights were recorded every week or every four days. At the end of the experiments, animals were sacrificed. Livers, other organs, and blood samples were collected. Liver weights were measured and liver pictures were taken. Tissue sections were prepared and

analyzed by IF, IHC, or H&E stains using commercially available antibodies as indicated. Serum samples were prepared from collected blood samples. The serum samples were analyzed by the service of Comparative Clinical Pathology.

Liver fibrosis was induced with Balb/C mice by administration of TAA and 10% ethanol in drinking water for 12 weeks. At the end of cirrhosis induction, the animals were treated via buffer. After the treatments, animal body weights, liver weights, and out-surface of livers were examined. All animal experiments in this study complied with the Association for Research in Vision and Ophthalmology Statement for the Use of Animals in Ophthalmic and Vision Research and complied with an approved animal protocol from the Institutional Animal Care and Use Committee at Georgia State University and the University of Georgia.

2.2.2 DEN induced Cirrhosis and HCC

For all of our studies, we employed female and male mice with C57BL/6 genetic background. Experiments involving animals were conducted in accordance with the NIH Guide for the Care and Use of Laboratory Animals and were approved by the Georgia State University IACUC. Animals were housed in a pathogen-free animal facility under a 12 h light/dark cycle and fed a standard rodent chow and water ad libitum. In order to induce liver tumor development, 14-day-old mice were treated with a single dose of DEN (Sigma–Aldrich # N0756) given dissolved in saline at a dose of 25 mg/kg body weight by i.p. injection on day 12. Mice in one randomly pre-assigned group were killed 10 months after DEN administration for histological and biochemical analyses. Mice were randomly distributed in various groups having equal males and females.

Immediately after euthanizing, livers were removed, weighed and the numbers of visible tumors on the liver surface were counted macroscopically. The largest lobes were fixed in formalin

and embedded in paraffin. Sections were stained with hematoxylin and eosin and examined microscopically.

2.2.3 Uveal melanoma liver metastasis model

All animal procedures performed in this study complied with the Association for Research in Vision and Ophthalmology Statement for the Use of Animals in Ophthalmic and Vision Research and complied with an approved animal protocol from Institutional Animal Care and Use Committee at Georgia State University and University of Georgia. To generate hepatic melanoma implantation model, C57BL/6 female mice, 7–10 wk old, were anesthetized with i.p. ketamine hydrochloride, 90 mg/kg, and xylazine, 10 mg/kg. After anesthesia, a small horizontal abdominal incision (1 cm) was made in the left upper quadrant such that the left lobe of the liver will be exposed. A total of 5 × 106 of mouse B16LS9 melanoma cells were drawn into a Hamilton syringe with a 29-gauge needle creating a 5-μL slurry that were injected into the parenchyma of the exposed liver under an operating microscope. Gentle pressure was applied to the hepatic injection site for 1 min with a cotton-tipped applicator after tumor cell injection. The left lobe of the liver was repositioned into the peritoneal cavity, and the abdominal wall was then closed with 5.0 sutures. To generate the uveal metastasis model, aliquots of 5 × 105 cells of B16LS9/2.5 μL were inoculated into the choroid of the right murine eye of 7- to 10- week-old PEDF-null C57BL/6 female mice (8), using a transscleral technique that allows the inoculated cells to remain in the eye. The mice were anesthetized and a tunnel was prepared from the limbus within the sclera to the choroid with a 30 1/2-gauge needle under the guidance of a dissection microscope. The tip of a 10-μL glass syringe with a blunt metal needle (Hamilton) was introduced into the choroid through the needle track, and no cells were inoculated until the needle tip was inside the eye. A 2.5-μL suspension of cells was inoculated. No tumor cell efflux from the eye occurred, and the

subconjunctival space remained free of tumor cells. The inoculated eyes were enucleated after 1 wk, fixed in 10% (vol/vol) formalin, and routinely processed for light-microscopic examination. Serially adjacent 5-μm-thick sections were stained with hematoxylin and eosin (H&E) and evaluated for the presence and location of melanoma. Hepatic tissue was collected at 3 wk after MRI.

Human uveal melanoma 92.1 cells were inoculated into the supra choroid space of the right eye using a transcorneal technique. For each inoculation, a million cells were delivered in a volume of 2.5 uL. The mice were anesthetized with intraperitoneal injection of ketamine and xylazine mixture. A tunnel was prepared from the limbus within the cornea, sclera and ciliary body to the choroid with a 301/2-gauge needle under a surgical microscope. The tip of a 10 uL glass syringe with a 31-gauge /45-degree point metal needle (Hamilton, Reno, NV) was used to introduce cell suspension into the supra choroid space through the needle track. The right eye was enucleated at 2 weeks after tumor cell inoculation [174, 175].

2.3 **Metal binding affinity measurements of ProCA32.collagen1**

In order to investigate the Gd^{3+} binding affinity of PEGylated ProCA32.collagen, a buffer system is used in which Tb^{3+} binding affinity can be measured since Gd^{3+} is spectroscopically silent. Then the Gd^{3+} binding affinity was calculated using a competition assay [83]. Determining Tb^{3+} binding affinity of ProCA32.collagen1 was based on the Tb^{3+} luminescence resonance energy transfer (LRET) experiment in which 30 μM ProCA32.collagen1 was prepared in 5 mM DTPA, 50 mM HEPES, and 150 mM NaCl at pH 7.2. The ratio of Tb-DTPA concentration ([Tb-DTPA]) and free DTPA concentration ($[DTPA]_{free}$) were controlled by titration of $TbCl_3$ in the system. The protein-Tb^{3+} LRET emission spectra were collected between 520 and 580 nm using an excitation wavelength of 280 nm. The free Tb^{3+} concentrations ($[Tb]_{free}$) in each titration point were

calculated by eqn (2-1). The dissociation constant between Tb^{3+} and ProCA32.collagen1 ($Kd_{Tb,ProCA}$) is calculated by the Hill equation (2-2).

$$[Tb]_{free} = K_{d_{Tb,DTPA}} \times \frac{[Tb - DTPA]}{[DTPA]_{free}} \quad (2\text{-}1)$$

$$f = \frac{[Tb]_{free}{}^{n}}{K_{d_{Tb,ProCA}}{}^{n} + [Tb]_{free}{}^{n}} \quad (2\text{-}2)$$

$[Tb^{3+}]_{free}$ is the free Tb^{3+} concentration calculated from the buffer system, $Kd_{Tb,\ DTPA}$ is the dissociation constant of $Tb^{3+}$and DTPA, the dissociation constants of Tb^{3+} to DTPA were obtained from National Institute of Standards and Technology Standard Reference Database [75]. [Tb-DTPA] is the concentration of Tb-DTPA complex that is formed during titrations, $[DTPA]_{free}$ is the free DTPA in the buffer, *f* is the fractional change of the LRET signal at each titration point and n is the hill number, $Kd_{Tb,\ ProCA}$ is the dissociation constant between $Tb^{3+}$and ProCA32.collagen1.

After achieving the binding constant of Tb^{3+} for ProCA32.collagen1, a competition assay was performed to measure the binding affinity of ProCA32.collagen1 for Gd^{3+}. The Tb^{3+} fluorescence spectra were recorded by tryptophan excitation at 280 nm and emission from 500 to 650 nm. 10 μM of ProCA32.collagen1 was used and 20 μM of Tb^{3+}were incubated with different concentrations of $GdCl_3$ from 0 to 1000 μM at room temperature overnight. The Tb^{3+}-FRET changes were measured by the emission at 545 nm. The apparent dissociation constants (Kd_{app}) were calculated by fitting the plot of LRET peak intensities over different concentrations of Gd^{3+} (eqn (2-3)) and the dissociation constants of Gd^{3+} to ProCA32.collagen1 ($Kd_{Gd,ProCA}$) were calculated by eqn (2-4).

$$f = \frac{([\mathrm{Tb}]_T + [\mathrm{Gd}]_T + K_{d_{app}}) - \sqrt{([\mathrm{Tb}]_T + [\mathrm{Gd}]_T + K_{d_{app}})^2 - 4 \times [\mathrm{Tb}]_T \times [\mathrm{Gd}]_T}}{2 \times [\mathrm{Tb}]_T} \quad (2\text{-}3)$$

$$K_{d_{Gd,ProCA}} = K_{d_{app}} \times \frac{K_{d_{Tb,ProCA}}}{K_{d_{Tb,ProCA}} + [\mathrm{Tb}]_T} \quad (2\text{-}4)$$

where f is the fractional change of the LRET signal, $[Tb]_T$ is the total Tb^{3+} concentration, $[Gd]_T$ is the total Gd^{3+} concentration in each titration point, and $Kd_{Gd,ProCA}$ is the dissociation constant between Gd^{3+} and ProCA32.collagen1 determined by eqn (2-2).

The Kd_{app} for ProCA32.collagen1 was calculated first and then this value was used to calculate the actual dissociation constant using the equation 4.

For determining the calcium binding affinity of ProCA32.collagen1, a calcium equilibrium buffer system was used where, 10 μM of ProCA32.collagen1 was added to the calcium–EGTA buffer system containing 50 mM HEPES, 150 mM NaCl, and 5 mM EGTA at pH 7.2. The system was titrated with different concentrations of $CaCl_2$ to alter the concentration ratio between the Ca-EGTA ([Ca-EGTA]) and free EGTA ($[EGTA]_{free}$). The tryptophan (Trp) fluorescence changes were monitored under the emission spectra between 300 and 390 nm as excited at 280 nm. The free calcium concentration at each titration point was calculated by eqn (2-5)

$$[\mathrm{Ca}]_{free} = K_{d_{Ca,EGTA}} \times \frac{[\mathrm{Ca-EGTA}]}{[\mathrm{EGTA}]_{free}} \quad (2\text{-}5)$$

Furthermore, free calcium concentrations in the buffer were tightly monitored and calculated using equation derived from Tsein's equation [176] with some modifications and the K_d of EGTA-Ca^{2+} =1.51×10^{-7} M was obtained from NIST. The K_d of Ca^{2+} to ProCA32.collagen1 ($Kd_{Ca,ProCA}$) was determined by eqn (2-6).

$$f = \frac{[\mathrm{Ca}]_{\mathrm{free}}{}^{n}}{K_{\mathrm{d_{Ca,ProCA}}}{}^{n} + [\mathrm{Ca}]_{\mathrm{free}}{}^{n}} \tag{2-6}$$

where f is the fractional change of Trp fluorescence intensity, $[Ca]_{free}$ is the free Ca^{2+} concentration in each titration point determined by eqn 5. The same data points were fitted using Adair equation [173] which will result in two separate association constants K_a for each binding site.

The Zinc binding affinity of ProCA32.collagen1 was determined using a similar assay by competition titration using Fluozin1 dye [79, 177]. The fluorescence of 2 µM Fluozin-1 was excited at 495 nm and the emission spectra were collected between 500 and 600 nm in the presence of 2 µM Zn^{2+} and different concentrations of ProCA32.collagen1. The apparent dissociation constant (Kd_{app}) was calculated by eqn 2-7.

$$f = \frac{([\mathrm{Zn}]_{\mathrm{T}} + [\mathrm{ProCA}]_{\mathrm{T}} + K_{\mathrm{d_{app}}}) - \sqrt{([\mathrm{Zn}]_{\mathrm{T}} + [\mathrm{ProCA}]_{\mathrm{T}} + K_{\mathrm{d_{app}}})^{2} - 4 \times [\mathrm{Zn}]_{\mathrm{T}} \times [\mathrm{ProCA}]_{\mathrm{T}}}}{2 \times [\mathrm{Zn}]_{\mathrm{T}}} \tag{2-7}$$

where f is the fractional change of the fluorescence intensity of Fluozin-1, $[Zn]_T$ is the total Zn^{2+} concentration, and $[ProCA]_T$ is the total concentration of protein contrast agent at each titration point. The dissociation constants between ProCAs and Zn^{2+} ($Kd_{Zn,ProCA}$) were then calculated by eqn (2-8).

$$K_{\mathrm{d_{Zn,ProCA}}} = K_{\mathrm{d_{app}}} \times \frac{K_{\mathrm{d_{Zn,Fluozin}}}}{K_{\mathrm{d_{Zn,Fluozin}}} + [\mathrm{Fluozin}]_{\mathrm{T}}} \tag{2-8}$$

where Kd_{app} is determined by eqn (2-7), $Kd_{Zn,Fluozin}$ is the Zn^{2+} affinity to Fluozin-1 and $[Fluozin]_T$ is the total Fluozin-1 concentration.

2.4 Histology analysis

2.4.1 Immunohistochemistry and Hematoxylin and Eosin analysis

For immunohistochemistry, paraffin-embedded liver sections were cut (4 μm) and mounted on slides (ProbeOn; Fisher Scientific). The sections were dried, deparaffinized, and hydrated with xylene and graded ethanol. Formalin-fixed samples were then stained with Sirius Red according to standard procedures. Sirius Red stained slides were analyzed by a pathologist, at Emory University School of Medicine, to score the amount of liver disease based on Ishak scoring system [178, 179] . Furthermore, CPA which is % area stained with Sirius Red, was calculated from the histology images using ImageScope.

For H&E Staining, livers were fixed in 10% (vol/vol) formalin. Then they were dehydrated in increasing concentrations of alcohol, cleared in xylene, and embedded in paraffin. Serial 5-μm sections were prepared, stained with H&E, and processed for light-microscopic examination.

2.4.2 Immunofluorescence staining

Immunofluorescence staining was performed on fibrotic tissues collected from the mice liver post injection of ProCA32-P40 and ProCA32.collagen1 for 48 hours. Tissues were immediately frozen in liquid nitrogen after dissection and stored in -80°C. After that the tissues were embedded in optimal cutting temperature (OCT) cryostat sectioning medium and cut with a thickness of 5 μm. ProCA32-P40 and ProCA32.collagen1 were stained by home-made rabbit antibody against ProCA32 and Alex Fluo 555-conjugated secondary antibody (red) against the rabbit antibody. The nuclei of the cells were stained by DAPI (blue).

2.5 **Mouse MRI imaging**

All mice were imaged on a 7-T Agilent MRI scanner at the University of Georgia. Animals were anesthetized using isoflurane and their respiration rate was monitored with a small animal physiological monitoring system. Anesthesia was adjusted to maintain a respiration rate of 65 ± 5 breaths per minute. T1 map (inversion recovery) and T2 map MRI images were collected before and after intravenous (I.V.) administration of 5 mmol/L of ProCA32.collagen1 or ProCA32-P40. T1 map images were acquired with inversion recovery times of 10, 222, 435, 648, 861, 1074, 1287, and 1500 ms. Other acquisition parameters include: repetition time of TR = 5000 ms, Effective TE=32.67 ms, field of view FOV = 35×35 mm, matrix = 256×256, slice thickness = 1.0 mm, and 12 image slices with no gap. T2 map images were collected before and after the contrast agent I.V. injection of 5 mM ProCA32-P40 or ProCA32.collagen1 with different time points using the MSME sequence with the following parameters: TR = 2000 ms, different echo times, TE (8, 16, 24, 32, 40, 48, 56, 64, 72, 80, 88, 96 ms), matrix = 256×256, FOV = 35×35 mm, and slice thickness = 1 mm and 12 image slices with no gap. The final T2 and R2 map images were generated by using a ImageJ plugin MRI T2 calculator, and the T1 and R1 map images were generated with MATLAB. After MRI experiment, animals were sacrificed and different organs including liver were collected for biodistribution, and histology experiments.

T1-wieghted MRI images were recorded with TR of 500 ms and TE of 15 ms with matrix resolution of 256×256, FOV = 35×35 mm, and slice thickness = 1 mm and 12 image slices with no gap. T2-weighted images were recorded with TR=2000 ms and TE of 8 ms with matrix resolution of 256×256, FOV = 35×35 mm, and slice thickness = 1 mm and 12 image slices with no gap. Heavy T2-weighted images were recorded with longer TE times in order to completely

remover the T1 effect. The TE used is 4000 ms and TE=10 ms. Other parameters remained the same.

2.6 Statistical analysis

Statistical analysis of signal to noise ratio (SNR) was performed using two-tailed Student's t test. The statistical analysis of contrast-to-noise ratio (CNR) of T_1- and T_2-weighted imaging were analyzed by one-way ANOVA. Statistical analysis was performed in GraphPad Prism 5 (GraphPad Software). Longitudinal relaxation rate (R1) maps and their associated histograms were generated from the images using a custom written MATLAB (Mathworks, Natick, MA) program for voxel wise fitting of the inversion recovery signal intensities as a function of inversion recovery time. The mouse group sizes were set to support statistically valid data and to minimize the use of the animal. Mice were randomly assigned to groups for the experiments. The animal studies were not blinded, because the same investigators performed the grouping, experiments, and analysis, rendering blinding of these studies unfeasible. An experienced pathologist was blinded to the groups of H&E and Sirius red staining to evaluate the staging of fibrosis as well as organ toxicity of contrast agents.

In addition, the change in liver longitudinal relaxation rate ΔR1 which is defined as $R1_{post}$-$R1_{pre}$ as well as Increase Rates of Liver R1 values (%) defined as

$$\text{Increase rate of R1 values} = \left[\frac{R1_{post} - R1}{R1_{pre}}\right] \times 100\,(\%) \tag{2-9}$$

Was calculated. Receiver Operating Characteristic (ROC) analysis used to demonstrate our developed contrast agent ability in staging liver fibrosis

2.7 Determination of r_1 and r_2 relaxivity values

The ability of a contrast agent to change a relaxation rate is represented quantitatively as relaxivity, r_1 or r_2, where the subscript refers to either the longitudinal ($1/T_1$) or the transverse rate ($1/T_2$). Relaxivity is simply the change in relaxation rate after the introduction of the contrast agent ($\Delta(1/T)_1$) normalized to the concentration of contrast agent or metal ion (M):

$$r_1 = \frac{\Delta(1/T_1)}{[\mathrm{M}]} \tag{2-10}$$

The relaxation rates of contrast agents (r_1 and r_2) were determined using different concentrations of $GdCl_3$ and protein (2:1) at 37 °C with 1.4 T Bruker Minispec using saturation recovery and CPMG sequence, respectively. Using the equation below the relaxation rate for both T_1 and T_2 were measured. The slope of the curve will be longitudinal (r_1) and transverse (r_2) relaxivities. Furthermore, the T_1 and T_2 of Gd-DTPA and ProCA32.collagen1 were also measured by using a 7 T Agilent scanner using saturation recovery and spin echo sequence. r_1 and r_2 were calculated by eqn 10.

$$r_i = \left(\frac{1}{T_{\mathrm{is}}} - \frac{1}{T_{\mathrm{ib}}}\right) \Big/ [\mathrm{Gd}^{3+}] \quad i = 1, 2 \tag{2-11}$$

2.8 Enzyme-linked immunosorbent assay (ELISA) assay

Collagen type I solution from rat tail (Sigma-Aldrich) was coated in 96-well plates at 4 °C overnight. After being blocked with 5% bovine serum albumin (BSA), a series of different concentrations of ProCA32.collagen1 was incubated with the collagen type I solution. After incubation at 4 °C overnight, the unbounded ProCA32.collagen1 was washed away with 1× TBST.

The homemade polyclone rabbit-anti-ProCA32 antibody was applied with 1: 1000 dilution as the primary antibody against protein contrast agent. A stabilized goat-anti-rabbit HRP-conjugated antibody (Pierce) was used as the secondary antibody. After a robust wash with 1× TBST, the remaining secondary antibody in the 96 well plate was visualized by using 1-Step™ Ultra TMB-ELISA Substrate Solution (Thermo Fisher Scientific). The absorbance intensity was detected by the FLUOstar OPTIMA plate reader at an absorbance wavelength of 450 nm.

2.9 Pharmacokinetics, distribution and toxicity studies

All the animals were injected with 5 mM of Gd-DTPA, ProCA32-P40, and ProCA32.collagen1. Different organ tissue samples from the mice were collected after euthanasia. The collected tissues (~ 0.2 g) were digested with 70% (wt/vol) ICP-grade HNO_3 at 40 °C overnight. The HNO_3 solution containing the digested tissues were collected the next day, filtered, and diluted with 2% (wt/vol) HNO_3 to 8 mL. Then each sample containing different organ was analyzed by ICP-OES to measure the Gd^{3+} concentration at wavelength of 342.246 nm. YCl_3 at 2 ppm was used as internal reference and different Gd^{3+} standard solutions with different concentrations ranging from 5 ppb to 1000 ppb were made.

For pharmacokinetics studies, the blood concentration-time profiles after intravenous injection of ProCA32.collagen1, ProCA32-P40, and Eovist in mice were analyzed using two-compartmental analysis using WinNonlin ™ 5.0.1 software (Pharsight Corp., Palo Alto, CA). Mean blood concentration values from 3-6 mice at each sampling time point were used for the mice pharmacokinetic analysis. The area under the blood concentration-time curve (AUC) was calculated using the log-linear trapezoidal rule. The elimination half-life ($t_{1/2}$) was calculated by the equation $t_{1/2} = 0.693/K$, where K was estimated from the terminal slope of the blood Gd^{3+} concentration versus time curve. The systemic clearance (CL) was determined from dose/AUC,

with AUC (area under the curve to infinity) by linear interpolation and extrapolation to infinity y from C_{last} x $t_{1/2\beta}$/0.693 (where C_{last} was concentration at each last sampling point). The volume of distribution at steady-state (Vss) was determined by the equation Vss = CL × (AUMC/AUC), where AUMC is the area under the first moment curve. The mean residence time (MRT) was calculated from AUMC/AUC.

For clinical chemistry test studies of ProCA32.collagen1, mice with an average body weight of 30 g were I. V. injected with 0.0012 mmol/kg of ProCA32.collagen1. The bloods of the mice were collected five days post injection using heparin-coated capillary. Then the serum of blood was obtained by centrifuge at 3000 rpm at 4 ˚C for 10 min. Approximately 300 μL of mice serum were collected for clinical chemistry tests conducted in IDEXX Laboratories. The clinical chemistry tests assessed the liver, kidney, and heart functions based on the levels of different liver enzyme, proteins, glucose and ions in the serum.

2.10 Serum stability and transmetallation of ProCA32.collagen1

About 300 μM of ProCA32.collagen1 complexed with Gd^3 was mixed with human serum with 1:1 ratio, and then incubated at 37 ˚C for different time points. SDS-PAGE gel was used to to detect the presence of Gd^{3+}-ProCA32.collagen1 after incubating in the serum for each time point. The protein separated by SDS-PAGE is stained by Coomassie brilliant blue or Ponceau S solution to monitor its stability. Transmetallation of ProCA32.collagen1 and clinical MRI contrast agents were evaluated by measuring the relaxivity changes in the presence of Zn^{2+} and phosphate over time. The relaxivity of ProCA32.collagen1 was monitored with 55 or 110 μM ProCA32.collagen1, 100 μM Gd^{3+}, 100 μM Zn^{2+}, and 1.2 mM $PO4^{3-}$.

2.11 Measurement of water coordination number in ProCA32.collagen1

The number of water ligands coordinated to ProCA32.collagen1 complexed with Gd^{3+} complex was determined by measuring Tb^{3+} luminescence decay in H_2O or D_2O using the previously published methods with some modifications [180]. Tb^{3+} was excited at 265 nm with a Xenon Flash lamp and the Tb^{3+} emission was collected at 545 nm at a series of time points in both H_2O and D_2O solutions. Luminescence decay lifetime of Tb^{3+} or Tb^{3+} complex with different chelators and ProCA32.collagen1 in H_2O and D_2O solution were determined by fitting monoexponential decay equation. A standard curve of water number (q) over ΔK_{obs} (the difference of the decay constant between H_2O and D_2O) was plotted using Tb- NTA (q=5), Tb-EDTA (q=3), Tb-DTPA (q=1) and Tb^{3+} in aqueous solution (q=9). The water number of ProCA32.collagen1 was calculated based on the standard curve.

3 DESIGN, EXPRESSION AND PURIFICATION OF PROCA32.COLLAGEN1

3.1 Introduction

As it was mentioned in Chapter 1, currently used MRI contrast agents are not sensitive enough for patient's needs in diagnosis and treatment monitoring, therefore development of new and more sensitive MRI contrast agents with targeting capability is urgently required. To design contrast agents based on proteins with improved in vivo and in vitro applications, there are several important criteria that need to be taken into consideration. First, protein- based MRI contrast agent should be stable and resistant to factors such as protease cleavage to prevent degradation in the body. Furthermore, protein-Gd^{3+} complex should be stable with protein binding strongly to Gd^{3+} to avoid competition with other physiological cations such as Ca^{2+} and Zn^{2+} and inions. Since free Gd^{3+} is toxic with LD50 of 0.2 mmol/kg [144], Gd^{3+} must bind to protein contrast agent to avoid free Gd^{3+} being released before excreted out. Second, the contrast agent should have high

sensitivity and therefore higher relaxivity to increase the dose efficiency. If relaxivity is higher, then the total injection dosage of Gd^{3+} will be decreased to reduce to the toxicity caused by free Gd^{3+} release. High relaxivity of contrast agent also improve the sensitivity of MRI for imaging biomarkers. Third, protein contrast agent should have a proper size to optimize organ/tissue distribution and blood retention time. It is recommended for contrast agents to have fast accumulation in the organ/tissue and fast excretion to reduce the toxicity. Fourth, immunogenicity of protein-based MRI contrast agent must be decreased, therefore, PEGlytion is one of the factors to reduce this effect. Fifth, protein contrast agent should have targeting capability, therefore, targeting moieties should be grafted inside or conjugated to improve the imaging specificity and enable quantitative biomarker imaging.

Previous members in our lab have designed two Gd^{3+} binding sites into a scaffold protein called rat α-parvalbumin and were able to increase relaxivity by tuning τ_c and secondary coordination shell contributors as well as improving metal binding affinities [83]. However, targeting specific biomarkers to image in different diseases was still a challenge and needed further investigation [78]. Design of ProCA32.collagen1

3.2 Design of ProCA32.collagen1 with collagen type I targeting capability

In order to design a protein contrast agent with targeting capability, collagen targeted protein MRI contrast agent, ProCA32.collagen1 was designed by covalently linking a collagen type I targeting peptide (KKWHCYTYFPHHYCVYG) moiety consisting natural amino acids to the C-terminal of protein contrast agent ProCA32 (with two Gd^{3+} binding sites). A flexible hinge was used to optimize the targeting capacity of the peptide [83] (Fig. 1.6). The collagen type I targeting peptide was chosen in way that residues in the peptide are contributing both to the binding and relaxivity by tuning correlation time. Cysteine residues can form a cyclic peptide to interact

with collagen I and Lysine residues are improving *in vivo* MR imaging through PEGylation. Lysine PEGylation of the whole contrast agent can improve protein solubility, blood retention time and reduce immunogenicity [84]. The designed ProCA32.collagen1 was bacterial expressed, purified, and modified and confirmed to form a 1:2 Gd-ProCA32.collagen1 complex using ICP-OES (Methods) [83] [177].

3.3 Results

3.3.1 Expression and purification of ProCA32.collagen1

Fusion of a collagen-targeting peptide to ProCA32 can generate collagen-targeted MRI contrast agent, ProCA32.collagen1 since ProCA32 has multiple Gd^{3+} binding sites and our protein-based MRI contrast agent will be able to quantitatively evaluate the collagen expression in different diseases such as uveal melanoma tumor in the liver and liver fibrosis. Therefore, this protein was expressed and purified. The transformation was carried out using B21 (DE3) plyss cell line. Then, small scale (250 mL of LB medium) and Large scale (1000 mL): 1 L of LB medium was used for expression. The temperature was 37°C for small scale and then the medium was transferred to large scale (1 L). After optical density of bacteria reached 0.6, 500 µL of IPTG was added to induce the expression of the protein and then the temperature was decreased to 25°C for overnight expression. Cell pellets are collected by centrifugation, and then HEPES (10 mM) buffer with pH=7.4 was added into the cell pellets. For cell pellets coming from 1 L of LB medium, 10 mL of PBS buffer was used plus 100 µL of PMSF and 1 µL of benzonulease (for DNA cleavage). Sonication was performed for 12 times until a homogenous solution was reached. The solution was centrifuged at 17000 rpm speed for 10 min and the supernatant was collected, and then boiled for 10 min. Again the solution was centrifuged for 6000 rpm for 10 min and supernatant was collected. 3% streptomyosin was added into the mixture and incubated at 4°C overnight to

precipitate the DNA and remove it from the protein. Centrifugation was carried out for another 10 min and the supernatant was collected (6000 rpm). The solution was then heated to 80-85°C for 10 min and then centrifuged down at 6000 rpm and supernatant was obtained. In the next step, the protein was dialyzed overnight in 10 mM HEPES buffer at pH=8.0. to be negatively charged (500 uL of PMSF was added). Then before injection of supernatant to FPLC for further purification, EGTA is added to the final concentration of 20 mM to remove any extra calcium and then the supernatant is filtered and injected to FPLC.

For purification using FPLC, an ion exchange column was used. A resin is chosen so that the protein binds to resin by a charge interaction. In the final step of FPLC, the concentration of salt in the buffer is increased in order to elute the protein out of the column. Figure 3.1 demonstrates the SDS-page results for expression and purification of ProCA32 with collagen targeting moiety.

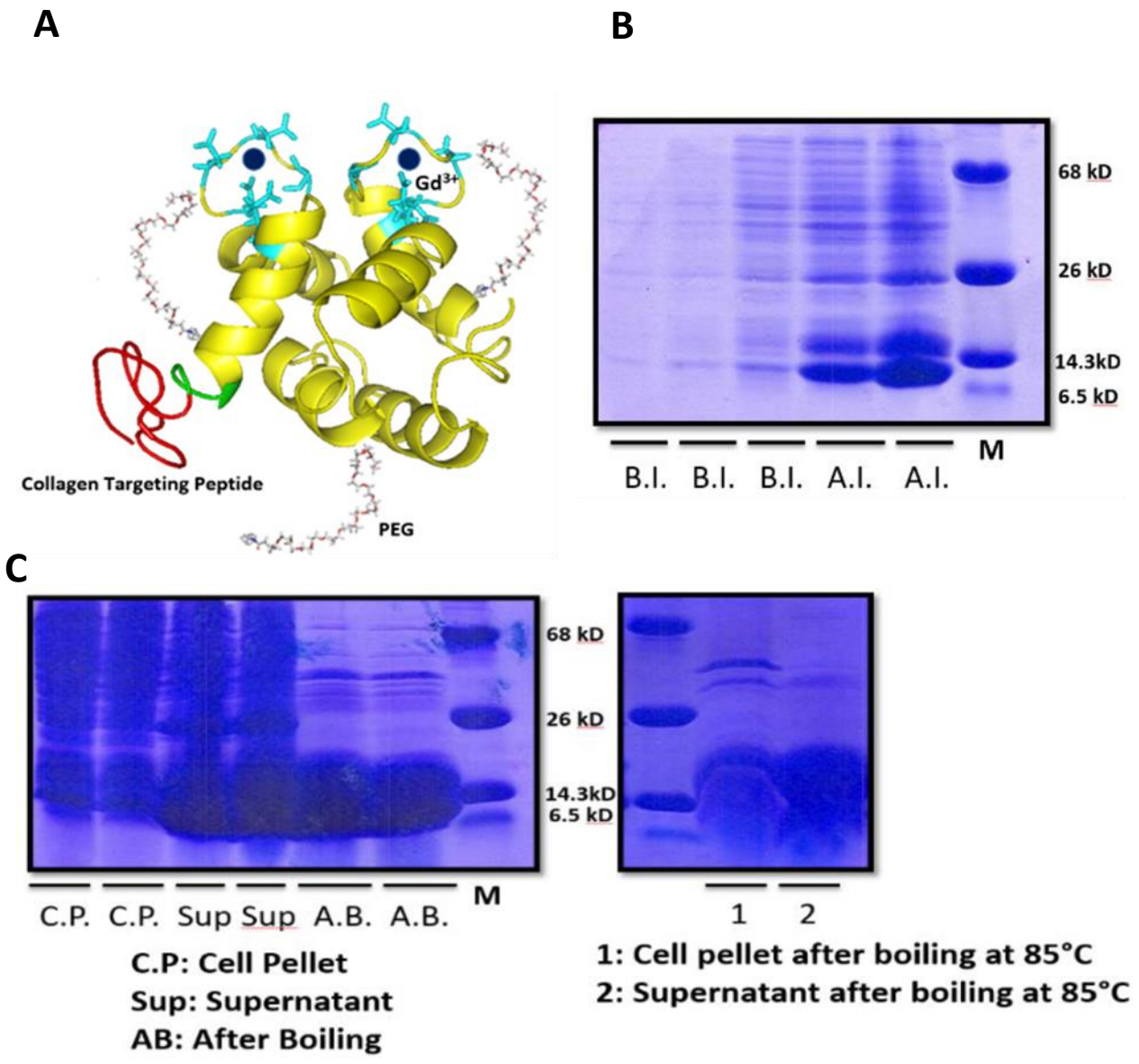

Figure 3.1 *Modeled structure of ProCA32.collagen1 and its expression and purification.* ***A****. Model structure of ProCA32.collagen1 based I-TASSER.* ***B****. Expression of ProCA32.collagen1 in BL21 (DE3) plys (BI: Before Induction, AI: After Indcution).* ***C****. Different steps of ProCA32.collagen1 purification.*

The results in Fig. 3.1 demonstrates that the protein has been successfully purified using our established purification protocol and furthermore, boiling the sample helps the purification and

elimination of unwanted proteins. As can be seen in Fig. 3B, after boiling, most of the undesired proteins were removed from our target protein. Figure 3.2 illustrates the FPLC spectra of the purified protein. As it can be seen in the figure, four major peaks can be observed. The first peak corresponds to undesired proteins and maybe some of our target proteins at very low amount. However, both peak 2 and 3 in the FPLC spectra belongs to our ProCA32.collagen1 with a slight difference. The second peak is the Holo form of our protein-based contrast agent (Ca^{2+}-bound) and the third peak is the Apo form of our protein (Ca^{2+}-free). Since our contrast agent binding sites are supposed to be occupied with Gd^{3+}, the Ca^{2+}-free form is desired for future experiments in order to avoid any effects on Gd^{3+} binding affinity of ProCA32.collagen1.

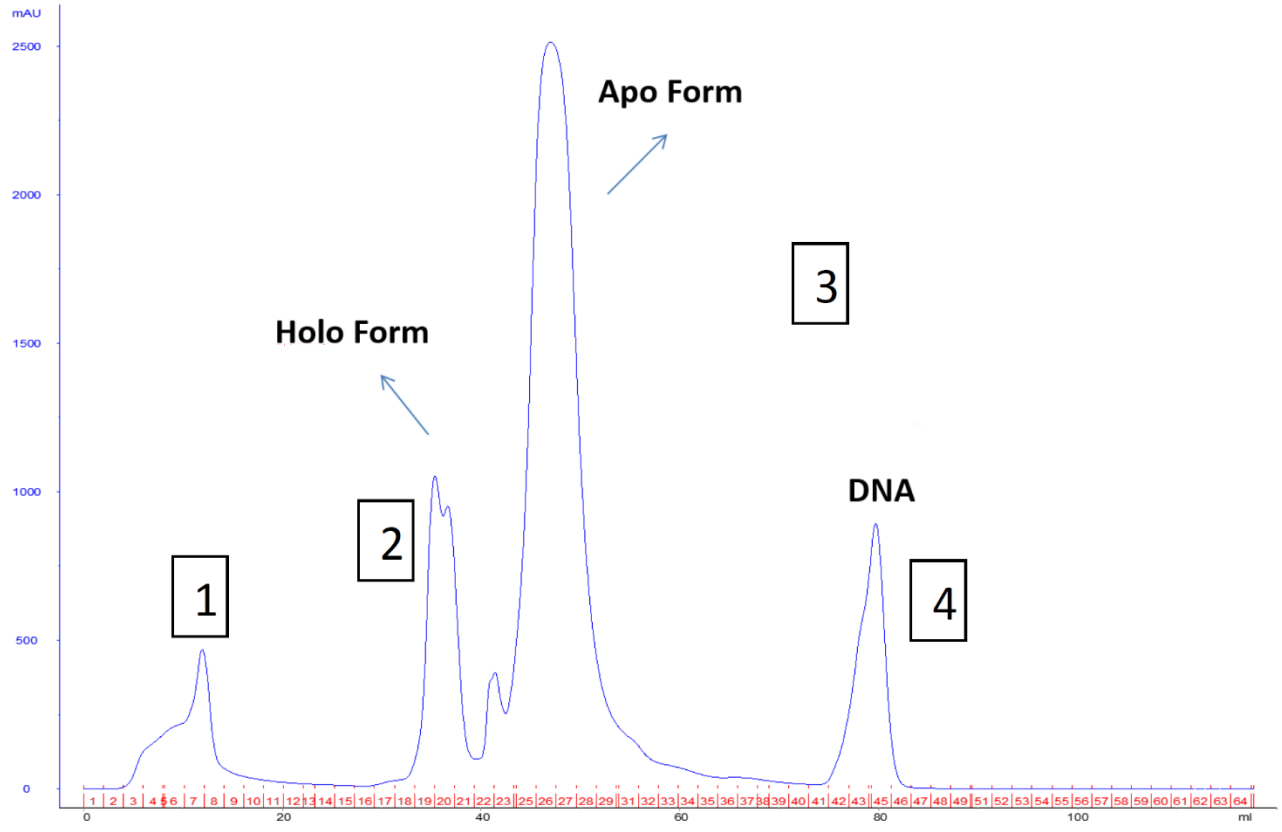

Figure 3.2 *Diagram of ProCA32.collagen1 purification using FPLC.*

The majority of Peak 1 include unwanted proteins, and peak 2 is the Ca^{2+}-bound form of ProCA32.collagen1 and peak 3 include the Ca^{2+} free form which is the desired form and peak 4 has DNA.

In the last peak, DNA will elute out as peak number four. At the end, all fractions for peak 3 were collected and combined, and a SDS-page gel electrophoresis was run to make sure the protein is completely pure. Then the concentration of the protein was measured using UV-Vis instrument. Figure 3.3 shows the UV-Vis spectrum of pure ProCA32.collagen1. A small shoulder right before 280 nm wavelength can be observed which is another indication for the presence of our protein.

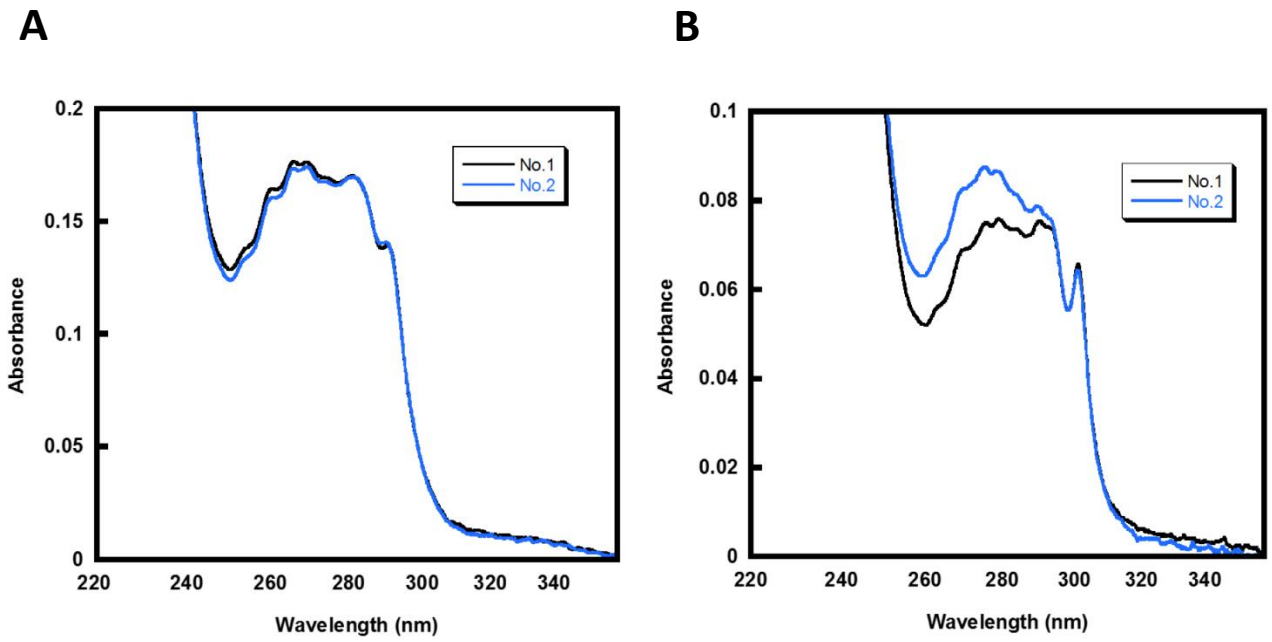

Figure 3.3 *UV-Vis spectrum of ProCA32.collagen1 after FPLC purification*

A. shows the Apo form of ProCA32.collagen1 after concentration of peak 3 and B. demonstrates the Holo form of ProCA32.collagen1 after concentration of peak 2 (No.1 and 2 correspond to different concentrations of the protein).

Two different batches of the protein were purified with different concentrations. To further confirm the purity of the protein, a sample was sent to mass spectrometry facility in order to obtain the electro spray ionization (ESI) spectrum.

3.3.2 Lysine PEGylation of ProCA32.collagen1

To optimize the protein solubility, blood circulation time, and avoid possible enzymatic degradation and reduction of immunogenicity; Poly ethylene glycol (PEG) conjugation with protein has been often used in pharmaceutical and biotechnical applications. The desired protein can be modified using several PEG conjugation strategies such as amino group modification, thiol group modification. For this purpose, ProCA32.collagen1 has been PEGylated with NHS-Ester on lysine residues.

The contrast agent was modified using Methyl-POEn-NHS ester, PEG-40 with molecular weight of 2 kDa and 40 repeating units of ethylene glycol. At first, ProCA32.collagen1 and PEG-40 were mixed with 1:5 ratios in 10 mM HEPES buffer (pH 7.2) and allowed to shake at room temperature for about 2 hours or at 4 °C overnight. Then, 100 mM Tris/HCL was added to the reaction mixture to stop the reaction by quenching the unreacted free PEG-NHS ester. The mixture was then concentrated about 4 times using concentrator with 3-6kDa membrane to remove the unreacted free PEG (MW 2 kDa). PEGylated protein was identified by Iodine staining and SDS-PAGE. Iodine can stain the free PEGylated protein along with free PEG in the solution while Coomassie brilliant blue can stain the protein that is already conjugated with PEG. Figure 3.4 shows the SDS-page results with Coomassie brilliant blue stain (left) and iodine stain (right) before and after PEGylation. As it can be seen most of the protein has been PEGylated.

PEGylation on Cysteine resides is also possible, however, due to possible role of cysteine in binding to collagen type I, Lysine PEGylation was chosen, further details will be discussed in the next chapter.

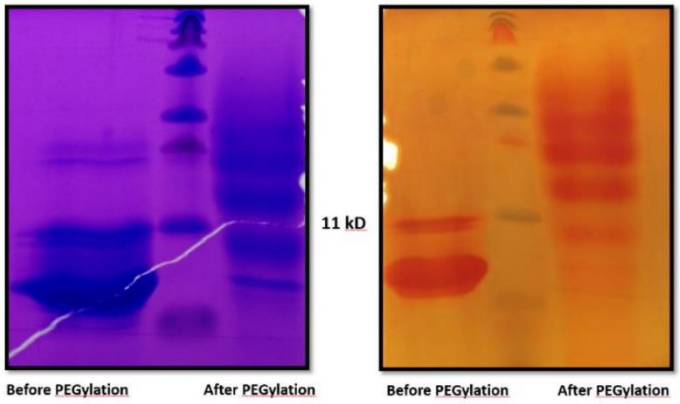

Figure 3.4 *SDS-page results for Lysine PEGylation of ProCA32.collagen1. Left (Coomassie blue stain) and right ($BaCl_2$/I stain) gels show ProCA32.collagen1 before and after Lys PEGylation. Multiple bands after PEGylation is showing that multiple Lys residues in the protein are PEGylated.*

Figure 3.5 demonstrates the structure of the contrast agent after PEGylation with PEG. As it can be seen in the figure, multiple sites have been PEGylated since there are multiple Lys residues in both the protein and targeting peptide.

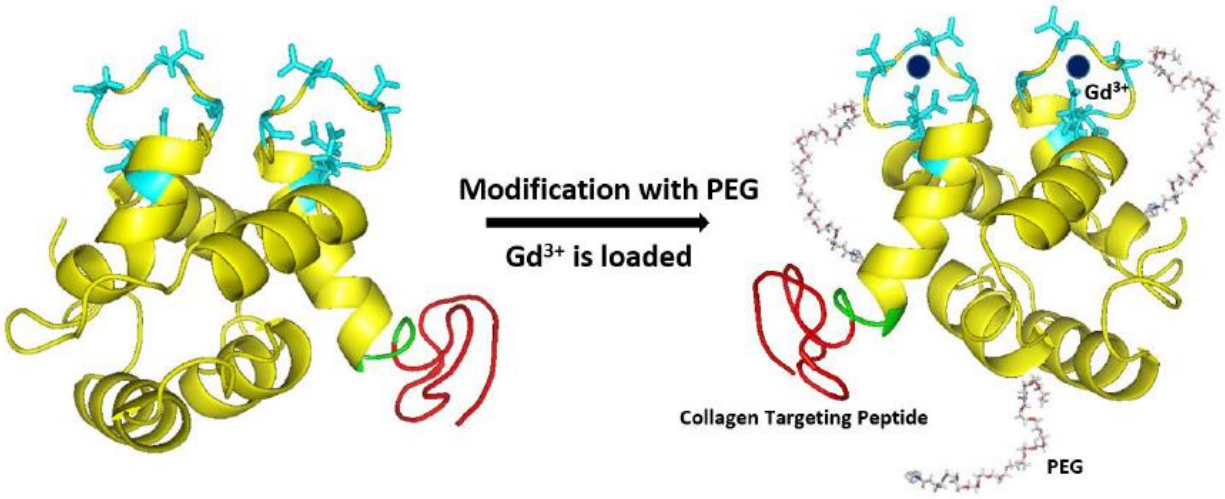

Figure 3.5 *Structure of ProCA32.collagen1 after PEGylation*

3.4 Discussion

3.4.1 Optimization of ProCA32.collagen1 purification

In order to improve the yield of ProCA32.collagen1, several modifications were made in the original purification protocol of parvalbumin to remove DNA contamination more efficiently and simplify the purification procedure. To remove DNA, additional step before FPLC for DNA precipitation was added. We added 3 % streptomycin sulfate and incubated at 4°C overnight. After centrifugation at 13000 rpm for 10 min, the supernatant was heated at 85°C for 5 min. After centrifugation, the supernatant was dialyzed against 10 mM Tris/HCl at pH 8.0 before injecting into FPLC column. Moreover, the buffer pH was increased from 7.5 to 8.0. Since the Q column is anion exchange column, increasing the pH of buffer improves the binding of ProCA32.collagen1 to the column. It was observed that our protein can be eluted out from Q column at 200 mM NaCl, therefore, the percentage of buffer B (containing 1 mM NaCl) during elution was decreased from 70% to 25%. In addition, the flow rate of FPLC was decreased from 5 mL/min to 2 ml=L/min to

improve the binding of ProCA32.collagen1 to Q column. Nine column volumes are usually used to let buffer B slowly increase from 0% to 25%. The very slow increase of salt gradient further helps the separation between ProCA32.collagen1 and DNA. After FPLC purification step, the remaining DNA can be further eliminated by concentrating protein using through 3-6 kDa membrane.

The FPLC purification curve is shown in Fig. 3.2. The UV absorbance at 280 nm from FPLC detector shows four peaks during the elution with buffer B. Each peak was collected and then measured by UV spectroscopy, SDS PAGE and agarose gel. The third fraction (peak 3) showed a single band at 14.3 kDa, which is consistent with the molecular weight of ProCA32.collagen1. UV spectrum of this fraction (Fig. 3.3A) is the same as parvalbumin (PV) in the old purification techniques. The first and second peaks have the Holo form of ProCA32.collagen1 and the last peak contains protein with a molecular weight of 30 kDa. DNA and UV absorbance data demonstrated that peak 1 and peak 4 has a lot of DNA/RNA since they showed high absorbance at 260 nm. The final yield of ProCA32.collagen1 is about 50-70 mg per liter bacteria expression in LB medium.

3.5 **Summary**

To design novel protein-based MRI contrast agent with collagen type I targeting ability (ProCA32.collagen1), PV was selected as the scaffold protein based on the criteria discussed for an ideal contrast agent. This developed protein is well folded, highly stable and soluble, tolerant to mutations, have a rigid structure and strong metal binding sites for Gd^{3+}. There is also no reported interaction between this protein and PV. We have chosen a collagen type I targeting peptide to create a targeting capacity and improve its relaxivity by altering PEGylation locations. We have constructed vectors for the bacteria expression. We have also optimized the bacterial

expression and tag-less purification procedures of ProCA32.collagen1 by selecting expression strains and removal of DNA contaminations. After purifying ProCA32.collagen1, different biophysical properties of the contrast agent such as metal binding affinity and selectivity, relaxivity, metal coordination ligands, and serum stability were examined. ProCA32.collagen1 was also PEGylated for in vivo studies, such as MR imaging, biodistribution, pharmacokinetics and toxicity.

4 STUDIES OF BIOPHYSICAL PROPERTIES OF PROCA32.COLLAGEN1

4.1 Introduction

Safety is one of the most important criteria in development of contrast agents, therefore, the contrast agent must have superior biophysical properties such as high Gd^{3+} stability, high metal selectivity as well as relaxivity. As it was mentioned before, long term toxicity of the contrast agent usually originates from the free Gd^{3+} release in the body because of the competition of other physiological cations and onions, such as Zn^{2+}, Mg^{2+} and $PO4^{3-}$. The ionic radius of Gd^{3+} is 0.93 Å, which is similar to the ionic radius of Ca^{2+}. Therefore, Gd^{3+} has the ability to bind to the physiological Ca^{2+} and occupy binding sites in Ca^{2+} binding proteins. It is very likely that this interaction can disrupt and affect the dynamic function of calcium binding proteins. Moreover, Gd^{3+} accumulation could cause NSF (Nephrogenic systemic fibrosis) in long terms, which is a lethal disease in patients with the impaired kidney function [181, 182]. A safe MRI contrast agent with high metal stability and Gd^{3+} selectivity is urgently required to reduce the toxicity caused by MRI contrast agent injection. Traditional techniques such as pH titration were applied to measure the meal binding affinities for the small-chelator based clinical contrast agents [183]. Small chelators, such as DTPA, has a Gd^{3+} binding affinity of 1.8×10^{-21} M. In proteins however, since there are multiple protonations of residues, traditional methods such as pH titration cannot be

applied to measure the dissociation constant (Kd) between ProCA32.collagen1 and Gd^{3+} or other metals. FERT methods that are based on Tb^{3+} or Eu^{3+} can be applied to determine protein-metal binding affinity measurement but one of the major limitations of these methods is the lack of sensitivity which they can only determine a Kd of around 1 μM or above. Due to this limitation, the metal binding affinity for Tb^{3+} reported for our previous contrast agents such as ProCA1 was around 10^{-7} M. With several other methods being developed such as the Ca45 flow dialysis, equilibrium dialysis, florescence dye titration and NMR for determination of metal binding affinities for calcium binding proteins [72, 184], the Gd^{3+} binding affinity of EF-hand binding proteins is still not accurately reported. The Ca^{2+} binding affinity of all EF-hand proteins for instance PV can reach to 10^{-9} M. Therefore, a more accurate method is required to measure Gd^{3+} binding affinity in the range between 10^{-22} and 10^{-18} M for our contrast agent, ProCA32.collagen1.

Relaxivity is another key parameter for MRI contrast agents as discussed thoroughly in Chapter 1. The MRI signals are generated based on the different relaxation properties of protons. However, such differences are very small among organs in vivo. The contrast and sensitivity of MRI can be improved by administrating the contrast agents. MRI contrast agent works as "catalyst" to catalyze the relaxation properties of each water molecule. By differential distribution in vivo, MRI contrast agents make the relaxation properties different in each organ. The relaxivity of clinical MRI contrast agent is around 5 $mM^{-1}s^{-1}$. The theoretical maximum relaxivity, however, is about 100 $mM^{-1}s^{-1}$, therefore, there is a strong need to develop MRI contrast with high relaxivity.

Since ProCA32.collagen1 is a targeted contrast agent, therefore, it needs to have proper binding affinity to collagen type I, in order to generate the targeting effect.

In this chapter, we first report a sensitive technique previously developed by our lab to measure metal binding affinities (Tb^{3+}, Gd^{3+}, Ca^{2+}, and Zn^{2+}) and selectivity of

ProCA32.collagen1. We then report our studies on determining relaxivity and water number of ProCA32.collagen1 designed in Chapter 1 and 2. In addition, using ELISA method, we report the collagen type I binding affinity of ProCA32.collagen1. At the end, we will report the detailed pharmacokinetic studies of ProCA32.collagen1 required for *in vivo* studies.

Contrast-enhanced magnetic resonance imaging is evolving rapidly with different clinical applications in imaging various diseases, therefore several important characteristics of MRI contrast agents such as their biodistribution, safety profile and pharmacokinetics have been well studied over the past few years. Based on their distribution, clinical MRI contrast agents can be categorized into three classes. First class is non-specific MRI contrast agents or Extracellular Fluid Agents (ECF), second class is liver specific MRI contrast agents, and third class is blood pool MRI contrast agents. Some clinical contrast agents such as Magnevist, Omniscan, ProHance, Optimark, and Dotarem are part of the non-specific MRI contrast agents. Due to their small size and low molecular weight and no interaction with biomarkers in the body, there are mainly distributed in blood vessels and extracellular-extravesicular spaces with very short blood half-life which is less than 5 min in mouse and less than 30 min in humans. The organ that these contrast agents are mainly accumulated is kidney which is their way of excretion from the body. Therefore, they can be used for kidney imaging.

In addition, this type of MRI contrast agents can accumulate in lesions and disease tissues with blood vessel damage, therefore, they can be used for cancer, and stroke imaging. Second class which are liver specific MRI contrast agents such as MultiHance and Eovist are also small chelator-based contrast agents, however, the major difference between these and non-specific MRI

contrast agents is that they are covalently incorporated with one hydrophobic moiety, which facilitates liver accumulation of these contrast agents. Clinical studies demonstrated that, 10% MultiHance and 50% of Eviost is excreted from the liver [185]. Mn-DPDP is another liver specific MRI contrast agent with similar structure as vitamin A which has uptake by liver cells. The accumulation of Mn-DPD in liver increases the MRI signal significantly, however, there are some stability concerns associated with DPDP in the liver which can cause Mn^{2+} release [21]. A blood pool MRI contrast agent, MS-325 is a new FDA approved drug which can reversibly binds to serum albumin. The binding of MS-325 to albumin can increase its relaxivity as well as its blood half-life which increases its circulation time. Due to its unique blood distribution properties, MS-325 has been approved for imaging blood vessel abnormalities [21]. In addition to clinical MRI contrast agents, nano-sized MRI contrast agents, such as dendrimers liposome, nanotubes, and emulsions have been developed with dramatically different pharmacokinetic and distribution properties. The pharmacokinetics, distribution and excretion of these contras agents are largely affected by the size, charge and targeting moieties of the contrast agents. One of the disadvantages of these contrast agents is that with a size larger than 7 nm, they cannot be eliminated from renal filtration, and therefore their blood retention time are much longer. Liver and spleen are the major sites of accumulation of these agents due to the phagocytosis of immune-cells. Nanoparticles with molecular weight larger than 30 kDa is accumulated in the tumor tissue due to EPR effects [31, 78].

4.1.1 Gadolinium deposition

These approved compounds were all designed to be completely excreted after injection. The pharmacokinetic studies in humans noted that recovery of gadolinium decreased in patients with severe renal insufficiency. From studies on NSF patients it is clear that some gadolinium is

retained. Several reports show Gd to be present in skin biopsies of NSF patients [186-191]. Recently Kay et al. [192] described a case report of a female patient who died with NSF. Gadolinium was found in all tissues surveyed and there were very high levels of Gd reported in the kidney and the heart. Swaminathan et al. [186] also noted high concentrations of Gd in the heart and vessels on postmortem analysis of NSF subjects. It is not yet established whether Gd is also retained in patients with renal impairment but who do not develop NSF. It is still not established what the form of Gd is in these patients. For instance, is the Gd^{3+} still part of the contrast agent? Is it present as some insoluble inorganic deposit like the carbonate or phosphate salt, since these are very insoluble. Or is the Gd removed from the chelate but bonded to the calcium binding site of a calcium binding protein since it is known that gadolinium can replaced calcium in proteins. If the Gd is released from the contrast agent, what is the mechanism for release? Frenzel et al. [157] recently reported the serum stability of approved contrast agents and found that about 20% of Gd was released from gadoversetamide and gadodiamide after 15 days in human serum at pH 7.4, 37 °C compared to <2% release for the linear ionic chelates, while the macrocyclic chelates showed no detectable Gd release. Gd release in serum was increased when phosphate concentration was increased [157]. This would suggest that in renally insufficient patients where the plasma half-life increases to days, there would be significant Gd release from gadodiamide and gadoversetamide. Factors influencing Gd release are the presence of metals that have high affinity for the Gd-binding ligand like Zn2+, Cu2+, or Fe3+ and/or the presence of ligands with high affinity for Gd such as phosphate and carbonate. Another potential mechanism for Gd release would be low pH in a lysosome if the contrast agent is taken up intracellularly, e.g. in the renal proximal tubules. It is well established that the rate of Gd release increases with decreasing pH.

Gibby and coworkers compared Gd levels in the bone of patients that were scheduled for hip transplant following a contrast enhanced MRI [21, 158]. Bone was taken about 4 days after Gd administration. Patients received either gadodiamide (N=9) or gadoteridol (N=10) at the standard 0.1 mmol/kg dose. They found 4-fold higher levels of Gd in the bone of subjects who received gadodiamide (1.77±0.704 μg Gd/g bone) than for those who received gadoteridol (0.477±0.271 μg Gd/g bone). Assuming a similar distribution to all bone and depending on the fractional weight of bone in the individual, this would equate to about 1 – 2% of the injected dose of gadodiamide being present in the bone after 4 days. This study did not identify whether the Gd was still associated as the contrast agent. However, since both gadodiamide and gadoteridol have similar clearance rates, the excess Gd remaining after gadodiamide injection is presumed to be dissociated Gd. It is unknown how fast the Gd will clear from the bone. In animal studies (see below), bone levels of Gd decreased with time after contrast agents were injected. For "free" Gd, which localizes mainly to liver and bone, elimination of Gd was on the order of 1–3% per day in rodents.

On the one hand it is straightforward to detect and quantify Gd in biopsy or autopsy samples. Since Gd is not an essential element and is not ubiquitous in the environment, there is no background signal to contend with. Elemental analysis techniques like inductively coupled plasma (ICP) with mass spectrometry (MS) or optical detection are sensitive means to quantify Gd. However, this is a destructive technique that reports only on the elemental composition and not on form of the Gd, i.e. whether it is still present as contrast agent. Scanning electron microscopy (SEM) with x-ray spectroscopy is also used. This can detect Gd and can also indicate the distribution of other heavy elements that are spatially localized with the Gd. However, SEM cannot indicate in what form the Gd exists in tissue. There is also potential bias in the SEM technique because this technique is sensitive to heavy atoms. For instance, a microcrystalline deposit of

gadolinium phosphate, with its high local concentration of Gd and P atoms, would be much more visible than a diffuse distribution of Gd still present as contrast agent or Gd bound to calcium-binding proteins. There remains a need for additional biophysical studies to determine the speciation of Gd in skin and other organs.

Although the ECF agents generally behave very similarly, there are some differences among their physical properties. The diamide complexes gadodiamide and gadoversetamide have considerably lower thermodynamic stability (log K~17 vs log K >21 for other Gd complexes) [193]. The linear complexes tend to be more reactive to metal substitution (transmetallation) or decomplexation. The incidence of NSF seems to reflect these physical chemistry findings. Most cases have been reported with gadodiamide, the least stable and least inert compound. Other cases have been reported with gadopentetate and gadoversetamide, while no non-confounding cases have yet been reported with the other contrast agents. In terms of market share, gadopentate > gadodiamide > gadoteridol > other agents.

4.1.2 Gadolinium deposition in animals in approved contrast agents

There have been concerns about Gd deposition in tissue since Gd-based contrast agents were first reported. A fundamental product criterion was full elimination of the Gd. In rodent studies the bone and the liver are target organs for Gd deposition. Tweedle and colleagues published a series of studies comparing Gd retention in rats and mice after injection of Gd-DTPA, GdHP-DO3A, Gd-DOTA, and Gd-DTPA-BMA as well as some other compounds, including “free Gd” administered as GdCl3 or gadolinium acetate [35, 194]. When “free Gd” is administered i.v. most of the dose is deposited in the liver and the bone of rodents. Very little is excreted and clearance has been reported to be on the order of 1 to 3% per day. When contrast agents are administered, the biodistributions of Gd-DTPA, GdHP-DO3A, Gd-DOTA, and Gd-DTPA-BMA

are very similar for the first 24 hrs. At 7 and 14 days the data begins to separate. The organs with remaining Gd are kidney, liver, and bone. In a direct comparison of 4 compounds the order of tissue retention was Gd-DTPA-BMA > Gd-DTPA ~ Gd-DOTA ~ GdHPDO3A [28]. There was no statistical analysis performed in that study but it is apparent from the values and standard deviations reported that there is significantly more Gd remaining in the whole body, liver, or femur of mice or rats treated with Gd-DTPA-BMA compared to the other agents. This difference was interpreted as being due to greater Gd release from the chelate. This hypothesis is supported by a double label study by Kosokat and Urich who used [153Gd] and [14C] labeled Gd-DTPA in rats and found a 153Gd:14C ratio of 6:1 in liver and 9:1 in bone. Tweedle et al. [28] also noted that formulated Omniscan which is a mixture of gadodiamide with 5% sodium caldiamide (Na[Ca-DTPA-BMA]) showed less whole body retention than gadodiamide injected alone. Animal studies with MS-325, Gd-EOB-DTPA, and Gd-BOPTA all showed very low values of Gd in bone at 7 or 14 days post injection similar to those reported for Gd-DTPA [195-200].

In renally impaired patients the exposure to Gd is increased; the longer plasma half-life results in a large AUC. Since the terminal plasma half-life in rats is 15–20 min compared to about 90 minutes in healthy humans for ECF agents, one way to mimic the increased Gd exposure in renally compromised subjects is to administer high doses of agent daily to rats. Sieber and colleagues recently reported a series of studies taking this approach. They administered formulated Omniscan, Optimark, Magnevist, Multihance, Gadovist, or Dotarem at 2.5 mmol/kg daily (except weekends) for four weeks to rats [198-200]. This daily dose is 25 times the standard 0.1 mmol/kg dose and resulted in a cumulative dose of 50 mmol/kg. They examined Gd levels in the skin, liver and femur at the end of the study. In all three organs the order of Gd deposition was the same with Omniscan > Optimark > Magnevist > Multihance ~ Gadovist ~ Dotarem in terms of how much

Gd was deposited. Although there were differences among the contrast agents, Sieber et al. [198-200] only reported statistical analysis to show the amount of Gd deposited after Omniscan injection was significantly higher compared to the other contrast media. No other comparisons were made. Interestingly the relative concentrations of Gd in the skin, liver, and femur differed. For instance, there was about 8 times more Gd in the skin following Omniscan compared to Magnevist, but about 3 times more in the femur or 2 times more in the liver. Interestingly liver levels were similar for the linear Magnevist complex and the macrocycles Dotarem and Gadovist, although there were clear differences in the skin or the bone (Magnevist higher).

In this same repeat dose model, Sieber et al. [198] also investigated the influence of excess ligand. Formulated Omniscan contains gadodiamide and 5% excess ligand as the calcium complex (caldiamide) while Optimark contains gadoversetamide and 10% excess ligands. They repeatedly gave either the gadolinium complex (gadodiamide or gadoversetamide), gadolinium complex + 5% excess ligand, or gadolinium complex + 10% excess ligand for 20 days to rats. The Gd concentration in the skin was significantly higher after treatment of the gadolinium complex alone compared with 5% excess ligand. By increasing the excess of ligand from 5% to 10%, the Gd concentrations in the skin were further reduced by a factor of three. The addition of 5% excess ligand in both contrast agents reduced Gd levels significantly in the femur and the liver, but additional excess ligand had no further benefit in these organs.

Approved gadolinium-based contrast agents have 3 categories of biodistribution extracellular with renal elimination, extracellular with mixed renal and hepatobiliary elimination, and intravascular with renal elimination. After intravenous injection the distribute in the blood and the extracellular space and transiently through the excretory organs. Preclinical animal studies and

the available clinical literature indicate that all these compounds are excreted intact Elimination tends to be rapid and for the most part, complete.

In renally insufficient patients the plasma elimination half-life increases substantially from hours to days depending on renal function. In patients with impaired renal function who then developed NSF, administration of the ECF agents gadodiamide, gadoversetamide, and gadopentetate dimeglumine have been shown to result in Gd deposition in the skin and internal organs. It is unknown whether Gd deposition results in non-NSF subjects as well and if so, whether such deposition correlates with impaired renal function. In one study of hip replacement recipients, at 4 days post Gd administration, patients that received gadodiamide had 4-fold higher Gd levels in bone than those who received gadoteridol which suggests that there may be Gd deposition in non-NSF subjects. In the cases of Gd deposition in NSF patients, it is likely that the Gd is no longer associated with its chelator, but this has still not been definitively shown. The speciation of Gd in human tissue remains an open question – is the Gd still bound to the chelate and if not, what is it bonded to? Is the form of Gd the same in skin deposits compared to internal organs? From the limited Gd distribution data available in NSF subjects, there appears to be differences in distribution compared to the preclinical rodent studies. For instance, high myocardial uptake of Gd in post-mortem analysis is not consistent with the rodent studies. Besides the speciation of Gd, the trafficking of Gd in NSF subjects is another open question, i.e. if dechelation occurs, then where does it occur and how is the Gd transported to other organs?

Finally, the route of administration is critical to understanding the biodistribution and potential Gd deposition of these GBCA. Despite this low incidence of NSF, GBCA have proven to be very safe especially when administered intravenously at approved dosages. The package insert should always be consulted for up to date safety information. Alternate routes of

administration (e.g. subcutaneous, intrathecal, etc), formulation (e.g. in a liposome or other nanoparticle), or cell labeling will likely alter the biodistribution and may impact Gd tissue deposition and/or toxicity. Such studies should be undertaken with caution.

4.2 Results

4.2.1 Metal binding affinity of ProCA32.collagen1

With a previously developed metal-buffer system in our lab, we were able to apply this system to measure metal binding affinities of ProCA32.collagen1. This metal-buffer system can control the free metal concentration in the solution, therefore, an accurate measurement of Kd can be achieved successfully for ProCA32.collagen1 and metal ions such as Ca^{2+}, Zn^{2+}, Gd^{3+} and Tb^{3+}.

4.2.1.1 Measurement of ProCA32.collagen1 binding affinity to Tb^{3+}

Since Gd^{3+} is a spectroscopically silent element, we first determined the binding affinity of ProCA32.cllagen1 to Tb^{3+} and then used a competition assay to measure the affinity to Gd^{3+}. To determine the accurate affinity of ProCA32.collagenl to Tb^{3+}, Tb^{3+}-DTPA buffer system previously developed was used. This system has 5 mM DTPA, 30 μM ProCA32.collagen1, 0.06 μM Rhod-5N, 5 mM HEPES, and 100 mM NaCl at pH 7.2 to mimic the physiological conditions. The Kd of DTPA to Tb^{3+} is 9.55×10^{-22} M. Tb-DTPA can generate a buffer ranging from 10^{-24} and 10^{-18} M of free Tb^{3+}. There is Rhod-5N present in the buffer system, which is a low-affinity-metal indicator with fluorescence properties which can increase the fluorescence signal when free [Tb^{3+}] is higher than 10^{-6} M. The Rhod-5N was introduced into the system as an internal standard and it is important to make sure that DTPA is not saturated by Tb^{3+}. Fig. 4.1 shows Tb-ProCA32.collagen1 LERT signal changes after Tb^{3+} titration. In a similar experiment performed in parallel, 5 mM DTPA without ProCA32.collagen1 was titrated with Tb^{3+} to monitor its background signal and Rhod-5N at each titration point. As it can be seen in Fig. 4.1 A, Tb^{3+}-

ProCA32.collagen1 LERT signal occurs in the Tb-DTPA buffer system, which demonstrates that ProCA32.collagen1 can bind to Tb^{3+} in concentrations between 10^{-23} and 10^{-19} M. Using Hill equation described in Chapter 2 (equation 2-2), we can calculate the Kd (Fig. 4.1 B). ProCA32.collagen1 has a Kd of 6.14×10^{-22} M to Tb^{3+}.

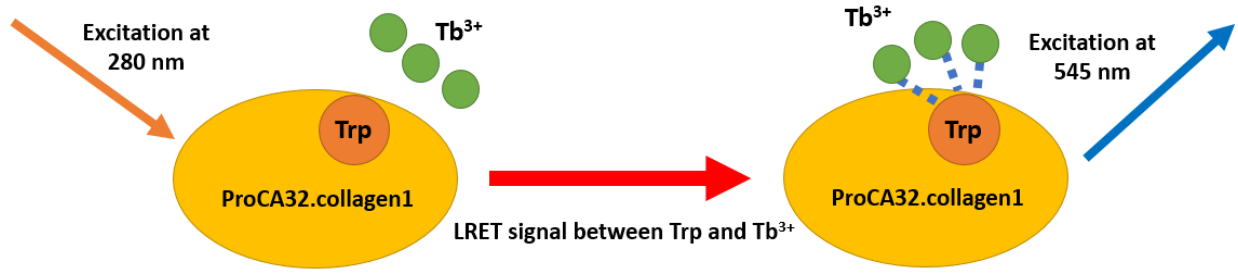

Figure 4.1 *Resonance energy transfer process between Tb^{3+} and Trp in ProCA32.collagen1*

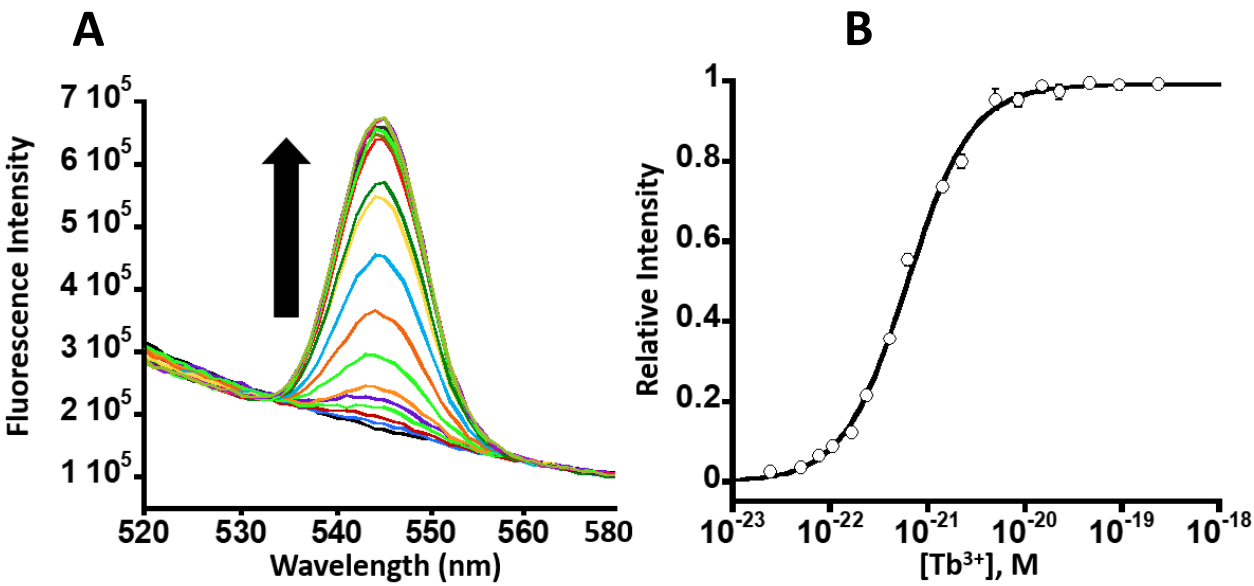

Figure 4.2 *Determination of Tb^{3+} binding affinity of ProCA32.collagen1.*

Determination of Tb^{3+} binding affinity of ProCA32.collagen1 using Tb-DTPA chelator buffer system in which Free [Tb^{3+}] was kept in a range between 10^{-23} and 10^{-17} M using a tightly

controlled concentration ratio between Tb^{3+}-DTPA and free DTPA. The interaction between Tb^{3+} and ProCA32.colagen1 was quantified by fluorescence intensity increase due to luminescence resonance energy transfer between Trp in ProCA32.colagen1 and Tb^{3+}.

It is worth mentioning that, PEGylated and non-PEGylated protein had similar binding affinities which shows that PEGylation did not affect the binding affinity, Moreover, ProCA32.collagen1 had similar Tb^{3+} binding affinity to non-targeted contrast agent, ProCA32-P40 which is an indication that addition of targeting moiety of collagen type I to the contrast agent did not change the affinity to Tb^{3+} (Table 4.1). As it is shown in Fig. 4.2 A, Terbium fluorescence spectrum changes after adding Tb^{3+} into 5 mM DTPA with 30 μM ProCA32.collagen1 in 50 mM HEPES with 100 mM NaCl at pH 7.2. Rhodamin 5N fluorescence changes also after adding Tb^{3+} into 5 mM DTPA with 0.06 Rhodamin 5N in 50 mM HEPES with 100 mM NaCl. In addition, fluorescence intensity does not change during Tb^{3+} titration in Rhodamin 5N and DTPA.

4.2.1.2 Measurement of ProCA32.collagen1 binding affinity to Gd^{3+}

After measuring Tb^{3+} binding affinity, Gd^{3+} binding affinity to ProCA32.collagen1 was measured using competition assay. In this experiment, 10 μM of Tb^{3+} and 5 μM ProCA32.collagen1 were incubated with different concentrations of Gd^{3+} at room temperature overnight in a similar buffer as the Tb^{3+} binding experiment. The next day, Tb-FRET fluorescence signal was measured at excitation 280 nm and emission at 545 nm. As shown in Fig. 4.3 A, Gd^{3+} can compete Tb^{3+} out of ProCA32.collagen1 with a decrease of FRET upon the gradual addition of Gd^{3+} with an apparent Kd (Kapp) of 6.4×10^{-6} M. Using the apparent Kd and FRET signal decrease, we then calculated Kd between Gd^{3+} and ProCA32.collagen1 using equation (2-3 and 2-4). As shown from Table 4.1, the Gd^{3+} binding affinity of ProCA32.collagen1 is 1.96×10^{-22} M which was similar to ProCA32-P40. This result shows that ProCA32.collagen1 has very similar

Gd^{3+} stability and affinity compared to most clinical MRI contrast agents, such as Gd-DTPA, Multihance, Eovist and Dotarem. and much better Gd-stability than Ominiscan and Optimark (Tale 4.2).

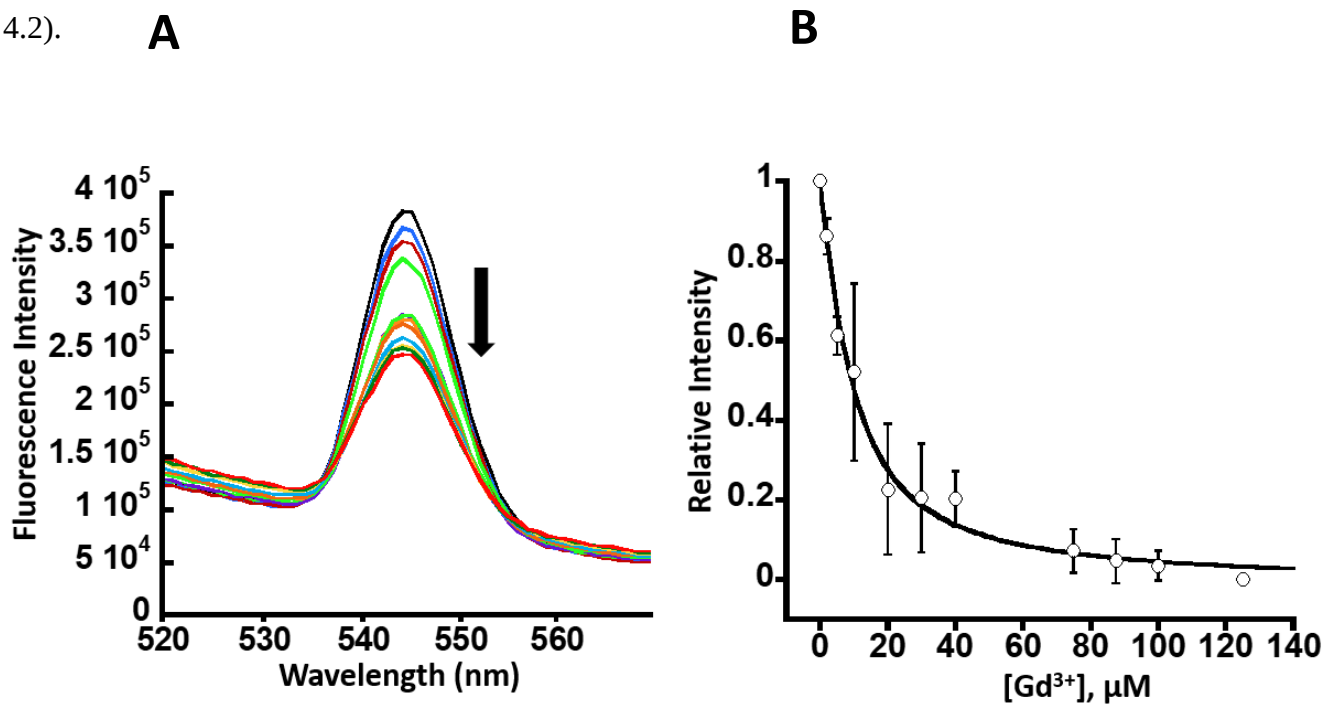

Figure 4.3 *Determination of Gd^{3+} binding affinity of ProCA32.collagen1.*

Gd^{3+} binding affinity was calculated using competition assay. Different concentrations of Gd^{3+} were incubated with Tb^{3+}- loaded ProCA32.colagen1. The fluorescence intensity decreases due to luminescence resonance energy transfer between Trp in ProCA32.colagen1 and bounded Tb^{3+} was quantified when Gd^{3+} competed Tb^{3+} out of the metal binding pocket.

4.2.1.3 Measurement of ProCA32.collagen1 binding affinity to Ca^{2+}

Development of metal-chelator buffer system can control the free metal concentration in solution which can then help us successfully measure the accurate Kd between ProCA32.collagen1 and metal ions such as Ca^{2+} and Zn^{2+}. As a contrast agent, it is extremely important that is has selectivity to Gd^{3+} and cannot be competed out by physiological ions such as Ca^{2+} and Zn^{2+} in the body.

Since ProCA32.collagen1 is based on α-parvalbumin, which is a calcium-binding protein, it has been reported that is has strong Kd around 10^{-9} M to Ca^{2+} [201] which is even stronger than EGTA, therefore we predicted that ProCA32.collagen1 should have similar Ca^{2+} binding affinity. This strong Kd cannot be accurately measured by regular fluorescent titration methods because of limitation in free metal background in solution as well as the sensitivity of these methods. Theoretically, in order to have an accurate method for Kd measurement, one needs to use protein and metal concentration close to the Kd. Development of metal-chelator buffer system can overcome these limitations and keep the free Ca^{2+} concentration between 10^{-13} M to 10^{-8} M, and then Trp fluorescence change in ProCA32.collagen1 which is close to the binding site can be used to monitor the Ca^{2+} binding affinity at very low concentrations of free Ca^{2+}. Fig. 4.4 demonstrates the experimental procedure of Ca^{2+}-EGTA buffer system. This buffer system has 5 mM EGTA, 100 mM KCl, 50 mM HEPES at pH 7.2. ProCA32.collagen1 was added into this system to a final concentration of 5 μM before the experiments. As it is observed, the system has 1000-times higher concentrations of EGTA compared to ProCA32.collagen1. This is to make sure that the majority of ProCA32.collagen1 can stay in the apo form or Ca^{2+} free form. Different concentration of Ca^{2+} was titrated into the system. The free Ca^{2+} concentration can be calculated based on Equation (2-5). Ca^{2+} binding to ProCA32.collagen1 can cause the fluorescent intensity changes and conformational change in the protein since Trp signal is being monitored. Based on this fluorescence signal change in each titration point, the fraction of the Ca^{2+} bound to ProCA32.collagen1 can be derived (Fig. 4.4 B). Then the data can be fit using the titration points (Fig. 4.4 A) and Hill Equation (Equation (2-6)).

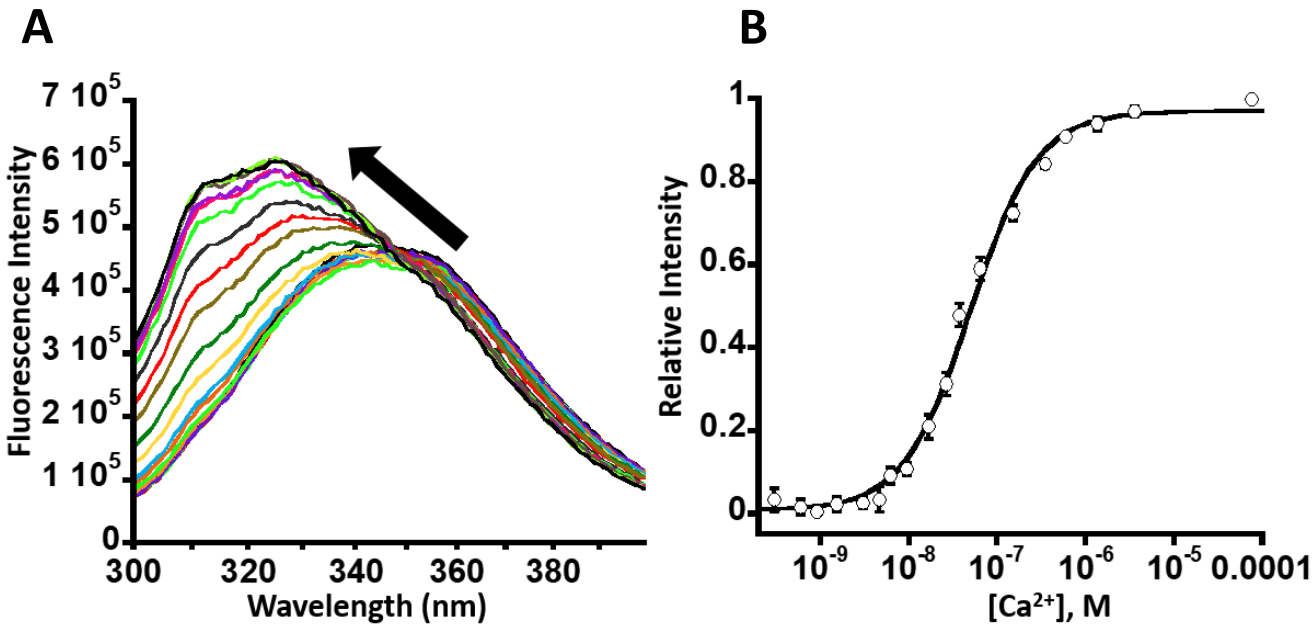

Figure 4.4 *Determination of Ca^{2+} binding affinity of ProCA32.collagen1. Determined Ca^{2+} affinity to ProCA32.collagen1 using the Ca^{2+}-EGTA buffer system. Free [Ca^{2+}] was kept in a range between 10^{-10} and 10^{-4} M by the tightly controlled concentration of Ca^{2+} and EGTA. The interaction between Ca^{2+} and ProCA32.colagen1 was monitored by the Trp fluorescence intensity increase by increasing Ca^{2+} concentration.*

It is important to point out that upon addition of Ca^{2+} to ProCA32.collagen1, not only the fluorescence signal increases but also Trp peak shifts to lower wavelengths which is an indication of conformational change in ProCA32.collagen1 upon Ca^{2+} binding. Fig. 4.5 illustrates how free Ca^{2+} concentration can be calculated based on total concentration of Ca^{2+} in the Ca^{2+}-EGTA buffer system. Generally, the total Ca^{2+} of the buffer system comes from three sources (1) basal Ca^{2+} in the buffer, even after dialysis with Chelex-100 bag to remove excess Ca^{2+}; (2) Ca^{2+} which has bound to ProCA32.collagen1 and introduced to the system upon addition of ProCA32.collagen1 before titration; (3) Known Ca^{2+} concentration titrated in to the system. The total basal Ca^{2+} concentration, $[Ca^{2+}]_{basal}$ can be measured by Fura-2 dye, which is around 10^{-7}-10^{-6} M after chelex-

100 treatment. According to Equation (2-5), $[Ca^{2+}]_{basal}$ is responsible for 10^{-12} - 10^{-11} M of free Ca^{2+} when total EGTA concentration is 5 mM. Concentration of ProCA32.collagen1 added in this experiment is 5 μM. If Kd of ProCA32.collagen1 to Ca^{2+} is 10^{-9} M, then we can generate 10 μM of total Ca^{2+} into the system, which further contribute 7.37×10^{-10} M of free Ca^{2+} in the system. The total Ca^{2+} concentration in each titration point is tightly controlled, and the exact total Ca^{2+} concentration titrated into the system is known. For instance, if we titrated 100 μM of total Ca^{2+} in the system, it generates 7.51×10^{-9} M free Ca^{2+} in the system according to Equation (2-5).

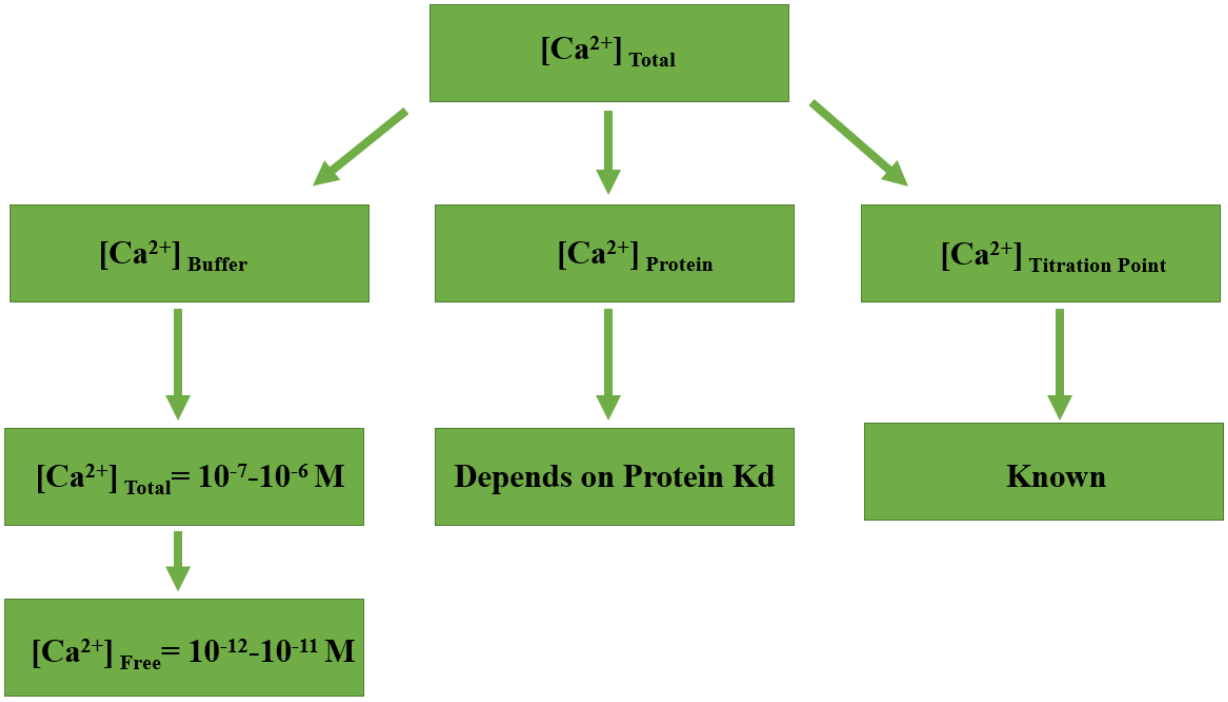

Figure 4.5 *Schematic demonstration of free Ca^{2+} calculation in Ca-EGTA buffer system*

After all the calculations, the Kd of ProCA32.collagen1 was 4.93×10^{-8} M which is similar to ProCA32-P40. In addition, each individual association constant (Ka) of ProCA32.collagen1 to Ca^{2+} can also be calculated using Adair equation. It has been hypothesized that binding affinity is not a fixed term, but dependent on ligand saturation. Having demonstrated that hemoglobin contained four Hemes (and therefore binding sites for oxygen), Adair equation works from the

assumption that fully saturated hemoglobin is formed in stages, with intermediate forms with one, two, or three bound oxygen molecules. The resulting fractional occupancy can be expressed as:

$$\bar{Y} = \frac{1}{4} \cdot \frac{K_I[X] + 2K_{II}[X]^2 + 3K_{III}[X]^3 + 4K_{IV}[X]^4}{1 + K_I[X] + K_{II}[X]^2 + K_{III}[X]^3 + K_{IV}[X]^4} \quad (4\text{-}1)$$

Or, for any protein with *n* ligand binding sites:

$$\bar{Y} = \frac{1}{n} \frac{K_I[X] + 2K_{II}[X]^2 + \ldots + nK_n[X]^n}{1 + K_I[X] + K_{II}[X]^2 + \ldots + K_n[X]^n} \quad (4\text{-}2)$$

After using equation 4-2, the data were fit and each individual Ka was calculated. Average K_{a1}=3.45×10 ^{7}M, Average K_{a2}=1.13×10 ^{7} M.

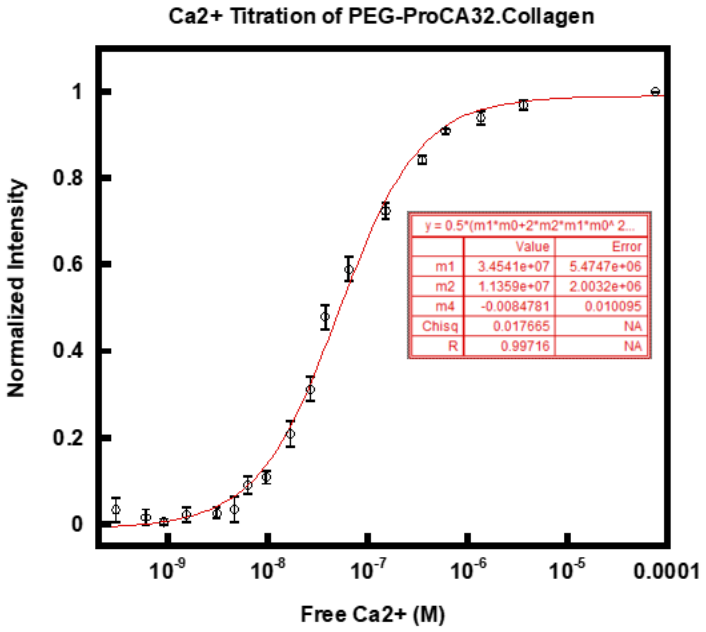

Figure 4.6 *Determination of Ca^{2+} binding affinity of ProCA32.collagen1 using Adair equation.*

4.2.1.4 Measurement of ProCA32.collagen1 binding affinity to Zn^{2+}

Another physiological metal ion which can compete with Gd^{3+} in contrast agents is Zn^{2+} causing transmetallation in contrast agents. The binding affinity of ProCA32.collagen1 to Zn^{2+} was determined using Fluozin-1 competition methods [79]. In this experiment, Zn^{2+} and Fluozin-1 were incubated together in 50 mM HEPES, 100 mM NaCl, pH 7.2. After that ProCA32.collagen1 was titrated into the solution. The fluorescence signal of Fluozin-1 was monitored in each titration point. Due to competition of ProCA32.collagen1, Zn^{2+} will be removed from Fluozin-1 during titration which causes the fluorescence signal of Fluozin-1 to decrease until it reaches a plateau (Fig. 4.7 A). After fitting the titration points with 1:1 binding equation (2-8), Zn^{2+} binding affinity of ProCA32.collagen1 was calculated to be 1.33×10^{-6} M (Table 4.1).

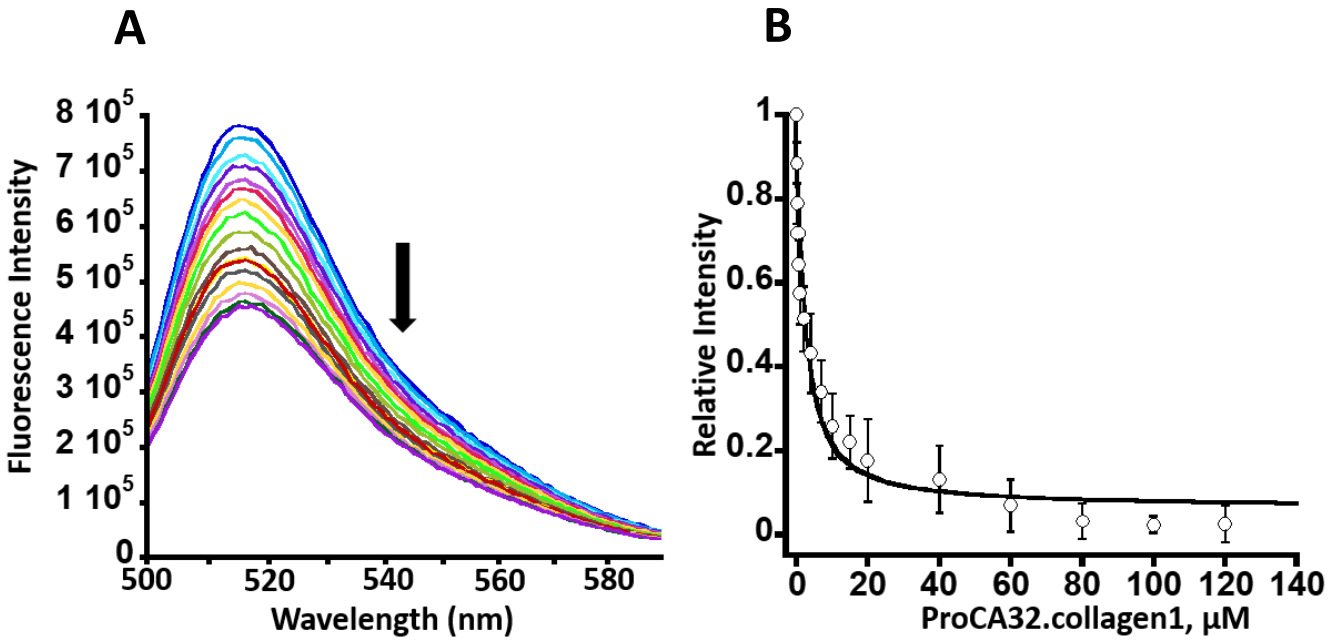

Figure 4.7 *Determination of Zn^{2+} binding affinity of ProCA32.collagen1.*

Zn^{2+} binding affinity was determined using Fluozin-1 competition assay in which ProCA32.collagen1 is competing with Fluozin-1 for Zn^{2+}.

Table 4.1 *Summary of metal binding affinities of ProCA32.collagen1 and clinical contrast agents*

Contrast Agent	Log (K_{Tb})	Injection Dosage [b] (mmol/kg)	Log (K_{Gd})	Log (K_{Ca})	Log (K_{Zn})	Log (K_{Gd}/K_{Ca})	Log (K_{Gd}/K_{Zn})
Magnevist (DTPA)	22	0.1	22.46	10.75	18.6	12.24	4.13
Eovist (EOB-DTPA)[a]	N/A	0.025	23.6	11.82	18.78	12.22	5.18
Dotarem (DOTA)	N/A	0.1	24.7	17.23	21.05	7.46	3.65
MultiHance (BOPTA)[a]	N/A	0.05	21.91	N/A	17.04	N/A	4.87
ProHance (HP-DO3A)	N/A	0.1-0.3	23.8	14.83	19.37	10.07	4.37
ProCA32-P40[a]	21.08	0.0013	22.44	9.55	8.77	13.1	14.3
ProCA32.collagen1[a]	22.53	0.0013	22.54	8.71	6.36	14.7	16.2
PEG-ProCA32.collagen1[a]	**22.80**	**0.0013**	**22.30**	**8.70**	**6.12**	**14.4**	**16.2**

[a] Liver specific agents
[b] Recommended dose in liver MR imaging examination in adults

4.2.2 Relaxivity measurements of ProCA32.collagen1

Relaxivity of ProCA32.collagen1 as the most important property of a contrast agent was measured in the buffer containing 50 mM HEPES, 100 mM NaCl, pH 7.2 at 37 ˚C. Since relaxivity depends on the field strength, and MRI instruments are evolving fast to higher magnetic fields for higher resolution, ProCA32.collagen1 relaxiviy was measured at both 1.4 T which is the most widely used clinical magnetic field and 7.0 T which is higher field strengths. We incubated different concentrations of Gd^{3+} with different concentrations of ProCA32.collagen1 in order to plot a curve for relaxivity. Four points were used plus zero point without any Gd^{3+}. These four points are: 80 µM ProCA32.collagen1:160 µM Gd^{3+}, 40 µM ProCA32.collagen1:80 µM Gd^{3+}, 20 µM ProCA32.collagen1:40 µM Gd^{3+}, and 10 µM ProCA32.collagen1:20 µM Gd^{3+}. We then plot the curve with Gd^{3+} concentration in the x axis in mM and relaxation rate in the y axis in s^{-1}. Bruker bench top 1.4 T relaxometer was used to measure T1 and T2 in ms.

We calculated the per Gd^{3+} relaxivity of ProCA32.collagen1. The final relaxivity was calculated with 1:2 ratio between Gd^{3+} and ProCA32.collagen1 at 37 ˚C 1.4 T. Fig. 4.8 shows the r_1 and r_2 measurements of PEGylated and non-PEGylated ProCA32.collagen1 at 1.4 T and 7.0 T.

Since ProCA32.collagen1 has two Gd^{3+} binding sites, 1:2 ratio was chosen to make sure that all sites have been occupied with Gd^{3+}. Interestingly, the per Gd^{3+} r_1 and r_2 of non-PEGylated ProCA32.collagen1 is 30 ± 0.3 and 42 ± 0.3 $mM^{-1}s^{-1}$, respectively and these values for PEGylated ProCA32.collagen1 were 34 ± 0.12 $mM^{-1}s^{-1}$ and 50 ± 0.16 $mM^{-1}s^{-1}$ for r_1 and r_2, respectively. It is important to point out that relaxivity of ProCA32.collagen1 increased after PEGylation. Moreover, these values are larger than ProCA32-P40 which is an advantage for this targeted contrast agent. Relaxivity values were also calculated for ProCA32.collagen1 at 7.0 T field strength. The results (Fig. 4.8 C) show a significant increase in r_2 (108 ± 1.2 $mM^{-1}s^{-1}$) value and a slight decrease of r_1 (21.3 ± 0.5 $mM^{-1}s^{-1}$). As Table 4.2 demonstrates, these values for ProCA32.collagen1 are significantly higher than clinical contrast agents and even higher than ProCA32-P40.

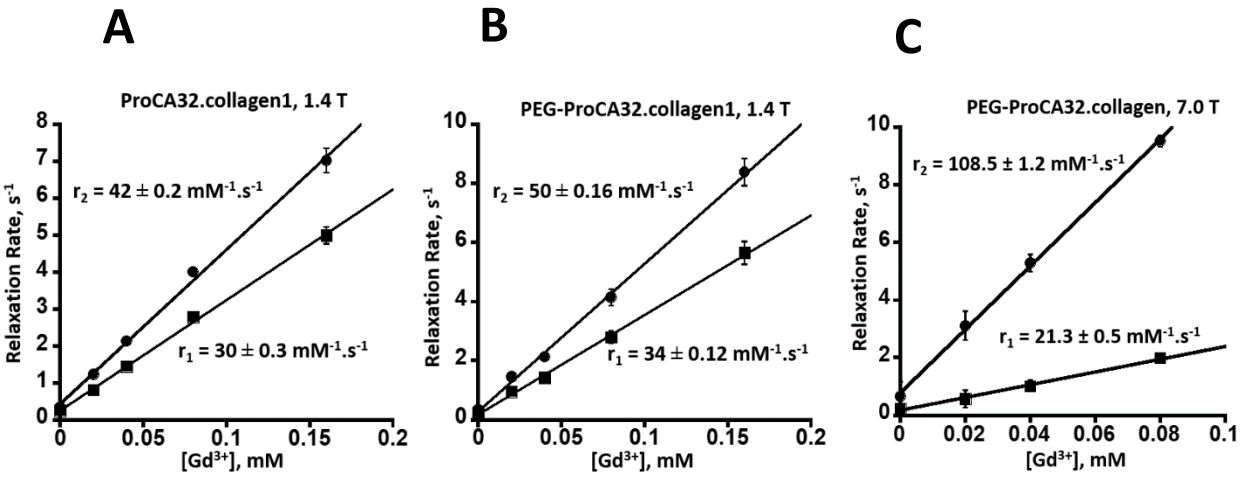

Figure 4.8 *Relaxation rate of ProCA32.collagen1 at different magnetic fields.*

(A) *Relaxation rate of non-PEGylated ProCA32.collagen1 at 1.4 T, 37 °C. Changes in r_1 and r_2 relaxation rates were plotted over various concentrations of [Gd^{3+}].* ***(B)*** *Relaxation rate of PEGylated ProCA32collagen at 1.4 T, 37 °C.* ***(C)*** *Relaxivity values (r_1 and r_2) of PEGylated ProCA32.collagen1 at 7.0 T, 37 °C.*

Table 4.2 *Summary of r_1 and r_2 relaxivity of ProCA32.collagen1 and clinical contrast agents*

Contrast Agent	r_1 at 1.4 T	r_1 at 7.0 T	r_2 at 1.4 T	r_2 at 7.0 T
Magnevist (Gd-DTPA)	3.3	5.1	3.9	9.4 ± 1.3
Eovist (EOB-DTPA)	5.38 ± 0.02	5.37	6.54 ± 0.06	7.01
Dotarem (DOTA)	3.9 ± 0.2	N/A	3.2 ± 0.7	N/A
MultiHance (BOPTA)	6.20	N/A	8.7	N/A
ProHance (HP-DO3A)	4.39	N/A	5.0	N/A
ProCA32-P40	33.14 ± 0.32	18.9	44.61 ± 0.12	48.6 ± 0.1
ProCA32.collagen1	30 ± 0.06	N/A	42 ± 0.1	N/A
PEG-ProCA32.collagen1	**34 ± 0.12**	**21.3 ± 0.5**	**50 ± 0.16**	**108.5 ± 1.2**

4.2.3 Serum stability of ProCA32.collagen1

Since ProCA32.collagen1 will be applied for in vivo studies with good metal stability and relaxivity, it needs to have good serum stability as well. Therefore, it is extremely important that PEGylated ProCA32.collagen1 will not be cleaved by the enzyme in the serum and maintain intact structure before secreting out of the body. In order to assess the stability of ProCA32.collagen1 with PEGylation, the contrast agent was incubated in the 50% serum and then detected by SDS-PAGE. As Fig. 4.9 shows, ProCA32.collagen1 is very stable in the serum for at least 13 days. After a couple of days, the native proteins in the serum start to degrade, however, ProCA32.collagen1 was still present in the blood serum. All of these data further confirm that ProCA32.collagen1 is as stable as ProCA32-P40 and can be a suitable contrast agent for in vivo studies.

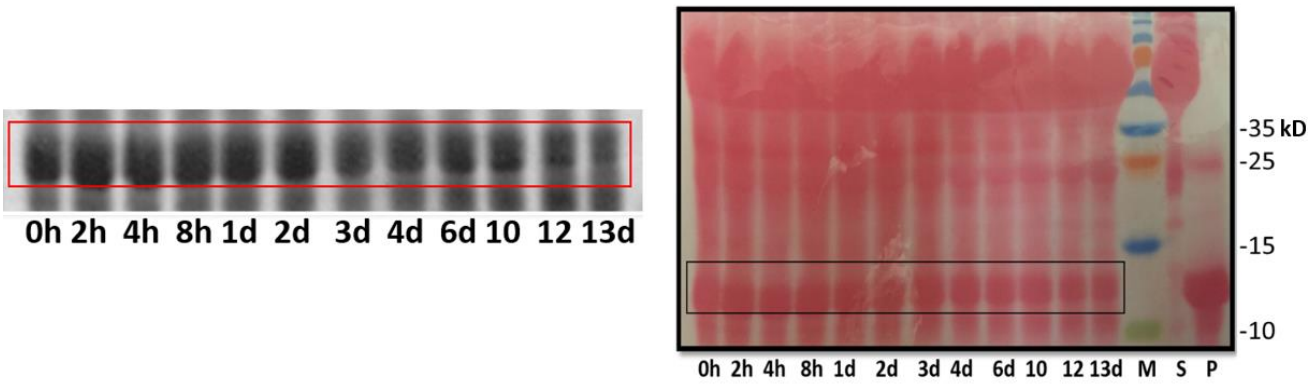

Figure 4.9 *ProCA32.collagen1 stability in human serum.*

ProCA32.collagen1 is stable after incubation in serum at 37 °C for up to 12 days as raveled by Coomassie Brilliant Blue Ponceau S solution staining.

4.2.4 Transmetallation studies of ProCA32.collagen1

Metal stability and selectivity is one of the important criteria for designing contrast agents and they are extremely needed for the development of contrast agents. Other physiological ions such as Zn^{2+} can compete with Gd^{3+} and force them out of the binding pocket of contrast agents. After measurement of the binding affinities of ProCA32.collagen1 to different metal ions such as Zn^{2+}, Ca^{2+} and Gd^{3+}, the results demonstrated higher selectivity of ProCA32.collagen1 compared to clinical contrast agents (Table 4.1). These results led us to assess the transmetallation property of ProCA32.collagen1 since it was going to be applied in vivo.

Zn^{2+} and $PO4^{3-}$ are the major competitors of Gd^{3+} in physiological conditions. To study the transmetallation of ProCA32.collagen1, relaxation rate changes of the contrast agent was measured over time in the presence of Zn^{2+} and $PO4^{3-}$. As reported in the literature, different clinical contrast agents had different transmetallation rates in this solution. (Fig. 4.10). The linear contrast agents with no charge such as Omniscan experienced the highest transmetallation effect, however, macrocyclic non-charged MRI contrast agents such as ProHance, had no transmetallation in the

presence of Zn^{2+} and PO_4^{3-} for at least 4 days based on the study [202]. For other clinical contrast agents, although the number of negative charge and ligand type are very similar, different ionic linear MRI contrast agents has different transmetallation rate.

We used the similar procedure to assess the transmetallation properties of ProCA32.collagen1 in the presence of Zn^{2+} and PO_4^{3-}. Due to the higher relaxivity, 25 times lower Gd^{3+} concentration, and 25-50 times lower chelator concentration was used in this study. To better compare the transmetallation properties of ProCA32.collagen1 with clinical MRI contrast agent, this experiment was applied using 25 times lower concentrations of Zn^{2+} and PO_4^{3-}. As shown in Fig. 4.10, the relaxation rate of ProCA32.collagen1 is not changed in the presence of Zn^{2+} and PO_4^{3-} for about 4 days, demonstrating that ProCA32.collagen1 is very selective to Gd^{3+} at these conditions.

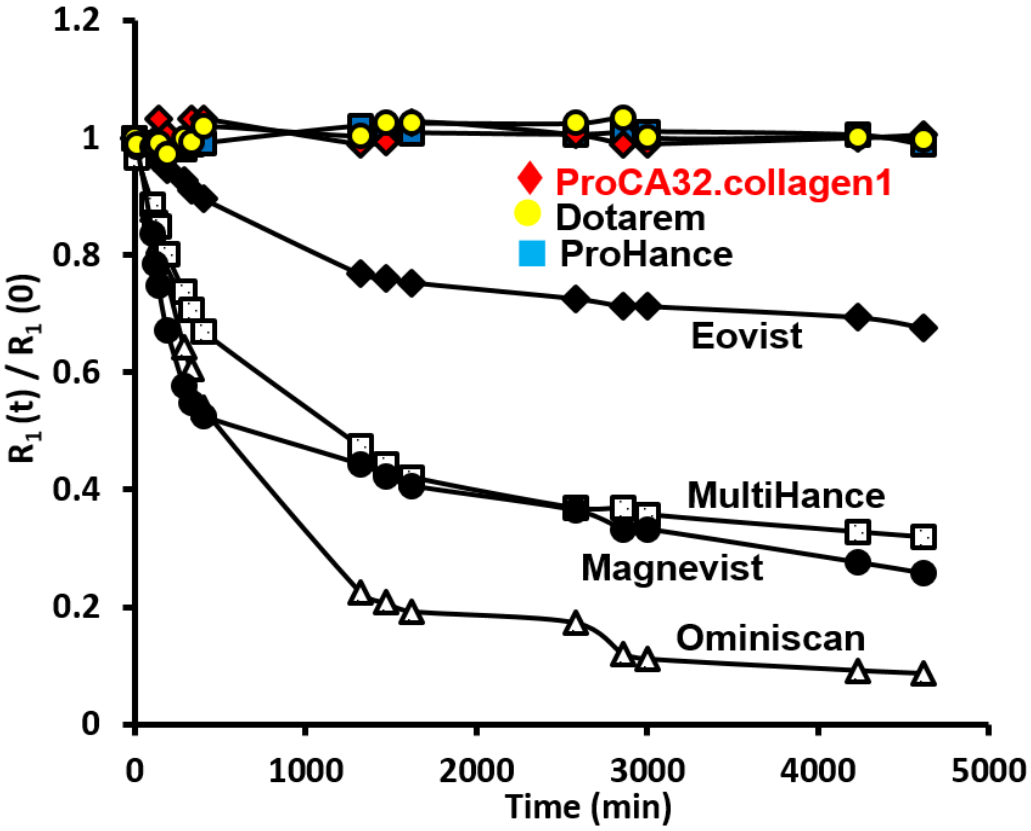

Figure 4.10 *Stability of ProCA32.collagen1 and clinical contrast agents.*

The relaxation rates change of clinical contrast agents (♦ Eovist; ● Magnevist; □ MultiHance; ⊿ Ominiscan; ■ ProHance; ○ Dotarem; and ProCA32.collagen1 (◊, loaded with Gd^{3+} to at approximately 1:1 ratio) in phosphate buffer in the presence of $ZnCl_2$ at different time points up to 4 days.

Transmetallation of ProCA32.collagen1 and clinical MRI contrast agents were evaluated by measuring the relaxivity changes in the presence of Zn^{2+} and phosphate over time. The relaxivity of ProCA32.collagen1 was monitored with 55 or 110 μM ProCA32.collagen1, 100 μM Gd^{3+}, 100 μM Zn^{2+}, and 1.2 mM PO_4^{3-}. In this experiment, when Zn^{2+} is competing Gd^{3+} out of the structure of contrast agents, Gd^{3+} will form a precipitate with PO_4^{3-} in the buffer which is an indication of instability of the contrast agent.

4.2.5 Water number determination of ProCA32.collagen1

Water number was one the factors discussed in Chapter 1 affecting the relaxivity of contrast agents. The number of water molecular interacting with Gd^{3+} at the same time is important. Furthermore, determination of water number can illustrate the special arrangement of the Gd^{3+} binding ligands. Tb^{3+} luminescence life time experiment was performed in order to test that the relaxivity and metal binding affinity of ProCA32.collagen1 can be tuned by changing water number [173, 176]. Generally, the fluorescence decay of the Tb^{3+} is caused by the radiative decay (Γ) and non-radiative decay (K). Non-radiative decay has many factors, such as molecular collation, quenching, energy transfer. H_2O molecule is one of the major factors which creates the non-radiative decay of the Tb^{3+} fluorescence, however, D_2O cannot generate non-radiative decay of Tb^{3+} fluorescence. As a result, the difference of the decay rates of Tb^{3+} in the presence of H_2O and D_2O (ΔK_{obs}) represents the number of water molecules interacting with Tb^{3+}-ProCA32.collagen1.

In order to measure the exact number of water number of ProCA32.collagen1, different organic chelators (NTA, EDTA, DTPA) and Tb^{3+} in aqueous solution were used to create a standard curve. The water number for NTA, EDTA, DTPA and Tb^{3+} and aqueous solution have been reported in the literature. X-ray diffraction was used to determine the water numbers of these chelators [173, 176]. To create a standard curve, Tb-DTPA, Tb-EDTA, Tb-NTA and free Tb^{3+} are prepared in H_2O and D_2O solution. Then Tb^{3+} fluorescence was excited at 280 nm and the fluorescence decays were monitored at 545 nm. The fluorescence decay was fitted by single exponential decay Equation. The decay rate (K_{obs}) and life time (τ) of Tb^{3+} in H_2O and D_2O were then calculated. After that the standard curve was plotted on the reported water number of these chelators and difference of K_{obs} in H_2O and D_2O (ΔK_{obs}) (Fig. 4.11). Water number of ProCA32.collagen1 was calculated and q=0.5 which is the same as ProCA32-P40.

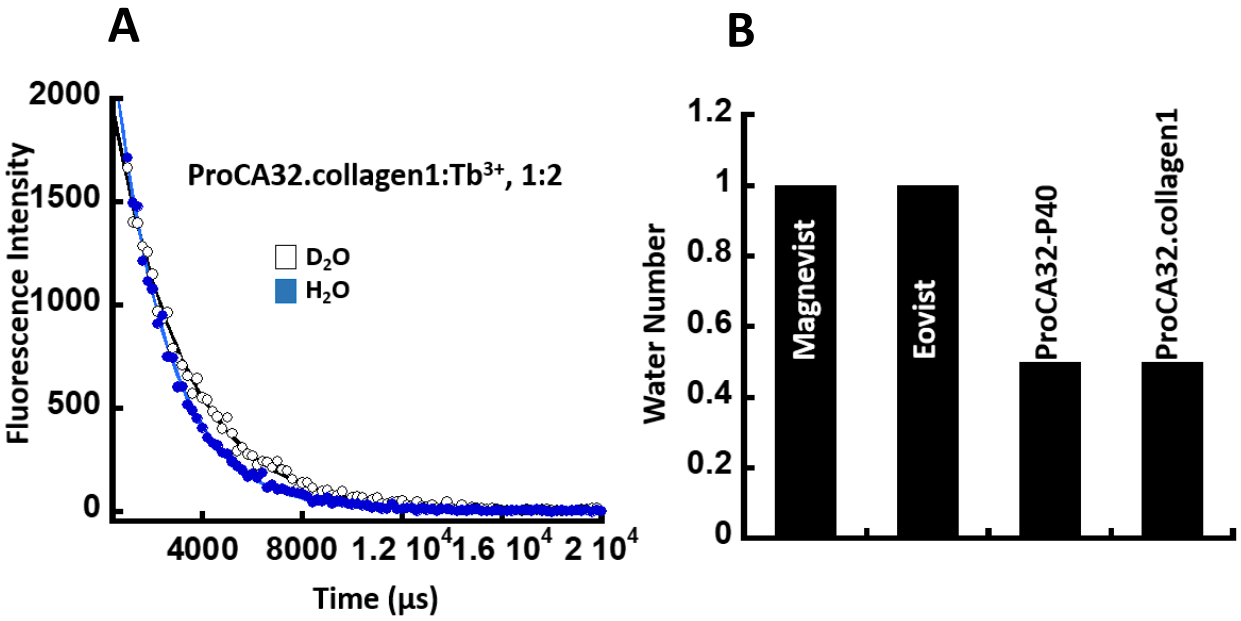

Figure 4.11 *The luminescence decay of Tb^{3+} in H_2O (blue) or D_2O (white) in solution of ProCA32.collagen1.* ***(A)*** *Tb^{3+} and ProCA32.collagen1 were mixed with 1 to 2 ratios.* ***(B)*** *Water number of Magnevist, Eovist, ProCA32-P40, ProCA32.collagen1.*

4.2.6 Collagen type I binding affinity of ProCA32.collagen1

Since ProCA32.collagen1 is a collagen type I targeted MRI contrast agent, its binding affinity to this biomarker needs to be measured. Collagen type I is the most abundant component of extracellular matrix (ECM), therefore it is more accessible to contrast agents than other biomarkers that are expressed on the membrane. Indirect ELISA (enzyme-linked immunosorbent assay) was used to determine the binding affinity of ProCA32.collagen1 to collagen type I. ELISA (enzyme-linked immunosorbent assay) is a plate-based assay technique designed for detecting and quantifying substances such as peptides, proteins, antibodies and hormones. Other names, such as enzyme immunoassay (EIA), are also used to describe the same technology. In an ELISA, an antigen must be immobilized on a solid surface and then complexed with an antibody that is linked to an enzyme. Detection is accomplished by assessing the conjugated enzyme activity via incubation with a substrate to produce a measurable product. The most crucial element of the detection strategy is a highly specific antibody-antigen interaction. Figure 4.12 shows the basic principles of ELISA.

In our experiment, collagen type I solution from rat tail with stock concentration of 4 mg/mL was coated in ELISA plate mixed with coating buffer (0.2 M sodium carbonate/bicarbonate, pH 9.4) overnight at 4°C. Approximately 30 µL of collagen type I was mixed with 80 µL of coating buffer. Coating buffer is used to activate the plate. It is important to pay attention to the capacity of the plate and how much protein is coated. In the next step, the plate is washed with 100 µL of 1×TBST (10×TBS +Tween 20) three times, each time for about 5-10 minutes under constant shaking at room temperature. Next, the blocking buffer (%5 of Bovine

Serum Albumin in 1×TBST) is prepared and 100 µL is added to the plate with constant shaking at room temperature for about 1.5-2 hours.

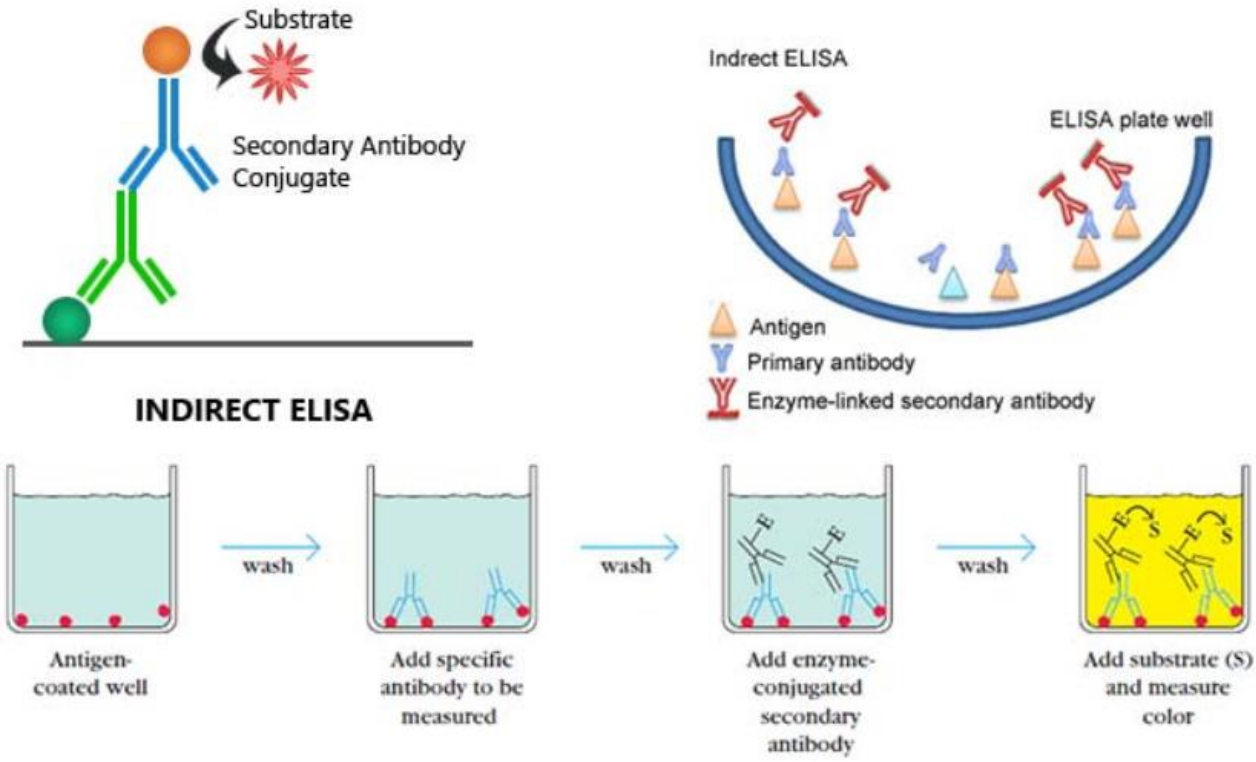

Figure 4.12 *Basic principles of ELISA.*

Different concentrations of ProCA32.collagen1 starting from 0 nM up to 164000 nM were added to the plate in the blocking buffer and incubated for either 2 hours at room temperature or 4°C overnight. Then the plate is washed again with 100 µL of 1×TBST (10×TBS +Tween 20) three times, each time for about 5-10 minutes under constant shaking at room temperature. Primary antibody (rabbit anti mouse) was added with 1:1000 dilution to the blocking buffer and then 100 µL was added to the plate with constant shaking at room temperature for 1.5-2 hours.

The plate was washed again with the same procedure, and the secondary antibody (goat anti rabbit) was added with 1:2000 dilution in the blocking buffer with shaking at room temperature for about 45 minutes. Then the plate was washed again and 1-Step Ultra TMB-ELISA

solution (100 µL) was added. It is important that each well in the plate has the same exposure time to the ELISA substrate solution for better results. In the last step, a stop solution (2M sulfuric acid) is added to stop the reaction. Then the absorbance in each well is read by plate reader.

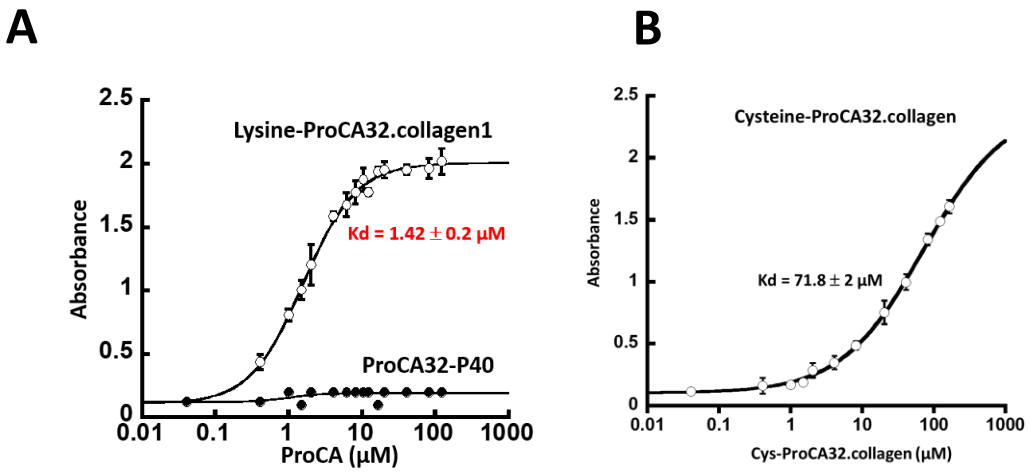

Figure 4.13 *The dissociation constant of Lysine and Cysteine PEGylated ProCA32.collagen1 to collagen type I using indirect ELISA. ProCA32-P40 without any targeting moiety did not show any specific binding.*

After measuring the absorbance of multiple concentration points, the data were fit with one to one binding equation and a dissociation constant of 1.4 ± 0.2 µM was calculated (Fig 4.13 A). It is important to point out that residue PEGylation affect the binding affinity of the contrast agent significantly as Cysteine residues reported to play a crucial role in the binding [120]. Cysteine PEGylated ProCA32.collagen1 showed much lower binding affinity to collagen type I (Kd=71.8 ± 2 µM) due to prevention of forming a cyclic peptide in the targeting moiety to bind to collagen I (Fig 4.13 B).

4.2.7 Pharmacokinetic studies of ProCA32.collagen1

In addition to metal affinity and relaxivity properties of ProCA32.collagen1, detailed pharmacokinetic characteristic of ProCA32.collagen1 was also studied. There is an excellent correlation between relaxivity, Gd^{3+} binding affinity and selectivity, and in vivo pharmacokinetics required for detection of different stages of liver fibrosis and metastasis as well disease heterogeneity. In order to obtain pharmacokinetic parameters, ProCA32.collagen1 (0.016 mmol/kg) was intravenously injected into mice (n=3-6) and blood was collected from saphenous vein at different time points before and after injection up to 7 days. After collection, serum of each sample was obtained and the Gd^{3+} concentration was measured using ICP-OES at a wavelength of 342 nm (Gd). Then the data were fit using two-compartment distribution model and pharmacokinetic parameters such as terminal half-lives (blood/plasma), volumes of distribution, and total clearance were calculated.

The blood concentration-time profiles after intravenous injection of ProCA32.collagen1 in mice were analyzed using two-compartmental analysis using WinNonlin ™ 5.0.1 software (Pharsight Corp., Palo Alto, CA). Mean blood concentration values from 3-6 mice at each sampling time point were used for the mice pharmacokinetic analysis. The area under the blood concentration-time curve (AUC) was calculated using the log-linear trapezoidal rule. The elimination half-life ($t_{1/2}$) was calculated by the equation $t_{1/2} = 0.693/K$, where K was estimated from the terminal slope of the blood Gd^{3+} concentration versus time curve. The systemic clearance (CL) was determined from dose/AUC, with AUC (area under the curve to infinity) by linear interpolation and extrapolation to infinity y from C_{last} x $t_{1/2\beta}/0.693$ (where C_{last} was concentration at each last sampling point). The volume of distribution at steady-state (Vss) was determined by

the equation Vss = CL × (AUMC/AUC), where AUMC is the area under the first moment curve. The mean residence time (MRT) was calculated from AUMC/AUC.

ProCA32.collagen1 has the terminal elimination half-life of 9.93 h. In addition, volume of distribution (V_c) and volume of distribution at steady state (V_{dss}) were 1.53 and 1.77 L/kg, respectively. Total body clearance (CL) for ProCA32.collagen1 was 0.36 mL/min/kg. Table 4.3 summarizes the pharmacokinetic parameters of ProCA32.collagen1 compared to ProCA32-P40 and Eovist.

The pharmacokinetic characteristics of ProCA32.collagen1 in the mouse showed a relatively high volume of distribution and vascular confinement of the contrast agent, which is superior than clinical contrast agents like Magnevist, where the agent is largely distributed to the extravascular extracellular space (outside the central nervous system) after intravenous administration. Blood ProCA32.collagen1 concentrations dropped to a significantly lower level by 2 days (Fig. 4.14) after its administration and mean residence time (MRT) for ProCA32.collagen1 was 14.51 h. ProCA32.collagen1 had an increased elimination half-life compared to Eovist and ProCA32-P40.

The systemic clearance of ProCA32.collagen1 was about 3 times higher than ProCA32-P40 which is a non-targeted contrast agent. The difference could be attributed to a potentially higher renal glomerular filtration rate or higher hepatic clearance of the agent. Biodistribution in mouse showed accumulation of ProCA32.collagen1 in the liver and spleen, consistent with reticuloendothelial system (RES) clearance of macromolecular contrast agents. The volume of distribution at steady state (V_{ss}) was two times higher than that of ProCA32-P40 which is an indication of contrast agent distribution in tissues.

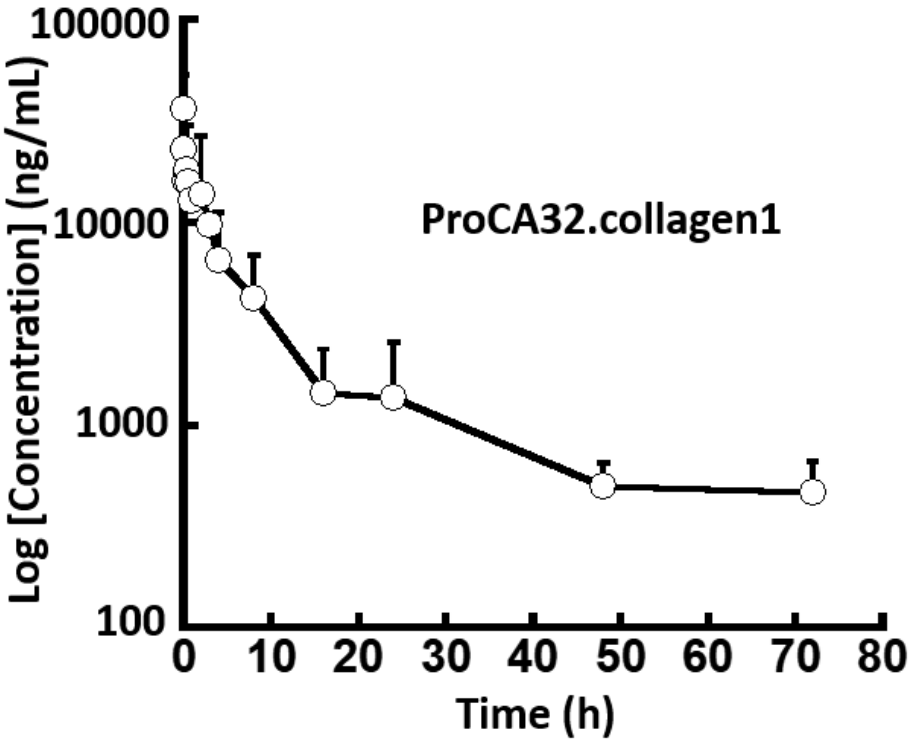

Figure 4.14 *Pharmacokinetics of ProCA32.collagen1.*

Gd^{3+} concentration in serum collected after injection of ProCA32.collagen1 (n = 3-6) at different time points measured by ICP-OES at 342 nm up to 7 days, however the data up to 72 h are shown. After injection, the Gd^{3+} concertation in serum decreased until it was below the detection limit of ICP-OES. The concentration of Gd^{3+} in serum samples were fit with exponential model in order to extrapolate the necessary PK parameters.

As Table 4.3 demonstrates, ProCA32.collagen1 has improved pharmacokinetic properties compared to non-targeted contrast agent, ProCA32-P40. ProCA32.collagen1 has slightly longer elimination half-life compared to ProCA32-P40 which is due to its targeting capability. However, its show much faster clearance rate with increased exposure time which is important for a targeted contrast agent.

Table 4.3 *Summary of PK parameters for ProCA32.collagen1 and ProCA32-P40.*

Contrast Agent	Eovist	ProCA32-P40	ProCA32.collagen1
$t_{1/2\beta}$ (h)	1.5	8.09	**9.93**
V_c (L/kg)	N/A	0.20	**1.53**
V_{ss} (L/kg)	0.21	0.76	**1.77**
CL (mL/min/kg)	0.4	0.11	**0.36**
MRT (h)	N/A	13.90	**14.51**
AUC (ng·h/mL blood)	N/A	30773.00	**140073.00**

4.2.8 Safety studies of ProCA32.collagen1

Due to safety issues related to Gd^{3+} toxicity of MRI contrast agents, ProCA32.collagen1 distribution in different mouse organs was studied. The Gd^{3+} concentration in each organ was measured using ICP-OES in order to assess the possible Gd^{3+} deposition in organs. Furthermore, clinical chemistry tests were performed after injection of high concentration of ProCA32.collagen1 and different enzymes and analytes reflecting the functions of liver and kidney were measured to investigate the toxicity of ProCA32.collagen1.

At the end, tissues of mice injected with ProCA32.collage1 were collected and H&E staining was performed on each tissue and assessed by a pathologist blinded to our studies and the results were then compared with control mice.

4.2.8.1 Distribution of ProCA32.collagen1 in different organs

As Fig. 4.15 demonstrates, each mouse organ was collected and Gd^{3+} concentration was measured 14 days after 0.025 mmol/kg injection of ProCA32.collagen1. For this procedure, approximately, 0.2 g of each tissue was sectioned and digested in 1 mL of ICP-grade concentrated

nitric acid overnight at room temperature until a clear solution was achieved then the solution was diluted with %2 nitric acid to 6-8 mL and then the Gd^{3+} concentration was measured.

As the results show, our contrast agent has very negligible accumulation in bone, skin and brain, however Eovist which is a clinical contrast agent showed high depositions of Gd^{3+} in bone, skin and brain as well as other organs.

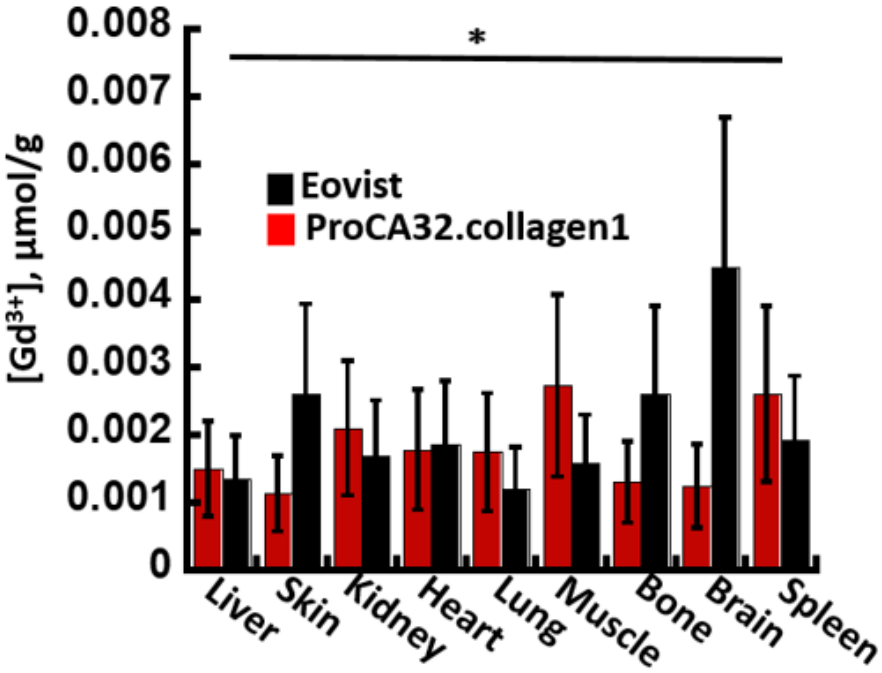

Figure 4.15 *Biodistribution analysis of ProCA32.collagen1.*

Long term organ toxicity demonstrates the biodistribution of ProCA32.collagen1 and Eovist 14 days after injection in mice in different organs using ICP-OES. As it can be seen, different organs such as brain, skin and bone have high accumulations of Gd^{3+} *which is an indication of free* Gd^{3+} *being released.*

4.2.8.2 Clinical chemistry tests

Clinical chemistry tests performed by an independent company. For this purpose, serum samples after injection of 0.025 mmol/kg ProCA32.collagen1 was collected and shipped. The mice clinical chemistry profiles were collected by analyzing mice serum samples 5 days after injection of saline (gray, n = 5), or 0.023 mmol/kg ProCA32.collagen1 (black). Data are expressed as mean ± SD. Different tests performed for clinical chemistry profile studies.

Alanine Transaminase (ALT) test is used by the body to metabolize protein. If the liver is damaged or not functioning properly, ALT is released into the blood. This causes ALT levels to increase. A high result on this test can be a sign of liver damage.

Aspartate Aminotransferase (AST) Test: Aspartate aminotransferase (AST) is an enzyme found in several parts of the body, including the heart, liver, and muscles. Since AST levels aren't specific for liver damage, it's usually measured together with ALT to check for liver problems. When the liver is damaged, AST is released into the bloodstream. A high result on an AST test might indicate a problem with the liver or muscles.

Alkaline Phosphatase (ALP) Test: Alkaline phosphatase (ALP) is an enzyme found in your bones, bile ducts, and liver. An ALP test is typically ordered in combination with several other tests. High levels of ALP may indicate liver damage, blockage of the bile ducts, or a bone disease.

Creatine Kinase (CK) Test: Measurement of serum creatine kinase (CK) activity is essential in the evaluation of suspected neuromuscular disease. In skeletal muscle CK plays a major role in energy generation, buffering cellular ATP and ADP concentrations by catalyzing the reversible exchange of high-energy phosphate bonds between phosphocreatine and ADP, regenerating ATP from ADP produced during muscle contraction. A diagnosis of liver disease should not be made with elevations of AST and ALT alone in the absence of concurrent

measurement of serum CK activity. If serum CK activity is not measured, misdiagnosis of a liver disease may be made when the actual problem is a myopathy.

Total Proteins test: Albumin is the main protein made by liver. It performs many important bodily functions. For example, albumin: Stops fluid from leaking out of your blood vessels Nourishes the tissues, Transports hormones, vitamins, and other substances throughout the body

An albumin test measures how well the liver is making this particular protein. A low result on this test indicates that the liver isn't functioning properly. Globulin is a set of sixty proteins including the antibodies or gamma globulins and protein-carbohydrate compounds known as glycoprotein. There are four basic groups of globulin proteins known as the alpha-1, alpha-2, beta and gamma proteins.

These are used to help transport proteins through the lipoproteins and assisting the blood in clotting. They also act as plasma cells which indicate whether there is an antibody deficiency in the blood stream. The liver produces much of the alpha and beta globulins used for this purpose.

The level of these proteins is measured against the levels of albumin, the other major type of protein in the bloodstream. Albumin and globulin are two types of protein in body. The total protein test measures the total amount albumin and globulin in your body.

Bilirubin and Creatinine Test: Bilirubin attached by the liver to the glucose-derived acid, glucuronic acid, is called direct, or conjugated, bilirubin. Bilirubin not attached to glucuronic acid is called indirect, or unconjugated, bilirubin. All the bilirubin in the blood together is called total bilirubin. Bilirubin is a waste product ordinarily processed by the liver. The breakdown of red blood cells creates this waste product. It passes through the liver before being excreted through stool. A damaged liver can't properly process bilirubin. This leads to an abnormally high level of bilirubin in the blood. A high result on the bilirubin test indicates that the liver isn't functioning

properly. If bilirubin is not being attached to the glucose-derived acid (conjugated) in the liver or is not being adequately removed from the blood, it can mean that there is damage to your liver. Testing for bilirubin in the blood is a good way of testing for liver damage.

Creatinine Test: Creatinine is a chemical waste molecule that is generated from muscle metabolism. Creatinine is produced from creatine, a molecule of major importance for energy production in muscles. Creatinine is transported through the bloodstream to the kidneys. The kidneys filter out most of the creatinine and dispose of it in the urine. The kidneys maintain the blood creatinine in a normal range. Creatinine has been found to be a fairly reliable indicator of kidney function. Elevated creatinine level signifies impaired kidney function or kidney disease.

As Fig 4.16 shows, liver and kidney function tests appeared to be normal after injection of ProCA32.collagen1 and the results were the same as control mice, therefore, ProCA32.collagen1 did not cause any toxicity after injection.

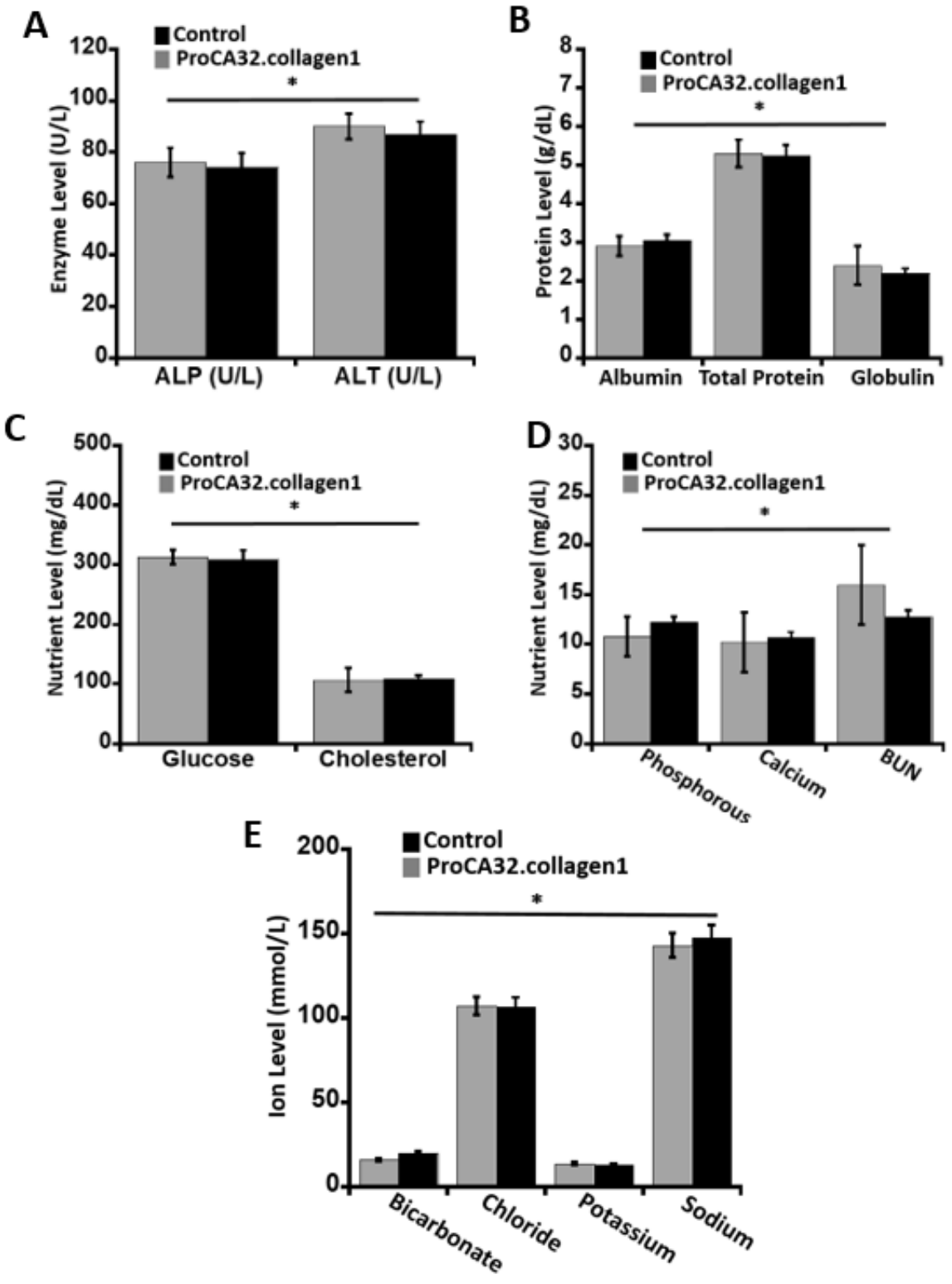

Figure 4.16 *Toxicity studies of ProCA32.collagen1.*

(A, B, C, D, E) *Clinical chemistry tests after injection of 0.023 mmol/kg, ProCA32.collagen1. The mice clinical chemistry profiles were collected by analyzing mice serum samples 5 days after injection of saline (gray, n = 5), or 0.025 mmol/kg ProCA32.collagen1 (black). Data are expressed as mean ± SD.*

4.2.8.3 Tissue toxicity of ProCA32.collagen1

The 0.0013 mmol/kg ProCA32.collagen1 or saline (control) was i.v. injected in CD-1 mice. H&E staining was used to evaluate the toxicity of the ProCA32.collagen1 to these tissues after injection. An experienced pathologist was blinded to the groups of H&E staining to evaluate the organ toxicity of ProCA32.collagen1. ProCA32.collagen1 shows no toxicity in all kinds of mice tissues and organs studied, including liver, kidney, muscle, spleen, brain, and heart. The images are representative of three independent experiments. As results show in Fig. 4.17, all the tissues in all viral organs appeared to be normal after injection of ProCA32.collagen1 which shows that the contrast agent does not cause any tissue damage due to Gd^{3+} deposition.

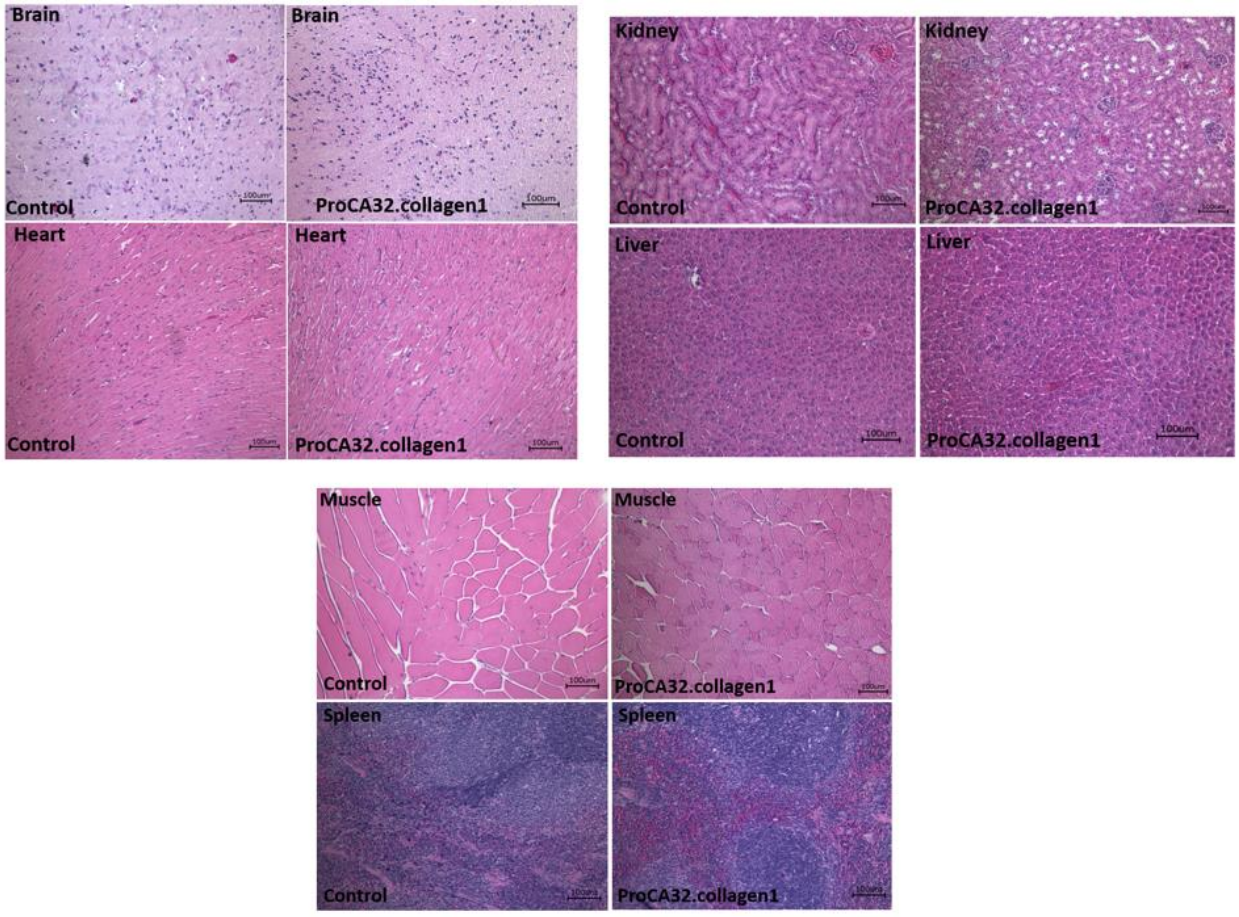

Figure 4.17 *Tissue toxicity studies of ProCA32.collagen1.*

The 0.0013 mmol/kg ProCA32.collagen1 or saline (control) was i.v. injected in CD-1 mice. H&E staining was used to evaluate the toxicity of the ProCA32.collagen1 to these tissues after injection. An experienced pathologist was blinded to the groups of H&E staining to evaluate the organ toxicity of ProCA32.collagen1. ProCA32.collagen1 shows no toxicity in all kinds of mice tissues and organs studied, including liver, kidney, muscle, spleen, brain, and heart. The images are representative of three independent experiments.

4.3 Discussion

4.3.1 Design of ProCA32.collagen1 with collagen targeting capability and dual high relaxivity

Collagen targeted protein MRI contrast agent, ProCA32.collagen1 was designed by covalently linking a collagen type I targeting peptide moiety consisting of natural amino acids to the C-terminal of protein contrast agent ProCA32 (with two Gd^{3+} binding sites). An intra-disulfide bond formed by two cysteine residues to stabilize conformation required for collagen I binding. In the modeled structure, Lysine residues are positioned to bind collagen type I while its PEGylation also increase relaxivity by tuning correlation time. A flexible linker was used to maximize targeting capacity and relaxivity yet maintaining metal binding capability [83]. PEGylation of the contrast agent can improve protein solubility, blood retention time and reduce immunogenicity [84]. The designed ProCA32.collagen1 was bacterial expressed, purified, and modified and confirmed to form a 1:2 Gd-ProCA32.collagen1 complex using ICP-OES (Methods) [83] [177].

We determined collagen I binding affinity of PEGylated ProCA32.collagen1 using enzyme linked immunosorbent assay (ELISA). The contrast agent exhibits high affinity to collagen type I with dissociation constant of K_d=1.42 ± 0.2 μM (fitted by 1:1 binding model) [135, 203]. On the other hand, PEGylated ProCA32 without addition of a collagen targeting moiety did not show any specific binding to collagen I.

The determined relaxivity of r_1 and r_2 of PEGylated ProCA32.collagen1 were 34 ± 0.12 $mM^{-1}s^{-1}$ and 50 ± 0.16 $mM^{-1}s^{-1}$ per Gd^{3+}, respectively at 37 °C and 1.4 T or 68 ± 0.25 $mM^{-1}s^{-1}$ and 100 ± 0.32 $mM^{-1}s^{-1}$ per particle, respectively. Interestingly, at high magnetic fields of 7.0 T, 37 °C, PEGylated ProCA32.collagen1 exhibits the highest r_1 (21.3 ± 0.5 $mM^{-1}s^{-1}$ per Gd^{3+} or 42.6 ± 1 $mM^{-1}s^{-1}$ per participle) and r_2 (108.5 ± 1.2 $mM^{-1}s^{-1}$ per Gd^{3+} or 217 ± 2.4 $mM^{-1}s^{-1}$, per particle) compared to reported contrast agents (Table 4.2). ProCA32.collagen1's r_1 and r_2 relaxivity values

are 5-10 and 12-17 times greater than those of clinical contrast agents at 1.4 and 7.0 T, respectively. Therefore, this targeted contrast agent can be applied to both low and high magnetic field strengths with both T1 and T2 weighted molecular imaging. Such large value of r_1 and r_2 are likely due to secondary shell water contribution since water number q in the first coordination shell determined by luminescence resonance energy transfer (LRET) using Tb^{3+} luminescence life time decay is 0.5.

4.3.2 High Gd^{3+} binding affinity and metal selectivity, and low toxicity of ProCA32.collagen1

To address one of the major causes of nephrogenic systemic fibrosis (NSF) associated with free Gd^{3+} toxicity, we next examined metal binding affinity and selectivity of ProCA32.collagen1. We determined the dissociation constant (K_d) of ProCA32.collagen1 to Tb^{3+} to be $6.14 \pm 0.2 \times 10^{-22}$ M using Tb^{3+}-DTPA buffer system and Tb^{3+} luminescence resonance energy transfer (Tb^{3+}-LRET) between Tb^{3+} and Trp adjacent to the metal binding sites. Addition of Gd^{3+} results in decrease of the LRET signal between Tb^{3+} and Trp due to competition of metal binding sites. The Gd^{3+} binding affinity of ProCA32.collagen1 is $2.0 \pm 0.25 \times 10^{-22}$ M which is comparable to the approved clinical contrast agents (Table 4.1). Since competition of physiological metal ions such as Zn^{2+}, Mg^{2+} and Ca^{2+} [6, 11] is considered to be one of the most important risk factors for Gd^{3+} release *in vivo*, we then determined metal binding constants for these metal ions [83, 176]. Table 4.1 shows that ProCA32.collagen1 exhibits 10^{14}-10^{16}-fold increases in metal selectivity (kinetic stability) for Gd^{3+} over Ca^{2+} and Zn^{2+} compared with all approved agents including macrocyclic "safe" agents Dotaram and ProHance. To the best of our knowledge, like ProCA32-P40, ProCA32.collagen1 has the greatest metal selectivity among all other approved Gd^{3+}-based contrast agents.

4.3.3 Additional improved safety properties of ProCA32.collagen1

ProCA32.collagen1 has several additional improved safety properties. Transmetallation studies demonstrate the relaxation rates of clinical contrast agents (Eovist; Magnevist; Ominiscan; ProHance) gradually decrease upon incubation with 2.5 mM Zn^{2+} in 30 mM $PO4^{3-}$ [83]. In contrast, the relaxation rates of ProCA32.collagen1 remain unchanged suggesting that ProCA32.collagen1 has strong capability against transmetallation, similar to approved "safe" contrast agents Dotarem and ProHance. Further, ProCA32.collagen1 remains intact without cleavage upon incubation with human serum at 37°C for 13 days. Recent brain deposition has underlined the importance of metal safety [204, 205]. Importantly, ProCA32.collagen1 does not have brain deposit possibly due to lack of penetration to blood barrier. Moreover, ProCA32.collagen1 did not show any acute toxicity as clinical chemistry test values are within the normal range demonstrating the normal function of organs specially kidney and liver. No tissue and organ toxicity was observed. More importantly, the projected required injection dosage of ProC32.collagen1 in human for significant MRI enhancement in liver is ~ 20-230-fold lower than clinical contrast agents such as MultiHance (Table 4.2).

Our developed ProCA32.collagen1 represents a major leap in addressing concerns about metal toxicity and Gd^{3+} deposition associated with current contrast agents in several aspects. Administration of contrast agents helps with visualization of diseases at MRI. Specifically, majority of clinical Gd^{3+}-based MRI contrast agents cause T1 shortening and signal enhancement on T1 map images, however most of these agents have been linked to the occurrence of nephrogenic systemic fibrosis (NSF) in renal impaired patients due to release and accumulation of Gd^{3+} from the agent because of transmetallation [157, 206] . Furthermore, they are all based on small-molecule chelates and have very low relaxivity (both r_1 and r_2) and sensitivity without

targeting capability, therefore, they are only able to detect moderate and advanced stage of diseases. The clinical contrast agents also use a high clinical injection dosage due to their low sensitivity with a short imaging window without the capability of enhancing the entire organ such as Eovist. ProCA32.collagen1 with high r_1 and r_2 relaxivity has very low injection dosage (Table 4.1) of 0.0013 mmol.kg^{-1} projected in humans which is 20-200-fold lower than clinical contrast agents. In addition, its high selectivity towards Gd^{3+} makes it a safer agent.

4.4 Summary

In summary in this chapter, some of the most important properties of a contrast agent was reported. ProCA32.collagen1 has very strong binding affinity to collagen type I and superior r_1 and r_2 relaxivity. The contrast agent has very high binding affinity and selectivity towards Gd^{3+} and is very resistant to transmetallation. ProCA32.collagen1 is also very stable in the human serum up to 13 days without any degradation. It is worth mentioning that PEGylation not only increases the stability and solubility of the contrast agent but also increase its relaxivity and sensitivity for in vivo applications which will be discussed in the coming chapters. ProCA32.collagen1 did not show any tissue and long-term organ toxicity based on low and negligible Gd^{3+} accumulations.

5 APPLICATION OF PROCA32.COLLAGEN1 IN IMAGING OF LIVER FIBROSIS

5.1 Introduction

5.1.1 Organ fibrosis

Fibrosis is a common feature in many different pathologies. It is characterized by the accumulation of extracellular matrix (ECM) components and is associated with up to 45% of deaths in industrialized countries [207]. In general, fibrosis mechanisms include exacerbated injury-related responses that are dysregulated versions of conventional tissue repair processes [208]. Core elements in disease progression can be acute, recurrent or persistent epithelial and

endothelial injuries that can both initiate and sustain fibrosis [209]. These pathogenic pathways furthermore involve changes in numerous inflammatory, endothelial and mesenchymal cells, resulting in increased production of fibronectin, osteopontin, hyaluronan, proteoglycans, laminins and a variety of collagen subtypes [210]. The abnormal ECM deposition which is typical of fibrosis leads to a disruption and distortion of the tissue architecture and function [211]. These fundamental fibrotic processes are shared across a variety of tissues and organs, including connective tissue, gastrointestinal tract, liver, kidney, lung and heart (Fig. 5.1). While the mechanisms of fibrogenesis are similar, the regenerative capacity and the ability to reverse advanced fibrosis vary tremendously. Resolution of fibrosis is for example possible in the liver when the underlying cause is removed; this is for instance the case in complete suppression of hepatitis B virus replication and curative treatment of hepatitis C [212].

The desmoplastic reaction and increased ECM production in tumors is remarkably similar to organ fibrosis [213]. Cancer-associated fibroblasts (CAF) are one of the most crucial components of the tumor microenvironment and have been implicated in angiogenesis, immunosuppression and metastasis [214, 215]. Fibrotic stroma affects disease progression in various tumors, e.g. breast cancer, in colon/colorectal cancer and in pancreatic tumors, as well as in head and neck cancer [216, 217]. In contrast to fibrosis as a common endpoint for all of the above organs and tissues, the etiologies causing fibrosis are highly diverse, encompassing an array of different triggers such as acute injury, chronic inflammation, autoimmune reactions and genetic alterations. In some cases, the exact etiology may even remain unknown. While a detailed description of these triggers and their disease-initiating mechanisms is beyond the scope of this review, several prototypic examples can be provided, to exemplify the high prevalence and far-reaching consequences of fibrotic processes in human diseases. Among the most obvious

etiologies for induction of fibrosis are exposure to ionizing irradiation and mechanical obstruction, resulting from e.g. myocardial infarction, surgical intervention, gall- and kidney-stones. Frequently accountable chronic illnesses with fibrotic elements include psoriasis, Crohn's disease, pneumoconiosis subtypes, steatohepatitis, viral hepatitis and glomerulosclerosis. Also, many autoimmune disorders, such as rheumatoid arthritis, systemic lupus erythematosus, Sjörgen's syndrome, progressive systemic sclerosis, Hashimoto's thyroiditis and ankylosing spondylitis are associated with fibrosis.

Underlying genetic predispositions that make individuals susceptible to fibrosis are neurofibromatosis, cystic fibrosis, alpha 1-antitrypsin deficiency, tyrosinosis, Wilson's disease and hemochromatosis, as well as hypertrophic and restrictive cardiomyopathy. There are multiple fibrosis related diseases, in which the exact triggers are unknown, such as sarcoidosis, idiopathic pulmonary fibrosis, retroperitoneal fibrosis, acute interstitial pneumonitis and dilated cardiomyopathy.

Accurate diagnosis and staging of fibrosis is essential for proper prognosis and progression monitoring. The presence and the severity of fibrosis actually are the best predictors for disease progression in chronic kidney disorders and in fatty liver disease [218]. Traditionally, needle-based biopsies have been the gold standard for fibrosis diagnosis and staging. Biopsies, however, are faced with multiple limitations, including their invasive nature, procedure-associated risks, limited representativeness for the entire organ, and inter- and intra-observer sampling variability [219].

In the recent years, increasing numbers of studies have focused on the development of non-invasive imaging techniques for fibrosis diagnosis, staging and treatment monitoring. Non-invasive imaging techniques such as X-ray imaging, computed tomography (CT), ultrasound (US), magnetic resonance imaging (MRI), photoacoustic imaging (PAI), optical imaging (OI), positron

emission tomography (PET) and single-photon emission computed tomography (SPECT) have all been employed for this purpose [220-223]. Biopsies and liquid biomarkers to assess fibrosis

An accurate determination of fibrosis stage is crucial for the prognosis, for determining surveillance strategies and for selecting a suitable therapeutic approach. Traditionally, needle-based biopsies are considered the gold standard and they often are the only available means for specific fibrosis assessment and exact disease differentiation. In the case of systemic lupus erythematosus (SLE), for instance, a renal biopsy is crucial to diagnose the specific form of lupus [224]. In general, multiple stainings can be employed for visual inspection, such as hematoxylin and eosin staining or more specifically trichrome or Sirius Red staining (marking collagenous fibers) or immunohistochemistry specific for certain types of collagens or other ECM components [225].

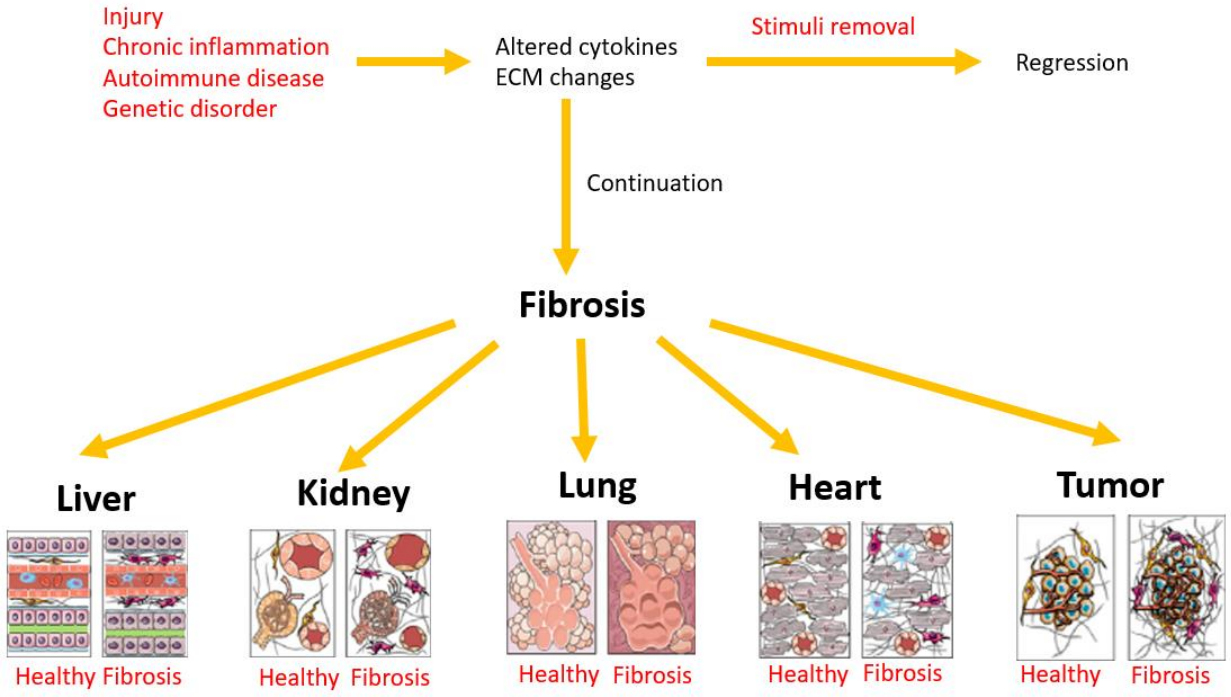

Figure 5.1 *Pathological characteristics of fibrosis in different tissues.*

To achieve optimal accuracy in the diagnosis of fibrosis, the biopsy bias has to be minimized, starting with the excised sample, which should have specific properties. An adequate kidney biopsy is 10 mm in length and at least 1.2 mm in width, and it should contain 10–15 glomeruli [226]. A liver biopsy is considered adequate if it has a length of at least 20 mm and contains at least 11 portal tracts (some experts even prefer 16 portal tracts) [227]. However, such "optimal" liver biopsies only represent 1/50,000 of the total liver volume. For the diagnosis of arthritic diseases, a biopsy sample of the synovial fluid is considered equally informative as a sample of the synovial tissue. The diagnosis of connective tissue disease is commonly performed on the basis hematological tests (complete blood count, erythrocyte sedimentation rate), biochemical analysis (C-reactive protein, hepatic function, renal function) and immunologic investigations (autoantibodies, rheumatoid factors, antinuclear antibodies, antibodies to DNA, antiphospholipid antibodies) [228].

In case of tumors, a biopsy is the standard diagnostic procedure to determine the nature and stage of the tumor, as well as its malignant potential. Although the essential role of desmoplastic processes for tumor growth and metastasis has been recognized [229], they are not considered in routine pathological assessments. Many studies have suggested that especially in invasive colorectal cancer [230-232] and in pancreatic ductal adenocarcinoma [233-235], the desmoplastic reaction is a key hallmark determining therapeutic outcome. Thus far, however, histopathological information on e.g. myxoid stroma as an indicator for epithelial-to-mesenchymal transition [230], has not yet managed to become broadly accepted and implemented for disease differentiation, prognosis assessment and treatment selection [236].

While needle-based biopsies inevitably play an important role in the diagnosis and staging of fibrotic diseases, they suffer from several drawbacks, including invasiveness with the risk of

life-threatening complications, sampling errors, and intra- and inter-observer variability [237, 238]. Moreover, repeated biopsy procedures are difficult and impractical, due to the increased risk of complications [121]. Nevertheless, because of the lack of reliable tools and technologies to obtain information noninvasively, up to 4 biopsies are still routinely taken in large phase III trials, e.g. in patients suffering from non-alcoholic steatohepatitis (NASH) [239].

In tumors, biopsy-based diagnosis is particularly complicated, because of intrinsic heterogeneity in the primary tumor, as well as heterogeneity between the primary tumor and metastases [240]. In such situations, also the accessibility of the pathological site(s) and the risk of spreading/seeding cancer cells play an important role [241]. In light of these limitations, liquid biopsies are increasingly emerging in the field of cancer diagnosis as a refined and non-invasive alternative (and/or as an add-on) to needle-based biopsies [242]. A liquid biopsy, in the form of a blood sample, can provide information on the genetic profile of cancerous lesions (and the heterogeneity therein) by means of analyzing circulating tumor cells or circulating cell-free tumor DNA [243, 244].

Because of their high applicability, reproducibility and widespread availability, liquid-based biopsies not only hold great promise for cancer diagnosis, but also for the assessment of classical fibrotic diseases. For the assessment of liver fibrosis, for instance, several serum biomarkers are available that are composite scores of not strictly liver-specific parameters as well as some that have been associated with fibrosis stage, but both types have been mainly proposed for patients with chronic hepatitis C [245]. The most commonly used tests include the FibroTest® (which combines alpha-2 macrolobulin, haptoglobin, apolipoprotein, bilirubin, gamma glutamyl transferase, age and gender into an algorithm), the aspartate-to-platelet ratio index (APRI) and the

Enhanced Liver Fibrosis score (ELF; which includes amino-terminal propeptide of procollagen type III (PIIINP), TIMP metallopeptidase inhibitor 1 and hyaluronic acid) [246, 247].

Shortcomings of liquid-based biomarkers are that they may not be organ-specific (enough), that they may be limited to the indication of impaired organ function or inflammatory state, and in particular that they may not specifically reflect fibrosis or discriminate between different stages of fibrosis [248, 249]. The abovementioned new biomarkers may help to provide more fibrosis-specific information, since they mostly assess molecules of the ECM. These novel markers now require validation in large cohorts of patients and in long-term studies [249]. In the future, such liquid biopsy techniques may be used in combination with other modalities, such as imaging, to improve the accuracy of fibrosis diagnosis and staging.

5.1.2 Non-invasive imaging of fibrosis

In the last decade, non-invasive imaging techniques have received a lot of attention for the assessment of fibrosis. Such set-ups and strategies typically include anatomical, functional and/or molecular imaging approaches that allow for the examination of the affected organ (or even the whole body) in a readily repeatable manner. In the case of fibrosis, this makes non-invasive imaging not only attractive for initial diagnosis, but also for staging and progression monitoring. Several imaging protocols have been evaluated for this purpose over the years, ranging from the basic assessment of anatomical/morphological changes, via the quantification of differences in functional properties, to the identification of molecular adaptations and disease-specific changes. Importantly, non-invasive imaging can also be employed for treatment monitoring, thereby potentially facilitating the clinical translation of novel anti-fibrotic therapies. In the following sections, using selected examples from the literature, we will provide an overview of the noninvasive imaging techniques that are commonly used in the context of fibrosis, and we will

discuss their (pre-) clinical application in systemic autoimmune diseases, in parenchymal organs, such as liver, kidney, lung and heart, and in desmoplastic tumors [249].

5.1.3 Liver fibrosis

The global burden of liver disease is already enormous [250-252] and an exponential increase is predicted for the next couple of decades [253]. A recent meta-analysis showed that fibrosis (in a stage-dependent manner) closely correlates with liver-related mortality, as well as with overall mortality [254, 255]. Consequently, the degree of liver fibrosis is of great importance for proper diagnosis, prognosis assessment and therapeutic intervention in chronic liver disease. Up to now, the histologically determined stage of fibrosis is the strongest independent risk factor for predicting liver-associated complications and the need for liver transplantation, as well as for liver-related and overall mortality [256]. Non-invasive assessment of liver fibrosis has thus far only been established for chronic hepatitis B and C virus infections, via the combination of two concordant tests, i.e. serum biomarkers plus transient elastography [245]. To distinguish between benign fatty liver disease and progressive non-alcoholic steatohepatitis, invasive biopsies are still required [257]. This biopsy procedure comes with multiple drawbacks, including the associated risks, sampling errors and intra and inter-observer variability. The latter is especially obvious, when semi-quantitative scoring systems are applied, which include grading (steatosis, ballooning, portal inflammation) and staging (fibrosis) [245, 247, 257].

In terms of anatomical imaging, standard gray-scale US is routinely used in the clinic for the assessment of liver disease. It provides baseline information on liver morphology and texture [247]. As an example, Choong and colleagues used gray-scale US to show that the liver surface progressed from being smooth to extremely nodular as the severity of the disease increased. The authors also reported coarsened echotexture and blunting of liver edges in patients with liver

fibrosis. However, this type of anatomical US imaging is limited to the detection of advanced stage fibrosis and does not provide sufficient accuracy for ruling out early-stage liver fibrosis [258]. Besides US, non-contrast enhanced CT has also been shown to be able to depict liver surface nodularity, and it does so with high accuracy and high intra- and inter-observer independency (upon assistance of an automated computer algorithm). So far, this technique has only been tested retrospectively for the differentiation of cirrhotic from non-cirrhotic livers, and further evaluations are needed to assess its reproducibility, as well as its (prospective) performance in intermediate-stage liver fibrosis [259].

Functional imaging of liver fibrosis has encompassed a variety of elastography modalities, which assess liver stiffness and which have had a massive impact on the non-invasive diagnosis of liver fibrosis. These elastography methods include transient elastography (TE), acoustic radiation force impulse imaging (ARFI), shear wave elastography (SWE) and MR elastography (MRE) [260]. FibroScan® was the first TE device which was approved for the rapid and user friendly quantification of fibrosis at the bedside [261]. The FibroScan® system consists of an US transducer combined with a vibrator that enables the direct relation of shear wave propagation to tissue stiffness [262, 263]. Initial inaccuracies and even application failures of TE devices in obese patients were partially overcome with an adapted XL probe that allows for deeper tissue penetration [264]. As opposed to TE, both ARFI and SWE use focused US pulses to estimate shear wave velocities in the liver which are related to tissue stiffness. ARFI is based on the elasticity information from the axis of the pushing beam that creates a 2D stiffness map, whereas SWE depends on the shear waves propagating sideways from the axis of the US beam [265, 266]. In liver SWE scans, fibrotic liver tissue is characterized by a higher stiffness as compared to healthy

liver tissue [267]. The elastic modulus of the depicted fibrotic liver is - with an average of 28 kPa - almost 5 times higher than the one measured in a healthy liver.

In comparison to the above-mentioned US elastography techniques, in which transient elastography in obese patients is compromised, MRE has been shown to have superior diagnostic performance not only for the detection of advanced fibrosis, but also for differentiating the individual progression states from simple steatosis to steatohepatitis [248, 268, 269]. In a recent prospective trial, MRE was found to be more accurate in identifying liver fibrosis (stage 1 or higher) than TE in patients with non-alcoholic fatty liver disease [270]. In this context, Chen and co-workers investigated the precision of MRE for discriminating patients with simple steatosis, steatohepatitis and hepatic fibrosis. A clear difference in hepatic stiffness manifested in all three conditions, and the highest stiffness was observed in patients with hepatic fibrosis followed by steatohepatitis and simple steatosis [271]. These results indicate that the use of MRE allows for separating patients with simple steatosis from the ones with steatohepatitis, which would allow for earlier and more specific therapeutic interventions. The MRE procedure can be incorporated into a routine liver MRI protocol with only a few minutes added to the total scan time [272, 273]. The postprocessing procedure is simple, but the hardware and software additions to the MRI are expensive and might impede clinical translation and implementation [274]. Recently, the feasibility of a cost-effective and portable photoacoustic imaging system (PAI) and US dual modality imaging setup has been evaluated in a preclinical CCl4- induced murine fibrosis model and it turned out to be an interesting addition to the currently available elastography techniques [214]. This alternative set-up relies on hemoglobin as a chromophore that absorbs light and the combination with US for proper selection of the liver region to be evaluated [275]. The PAI signal is increased in fibrotic livers due to the more heterogeneous tissue structure caused by ECM

deposition and angiogenesis. Analogously, PAI - in the form of a multispectral optoacoustic tomography set-up (MSOT) - has recently also gained interest for application in several other fibrosis-related diseases, including Crohn's disease [276, 277].

Moreover, a number of tools and technologies have been proposed for molecular imaging of liver fibrosis. These include MRI and nuclear imaging techniques that are used in combination with targeted contrast agents. The liver-specific contrast agent gadolinium ethoxybenzyl dimeglumine (Gd-EOB-DTPA), also known as Primovist® in Europe or Eovist® in the USA, is a MRI contrast agent that was originally developed for the detection of liver metastasis and hepatocellular carcinoma (HCC) [278, 279]. After intravenous injection Gd-EOB-DTPA progressively distributes into the hepatocytes via the organic anion transporter polypeptides OATP1B1 and OATP1B3 and excretes into the bile ducts via the multi drug resistance protein 2 (MRP2) [280]. The uptake and excretion of Gd-EOB-DTPA by the hepatocytes is also impaired in liver fibrosis, which enables the detection of severe fibrosis and cirrhosis in patients [281].

Molecular MRI has also shown promise in case of imaging of ECM components, such as elastin and collagen. Evidence for the use of ECM-targeted MR contrast media has been obtained in several liver fibrosis animal models. Elastin has been used as a target for molecular MRI, a significantly higher contrast enhancement in the perivascular regions in CCl4- treated fibrotic mice was observed as compared to healthy mice upon the administration of the Gd-containing elastin specific contrast agent, ESMA [282]. Similarly, Farrar and colleagues demonstrated that the Gd-containing collagen I-specific contrast agent EP-3533 not only allowed for staging of liver fibrosis via 3D molecular MRI, but also enabled accurate therapy monitoring in mouse and rat models [110, 283].

Besides MRI, also radionuclide-based imaging techniques such as SPECT and PET have been used for molecular imaging of liver fibrosis in preclinical setups. In case of SPECT, Li and colleagues reported on the use of 99mTc-labeled cyclic RGD penta-peptide for imaging hepatic stellate cells (HSC) in fibrotic rats [284]. The RGD peptide is known to have a high binding affinity to αvβ3 integrins, which are upregulated in hepatic fibrosis [285, 286]. Specifically, it was shown that the expression levels of αvβ3 integrins on HSC correlate with fibrosis stage, and that non-invasive SPECT-based staging of liver fibrosis is possible with 99mTc-labeled cRGD [284]. In line with this, PET in combination with CT has been used for the imaging of translocator protein (TSPO) expression in progressive liver fibrosis. The TSPO is a convenient biomarker since it is mainly expressed by macrophages and HSC. The accumulation of the TSPO specific radiotracer 18F-FEDAC correlated well with the severity of liver damage in rats exposed to CCl_4 [287]. In order to facilitate clinical translation, further studies are needed to optimize molecular imaging probes and protocols which are specific for HSC [288] and other fibroblast-like cells, which e.g. express the platelet-derived growth factor receptor-β [289].

In summary, significant progress has been made at the clinical level in anatomical and functional imaging of liver fibrosis. However, the abovementioned techniques and protocols entail multiple disadvantages and they do not really permit accurate fibrosis staging and treatment monitoring. At the preclinical level, molecular imaging of liver fibrosis via MRI, PET and SPECT has hinted towards more specific detection of changes in biomarker levels that correlate with disease progression and/or treatment responses, indicating that such probes and protocols may start impacting the diagnosis and treatment of liver fibrosis in the clinic in the near to distant future.

Collagen type I is an important target for molecular imaging of liver fibrosis since its accumulation is a characteristic of most types of chronic liver diseases (CLD) [290]. In this paper,

we report the development of a protein MRI contrast agent for molecular imaging of the collagen level (ProCA32.collagen1) extending the targeting capability of our recently reported ProCA32-P40, a protein MRI contrast agent [83]. ProCA32.collagen1 with high dual relaxivity values for r_1 and r_2 per Gd^{3+} at both 1.5 and 7.0 T as well as strong collagen targeting capability enables the first robust detection of early and late stage of liver fibrosis as well as heterogonous expression of collagen by multiple molecular dynamic imaging. The development of collagen-targeted protein MRI contrast agent is expected to overcome the major clinical barriers in early diagnosis, noninvasive detection and staging of liver fibrosis, and have strong application in facilitating effective treatment and stop further progression toward major clinical consequences including cirrhosis, impaired liver function, and hepatocellular carcinoma.

Chronic liver disease (CLD) is a major cause of morbidity and mortality worldwide[110, 121, 161, 283]. Hepatic fibrosis can develop in patients with any type of chronic liver disease (CLD), including alcoholic liver disease (ALD), hepatitis C, hepatitis B, nonalcoholic fatty liver disease (NAFLD) and autoimmune hepatitis. The Centers for Disease Control (CDC) estimates that 19,388 people died in the US from alcohol related liver disease in 2014 [291]. Chronic liver disease originates from a variety of causes such as viral hepatitis, metabolic dysfunction, as well as alcohol abuse and autoimmune disease and almost all chronic liver injuries can cause liver fibrosis [291, 292].

Biopsy coupled with histological analysis is the gold standard for diagnosis and staging of liver fibrosis as it relies on stage-dependent characteristic patterns of collagen expression. Collagen type I is heterogeneously accumulated in liver fibrosis depending on etiology which leads to fibrosis that disrupts liver cytoarchitecture and function [293]. Sequential histological grading of inflammation and staging of fibrosis based on collagen 1 are used to decide the risk of disease

progression. However, biopsy has many limitations such as sampling errors, high inter-observer variability with 33-50% error rate even for diagnosis of advanced stages of liver fibrosis such as cirrhosis likely due to heterogeneity [283]. Tremendous effort have been devoted into development of noninvasive imaging techniques based on stiffness associated with fibrosis such as ultrasound apparent diffusion coefficient (ADC), magnetic resonance elastography (MRE), T1, T2, relaxation in the rotating frame ($T_{1\rho}$) [294], magnetization transfer [295], and proton density fat fraction (PDFF). However, these techniques cannot provide accurate detection of early stage liver fibrosis and visualization of heterogeneity.

A prerequisite for early detection and efficient treatment of liver fibrosis is a reliable non-invasive diagnostic method to accurately stage fibrosis progression and response to therapy. MRI offers several unique advantages compared to other clinical imaging modalities with its deep tissue penetration, high spatial resolution, and coverage of the entire liver. Since MRI does not require the use of ionizing radiation, it is well suited for screening and monitoring the progression and regression of fibrosis [296, 297]. However, an early stage of patient liver fibrosis with regional heterogeneity cannot be ambiguously detected by MRI due to limitations of currently available MRI contrast agents.

To differentiate “invisible” fibrotic cells from heterogeneous tissue background without clear boundary requires novel MRI contrast agents and imaging methodology to have a strong specificity for both organ and diseased cells as well as much improved relaxation properties. Iron oxide-based contrast agents such as ferumoxides create negative (dark) T2 /T2* effects that are reported to yield images with signal voids with very limited accuracy[278, 298]. Like all other approved Gd^{3+} MRI contrast agents, Gd-BOPTA (Multihance) and Gd-EOB-DTPA (Eovist US; Primovist, Europe) have Gd^{3+} r_1 relaxivity strong enough to lead to a positive (bright) imaging.

[299]. These two clinical agents have liver distribution and able to detect late stage fibrosis *in vivo* with r_1 increase using T_1-weighted sequence at a short arterial phase and a short hepatobiliary uptake phase [300, 301]. In addition, severity or the stage of fibrosis assessment is also necessary when making decision in diseases diagnosis, prognosis of chronic liver diseases and even while screening for various forms of HCC. Recent developments of collagen targeted contrast agent using approved DTPA (Magnivest) have shown to be able to image liver fibrosis with improved sensitivity and specificity but largely depending on the animal models[121], however, safety concerns about Magnevist underscore the pressing need of a safe MRI contrast agent with strong capability in detecting early stage fibrosis and delineating liver heterogeneity [302].

We reasoned that precision dual imaging capability (r_1 and r_2) of stage-dependent characteristic expression patterns of collagen type I will lead us to differentiate "invisible" fibrotic cells from heterogeneous tissue background without clear boundary in early stage and extracellular matrix heterogeneity associated with late liver fibrosis depending on etiology, liver cytoarchitecture and function [293]. In this chapter, we report the development of a protein MRI contrast agent (ProCA) for molecular imaging of the collagen level (ProCA32.collagen1) in two models of liver fibrosis extending the targeting capability of our recently reported ProCA32-P40 [83] (Fig. 5.2). ProCA32.collagen1 with high dual relaxivity values for r_1 and r_2 per Gd^{3+} at both 1.5 and 7.0 T as well as strong collagen targeting capability enables the first robust detection of early and late stage liver fibrosis as well as heterogonous expression of collagen by multiple dynamic molecular imaging properties. In addition, ProCA32.collagen1 is able to demonstrate vascular and architectural alterations during late stage fibrosis which has not been achieved before. The development of collagen-targeted protein MRI contrast agent is expected to overcome the major clinical barriers in early diagnosis, noninvasive detection and staging of liver fibrosis, and

have strong application in facilitating effective treatment and stop further progression toward major clinical consequences including cirrhosis, impaired liver function, and hepatocellular carcinoma.

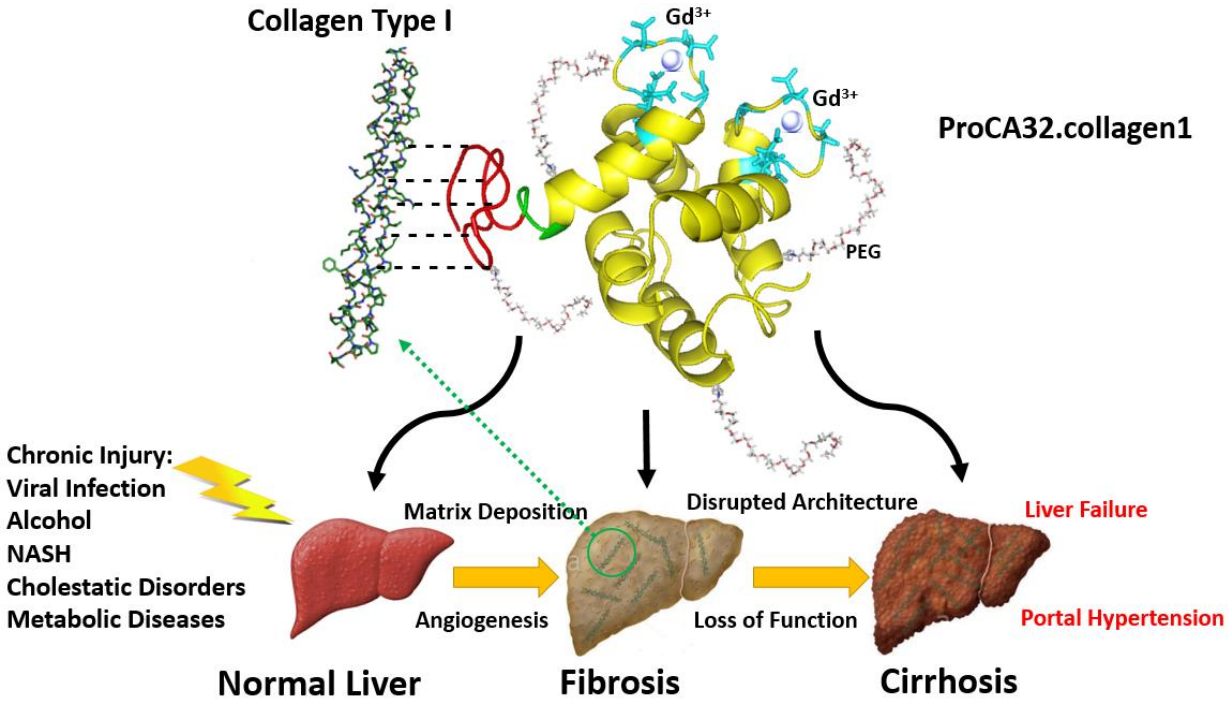

Figure 5.2 *Development of ProCA32.collagen1 for molecular imaging of liver fibrosis. ProCA32.collagen1 was developed by linking collagen type I targeting moiety at its C-terminal to be applied in early detection of liver fibrosis as well as late stage liver cirrhosis.*

5.2 Results

5.2.1 Robust detection of early and late stages liver fibrosis with dual contrast property

We tested whether molecular MR imaging with ProCA32.collagen1 is able to unambiguously and quantitatively detect early stage and late stage of liver fibrosis *in vivo* taken advantage of high r_1 and r_2 values (Fig. 5.3). Early and late stages of liver fibrosis of BALB/c mice were induced by injection of thioacetamide (TAA) and fed with 10% alcohol in drinking water either for 6 weeks or 12 weeks, respectively (Fig. 5.4). Fig. 5.3 shows R1 map inversion recovery

MRI images collected before and 24 hrs after intravenous (I.V.) injection of contrast agents (100 µL, 5 mM) of ProCA32.collagen1, ProCA32-P40 (non-targeted), and Eovist. After 24 hours post injection, ProCA32.collagen1 demonstrates a dramatic increase in R1 to 2.4 ($\Delta R1 \sim 0.78\ s^{-1}$, about 50% increase in liver area) in early stage fibrotic liver in mouse. Such change is increased with R1 enhancement to ~ 2.85 s^{-1} (78 % increase) and $\Delta R1$ to approximately 1.40 s^{-1} compared to pre-injection for late stage fibrotic liver in mice. The R1 increase at 24-hour post injection is highly specific since it gradually decreased 48 hrs post injection due to excretion (Fig. 5.5). In contrast, this targeting agent does not result in a significant change for the mouse with normal liver (< 0.2 s^{-1} and 10% increase in liver area) at 24-hour time point (Fig. 5.3). In addition, ProCA32-P40 without collagen binding capability does not result in any significant enhancement at this time point. On the other hand, clinical approved liver contrast agent, Eovist for the fibrotic liver, at the same stage (1A-Mild) and Ishak=3 did not result in any increase in R1 or $\Delta R1$, 24 hrs after injection. Consistent with R1 map, T2 map results also exhibit the same pattern at 24 hours for both early and late stages of fibrosis with higher changes for late stage than early stage of TAA/alcohol model (Fig. 5.6). Further quantitative analysis of R1 map and T2 map can be observed in Fig, 5.7.

Taken together, these results demonstrate that the dual contrast property of ProCA32.collagen1 enables the first robust detection of early stage Ishak=3 mouse liver fibrosis with unprecedented sensitivity and quantification of both early and late stage liver fibrosis with significant enhancement in both $\Delta R1$ and $\Delta R2$ that correlate well with the severity of fibrosis (Fig. 5.9).

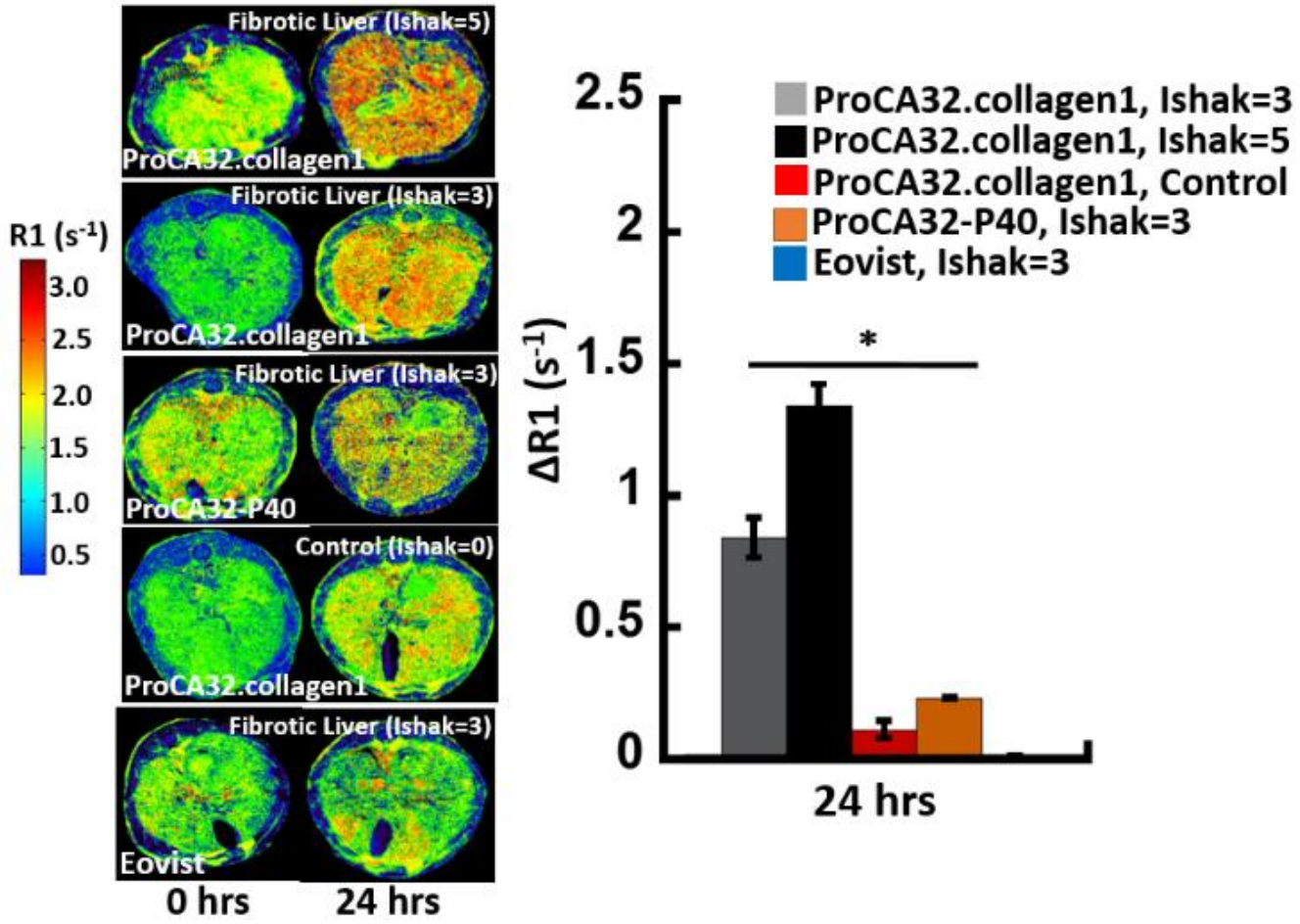

Figure 5.3 *Early and late stage liver fibrosis detection using ProCA32.collagen1. Demonstrates the R1 map of fibrotic (Ishak=3), normal (Ishak=0) and cirrhotic liver (Ishak=5) before and 24 hrs after injection of ProCA32.collagen1, ProCA32-P40 and Eovist. ΔR1 values of fibrotic (Ishak=3, and 5) and normal (Ishak=0) liver 24 hours after injection of ProCA32.collagen1, ProCA32-P40, and Eovist shows the targeting capability of ProCA32.collagen1 in differentiating different stages of liver fibrosis as the late stage shows the highest ΔR1 compared to early stage and normal liver.*

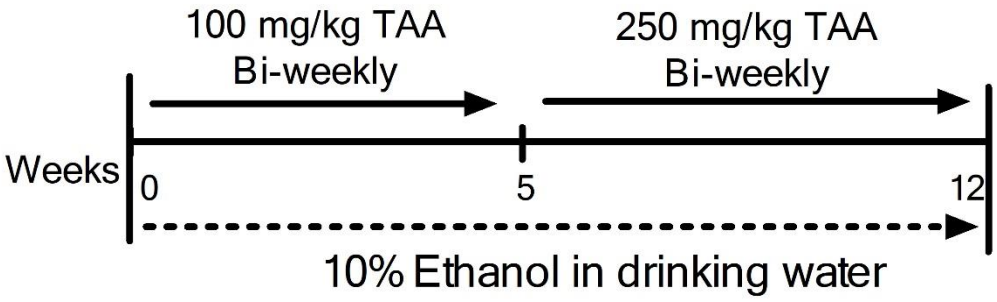

Figure 5.4 *TAA/alcohol-induced liver fibrosis animal model procedure*

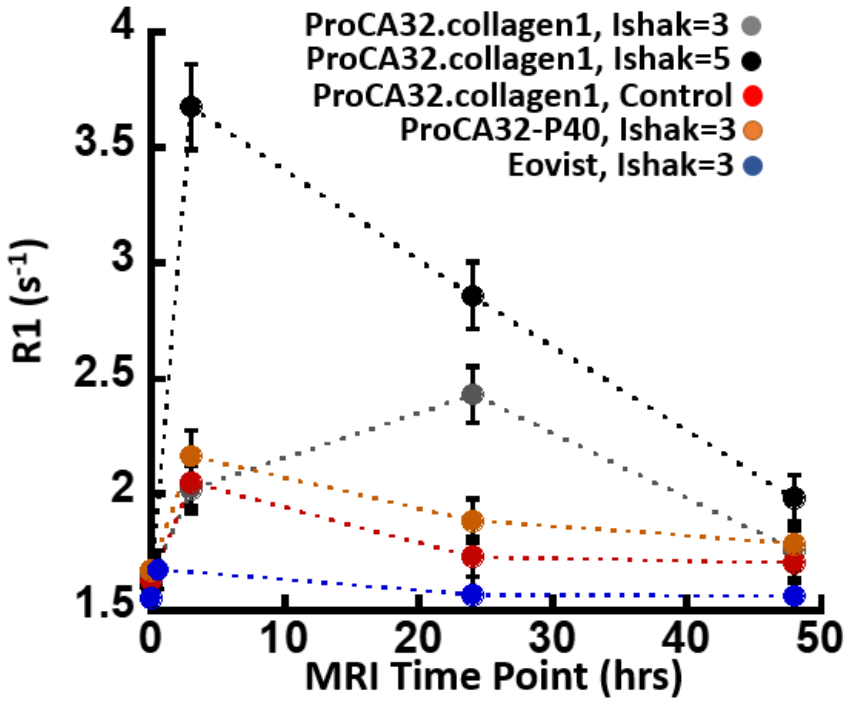

Figure 5.5 *R1 changes of liver over different MRI time points after injection of ProCA32.collagen1, ProCA32-P40 and Eovist. It shows the dynamic enhancement by ProCA32.collagen1 based on stage of fibrosis and its targeting capability.*

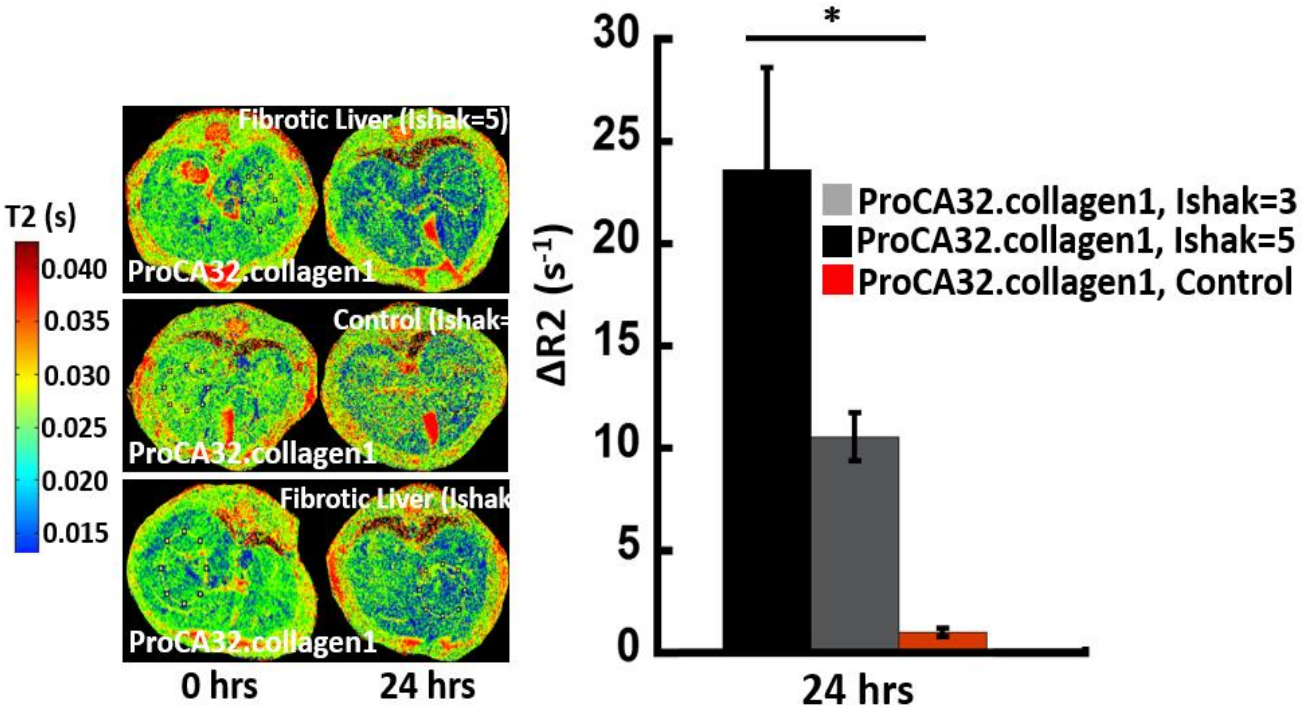

Figure 5.6 *T2 map MRI images of normal and fibrotic livers.*

T2 map MRI results are consistent with R1 map showing a significant decrease in T2 value (increase in R2) of late stage fibrotic liver (Ishak=5) after 24 hours post injection of ProCA32.collagen1, in addition, early stage fibrotic liver (Ishak=3) also shows decrease in T2 which is more than normal liver but decrease is not as high as late stage. ΔR2 values shows that 24 hrs is the time which demonstrates the significant difference between normal liver (Ishak=0), late (Ishak=5) and early stage (Ishak=3) fibrotic liver.

5.2.2 Histological validation of early and late stage fibrosis and correlation with MRI

Detailed histological analysis including H&E, alpha smooth muscle actin (αSMA) levels (brown) and Sirius Red staining for collagen content (red) as well as quantitative analysis of CPA confirmed stage 3 in Ishak scoring system and late stage (Ishak=5). (Fig. 5.8).

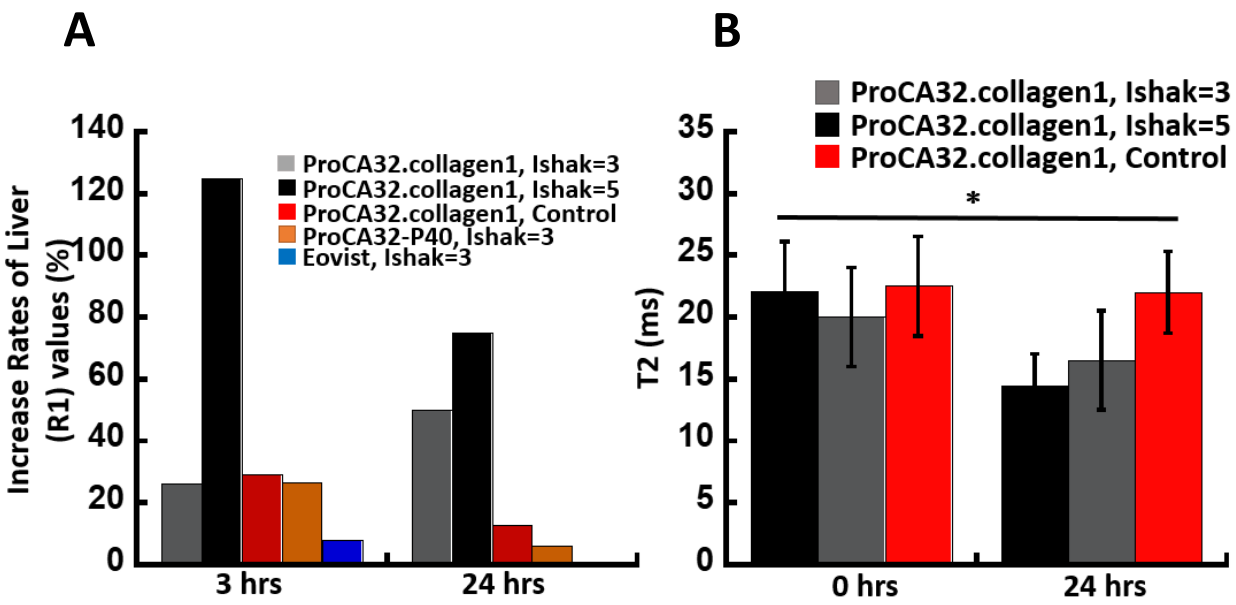

Figure 5.7 *Quantitative analysis of T1 and T2 map.*

(A) *Increase rates of liver (R1) values (%) for R1 map in TAA/alcohol induced mouse liver fibrosis compared to control showing different degree of increase based on contrast agent and time point.* ***(B)*** *T2 map values of normal and fibrotic livers with quantitative analysis. T2 map MRI results are consistent with R1 map showing a significant decrease in T2 value (increase in R2) of late stage fibrotic liver (Ishak=5) after 24 hours post injection of ProCA32.collagen1, in addition, early stage fibrotic liver (Ishak=3) also shows decrease in T2 which is more than normal liver but decrease is not as high as late stage.*

Furthermore, collagen proportional area (CPA) for TAA/alcohol and DEN model by pathologist confirmed early stage liver fibrosis (Mild-1A, zone 3, perisinusoidal) based on the NASH/CRN scoring. ProCA32.collagen1 distribution in normal and fibrotic liver is well-correlated with the stage of the disease. The late stage of liver cirrhosis. αSMA levels (brown) are much higher in later stage of liver fibrosis and CPA is 16% for Ishak= 5 (Fig. 5.8).

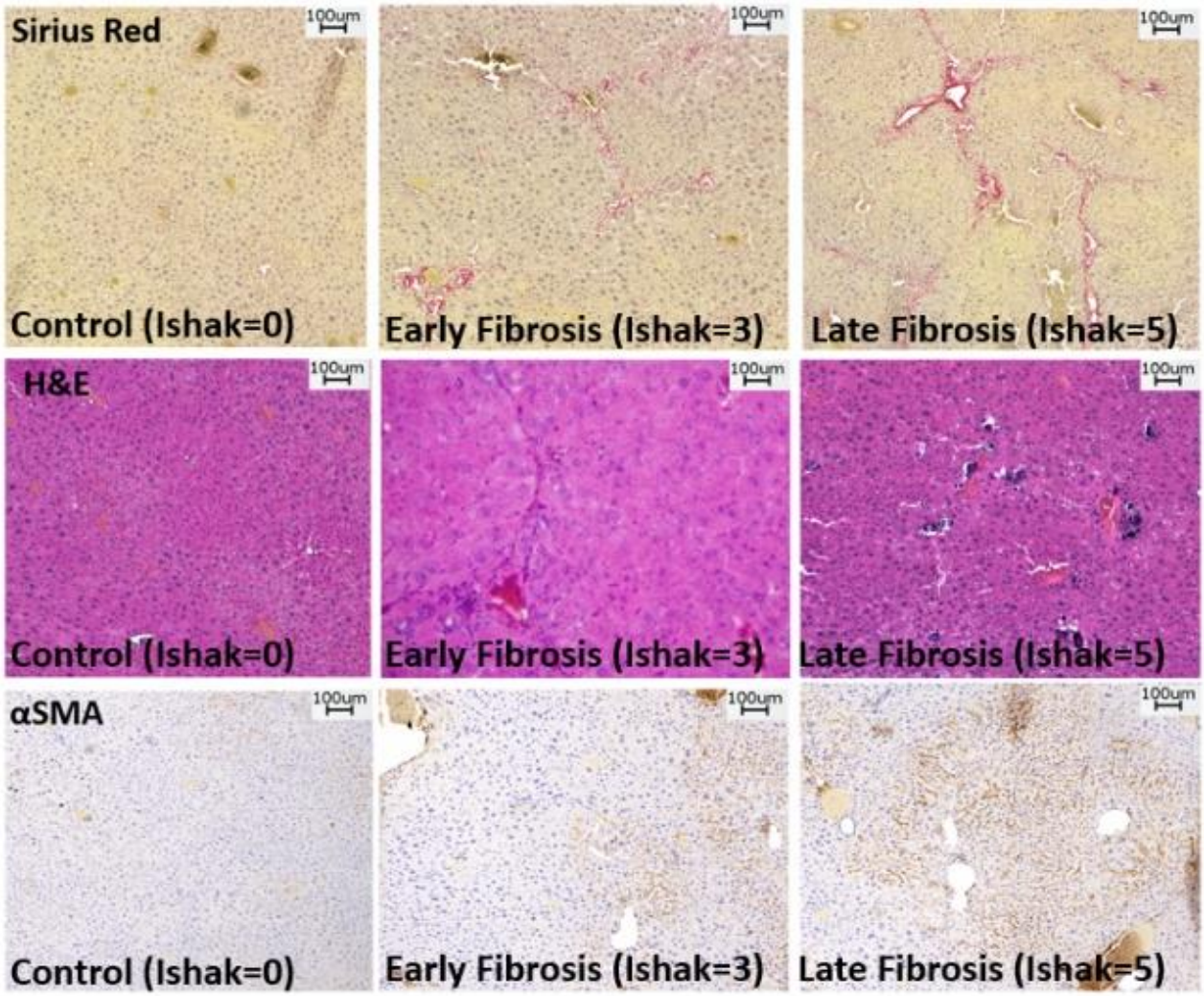

Figure 5.8 *Histology validation of different stages of TAA/alcohol-induced liver fibrosis. Sirius red, H&E and αSMA staining of early and late stage fibrotic liver compared to normal liver confirms the stage of liver fibrosis, as more collagen and αSMA content and dead hepatocytes are the indications of the disease stage.*

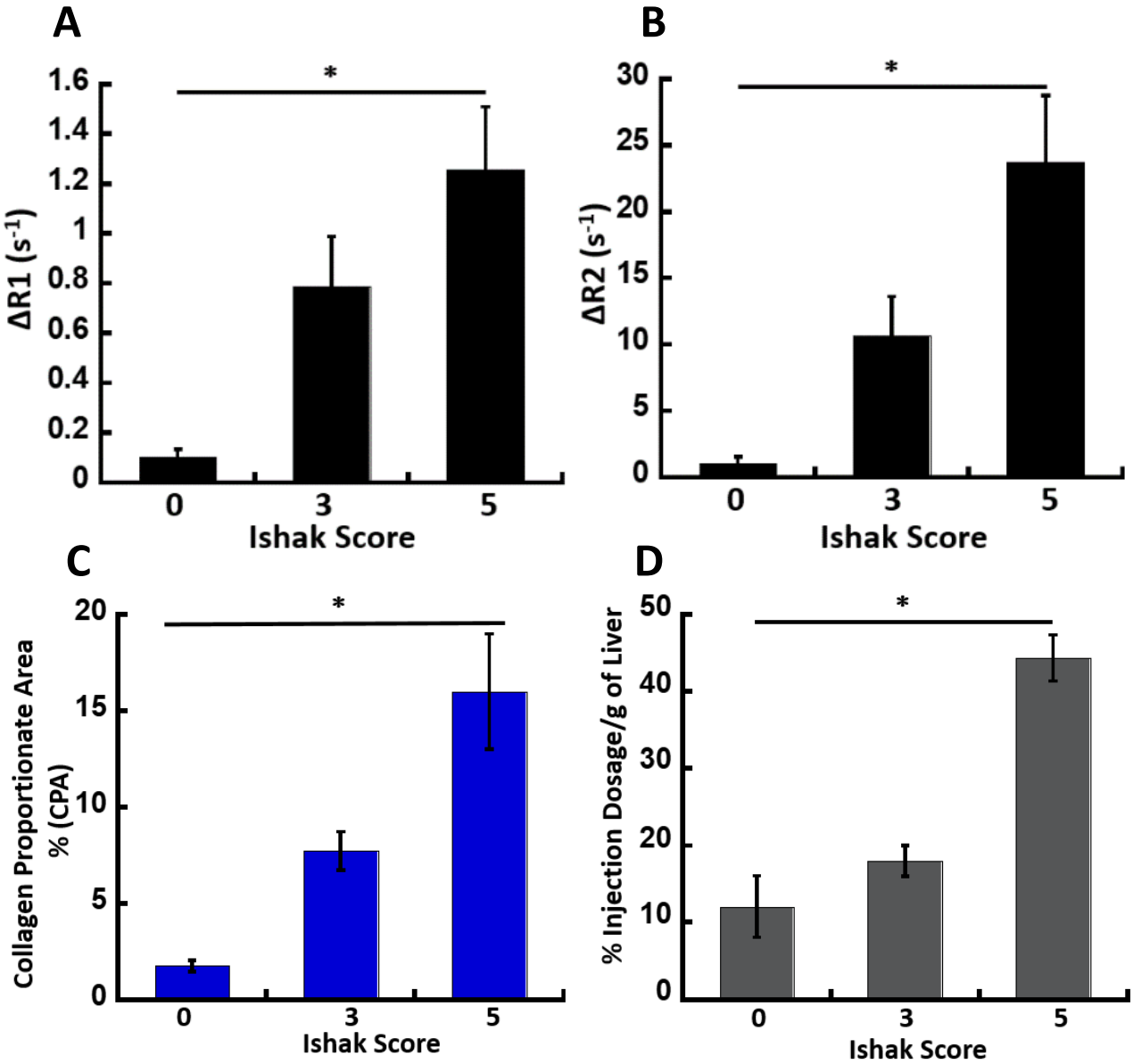

Figure 5.9 *Correlation of MRI with histology analysis in detection of different stages of liver fibrosis.*

(A, B) *Demonstrate the ability of ProCA32.collagen1 to distinguish early and late stages of liver fibrosis with ΔR1 and ΔR2 and its correlation with collagen proportionate area (CPA).* ***(C)*** *Collagen proportionate area analysis using ImageScope and its correlation with Ishak scoring system shows the stage of both early (Ishak=3) and severe fibrosis (Ishak=5) in TAA/alcohol induced mouse model.* ***(D)*** *Demonstrates a correlation between* Gd^{3+} *concentration in liver with*

Ishak score. As the fibrosis becomes more severe, more Gd^{3+} as an indication of more ProCA32.collagen1 is in the fibrotic liver ($P < 0.05$, student's t-test).*

As Fig. 5.9 demonstrates, ProCA32.collagen1 is capable of distinguishing early stage fibrosis (Ishak=3) from normal liver (Ishak=0) and late stage fibrosis (Ishak=5) based on both R1 and R2 mapping. With both ΔR1 and ΔR2 increasing based on the stage of the fibrosis, ProCA32.collagen1 can detect different stages with more confidence. Moreover, there is a strong correlation between Gd^{3+} concentration in liver with Ishak score. As the fibrosis becomes more severe, more Gd^{3+} as an indication of more ProCA32.collagen1 is in the fibrotic liver.

5.2.3 Biodistribution and pharmacokinetics of ProCA32.collagen1

Biodistribution analysis of ProCA32.collagen1 (Fig. 5.10) further supports the MRI results showing the targeting capability of the contrast agents. Severe fibrotic liver (Ishak=5) showed the highest concentration of Gd^{3+} and after that fibrotic liver (Ishak=3) supporting that the contrast agent targets based on collagen levels. Moreover, other organs did not show significant levels of contrast agent, all of them had less than %2 injection dosage per gram of tissue (Fig. 5.10).

Detailed pharmacokinetic characteristic of ProCA32.collagen1 revealed that clearance of ProCA32.collagen1 was low and 0.36 mL/min/kg (less than 1% of liver blood flow of 90 mL/min/kg) but more than 3 times higher than ProCA32-P40 and showed very high exposure (> 100000 ng.h/mL blood). ProCA32.collagen1 has the terminal elimination half-life of 9.9 h that was slightly higher than ProCA32-P40 (8.09 h) with mean residence time of 14.51 h that was higher than 13.9 h of ProCA32-P40. In addition, volume of distribution (V_c) and volume of distribution at steady state (V_{dss}) were 1.53 and 1.77 L/kg, respectively, which were more than 2-7 times higher than ProCA32-P40. Taken together, these results demonstrate that the dual contrast property of ProCA32.collagen1 enables the first robust detection of early stage Ishak=3 mouse

liver fibrosis with unprecedented sensitivity and quantification of both early and late stage liver fibrosis with significant enhancement in both ΔR1 and ΔR2 that correlate well with the severity of fibrosis.

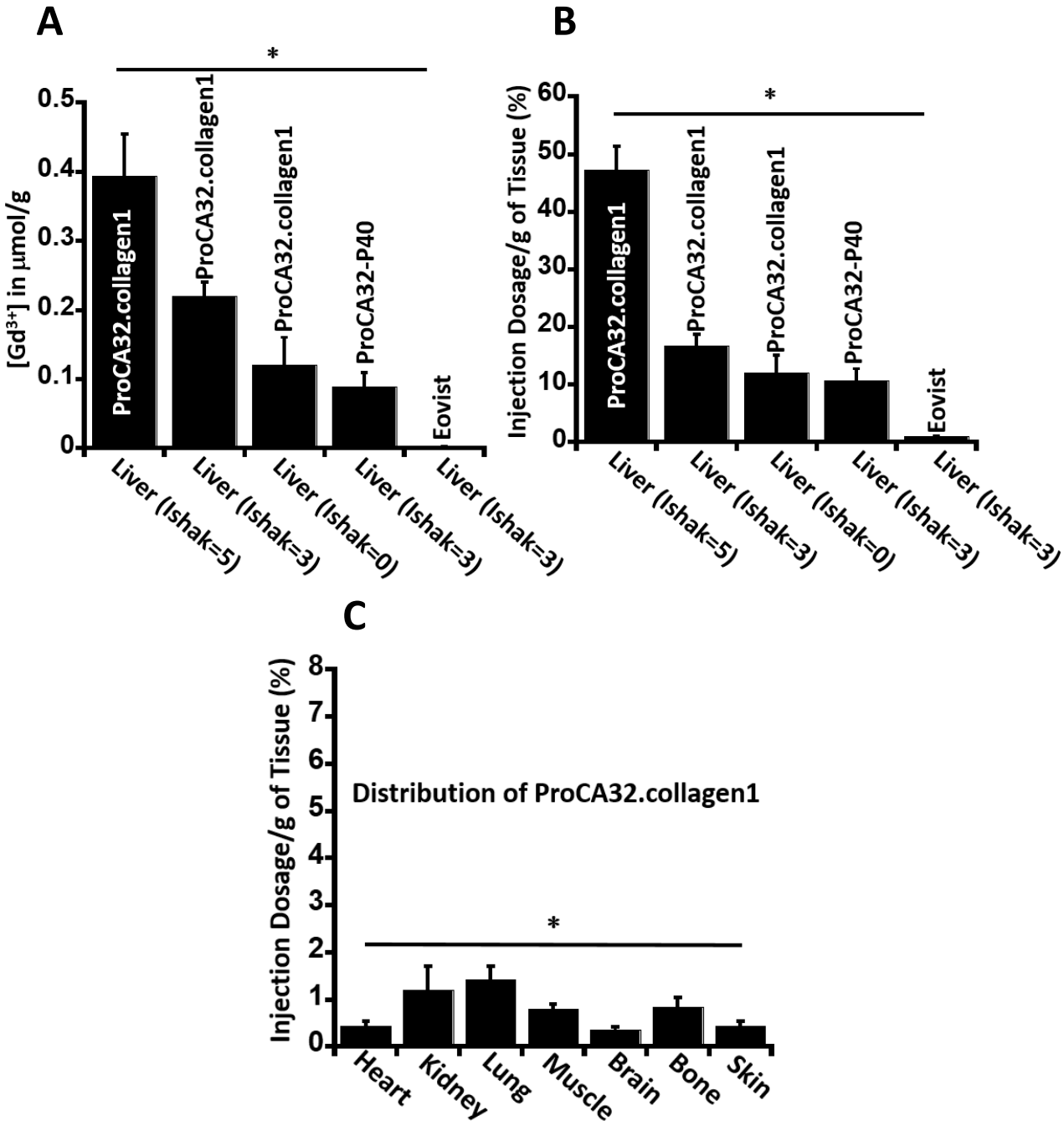

Figure 5.10 *Biodistribution analysis of contrast agents using ICP-OES.*

(A, B) *Shows percent injection dosage and [Gd^{3+}] of contrast agents, in different diseased livers. Sever fibrotic liver (Ishak=5) shows the highest Gd^{3+} concentration and injection dosage/g of tissue among other livers.* ***(C)*** *Shows percent injection dosage of ProCA32.collagen1 based on [Gd^{3+}], in other organs. ProCA32.collagen1 does not have a brain deposit possible due to lack of penetration to blood barrier.*

5.2.4 Detection of vascular and architectural alterations with dynamic molecular imaging

Here we report the first dynamic molecular imaging (DMI) as a function of time of collagen for both early and late stages of fibrosis to reveal intrahepatic angiogenesis (Fig. 5.11). The dynamic molecular imaging curve of collagen as a function of time for both early and late stage of fibrosis are very different at 3 and 24 hours (Fig. 5.5) despite the similarity for pre-injection and later time points 48-72 hrs due to excretion and washout of ProCA32.collagen1 at 48-hour post injection which both R1 and R2 enhancement for both early stage and late largely reduced to their initial values. Strikingly, at early blood pool phase 3-hour post injection of ProCA32.collagen1, R1 of cirrhotic liver increased dramatically to > 3.5 s^{-1} with $\Delta R1 > 2.0$ s^{-1} (Fig. 5.11). Furthermore, the R1 increase rate of fibrotic liver was more than 120 % suggesting vascular distortion (Fig. 5.7 A, 5.12, 5.13). Detailed histogram analysis of R1 map MRI images further shows in late stage fibrosis, different areas of the liver have heterogeneous enhancement reflecting these vessel changes at both 3 and 24 hrs post injection of ProCA32.collagen1 (Fig. 5.14). Normal liver has a symmetric Gaussian distribution of relaxivity plot consistent with sinusoid arrangement in the normal liver. On the other hand, several bi-mode or multiple-mode distributions of relaxivity also consistent with the addition of intrahepatic angiogenesis with enlarged extracellular space (Fig. 5.14). Consistently, the early stage liver fibrosis exhibits a small addition of R1. Significantly increased vessel formation stained by CD31 with quantitative analysis have also been observed

for late stage fibrosis supporting the first visualization of large vessel structure changes due to formation of severe fibrosis (Fig. 5.12, and 5.13). We further show (Fig. 5.12) the existence of the portal hypertension associated with severe fibrosis in mouse liver (Ishak=5) reflecting the targeting ability of ProCA32.collagen1 with slow washout from the liver. Thus, we have achieved the first characterization of dynamic molecular contrast profiles to distinguish different stages of liver fibrosis with differential vessel structures and distortion of the hepatic vasculatures as well as collagen expression.

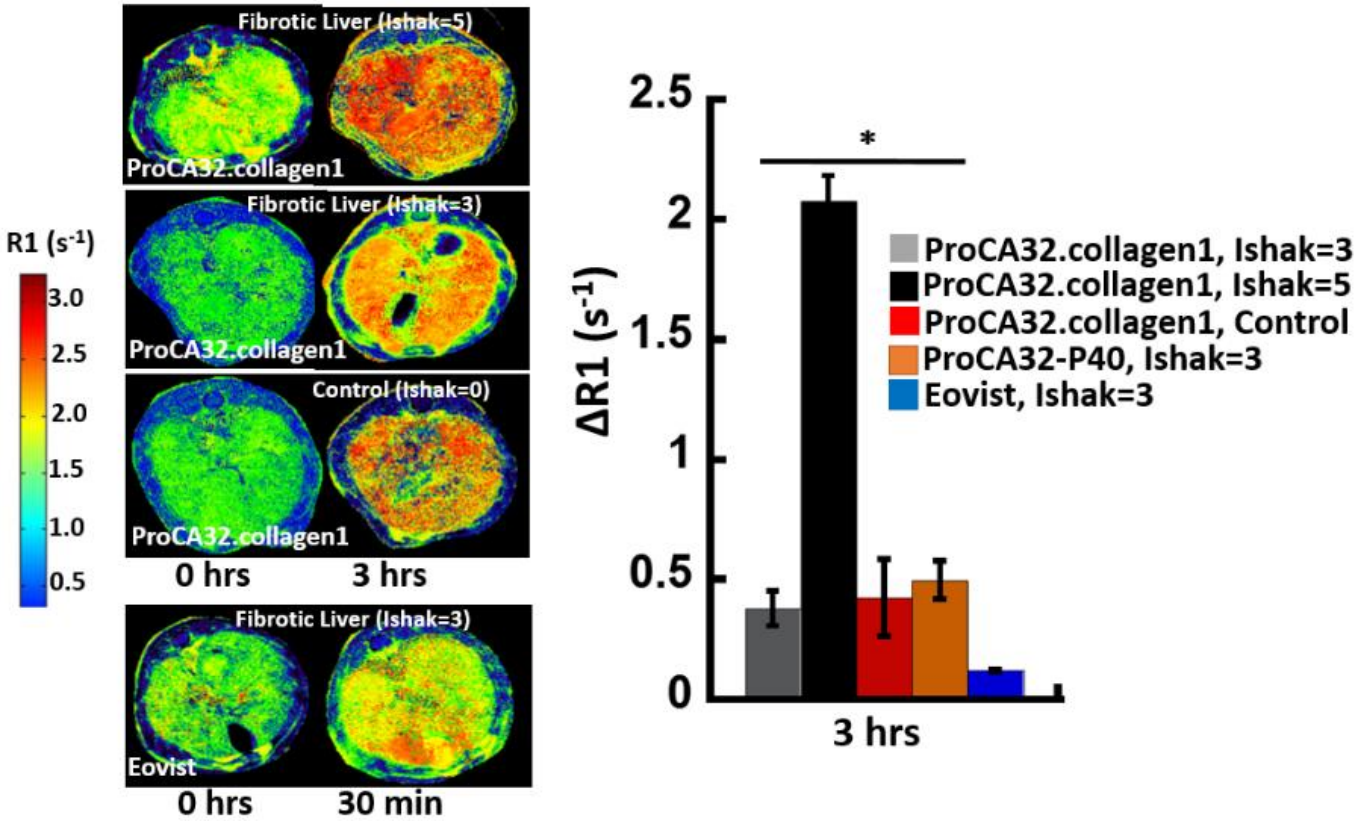

Figure 5.11 *Detection of vasculature structural changes during late stage fibrosis with ProCA32.collagen1.*

Demonstrates the R1 map of fibrotic (Ishak=3), normal (Ishak=0) and cirrhotic liver (Ishak=5) before and 3 hrs after injection of ProCA32.collagen1 and Eovist. ΔR1 values of fibrotic (Ishak=3, and 5) and normal (Ishak=0) liver 3 hours after injection of ProCA32.collagen1 and 30

min for Eovist shows the capability of ProCA32.collagen1 in detecting and revealing the vascular distortion occurring in severe fibrosis as ΔR1 has the highest value compared to early stage and normal liver.

As it is observed from Fig. 5.12, normal liver sinusoidal endothelial cells (SEC) have fenestrae and express SE-1 marker but not CD31, however, in late stage of fibrosis, SEC upon activation lose fenestrae and these defenstrated SECs do not express SE-1 and they express CD31 (Fig. 5.13). Defenestration of SECs lead to portal hypertension since the blood entering to the liver cannot go to central vein as the blood flow out of the liver is significantly lowered. In late stage fibrosis, intrahepatic angiogenesis occurs which does not increase blood flow, but blood has to flow through more capillaries to reach same central vein which still does not increase portal flow but creates more resistance, therefore after 3 hrs post injection, ProCA32.collagen1 is revealing sinusoidal remodeling, and portal-vein blood flow resistance which has not been reported by any MRI contrast agent before.

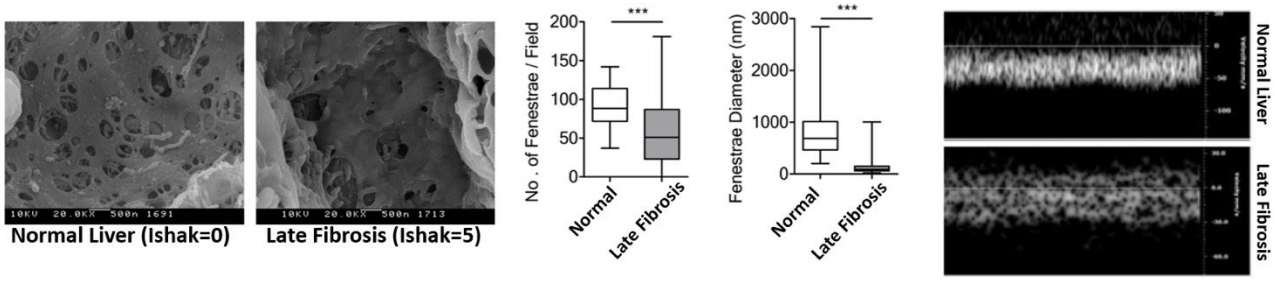

Figure 5.12 *Representative SEM images and ultrasound of sections from mice with normal and severe fibrotic liver (Figure provided by Ravi Chakra).*

Representative SEM images of sections from mice with late stage cirrhotic liver (Ishak=5). Quantitation of number and size of fenestrations of liver sinusoids in mice with late stage cirrhotic liver (Ishak=5) measured by manually counting/measuring number and the diameters of fenestration in the SEM images confirm vasculature structural changes detected by

ProCA32.collagen1. Fenestration size is average diameters (in micro Meter) of fenestrate from the SEM image analyses. Velocity of portal vein blood flow is measured by Doppler ultrasound imaging shows high portal hypertension detected at 3 hrs after injection of ProCA32.collagen1. The flow velocity is presented as mm per second.

In Fig. 5.13, it is shown that CD31 is highly expressed in late stage fibrosis which is a confirmation for intrahepatic angiogenesis.

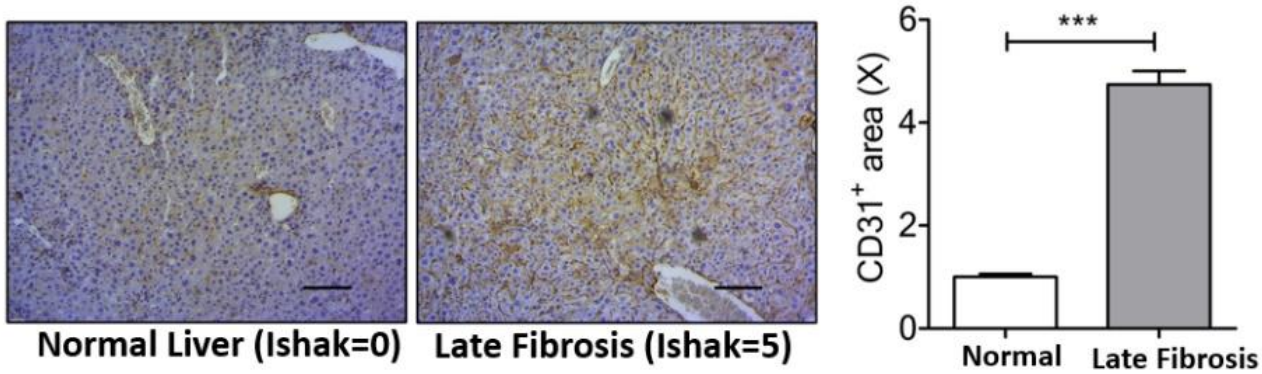

Figure 5.13 *Representative images of IHC stains of CD31 and quantitation of CD31.*

IHC stains of liver tissue in mice with late stage cirrhotic liver (Ishak=5) confirming intrahepatic angiogenesis. The quantity of CD31 IHC is presented fold changes in CD31 stains compared to that of non-fibrotic mice (normal) (Figure provided by Ravi Chakra).

As Fig. 5.14 demonstrates, histogram analysis performed by MATLAB is showing different patterns of enhancement in normal liver and early and late stage fibrotic livers based in different time points (3 hrs, and 24 hrs) post injection of ProCA32.collagen1. Furthermore, it shows heterogenous distribution of voxels across livers demonstrating a wide range of R1 values.

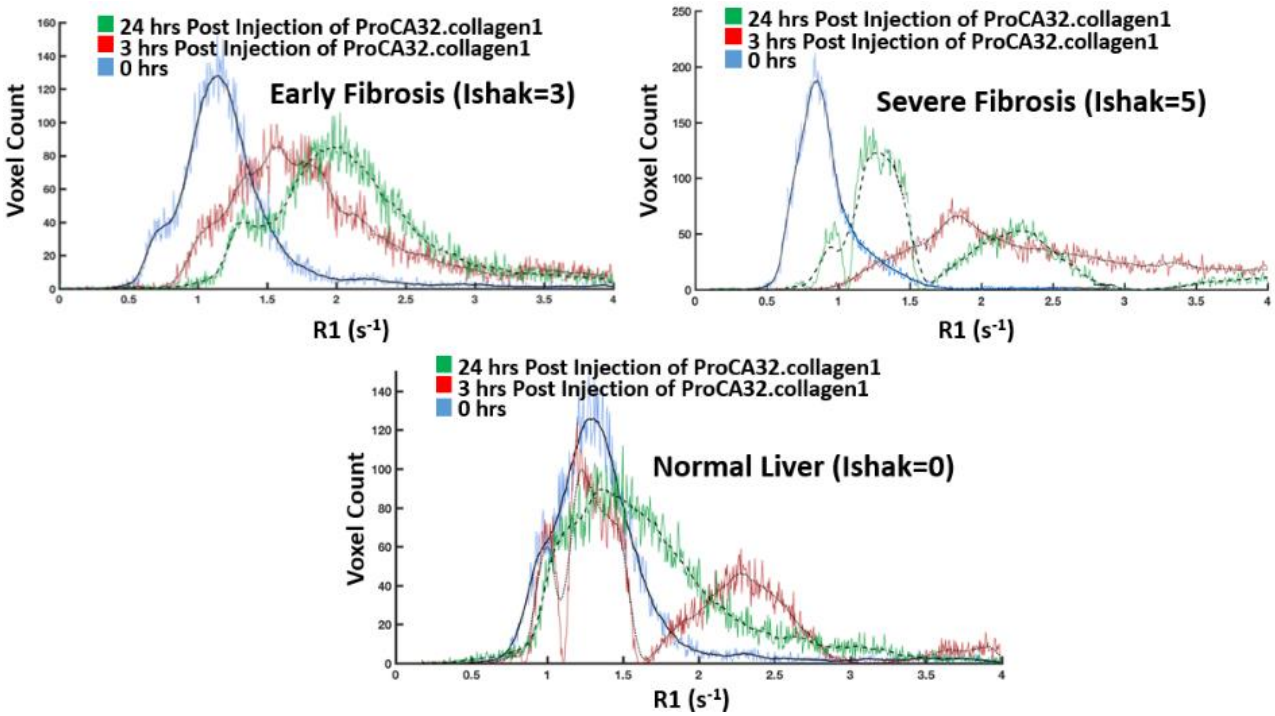

Figure 5.14 *R1 map histograms analysis of mouse livers.*

R1 map histograms analysis of early stage (Ishak=3), late stage fibrosis and normal liver (Ishak=0) pre (blue) and 3 hrs (red) and 24 hrs (green) post injection of ProCA32.collagen1 in TAA/alcohol-induced fibrosis mouse model demonstrates the dynamic ability of ProCA32.collagen1 in revealing both heterogeneity and vascular distortion of severe liver fibrosis

5.2.5 Quantitative mapping of liver fibrosis heterogeneity

Liver fibrosis heterogeneity can be regarded as one of the major limitations of liver biopsy and other imaging modalities since it has differential special distribution and also dependent on animal models and causes [303-306]. We then address liver fibrosis heterogeneity induced by both TAA and DEN byProCA32.collagen1 enabled molecular imaging (Fig. 5.15). This DEN-induced late stage cirrhosis mouse model exhibits strong liver heterogeneity mimicking patient cirrhosis [307, 308]. Fig. 5.16 show that right segment of the mouse liver has CPA of 12% (Sirius

red staining) while left segment has CPA of 6.7%. Consistent with TAA/alcohol model, both T_1-, T_2-weighted and T1 inversion recovery images have enhancement of cirrhotic liver 3 and 24 hours post injection of ProCA32.collagen1 with the maximum enhancement at 3 hours post injection specifically at the right segment of the liver confirming the histology data (Fig. 5.17). Histogram analysis of the MRI images show different heterogeneous distribution of voxels in MRI based on different pulse sequences (Fig. 5.18). In addition, R1 map data demonstrate further heterogeneity in the liver (Fig. 5.19.)

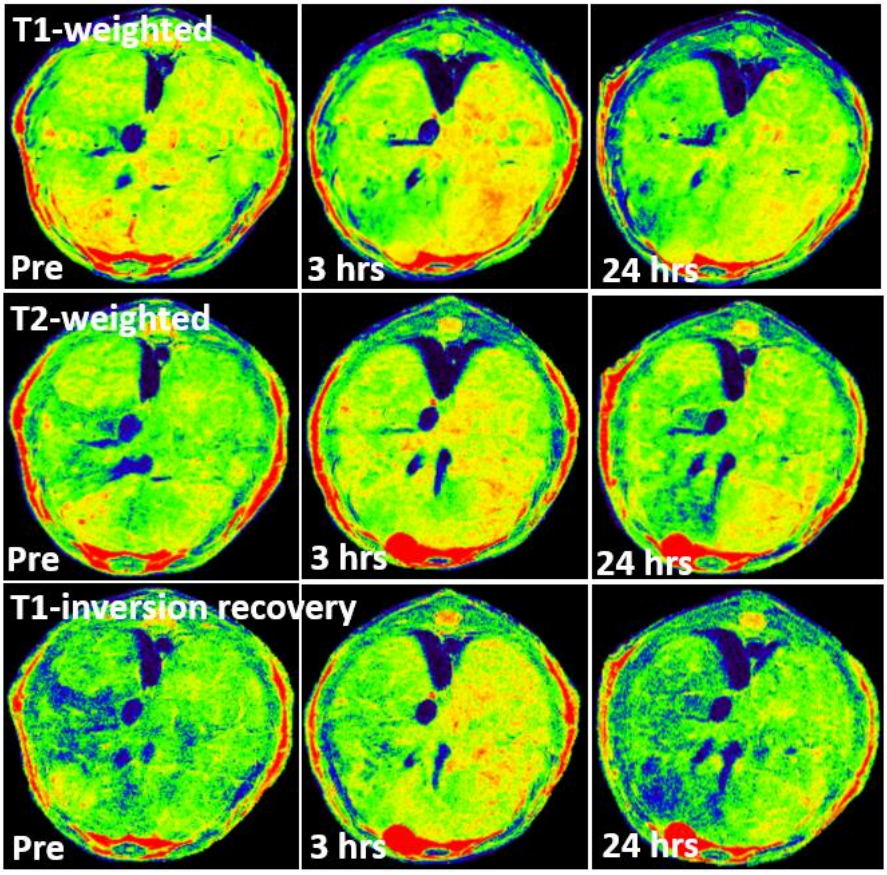

Figure 5.15 *Mapping liver cirrhosis heterogeneity with ProCA32.collagen1.*

T_1, T_2-weighted and T1 inversion recovery images of DEN-induced cirrhotic mouse liver before and 3 and 24 hrs post injection of ProCA32.collagen1 demonstrating heterogeneity of liver in the right segment.

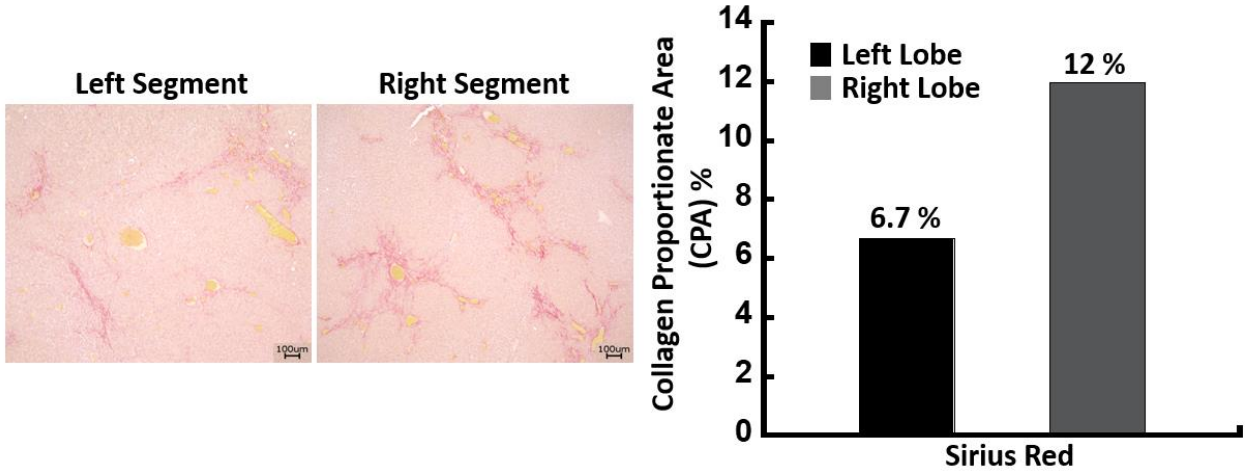

Figure 5.16 *Sirius red staining and collagen proportionate area analysis.*

Sirius red staining and collagen proportionate area analysis confirm that the right segment is more cirrhotic than the left region which correlates with MRI.

Contrast to noise ratio (CNR) analysis of different pulse sequences demonstrate the right segment enhancement compared to left segment which is in agreement with histology and CPA analysis. Moreover, as shown in Fig. 5.18, histogram analysis also confirms the heterogenous distribution of voxels in the liver correlating with MRI data.

R1 map analysis of DEN-induced liver cirrhosis also demonstrates heterogeneity of liver as shown in Fig. 5.19. In addition, histogram analysis performed for R1 map further confirms the data.

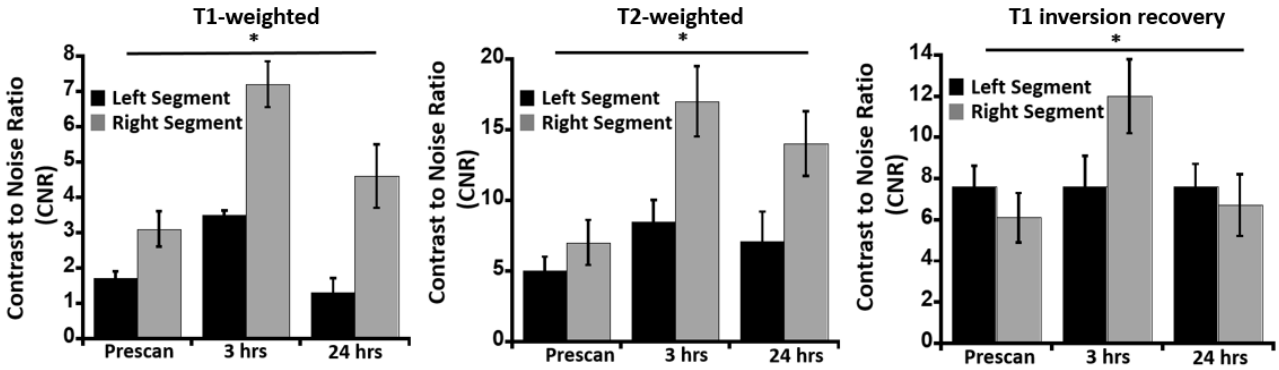

Figure 5.17 *Quantitative analysis of contrast to noise ratio of liver.*

T_1, T_2-weighted and T_1-inversion recovery images all demonstrate a higher contrast to noise ratio (CNR) of right segment of cirrhotic liver after 3 hours of ProCA32.collagen1 injection compared to left segment.

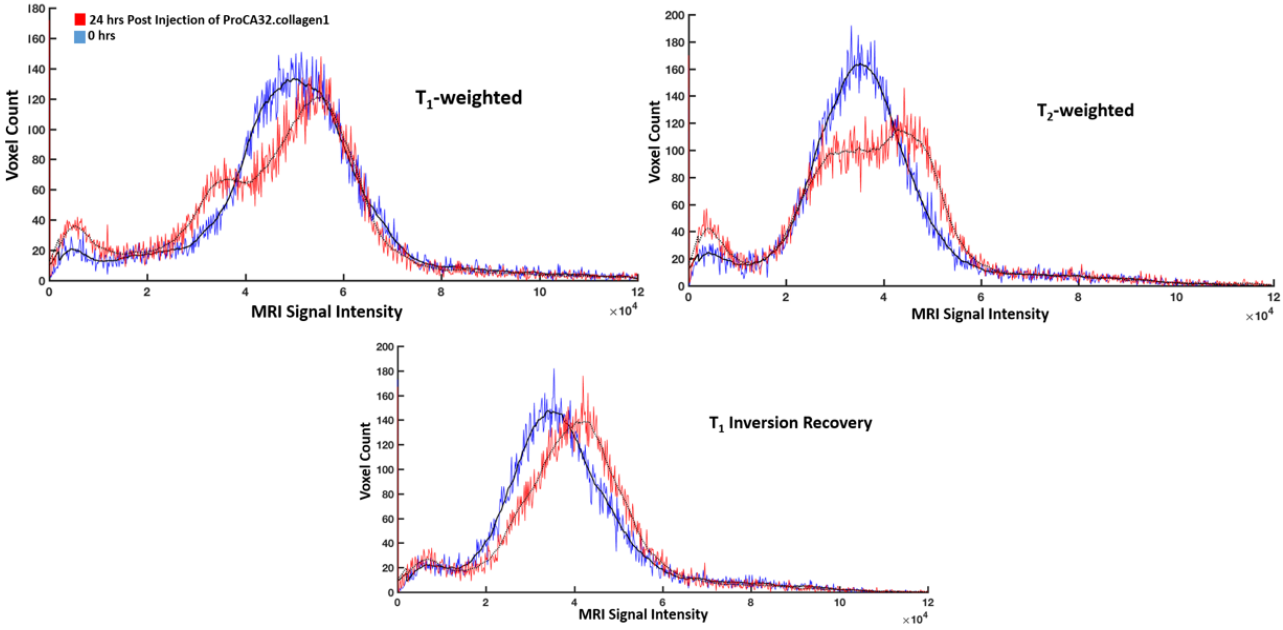

Figure 5.18 *Histogram analysis of DEN-induced cirrhotic liver.*

Histogram analysis of DEN-induced cirrhotic liver pre (blue), 3 hrs (red) and 24 hrs (green) post injection of ProCA32.collagen1.

Taken together, further analysis of DEN-induced cirrhotic liver shows that ProCA32.collagen1 is capable of a time-dependent heterogenous enhancement of liver with specific areas of liver highlights at 3 hrs and 24 hrs and specific areas that remained enhanced or washed out at different time points. Similarly, detailed analysis of R1 map MRI images of TAA/alcohol model in late stage fibrosis, different areas of the liver have heterogeneous enhancement reflecting vessel changes at both 3 and 24 hrs post injection of ProCA32.collagen1.

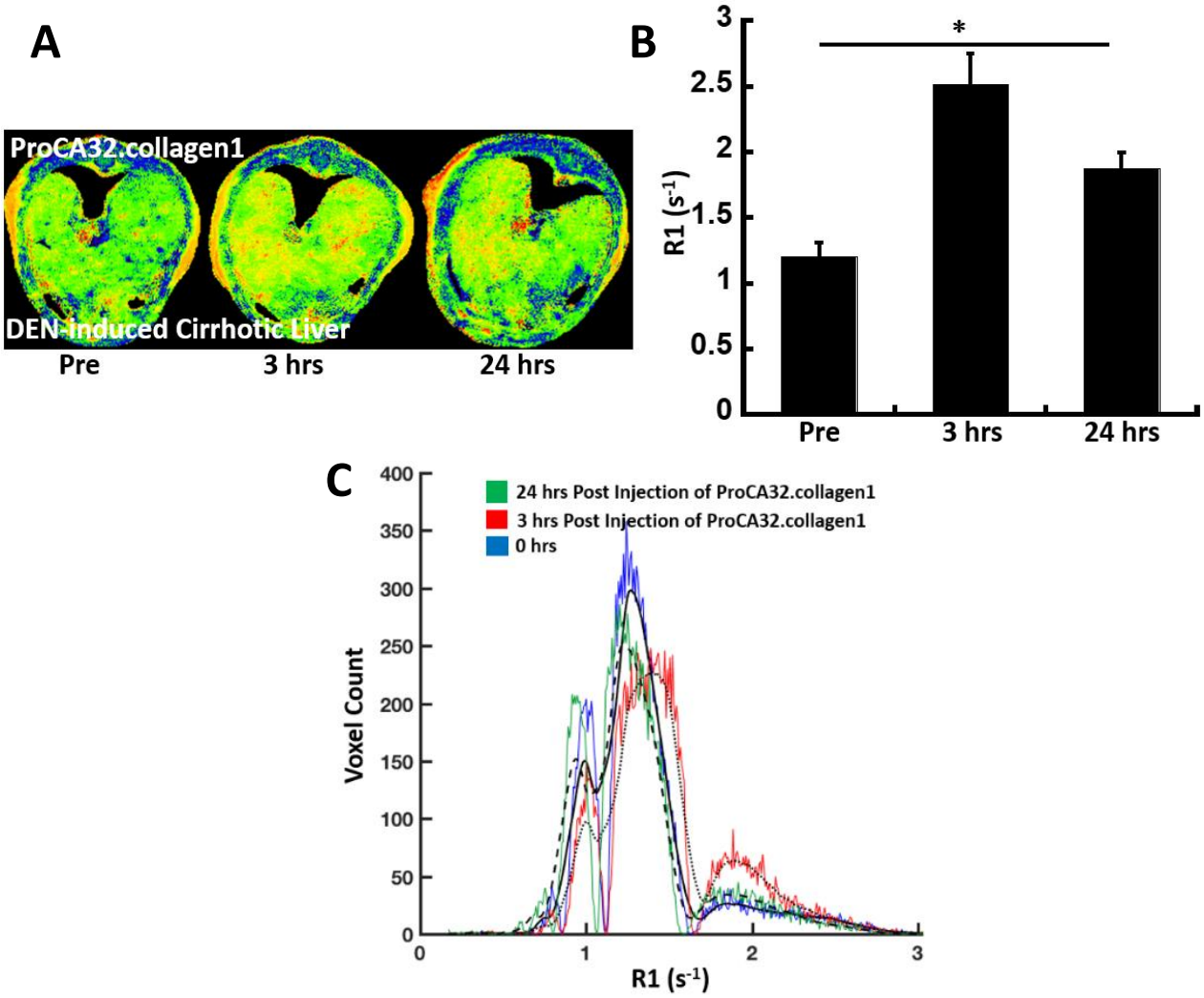

Figure 5.19 *R1 map analysis of DEN-induced liver cirrhosis.*

(A) *R1 map results showing heterogeneity in DEN-induced liver cirrhosis 3 and 24 hours post injection of ProCA32.collagen1.* ***(B)*** *Quantitative analysis of R1 values showing a significant increase in 3 hours post injection as well as showing heterogeneity.* ***(C)*** *Histogram analysis of DEN-induced cirrhotic liver pre (blue), 3 hrs (red) and 24 hrs (green) post injection of ProCA32.collagen1 (* $P < 0.05$, *student's t-test).*

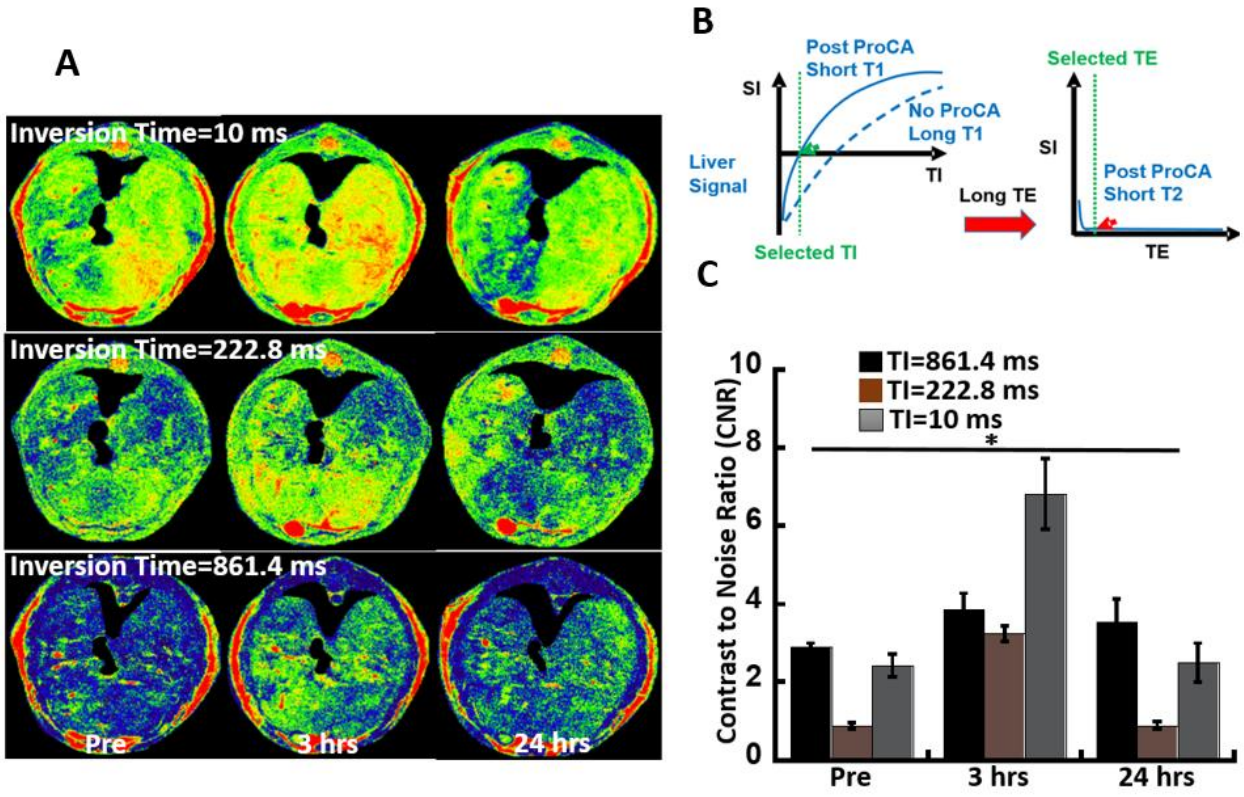

Figure 5.20 *Combination of STIR with long TE methodology with a T1-T2 MRI contrast agent.*

(A) *T1 inversion recovery at different inversion times showing different heterogeneity of cirrhotic liver.* ***(B)*** *Schematic demonstration of STIR with long TE methodology with ProCA32.collagen1. ProCA32.collagen1 has high accumulation in the liver. As a result, liver has shortened T1, first, inversion time was used to suppress liver signal. Second, since liver also has short T2, we then use long TE to further suppress the liver signal.* ***(C)*** *Contrast to noise ratio (CNR) of cirrhotic liver before, 3 and 23 hours after injection of ProCA32.collagen1 at different inversion times (*P < 0.05, student's t-test).*

Figure 5.20 shows one of the advantages of combining T1 inversion recovery with a dual mode contrast agent like ProCA32.collagen1. We applied this pulse sequence which is STIR (short tau inversion recovery) with long TE and combined it with ProCA32.collagen1 and studied its

effects in contrast to noise ratio in DEN-induced mouse model of cirrhotic liver. It is observed that ProCA32.collagen1 combined with this imaging methodology can enhance different regions of cirrhotic liver at different time points (3 hrs and 24 hrs) by changing inversion times (TI) which can suppress the liver signal.

5.2.6 Immunofluorescence staining of fibrotic liver

In order to further confirm the targeting capability of ProCA32.collagen1, the contrast agent was co-stained with collagen type I in fibrotic liver. For this purpose, frozen sections of liver tissues were collected. Then the tissues on slides were fixed with either ethanol or methanol in -20°C for 20 minutes to remove OCT which is a gel-like medium for embedding the tissues.

After the tissues were dried, the blocking buffer is added for 2 hours at room temperature. Then the slides are washed with 1×TBST for once, and the primary antibody is added (Collagen type I) with 1:50 or 1:200 dilution and left for incubation in 4°C overnight. The slides are washed again with 1×TBST for three times, each time for 5 min. The second primary antibody is then added (ProCA32.collagen1) with 1:50 dilution for 2 hours at room temperature.

In the next step, the slides are washed again three times, and secondary antibody is added for both of the primary antibodies (anti goat) and left for 1 hour at room temperature. Then DAPI is added to the slides and they are covered with glass and left at 4°C until they are dried.

As Fig. 5.21 demonstrates, left picture shows fibrotic liver which was injected with ProCA32.collagen1. It is observed that ProCA32.collagen1 (red) is targeting collagen type I (green) in the liver, however, on the right picture, the fibrotic liver injected with ProCA32-P40 is shown. In this picture, there is no sign of the contrast agent which confirms its lack of targeting collagen type I.

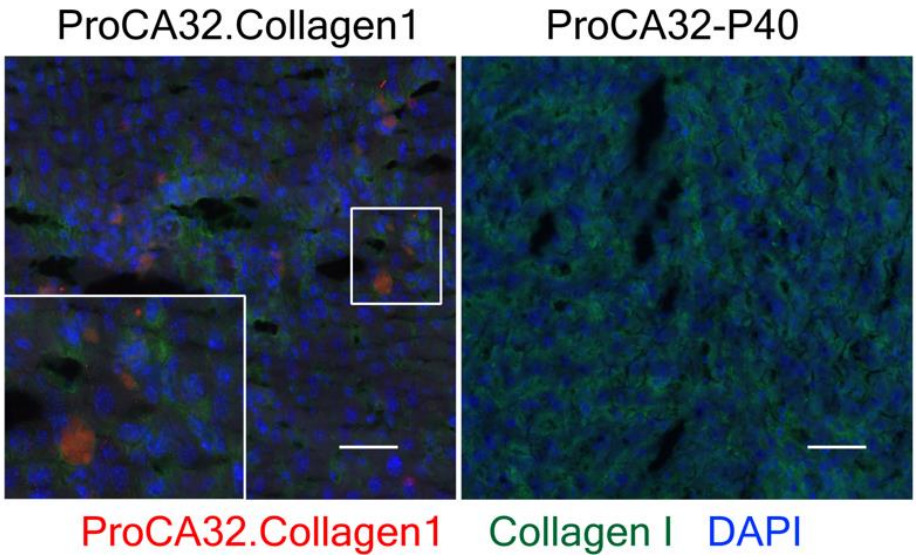

Figure 5.21 *Immunofluorescence staining of ProCA32.collagen1 and collagen type I in fibrotic liver tissues. Fibrotic liver injected with ProCA32.collagen1 clearly demonstrates that ProCA32.collagen1 (red) can target collagen type I (green) in liver, however, ProCA32-P40 does not show any targeting capability as it cannot be detected by Immunofluorescence staining in fibrotic liver.*

5.2.7 Treatment monitoring of liver fibrosis with ProCA32.collagen1

Since liver fibrosis can be treated and reversed if detected early and several drugs are under development for treatment of liver fibrosis, and clinical contrast agents cannot follow up and monitor treatments, it is extremely crucial to design MRI contrast agents capable of treatment monitoring.

Therefore, ProCA32.collagen1 was tested for treatment monitoring of late stage liver cirrhosis using ProAgio drug. ProAgio is a protein-based drug derived from domain 1 of CD2 protein developed by our collaborator Dr. Zhi-Ren Liu, and it has shown promising results for

reversal of late stage cirrhosis. We injected ProCA32.collagen1 to mice treated with ProAgio and mice with normal liver to assess the capability of the contrast agent in distinguishing drug treated liver from normal liver (Fig. 5.22).

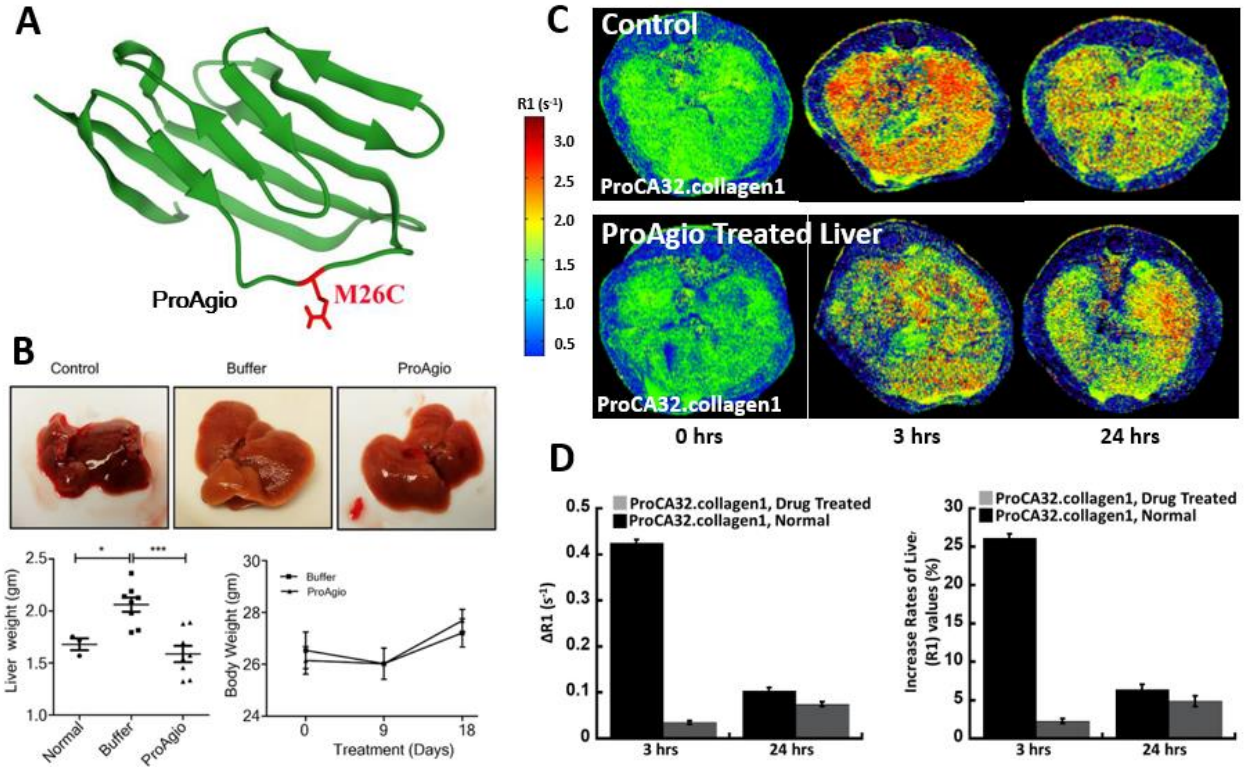

Figure 5.22 *Liver cirrhosis treatment monitoring using ProCA32.collagen1.*

(A) ProAgio structure with M26C mutation for treatment of liver cirrhosis. (B) ProAgio can reverse liver cirrhosis as observed by decrease in liver weight. (C) R1 map MRI results before and 3 and 24 hrs post injection of ProCA32.collagen1 is able to show the difference between ProAgio treated liver and normal liver at 3 hrs time point. (D) Quantitative analysis of ΔR1 at 3 and 24 hrs after injection of ProCA32.collagen1 is showing that normal liver has significant increase at 3-hour time point, however ProAgio treated liver does not show any enhancement.

As Fig. 5.22 C and D are showing, at 3-hour time point, ProCA32.collagen1 is able to show the different between ProAgio treated liver and normal liver. At 3 hours post injection, ProCA32.collagen1 is causing a dramatic increase in ΔR1 values, however, drug treated liver does not show any increase suggesting that the contrast agent is being washed our rapidly from the liver. The normal liver R1 value increased to more than %25 at 3 hours but ProAgio treated liver increased only %2.

5.2.8 Dynamic multi-color mapping of liver cirrhosis heterogeneity with ProCA32.collagen1

Since we observed a dynamic property in ProCA32.colllagen1 in enhancement of DEN-induced mouse liver cirrhosis, a multi-color heterogenous cirrhotic mouse liver was created in order to better reflect the liver enhancement at different time points (3 hrs and 24 hrs). For this purpose, MATLAB was used to create a multi-color map with voxel by voxel quantitative analysis. Since ProCA32.collagen1 has both r_1 and r_2 property and we scanned multiple pulse sequences, and this approach was used in both T2-weighted and T1 inversion recovery sequences. Two general color maps were generated for T2-weighted pulse sequence. First, a color map was created to summarize and demonstrate the voxels that enhanced 3 hrs and 24 hrs post injection of ProCA32.collagen1 and then a percentage of relative enhancement was calculated using this equation: Intensity (post) – Intensity (pre) / Intensity (pre). Figure 5.23 shows the T2-weighted color map 3 and 24 hrs post injection enhancement of ProCA32.collagen1. Then a separate color map was generated to show the regions that stayed enhanced after 24 hrs and the areas that washed out after 24 hrs (Fig.5.24). In figure 5.24, the color bar shows the percentage of areas that maintained up to %200 and the regions that washed out completely within 24 hrs.

The same procedure was performed for T1 inversion recovery and T1-weighted pulse sequences.

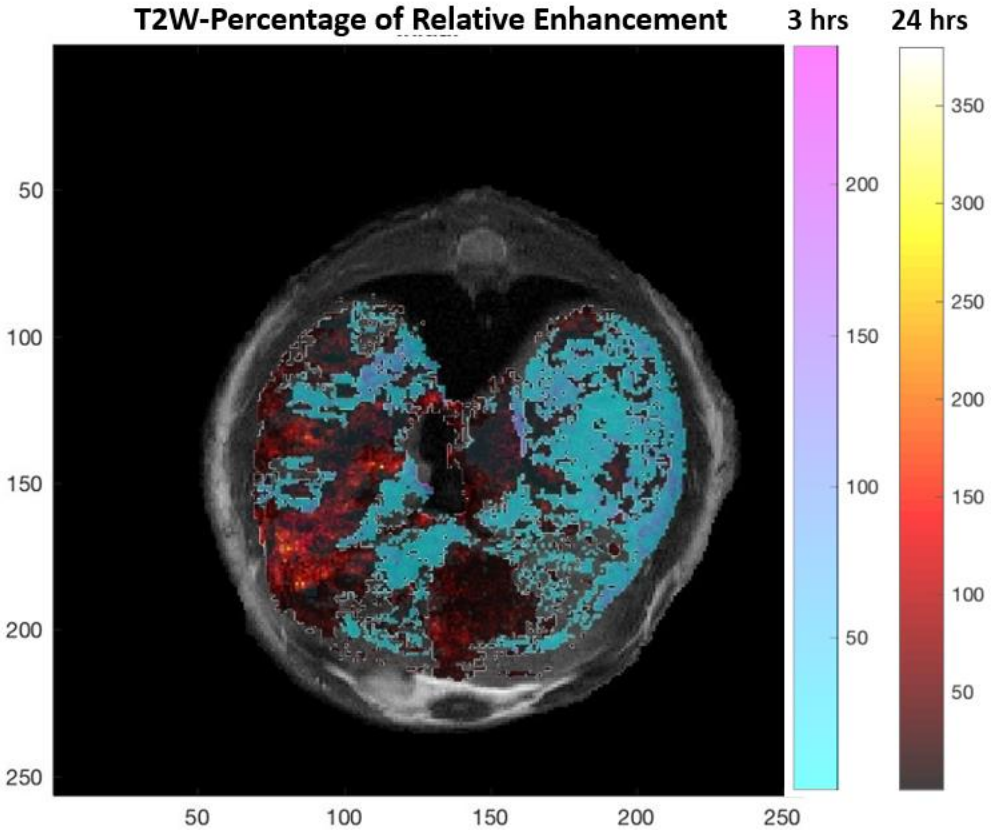

Figure 5.23 *T2-weighted Multi-color map of 3 and 24 hrs enhancement in DEN-induced cirrhotic mouse liver.*

The color map demonstrates the dynamic enhancement of cirrhotic regions 3 (blue) and 24 (red) hrs post injection of ProCA32.collagen1. Right segment of liver is enhanced more at 3 hrs and left segment was enhanced more at 24 hrs. The bar on the right shows the percentage of relative enhancement.

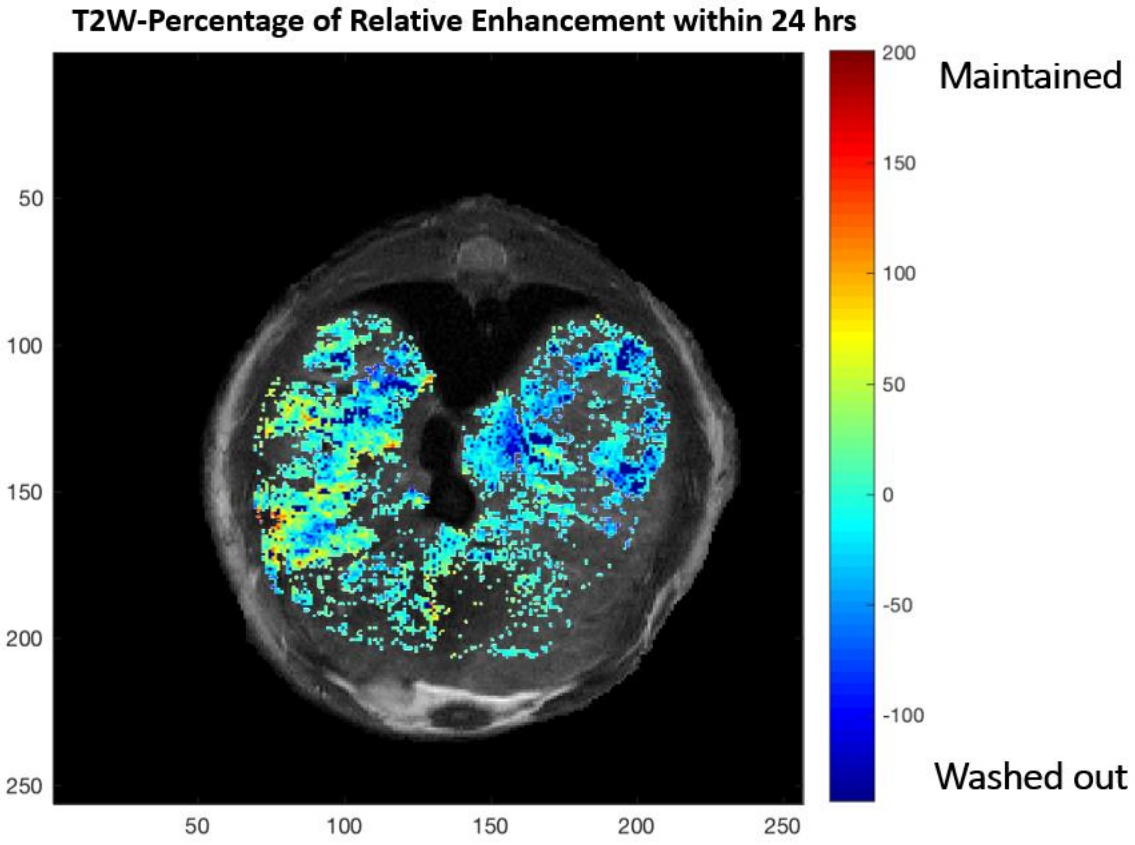

Figure 5.24 *T2-weighted Multi-color map of maintained vs washed out within 24 hrs of contrast agent injection in DEN-induced cirrhotic mouse liver.*

The color map demonstrates the dynamic enhancement of cirrhotic regions within 24 hrs, and the areas that the contrast agent remained in the liver are shown in a red color and the areas that the contrast agent is washed from the liver are shown in more blue color. The bar on the right shows the percentage of relative enhancement.

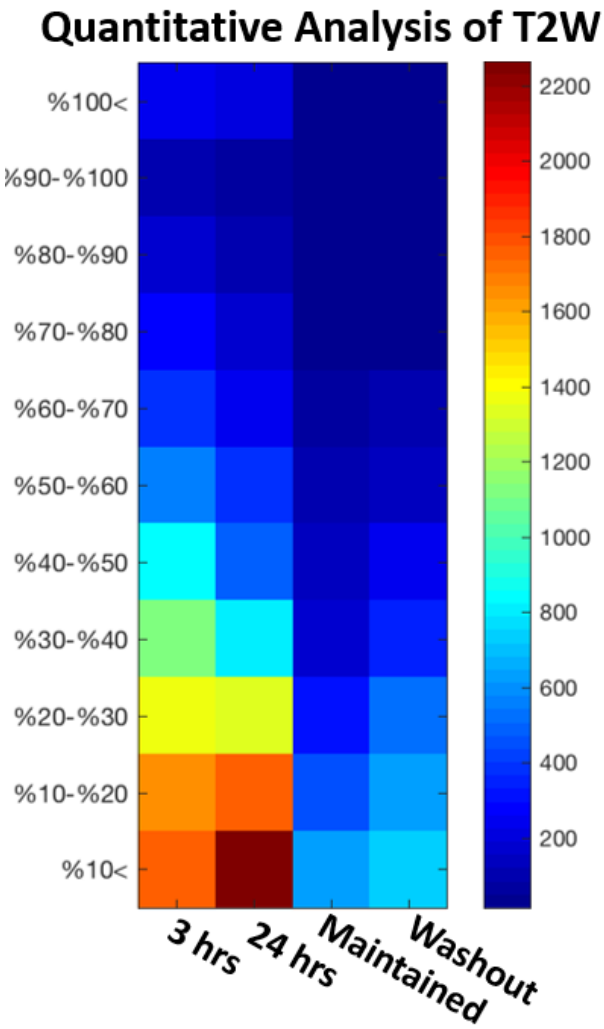

Figure 5.25 *Quantitative analysis of T2-weighted cirrhotic liver enhancement post injection of ProCA32.collagen1.*

The bar on the right represents the voxel number which different parentage of increase at different time points. For instance, at 3 hrs, approximately, 1600 voxels had enhancement of less than %10.

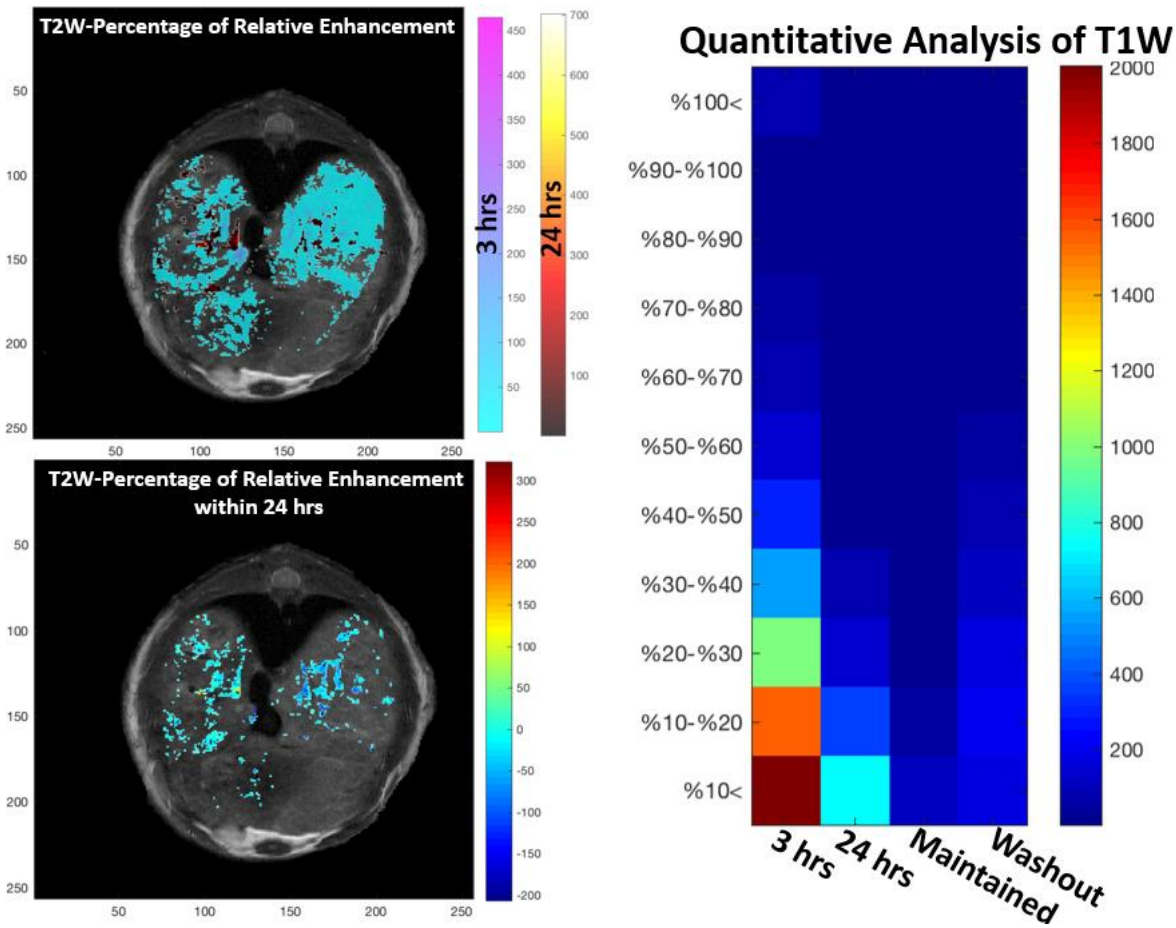

Figure 5.26 *T1-weighted Multi-color map and quantitative analysis of maintained vs washed out regions within 24 hrs of contrast agent injection in DEN-induced cirrhotic mouse liver.*

This is the summary of T1-weighted images demonstrating dynamic property of ProCA32.collagen1. At each time point, different regions of liver are enhanced.

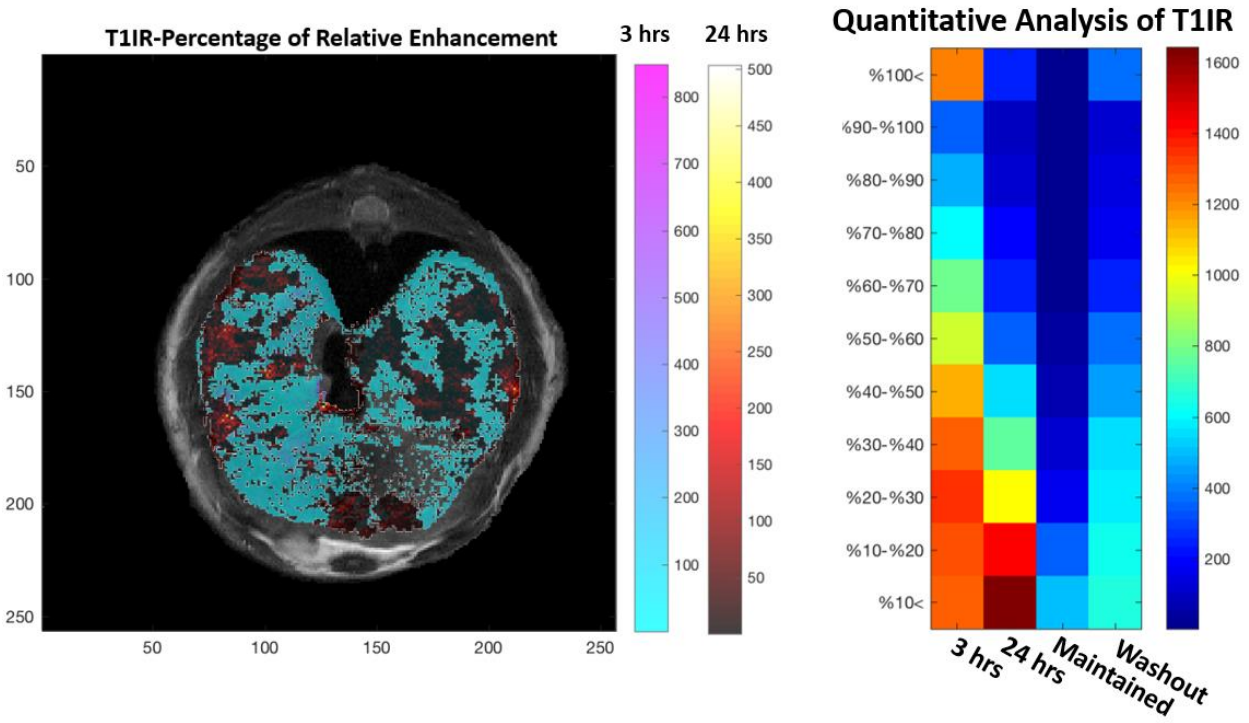

Figure 5.27 *T1 inversion recovery Multi-color map and quantitative analysis of 3 and 24 hrs post injection of ProCA32.collagen1.*

The color map demonstrates the dynamic enhancement of cirrhotic regions 3 (blue) and 24 (red) hrs post injection of ProCA32.collagen1. In contrast to T2-weighted sequence, areas of enhancement at each time point are limited more to right or left segments of liver and are spread across the liver.

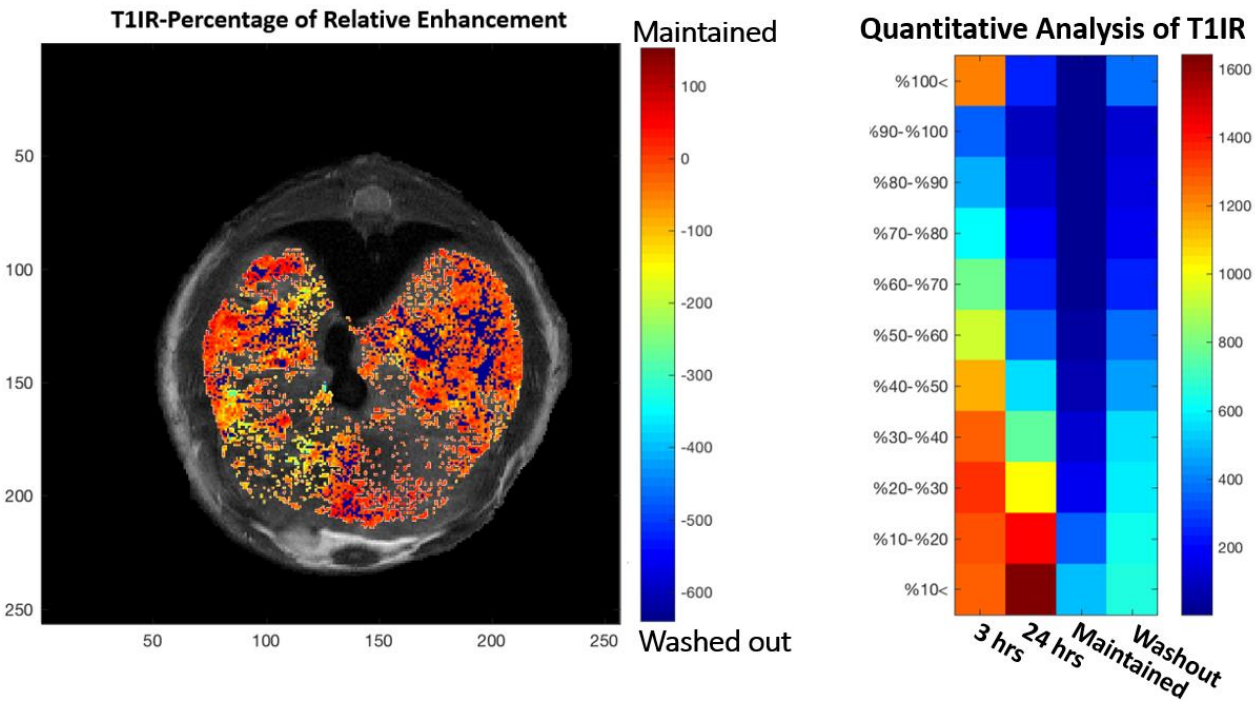

Figure 5.28 *T1 inversion recovery Multi-color map of maintained vs washed out within 24 hrs of contrast agent injection in DEN-induced cirrhotic mouse liver.*

The color map demonstrates the dynamic enhancement of cirrhotic regions within 24 hrs, and the areas that the contrast agent remained in the liver are shown in a red color and the areas that the contrast agent is washed from the liver are shown in more blue color. The bar on the right shows the percentage of relative enhancement.

5.3 Discussion

Liver fibrosis heterogeneity currently cannot be accurately detected by any methods. Spatial heterogeneity in fibrosis is one of the major limitations and challenges of liver biopsy and elastography-based techniques as they sample a small volume of liver which does not accurately reflect the overall extent and stage of fibrosis [306]. Collagen type I is an important target for molecular imaging of liver fibrosis since its accumulation is a characteristic of most types of chronic liver diseases (CLD) [290].

5.3.1 Implication for early detection: Our developed contrast agent enabled novel imaging methodology for early detection of liver fibrosis.

Early fibrosis can be reversed if it is detected early [309, 310]. However, current techniques including Fibroscan and MRE as well as MRI with clinical contrast agents in the market failed to detect fibrosis at early stage despite of rapid progress [311]. To overcome the limitation of small chelator-based contrast agents for detection of early stage fibrosis, targeting extracellular matrix (ECM) proteins with probes in molecular imaging techniques has attracted great attention for detection, monitoring disease progression as well as treatment [312]. Type I collagen is immediately secreted into the ECM as soon as the hepatic stellar cells are activated at the very early stage. Its expression level and spatial distribution patterns play important role for the ECM remodeling and directly reflect fibrosis progression. Elastin, on the other hand, is more involved in the late stage fibrosis and cirrhosis [313]. Collagen targeting molecular magnetic resonance imaging demonstrates a unique application of MR technology to view biological processes at the cellular and molecular level. [314], [122], [315]. However, recent works reported that collagen targeting MRI contrast agents have more sensitive than other MRI techniques including using

endogenous relaxation times, diffusion, and magnetization transfer measurements [283], however, have limited capability in monitoring early stage of fibrosis in a rat DEN model.

We have shown that early stage liver fibrosis (stage 3 based on Ishak and CPA analysis) can be detected using both R1 map and R2 (24 hours post injection). The detected MRI signals for both early and late stages are correlated well to those from histology analysis from CPA and further validated by Gd^{3+} contention detection with ICP-OES.

Our developed protein-based MRI agent with collagen type I targeting moiety ProCA32.collagen 1 can have robust detection of early stage of liver fibrosis with large dynamic range with dramatic increased sensitivity.

We have shown that ProCA32.collagen1 exhibits 5-fold increase in r_1 relaxivity that clinical approved ones including Magnevist, and liver specific reagents such as MultiHance and Evoist. More importantly, ProCA32.collagen1 also has a high r_2 value that enables application of several imaging methodologies including both T1 and T2 imaging to overcome the subtle changes of liver morphology without defined boundary at early stage liver fibrosis. More importantly, the precision is doubled. In contrast to the risk to trade off targeting capability and relaxivity reported by previously reported studies, here we demonstrate that we can further increase relaxivity properties for both r_1 and r_2 since ProCA32.collagen1 has higher relaxivity compared to ProCA32-P40. Previously we have shown that the addition of targeting moiety to ProCA32 does not have a reduction of the relaxivity, a problem associated with the addition of targeted capability [316]. Here, we attribute the additional contribution of water from outer-sphere to the relaxivity by PEGylation at nearby Lys sites to the increase of relaxivity of ProCA32.collagen1 compared to ProCA32-P40. Second, ProCA32.collagen1 also exhibits the highest binding affinity to collagen type I (Kd of 1.4 μM) among all other imaging agents available [121] likely due to the proper

design of the targeting moiety. This strong binding affinity to collagen type I provides required sensitivity to detect early stage of secreted collagen in liver (1–20 $nmolg^{-1}$) [313]. Third, ProCA32.collagen1 has a unique tissue penetration as revealed by its capability in distinguishing early and late stage fibrosis at 24-hour time point which correlates well with CPA quantification in histology.

ProCA32.collagen1 has the organ distribution and retention time required by the new dynamic molecular imaging capability for temporal and spatial resolution of intrahepatic angiogenesis, portal hypertension and liver heterogeneity. The PK/PD studies have shown ProCA32.collagen1 has a relatively high volume of distribution and vascular confinement and very high exposure (> 100000 ng.h/mL of blood) which is superior than clinical contrast agents like Magnevist and even ProCA32-P40 demonstrating its targeting capacity.

5.3.2 Implication for detection of heterogeneity, intrahepatic angiogenesis and portal hypertension

Liver fibrosis heterogeneity and the process for the formation of liver fibrosis currently cannot be accurately detected by any methods. Spatial heterogeneity in fibrosis is one of the major limitations and challenges of liver biopsy and elastography-based techniques as the lack of whole liver volume coverage cannot accurately reflect the overall extent and stage of fibrosis[306]. Collagen type I is heterogeneously accumulated in liver fibrosis depending on etiology which leads to fibrosis that disrupts liver cytoarchitecture and function [293].

Normal liver sinusoidal endothelial cells (SEC) have fenestrae and express SE-1 marker but not CD31, however, in late stage of fibrosis, SEC upon activation lose fenestrae and these defenestrated SECs do not express SE-1 and they express CD31. Defenestration as can be seen from SEM images lead to portal hypertension in late stage fibrosis since the blood entering to the

liver cannot go to central vein as the blood flow out of the liver is significantly lowered. In late stage fibrosis, vascular remodeling leading to capillarization of the sinusoids with generation of intrahepatic shunts creates hepatic angiogenesis which contributes to the progression of the disease[317]. Angiogenesis is also a key event in the emergence and recognition of early HCC and development of recurrence after potentially curative therapy and for the progression of liver cancer [318-320]. Observation of such process has only reported via histological staining and is not possible to be detected by any noninvasive methods. Early studies reported that in most cases MRI can detect morphological characteristics of liver cirrhosis including surface nodularity, widening of fissures, expansion of the gallbladder fossa, notching and atrophy of the right lobe, and relative enlargement of the lateral segments of the left lobe and caudate lobe, in some cases however, cirrhotic liver can appear completely normal with confirmation of the diagnosis requiring biopsy [307, 308].

Here we report that ProCA32.collagen1 is also able to detect intrahepatic angiogenesis, portal hypertension and map heterogeneity via DMI. Dynamic contrast enhancement (DCE) is largely applied to report the cellular and tissue changes of various diseases and the responses upon drug treatment [321-323]. However, dynamic molecular contrast imaging was not achieved due to several major limitations of reported contrast agents. In addition to lack of targeted contrast agents with required sensitivity, DMI also requires targeted contrast agents to have adequate penetration and retention time to liver tissue to report the formation of new vascular structures. Detailed histological and PK/PD analysis revealed that ProCA32.collegen1 exhibits required targeting capability, sensitivity as well as the penetration capability. Thus, vascular changes results from shunting of the portal and arterial blood supply directly into the hepatic outflow (central veins), compromising exchange between hepatic sinusoids and the adjacent liver

parenchyma causing fibrous portal-tract expansion, central-vein fibrosis and capillarization of the sinusoids [324] have been unambiguously detected by dual contrast property of ProCA32.collagen1. We further provided dynamic map of regions of cirrhotic liver with three distinguished vascular features. ProCA32.collagen1 reveals sinusoidal remodeling, and portal-vein blood flow resistance that has not been reported by any MRI contrast agent before. We show that DEN- and TAA/alcohol-induced models exhibit differential map. Such information is essential for understanding molecular mechanism for fibrosis formation and treatment. It will also be very helpful for image-guided biopsy. Detection of angiogenesis as a promising therapeutic target by MRI contrast agents may be a useful noninvasive approach in follow-up of both disease progression and response to anti angiogenic therapies and even choosing treatment strategies [325].

In this chapter, two different late stage cirrhosis models were used to test the contrast agent. First, late stage cirrhosis in TAA/alcohol model was tested to compare the ΔR1 values with early stage fibrosis. In late stage liver cirrhosis, the contrast agent shows its maximum effect in shorter time point of 3 hrs compared to 24 hrs of early stage. The increase in ΔR1 is more than 2.0 s^{-1} and the R1 increase rate is more than %100 which shows the huge difference between ΔR1 and R1 increase rate for early stage fibrosis at both 3 and 24-hour time point. This bigger enhancement displays the great capacity of ProCA32.collagen1 in staging different degrees of fibrosis from early to moderate to late stage. After 24 hrs post injection, ΔR1 is decreasing due to fast washout of the contrast agent. It is worth mentioning that, ICP-OES analysis shows the highest accumulation of Gd^{3+} in late stage cirrhotic liver. In DEN-induced model, the highest enhancement in the liver was observed again at 3-hour time point after injection of the contrast agent. After injection of the contrast agent, a clear heterogeneity of cirrhotic liver due to heterogeneous increase in CNR of T_1-

and T_2-weighted and T1 inversion recovery images was observed. This result is significant compared to homogenous enhancement of liver in TAA/alcoholic model. Before injection of contrast agent, the liver looks homogenous which makes biopsy difficult in stage determination and even detection of the disease due to sampling error and small sample collection. Detecting liver heterogeneity after the injection ProCA32.collagen1 can facilitate the biopsy process and stage determination.

ProCA32.collagen1 not only detects late stage fibrosis but also reveals vascular changes results from shunting of the portal and arterial blood supply directly into the hepatic outflow (central veins), compromising exchange between hepatic sinusoids and the adjacent liver parenchyma causing fibrous portal-tract expansion, central-vein fibrosis and capillarization of the sinusoids [324]. Furthermore, with dual contrast property of ProCA32.collagen1 different regions of cirrhotic liver is enhanced which helps the efficiency and facilitation of biopsy.

5.3.3 Safety: Advantages of ProCA32.collagen1 Compared with Imaging Agents of Liver Fibrosis

Increased evidences have demonstrated that the occurrence of nephrogenic systemic fibrosis (NSF) in renal impaired patients is associated with the release and accumulation of Gd^{3+} from the agent because of transmetallation [157, 206]. Recent concerns about Gd^{3+} depositions in animals and patients have led to withdrawn of four Gd^{3+} contrast agent from Europe by European Medicines Agency (EMA) [326]. Due to necessity for liver applications, Eovist and MultiHance remain in use. Our developed ProCA32.collagen1 represents a major leap in addressing concerns about metal toxicity and Gd^{3+} deposition associated with current contrast agents in several aspects. First, we have demonstrated that ProCA32.collagen1 can mitigate metal toxicity with largely reduced dose and strong resistance against transmetallation (10^4-10^{12}-fold higher metal selectivity

for Gd^{3+} over Ca^{2+} and Zn^{2+}) compared to existing contrast agents. In addition, we have not observed any brain depositions possibly due to its incapability in blood-brain barrier (BBB) penetration. Further, ProCA32.collagen 1 has strong liver preference and is able to specifically target molecular biomarkers, a property that lacks in all approved Gd^{3+} contrast agents. More important, ProCA32.collagen1 with high r_1 and r_2 relaxivity has very low injection dosage of 0.0013 $mmol.kg^{-1}$ projected in humans which is 20-200-fold lower than clinical contrast agents. Indeed, detailed clinical chemistry and tissue analysis demonstrate that no acute tissue toxicity have been observed.

Our developed ProCA32.collagen1 represents a major leap in addressing concerns about metal toxicity and Gd^{3+} deposition associated with current contrast agents in several aspects. Administration of contrast agents helps with visualization of fibrosis at MRI. Specifically, majority of clinical Gd^{3+}-based MRI contrast agents cause T1 shortening and signal enhancement on T1 map images, however most of these agents have been linked to the occurrence of nephrogenic systemic fibrosis (NSF) in renal impaired patients due to release and accumulation of Gd^{3+} from the agent because of transmetallation [157, 206] . Furthermore, they are all based on small-molecule chelates and have very low relaxivity (both r_1 and r_2) and sensitivity without targeting capability, therefore, they are only able to detect moderate and advanced stage of fibrosis, cirrhosis. The clinical contrast agents also use a high clinical injection dosage due to their low sensitivity with a short imaging window without the capability of enhancing the entire liver such as Eovist. ProCA32.collagen1 with high r_1 and r_2 relaxivity has very low injection dosage of 0.0013 $mmol.kg^{-1}$ projected in humans which is 20-200-fold lower than clinical contrast agents. In addition, its high selectivity towards Gd^{3+} makes it a safer agent.

5.4 Potential Application and Significance

ProCA32.collagen1 with collagen type I targeting moiety was successfully developed and used in detection of liver fibrosis. Based on our results, the contrast agent is able to detect and distinguish different stages of the disease from early stage 3 (Ishak system) to late stage 5 liver fibrosis with high sensitivity. This sensitivity can be well demonstrated by increase in ΔR1 of fibrotic liver 3 and 24 hours after injection of ProCA32.collagen1 using R1 map MRI. Furthermore, this increase in ΔR1 is approximately 5-fold higher than Eovist, a clinical contrast agent. The early and late stage of fibrosis was further confirmed with histology analysis. Furthermore, ProCA32.collagen1 is capable of detecting cirrhosis heterogeneity in DEN-induced model which can significantly help other procedures such as biopsy for more accurate sample collection. To the best of our knowledge, this study describes the first early detection of liver fibrosis in the literature. This is a significant achievement since early fibrosis can be reversed if it is detected early, however, clinical contrast agents in the market have failed to detect fibrosis at early stage. Targeting capability of the contrast agent was further confirmed with ICP-OES and immunofluorescence staining as well as ELISA studies. The development of collagen targeting contrast agent is expected to have broad applications in detection and staging of fibrosis in chronic diseases and liver metastasis from various types of cancer and probing heterogeneous microenvironment changes upon disease progression and treatment. Furthermore, less injection dosage can be used to avoid toxicity as our results demonstrate. ProCA32.collagen1 combined with MRI can be used as a quantification and promising method for diagnosing stage specific chronic liver diseases. More results based on DEN-induced cirrhosis and HCC will be demonstrated in Chapter 7. Please visit Chapter 9 for results regarding nonalcoholic steatohepatitis detection.

5.5 Summary

Early diagnosis and noninvasive detection of liver fibrosis and its heterogeneity remain as major unmet medical needs for stopping further progression toward severe clinical consequences. We have developed a collagen type I targeting protein-based contrast agent (ProCA32.collagen1) (K_d of 1.4 μM). ProCA32.collagen1 possesses high relaxivities (r_1 and r2 are 68 and 100 $mM^{-1}\cdot s^{-1}$ at 1.4 T and 42.6 ± 1.0 and 217 ± 2.4 $mM^{-1}s^{-1}$ at 7T) per particle with a T1-T2 dual mode action. ProCA32.collagen1 enables the first robust detection of early (Ishak=3) and late stage of liver fibrosis and mapping liver fibrosis heterogeneity in animal models by its dynamic molecular imaging property by revealing vascular distortion during the late stage cirrhosis with largely reduced dose and strong resistance against transmetallation (10^4-10^{12}-fold higher metal selectivity for Gd^{3+} over Ca^{2+} and Zn^{2+}) compared to existing contrast agents.

Based on our results, ProCA32.collagen1 with collagen type I targeting moiety can detect early stage 3 (Ishak system) with high sensitivity with dual mode r_1 and r_2 property and high collagen affinity which has not been achieved before. This sensitivity can be well demonstrated by increase in ΔR1 and ΔR2 of fibrotic liver 24 hours post injection of ProCA32.collagen1. Furthermore, during late stage fibrosis, ProCA32.collagen1 is capable of detecting heterogeneity, portal hypertension and intrahepatic angiogenesis in different animal models 3 hours post injection which can significantly help biopsy and treatment strategies for more accurate theranostics. It has no toxicity as demonstrated by clinical chemistry tests, tissue staining and injection dosage. To the best of our knowledge, this study describes the first early detection of liver fibrosis with high sensitivity as well as sinusoidal remodeling and portal hypertension during the late stage of the disease by any MRI contrast agent. The development of collagen-targeted protein MRI contrast agent is expected to overcome the major clinical barriers in early diagnosis, noninvasive detection

and staging of liver fibrosis, and have strong application in facilitating effective treatment and stop further progression toward major clinical consequences including cirrhosis, impaired liver function, and hepatocellular carcinoma.

Furthermore, ProCA32.collagen1 is capable of detecting cirrhosis heterogeneity in DEN-induced model which can significantly help other procedures such as biopsy for more accurate sample collection. To the best of our knowledge, this study describes the first early detection of liver fibrosis in the literature. This is a significant achievement since early fibrosis can be reversed if it is detected early, however, clinical contrast agents in the market have failed to detect fibrosis at early stage. Targeting capability of the contrast agent was further confirmed with ICP-OES and immunofluorescence staining as well as ELISA studies. The development of collagen targeting contrast agent is expected to have broad applications in detection and staging of fibrosis in chronic diseases and liver metastasis from various types of cancer and probing heterogeneous microenvironment changes upon disease progression and treatment.

The development of collagen-targeted protein MRI contrast agent is expected to overcome the major clinical barriers in early diagnosis, noninvasive detection and staging of liver fibrosis, and have strong application in facilitating effective treatment and stop further progression toward major clinical consequences including cirrhosis, impaired liver function, and hepatocellular carcinoma.

6 APPLICATION OF PROCA32.COLLAGEN1 IN IMAGING OF UVEAL MELANOMA LIVER METASTASIS

6.1 Introduction

Liver as a vital organ in human body and determinant of survival from cancer is one of the major sites of metastasis such as gastrointestinal and extragastrointestinal cancers, melanoma,

breast, pancreatic, and renal cancer. The liver as the largest organ of the body has unique architecture for its diverse functions such as protein biosynthesis and detoxification of portal blood[327, 328]. Uveal melanoma as the most common intraocular malignancy typically metastasizes through blood and occurs in adults with an age-adjusted average of 5.1 per million [329]. Uveal melanoma accounts for 3.7% of all reported melanoma cases in the United States[330]. Approximately half of the patients with a primary uveal tumor will have metastasis[331]. Typically there is 40% chance of uveal melanoma to metastasize to the liver however, in hepatic metastasis cases, this chance is more than 90-95% in patients [329, 332]. Although the reported 5-year relative survival rate from diagnosis of a primary uveal melanoma is approximately 80% [329], the prognosis for patients with uveal melanoma liver metastases is poor, with a median survival of less than 6 months [333, 334]. Currently, the life expectancy of patients with metastatic UM is only 4-6 months since there are no highly effective treatments for these metastasis[332, 335].

Previous studies have shown that there are three stages of uveal melanoma metastasis to liver: In stage I: <50-μm-diameter micrometastasis occurs within the sinusoidal space; stage II: 51- to 500-μm-diameter metastasis forms expanded collections of cells within the sinusoidal space; and stage III: >500-μm-diameter collections of cells will generate two distinctive patterns. These two patterns in stage III are called the “nodular” or “portal” and “infiltrative” or “lobular” patterns. The infiltrative pattern is an expansion of stage I to III intrasinusoidal growth, which has penetrated the portal lobule and is surrounded by fibrous septae (**Fig. 6.1**). In contrast, the nodular pattern appeared to efface, rather than infiltrate, the surrounding liver; it has been reported that the nodular pattern originates from the perivascular area of the portal triad with distinct clusters of tumor cells located around the portal venules [336].

In the infiltrative pattern, tumor cells are supplied by blood vessels in the sinusoidal or pseudosinusoidal spaces, and angiogenesis is minimal [332], however, in the nodular pattern, the tumors are adjacent to portal venules and demonstrate angiogenesis as the metastatic focus grows with new tumor blood vessels formed and extend from branches of the hepatic arteriole [337].

It is vital to distinguish different UM tumor growth pattern characteristics in the liver in terms of diagnosis and therapy since their recognition in the liver has important clinical implications [334, 336]. In histological point of view, nodular and infiltrative pattern show differences in the host immune response. In infiltrative pattern, there are natural killer cells but in the nodular form cytotoxic T lymphocytes are the major cells [332].

In previous studies, infiltrative and nodular patterns of metastatic UM have been distinguished by hepatic angiography and it was concluded that it can be used to predict response to hepatic arterial chemoembolization [338]. In addition, it has been reported that radioembolization can be effective in treating nodular liver metastases, but not infiltrative sinusoidal metastases[334]. In that particular study, nodular tumors in liver decreased in size with radioembolization without the infiltrative tumors responding to treatment[334]. Furthermore, it has been shown that patients with angiographically determined nodular tumor appearances survived longer than patients with infiltrative lesions (overall survival, 621 vs. 114 days) [339], therefore, distinguishing these patterns on any imaging modality is an important consideration when determining the treatment plan for patients with metastatic UM [339].

Current clinical imaging techniques have significant limitations in the early detection, diagnosis and differentiation of UM micrometastasis to liver as well as their different growth patterns. Magnetic resonance imaging (MRI) is a powerful technique for high-resolution visualization of the anatomic structure and function of soft tissues, including tumors without the

use ionizing radiation [340-342]. MRI offers several unique advantages compared to other clinical imaging modalities with its deep tissue penetration, high spatial resolution, and coverage of the entire liver. Since MRI does not require the use of ionizing radiation, it is well suited for screening and monitoring the progression and regression of different diseases [296, 297]. Existing methods such as apparent diffusion coefficient (ADC), magnetic resonance elastography (MRE), T1, T2, relaxation in the rotating frame ($T_{1\rho}$) [294], magnetization transfer [295], and proton density fat fraction (PDFF) cannot provide accurate detection of liver lesions, their patterns and heterogeneity.

More than 35% of MRI scans require contrast agents [341]. Differentiation of micrometastasis from heterogeneous tissue background without clear boundary requires even more sensitive contrast agents and imaging methodology to have specificity for diseased cells as well as improved relaxation properties. Iron oxide-based contrast agents such as ferumoxides create negative (dark) T2 /T2* effects that are reported to yield images with signal voids and very limited accuracy[278, 298]. Two Gd^{3+}-based contrast agents approved for liver imaging, Gd-BOPTA (Multihance) and Gd-EOB-DTPA (Eovist US; Primovist, Europe) have positive (bright) imaging. Along with all other approved Gd^{3+} MRI contrast agents, they have per Gd^{3+} relaxivity (r_1) values ~5 $mM^{-1}.s^{-1}$ which is ~20-fold lower than a theoretical value [299]. Such low relaxivity limits their sensitivity for detecting small liver lesions. In addition, these agents are extracellular with r_1 increase using T_1-weighted sequence at a short arterial phase and a short hepatobiliary uptake phase. Furthermore, a high injection dose of 0.025-0.3 mmol/kg is required to generate detectable contrast. Such high injection doses contribute to metal toxicity and have resulted in a black box warning.

Small molecular Gd^{3+} agents that are routinely used for clinical cancer imaging to enhance image contrast by shortening the relaxation times of the surrounding water protons [47] are non-

specific contrast agents and cannot differentiate tumor growth patterns or provide efficient detectable contrast in small tumors and micrometastasis. As a result, biomarker-specific molecular imaging reflecting tumor microenvironment can be an effective and sensitive approach towards the early detection and differential diagnosis of UM liver micrometastasis [343].

Tumor microenvironment plays a vital role in tumor progression and metastasis [344, 345]. Extracellular matrix (ECM) is a major part of the microenvironment and collagen type I is the most abundant component [155]. Furthermore, Collagen as the major part of tumor microenvironment can affect its regulation of ECM remodeled by collagen degradation and re-deposition, as well as promotion of tumor infiltration, angiogenesis, invasion and migration[155].

Collagen has been extensively used as both imaging and therapeutic agents such as delivery systems for many kinds of bioactive proteins and drugs and engineered collagen hydrogels for the sustained release of biomolecules and imaging agents in various collagen-related diseases [346, 347].

Since there are significant differences in the formation of collagen in these two distinctive patterns of UM micrometastasis [332] and differentiation can affect the choice of treatment regimens in the future, in this paper, we report the development of protein MRI contrast agents for molecular imaging of the collagen level (ProCA32.collagen1) extending the targeting capability of our recently reported ProCA32-P40, a protein MRI contrast agent [83]. ProCA32.collagen1 with high dual relaxivity values for r_1 and r_2 per Gd^{3+} at both 1.5 and 7.0 T as well as strong collagen targeting capability enables the first robust early detection of stage II UM micrometastasis to the liver. Furthermore, for the first time, ProCA32.collagen1 is capable of differentiating nodular vs infiltrative pattern at this stage which has been achieved before (**Fig. 6.2**). The development of collagen-targeted protein MRI contrast agents are expected to overcome the major clinical barriers

in early diagnosis, noninvasive detection and staging of UM micrometastasis to liver, and have strong application in facilitating effective treatment toward major clinical consequences.

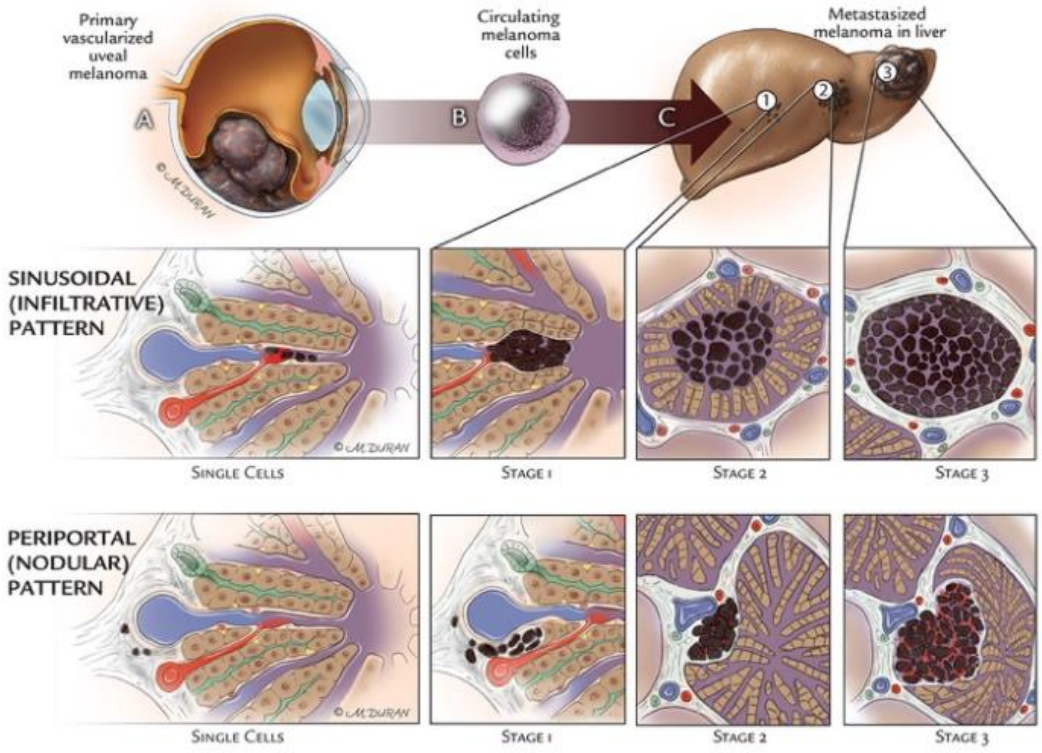

Figure 6.1 *. Schematic cartoon of metastatic UM to the liver [332].*

Melanoma arises in the choroid of the eye, extravasates into tumor blood vessels, and then travels via the systemic circulation as circulating melanoma cells with tumor stem cell–like properties, where it enters the liver as single cells. These single cells likely arise from hepatic arterioles and seed the sinusoidal space causing the infiltrative pattern of growth, which progresses to stage I (0-50 μm) micrometastases, stage II (51-500 μm) intermediate metastases, which are bathed by serum in the sinusoidal space, and eventually stage III (>500 μm) metastases, which replace the hepatic lobule.

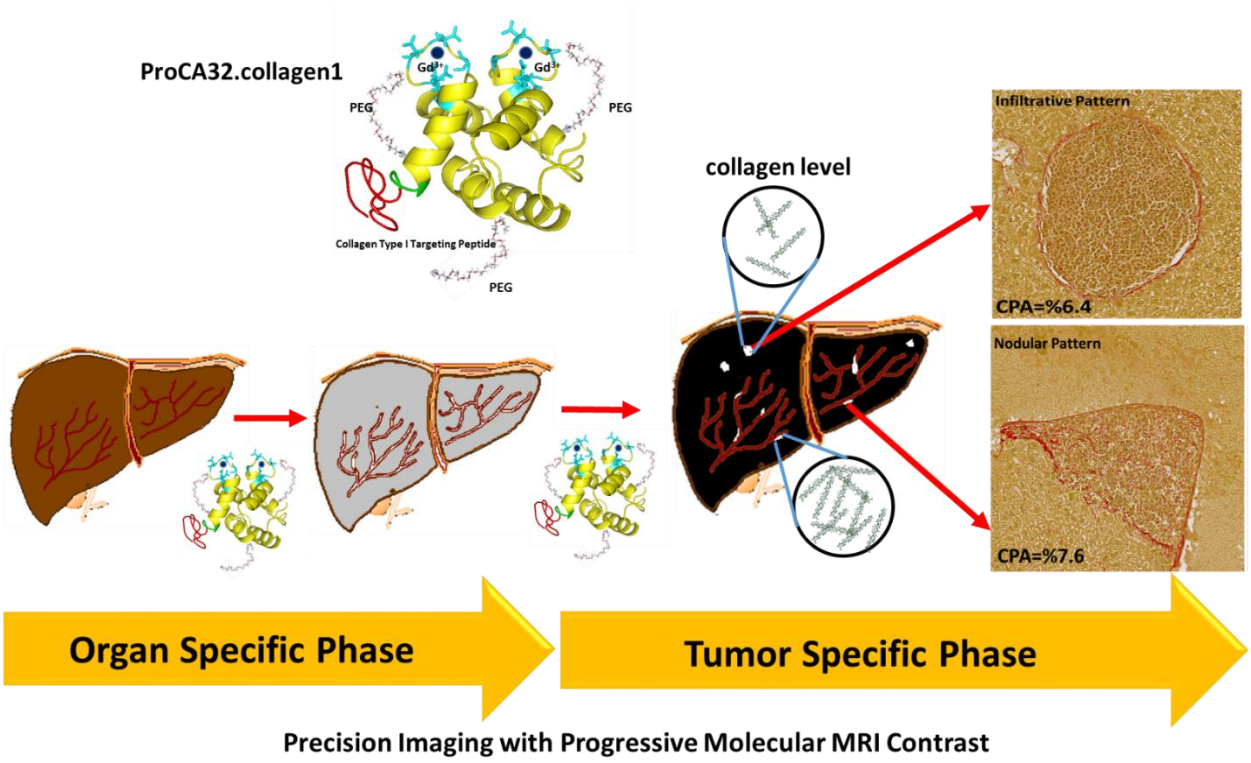

Figure 6.2 *Precision imaging with progressive molecular MRI contrast agent, ProCA32.collagen1.*

Schematic illustration of ProCA32.collagen1 capability in early detection and differentiation of UM tumor growth patterns micrometastasis in liver. Nodular pattern showing different pattern and higher levels of collagen compared to infiltrative.

6.2 Results

In order to assess the application of ProCA32.collagen1 with collagen type I targeting moiety in detection of small lesions of micrometastasis, the contrast agent was used in different animal models of uveal melanoma liver metastasis.

6.2.1 Molecular imaging of implanted mouse Uveal Melanoma in liver

In order to test our contrast agent capability for in vivo imaging of the tumor, mouse uveal melanoma (B16LS9) was implanted in the liver. Then, the PEGylated contrast agent (100 µL, 5

mM) has been injected in the mice in the tail vein. Fig. 6.4 A illustrates the tumor in the liver of the mice. T_1-weighted, T_2-weighted and inversion recovery MRI images of the tumor in the liver were collected using a 7.0 T MRI instrument. T_1-wighted images showed approximately 6-fold enhancement in the relative contrast of the tumor 40 hours post injection of ProCA32.collagen1. Fig. 6.4 A and B show the T_1-weighted images and quantitative analysis of the tumor enhancement after injection. T_2-wieghted images also showed about 4-fold enhancement in the relative contrast of the tumor 40 hours post injection of ProCA32.collagen1 compared to pre-injection. Fig. 6.4 A demonstrated the T_2-wieghted images.

An inversion recovery pulse sequence was also used for molecular imaging of the tumor in the liver. In this method, both liver and tumor signal were suppressed in order to achieve a high contrast between liver and tumor. As can be seen in Fig. 6.4 A and B summarize the results using different techniques. In these techniques, tumor images can appear as both bright and dark spots depending on the type of signal suppression. Fig. 6.3 demonstrates the procedure in which the liver signal is suppressed with the use of inversion recovery pulse sequence combined with ProCA32.collagen1.

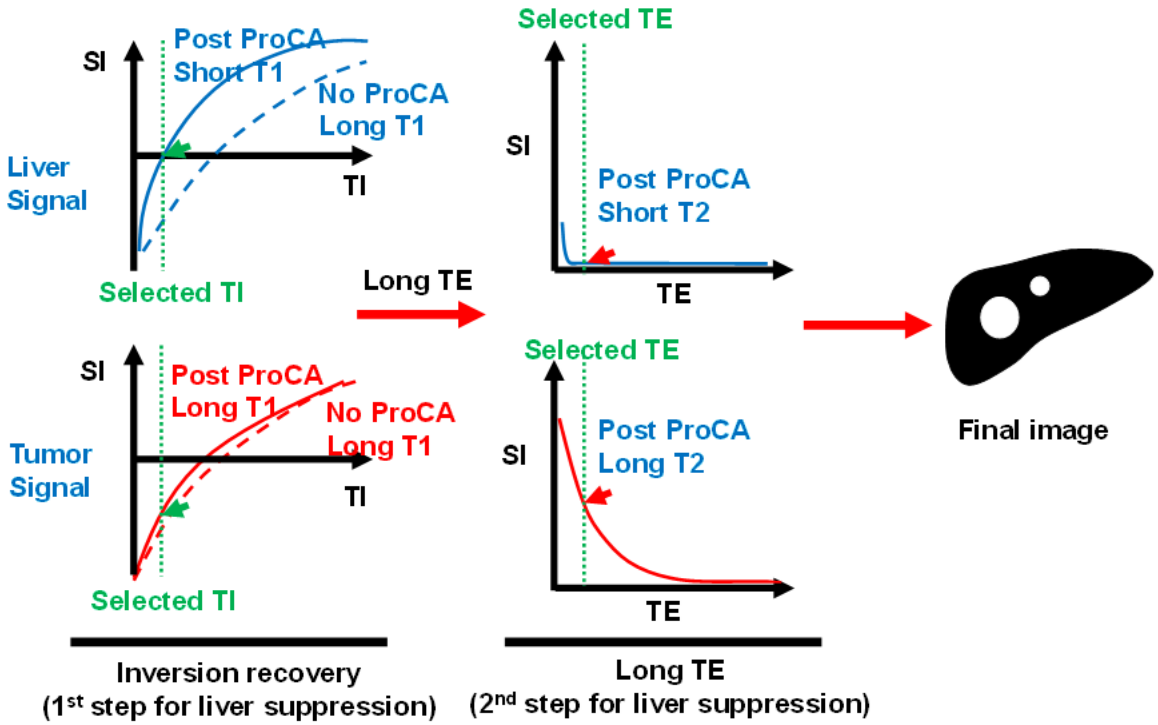

Figure 6.3 *Demonstration of STIR with long TE sequence for the double suppression of liver signal for tumor imaging.*

After injection of ProCA32.collagen1 for about 3 hours, contrast agent has high accumulation in the liver than tumor. As a result, liver has shortened T1, while tumor T1 doesn't change much. This sequence has two steps to suppress liver signal. First, we will use inversion time to suppress liver signal. Second, since liver also has short T2 compared with tumor, we further using TE to further suppress the liver signal, while tumor signal still can be detected due to long T2.

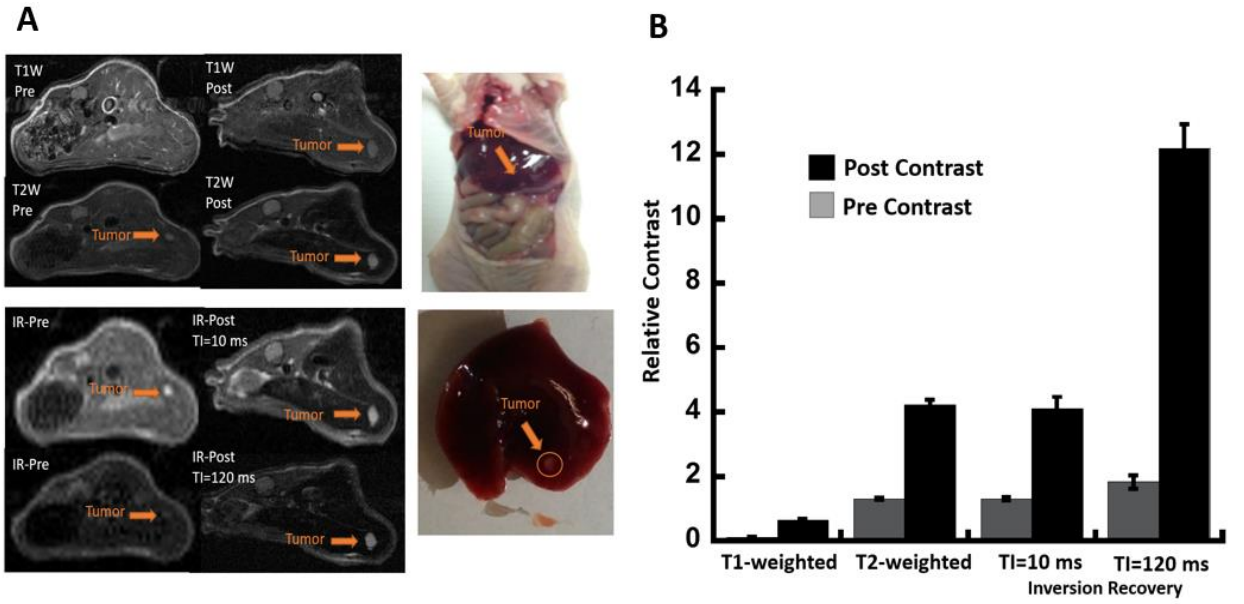

Figure 6.4 *MRI images of B16LS9 mouse implanted UM tumor before and after injection of ProCA32.collagen1 in liver.*

(A) T1-weighted, T2-weighted, and T1 inversion recovery images (B) Quantitative analysis of relative contrast of tumor before and 40 hours after injection of ProCA32.collagen1 demonstrates a great enhancement in tumor post injection of the contrast agent in T1-weighted, T2-weighted, and T1 inversion recovery with different inversion times.

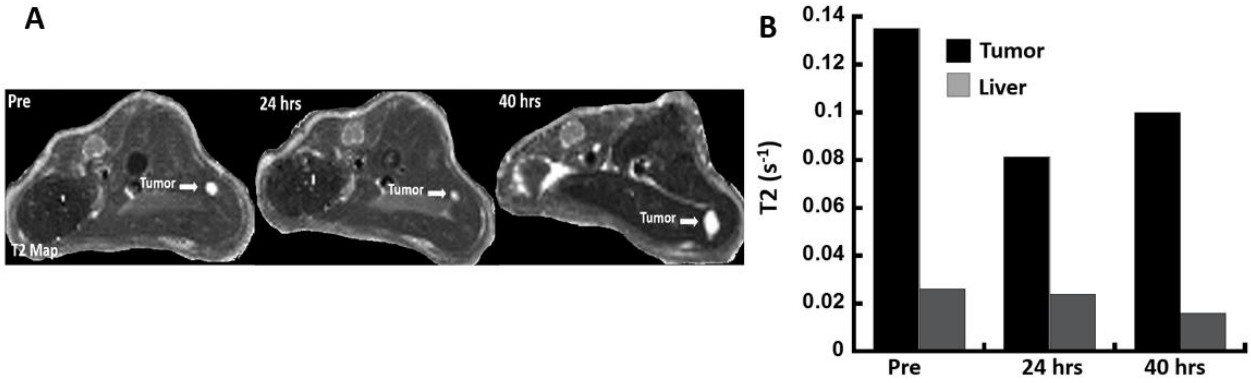

Figure 6.5 *T2 map MRI images of B16LS9 mouse implanted UM tumor.*

(A) *T2 map MRI images of B16LS9 mouse implanted UM tumor before and 24 and 40 hours post injection of ProCA32.collagen1.* ***(B)*** *T2 map analysis of tumor before and 24 and 40 hours post*

injection of ProCA32.collagen1 shows the contrast agent is penetrating into the tumor causing a noticeable decrease in T2 post 24 hrs.

In addition to those three mentioned pulse sequences, T2 maps of liver with implanted tumor was also collected before and 24 and 40 hours post injection of ProCA32.collagen1. Fig. 6.5 A and B demonstrate the results with quantitative analysis of T2 values. As it is observed from Fig. 6.5 B, tumor T2 value was significantly decreased from 0.13 s (pre) to 0.08 s (24 hours) post injection of ProCA32.collagen1. This result is an indication of targeting capability and tumor penetration of ProCA32.collagen1. The T2 value then gradually increased at 40 hours since the contrast agent is being washed out. The liver T2 value slightly decreased at 24 hours post injection and deceased more at 40 hours post injection but the majority of T2 reduction occurs at tumor site.

6.2.2 Immunofluorescence and collagen staining

In order to further confirm the targeting capability of ProCA32.collagen1, the liver frozen sections with tumor were stained for collagen and contrast agent with Sirius red and rabbit antibody, respectively. For this purpose, for contrast agent staining, frozen sections of liver tissues were collected. Then the tissues on slides were fixed with either ethanol or methanol in -20°C for 20 minutes to remove OCT which is a gel-like medium for embedding the tissues.

After the tissues were dried, the blocking buffer is added for 2 hours at room temperature. Then the slides are washed with 1×TBST for once, and the primary antibody is added (ProCA32.collagen1) with 1:50 dilution and left for incubation in 4°C overnight. The slides are washed again with 1×TBST for three times, each time for 5 min.

In the next step, the slides are washed again three times, and secondary antibody is added for the primary antibody (anti goat) and left for 1 hour at room temperature. Then DAPI is added to the slides and they are covered with glass and left at 4°C until they are dried.

As Fig. 6.6 demonstrates, A is showing heart tissue without any collagen present and B is liver with tumor exhibiting large packs of collagens in pink color and C is showing the liver with implanted tumor. D and E are uveal melanoma tumors in the liver showing two distinctive patterns demonstrated by collagen (blue). F is immunofluorescence staining of ProCA32.collagen1 showing the contrast agent is targeting the liver with tumor.

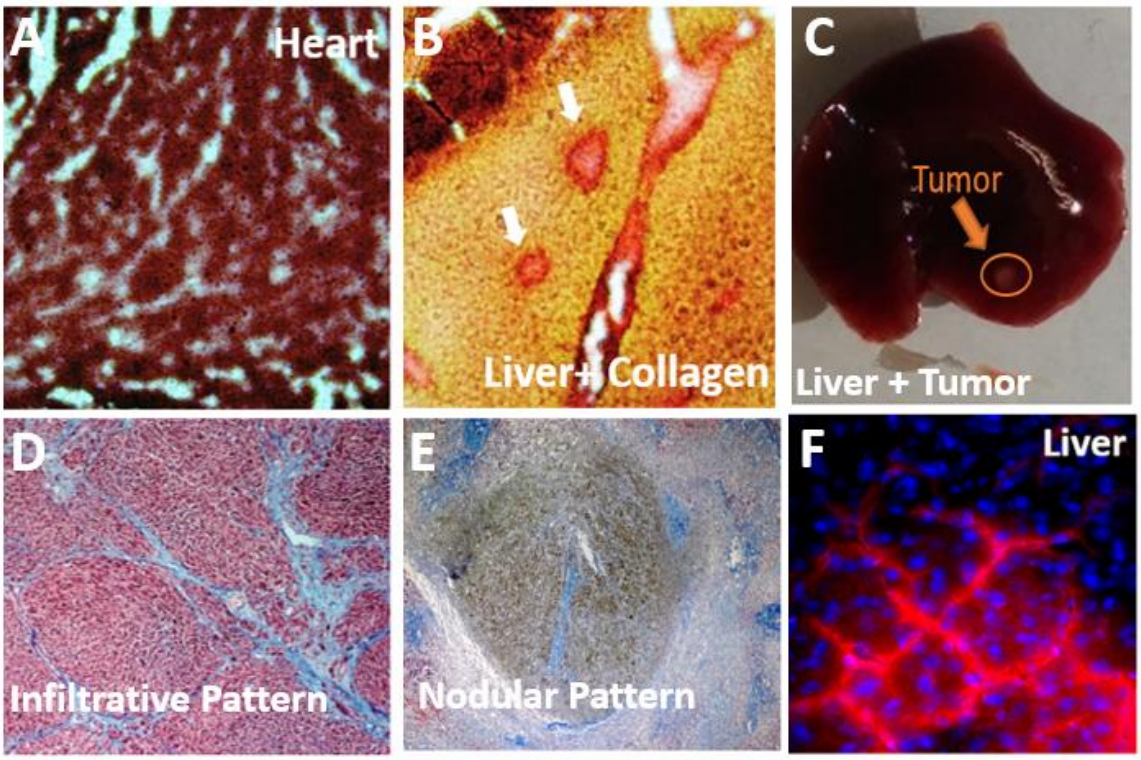

Figure 6.6 *Immunofluorescence and collagen staining*

(A) Heart as a negative control showing no signs of collagen. (B) Liver tissues with tumor show collagen packs in pink color. (C) Image of liver with implanted uveal melanoma tumor. (D, E) Liver with two different uveal melanoma tumor growth patterns showing different in collagen pattern as well. (F) Immunofluorescence staining of ProCA32.collagen1 in liver with uveal melanoma implanted tumor shows the heterogenous distribution of the contrast agent.

6.2.3 Molecular imaging of M15 Uveal Melanoma metastasized to the liver

Human UM M20 orthotopic mouse model metastasized to the liver was generated and PEGylated contrast agent (100 µL, 5 mM) was injected in mice in the tail vein. T_1-weighted, T_2-weighted and inversion recovery MRI images of the tumor in the liver have been collected using a 7.0 T MRI instrument. Fig. 6.7 shows the T1 inversion recovery of mouse liver before and after injection of ProCA32.collagen1 at different inversion times. The mouse model is M20 with human uveal melanoma tumor metastasized to the liver from the eye. As it can be seen from MRI images, tumors are showing up 24 hours after injection of ProCA32.collagen1 based on the inversion time used. The same results can be observed in T1- and T2-wieghted MRI images. Inversion recovery pulse sequence was also used in this experiment with different inversion times. The best MRI image with tumors lighting up in the dark background of the liver can be obtained in the optimized inversion time of 0.01s (Fig. 6.7). Inversion time of 0.12 s surprisingly did not show any tumors in the liver. Different inversion times at 48-hour time point was also tested to identify the best inversion time for better contrast of the tumor.

Therefore, inversion time of 0.01 s can provide the best enhancement of tumors 24 hours post injection of ProCA32.collagen1. Other contrast agents such as non-targeted agent, ProCA32-P40 and Eovist were tested later in 0.01 s inversion time to assess the targeting ability of ProCA32.collagen1.

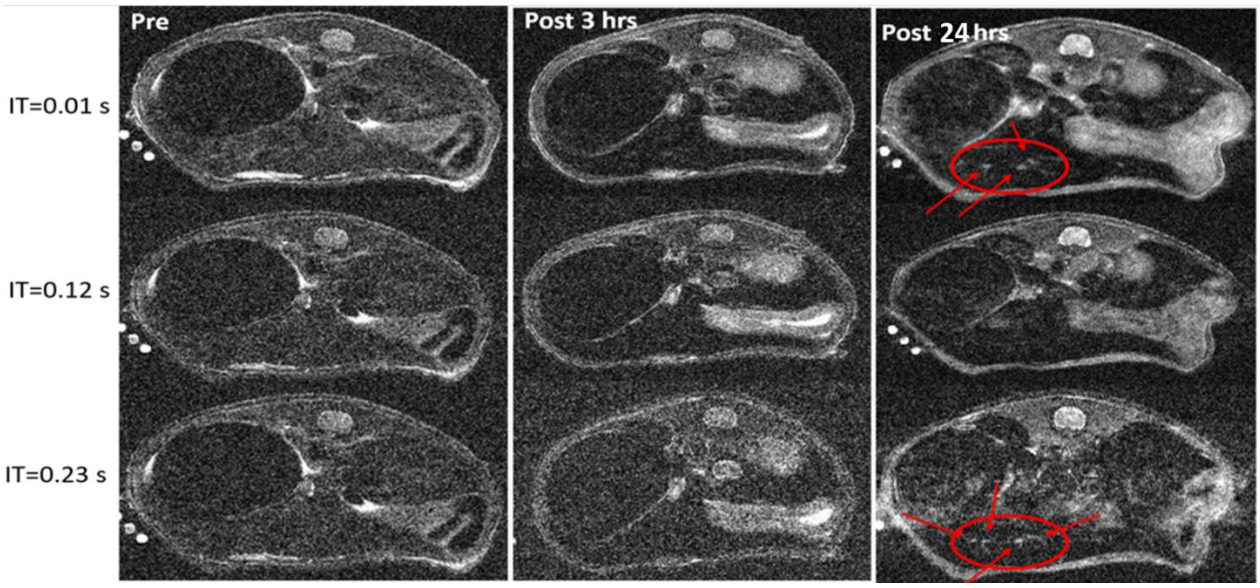

Figure 6.7 *Imaging of UM Tumor with different inversion times.*

Different invasion times of 0.01, 0.12 and 0.23 seconds were tested in inversion recovery pulse sequence in order to obtain the best enhancement for tumors. Inversion times of 0.01 s and 0.23 s were able to show tumors; however, inversion time of 0.12 s did not show any tumors, therefore, 0.01 s was used for further analysis.

We have used other contrast agents such as ProCA32-P40, and Eovist to test the targeting efficiency of ProCA32.collagen1. As Fig. 6.8 demonstrates, Eovist, a liver specific clinical contrast agent cannot show any tumors in the liver although histology analysis confirmed the UM metastasis to the liver. Moreover, ProCA32-P40 which has also good relaxivity and sensitivity but lacks collagen type I targeting capability failed to show any tumors. These results exhibit the advantage of having a targeting moiety in ProCA32.collagen1.

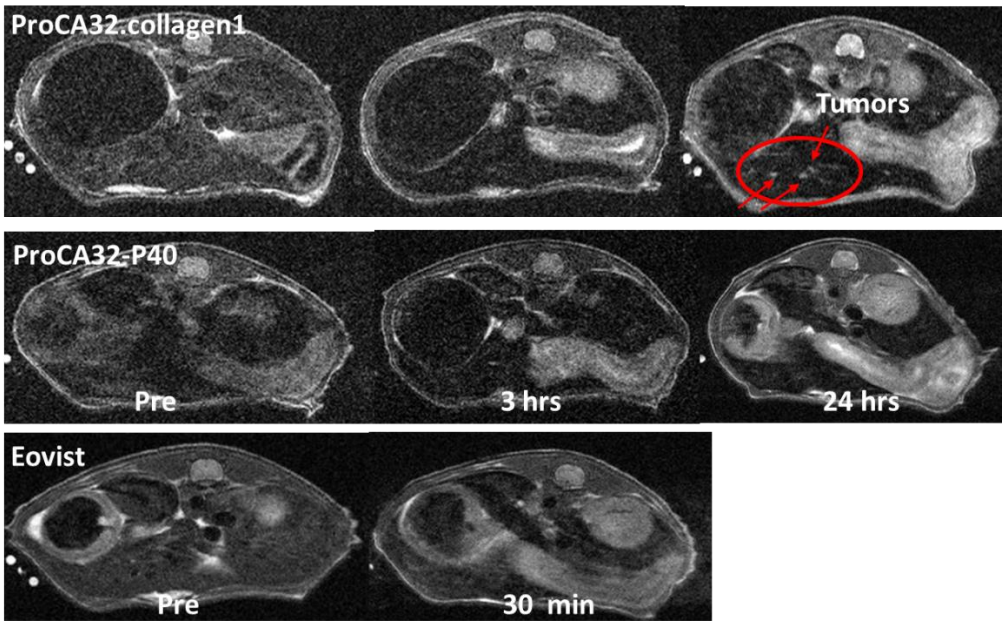

Figure 6.8 *T1 inversion recovery (IT=0.01 s) MRI images of mouse livers with M15 UM metastasis model.*

Only ProCA32.collagen1 can show UM micrometastasis 24 hrs post injection confirmed with histology. Eovist and ProCA32-P40 cannot show any tumors in the liver after injection despite the presence of tumors in histology.

6.2.4 Correlation of MRI with histology of Uveal Melanoma

Hematoxylin and eosin stain or hematoxylin and eosin stain (H&E stain or HE stain) is one of the principal stains in histology. It is the most widely used stain in medical diagnosis and it is often the gold standard. In M20 model, the liver tissues were stained with H&E and tumors were correlated with MRI image (inversion recovery at 24-hour time point). As it can be seen in Fig.6.9 A, total number of six isolated tumors with nodular and infiltrative patterns along the portal vein were detected by H&E staining. The same tumors were detected in MRI by injecting ProCA32.collagen1 contrast agent considering that tumors with nodular pattern have high levels of collagen type I surrounding them. Most importantly, the contrast agent is able to detect the

nodular pattern of tumors which has significant clinical implications. The tumors in the MRI can be well correlated with H&E staining of liver tissue. Fig 6.9 B shows the good correlation between tumor size in histology and tumor size in MRI. Moreover, the limit of detection has been significantly lowered with the use of ProCA32.collagen1 as tumor as small as 0.250 mm^2 was detected. Tumor heterogeneity can also be observed after injection of the contrast agent as shown in Fig 6.9 C. Contrast to noise ratio analysis of tumors show the significant enhancement of tumors 24 hours post injection of ProCA32.collagen1. A 14-fold increase was observed in the CNR (24 hour) compared to pre (Fig. 6.9 D).

In addition, the tumors were stained with collagen type I antibody to confirm that collagen type I is surrounding the tumors. Collagen type I in Fig.6.10 A can be seen in brown color and can be correlated with H&E staining at the same time.

In Fig. 6.10 A, brown colors can be seen that are surrounding the UM tumor in dark purple. In addition, the tumors in the liver were stained with S100 antibody staining to confirm the Uveal Melanoma tumor in the liver. The result can be seen in Fig. 6.10 B. Fig. 6.10 C and D are demonstrating Sirius red staining for collagen in uveal melanoma tumors. These images are showing two different patterns of UM with different collagen levels and patterns (red). It can be seen that nodular pattern has more collagen levels compared to infiltrative pattern, furthermore, collagens in nodular pattern are present both inside and outside of the tumor, however, in infiltrative pattern collagens are surrounding the tumor.

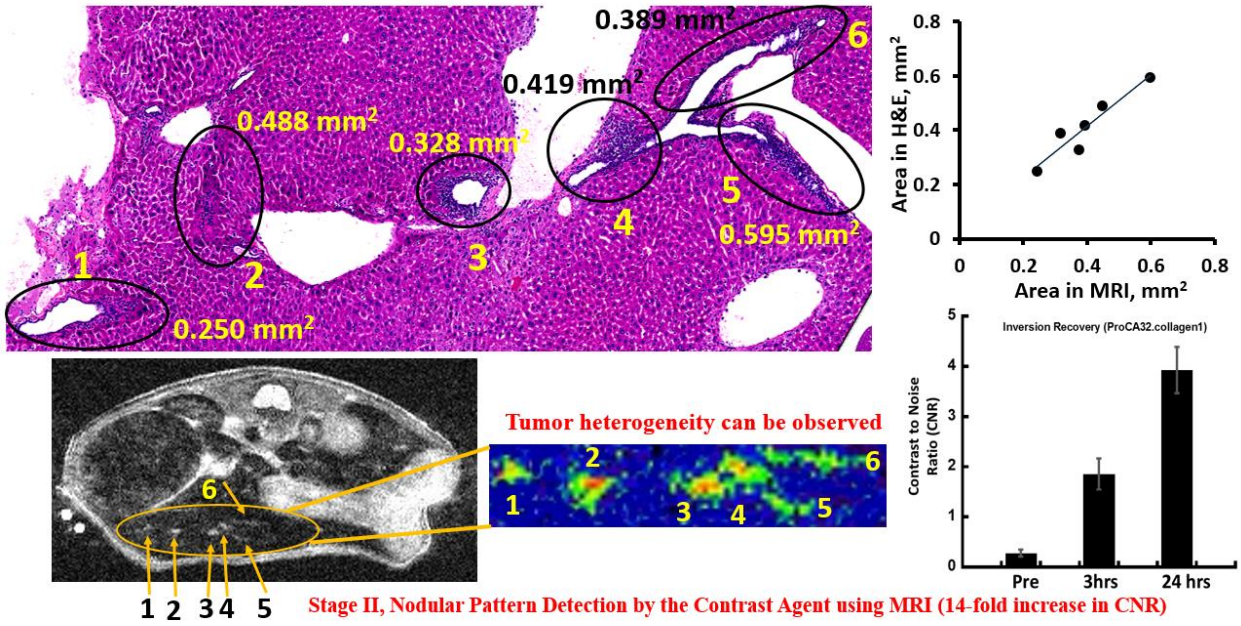

Figure 6.9 *MRI and histology correlation of UM tumor detected by ProCA32.collagen1.* ***(A)*** *H&E staining of 6 tumors with different patterns corresponds with MRI image demonstrating the high sensitivity of ProCA32.collagen1 in early detection and distinguishing of UM patterns. Tumor numbers 1-4 showing infiltrative pattern and tumor number 5 and 6 are representing the nodular pattern. Based on histology, stage II, nodular and infiltrative patterns can be detected by the contrast agent using T1 inversion recovery (TI=IT=0.01 s).* ***(B)*** *Histology results showing correlation with MRI image. Tumors area in* mm^2 *in MRI is very close to the area of tumors in H&E.* ***(C)*** *Contrast to noise ratio (CNR) calculations showing a 14-fold increase in tumor after injection of ProCA32.collagen1.*

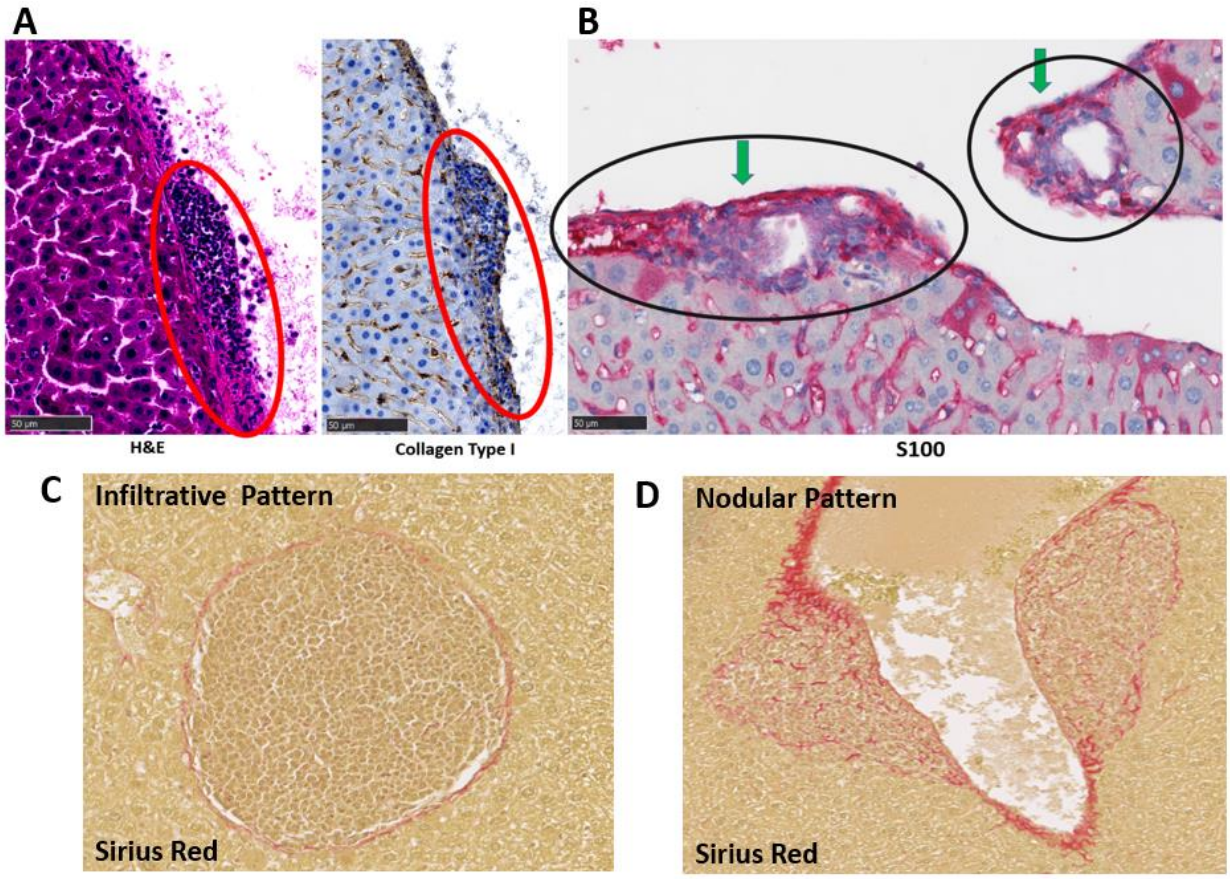

Figure 6.10 *Histology confirmation of UM tumor and collagen expression.*

(A) *UM nodular tumor in liver with collagen type I surrounding it in brown color.* ***(B)*** *S100 antibody staining confirms the Uveal Melanoma tumor in the liver.* ***(C)*** *Sirius red staining of infiltrative pattern UM tumor in liver showing collagen (red) surrounding the tumor.* ***(D)*** *Sirius red staining of nodular pattern UM tumor in liver showing collagen (red) surrounding the tumor as well as inside the tumor. The collagen pattern is clearly different based on tumor pattern.*

6.2.5 ICP-OES organ distribution

The Gd^{3+} concentration in different organs were measured post injection of contrast agents using ICP-OES. Based on the measurements, the Gd^{3+} concertation in liver with uveal melanoma 48 hours post injection of ProCA32.collagen1 was approximately 0.08 μmol/g. Overall, liver 48 hours after injection of ProCA32.collagen1 showed the highest Gd^{3+} concentration among other organs including the liver injected with non-targeted contrast agent, ProCA32 (ProCA32-P40), which demonstrates the targeting capability of ProCA32.collagen1 towards collagen type I in liver with uveal melanoma. The Gd^{3+} injection dosage per gram of tissue in liver with ProCA32.collagen1 was approximately 3-fold higher than ProCA32-P40. Further results in Fig. 6.11 A and B show that the Gd^{3+} content is much lower in other organs compared to liver.

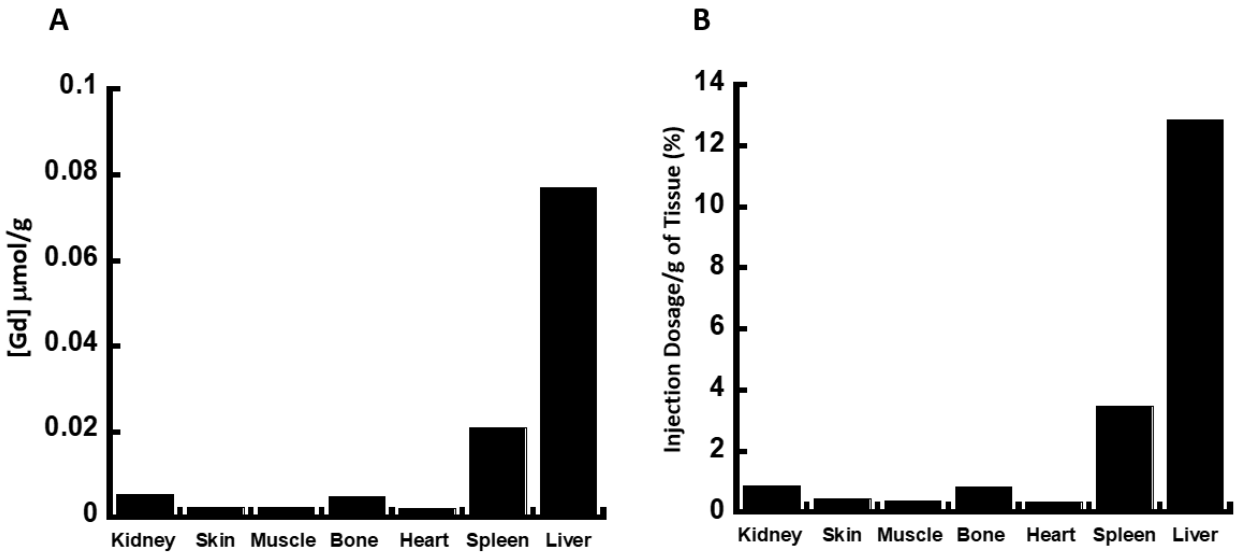

Figure 6.11 *Gd^{3+} concentration measurements showing contrast agent distribution in different organs 48 hours post injection of ProCA32.collagen1.*

(A) *$Gd3^{+}$ concentration measurements in (μmol/g) in different organs using ICP-OES.* ***(B)*** *Injection dosage of contrast agents per gram of tissues in different organs using ICP-OES.*

6.3 Discussion

We have developed a protein-based MRI agent with collagen type I targeting moiety attached to its C-terminal. In order to meet the requirements for MR imaging of liver metastasis, the targeting peptide was added to the C-terminal to avoid any alterations in the protein structure and its metal binding affinities which is very different from other approaches. We have demonstrated that it is possible to increase relaxivity by addition of a targeting moiety to a protein MRI contrast agent without sacrificing relaxation and metal binding properties, such as affinity and metal specificity.

ProCA32.collagen1 as an MRI contrast agent has several advantages over clinical contrast agents based on small chelators such as Gd-DTPA in functional and molecular imaging applications. First, it greatly increases the CNR and SNR. Second, it improves dose efficiency with reduced metal toxicity. Three, it prolongs the tissue retention time, which enables imaging of different stages of the disease that requires prolonged tissue enhancement; and fourth, it functions as a protein carrier that can conjugate target-specific ligands to collagen 1 for targeted molecular MR imaging. Although the diffusion rate of a protein with proper size (3-5 nm) is slower than that of small chelators, ProCA32.collagen1 has the capability to diffuse to the target.

One of the most important characteristic of an MRI contrast agent specifically for liver metastasis is its sensitivity. An MRI contrast agent with high relaxivity determines the sensitivity and limit of detection of the agent capable of detecting a disease. This is extremely crucial for liver metastasis since the early stage of the disease cannot be detected by MRI due to small sizes of micrometastasis. In addition, clinical contrast agents do not have the capacity to detect UM tumor growth patterns (nodular vs infiltrative) in order to make a difference in treatment strategies. Given the fact that collagen type I is an important biomarker in assessing the growth patterns of UM

tumors, ProCA32.collagen1 was designed and developed to overcome the major limitations of clinical contrast agents. ProCA32.collagen1 with targeting capability is able to not only detect small UM micrometastasis in liver at early stage but also has the ability to distinguish nodular and infiltrative tumor patterns and therefore, facilitate the treatment of these tumors.

6.3.1 Advantages of ProCA32.collagen1 Compared with Imaging Agents of Liver Metastasis

Administration of contrast agents helps with visualization of tumors using MRI. Specifically, majority of clinical Gd^{3+}-based MRI contrast agents cause T1 shortening and signal enhancement on T1 map images, however most of these agents have been linked to the occurrence of nephrogenic systemic fibrosis (NSF) in renal impaired patients due to release and accumulation of Gd^{3+} from the agent because of transmetallation [157, 206] . Furthermore, they are all based on small-molecule chelates and have very low relaxivity (both r_1 and r_2) and sensitivity without targeting capability, therefore, they are only able to detect late stages of UM when the tumor sizes are in cm. The clinical contrast agents also use a high clinical injection dosage due to their low sensitivity with a short imaging window without the capability of enhancing the entire liver such as Eovist.

Several research-based probes and Gd^{3+}-based contrast agents targeting extracellular matrix (ECM) proteins have been evaluated in animal models of breast cancer in the past several years. Zhou et al has developed penta-peptide conjugated to Gd-DOTA to target fibrin–fibronectin complexes in tumor microenvironment[343] ENREF 49. All of these MRI contrast agents have low relaxivity values for both r_1 and r_2 and rely only on their T1 property. ProCA32.collagen1 with high r_1 and r_2 values allow both T1 and T2 imaging to increase the confidence of MRI scans. ProCA32.collagen1 enhances the entire liver for at least 3 h, which substantially widens the MRI detection window for high-quality imaging of liver, allowing us to introduce both T1 and T2

property of the contrast agent since the small tumor micrometastasis are usually not well visualized during the arterial and early venous phases, upon the administration of clinical contrast agents. In addition, tumor growth pattern cannot be visualized either.

6.3.2 Noninvasive Biomarkers of Uveal Melanoma Liver Metastasis

Uveal melanoma (UM) has high tendency to metastasize to the liver [348, 349]. Although the local treatment of the intraocular tumor has progressed, the survival rate of UM patients remained unchanged or changed little over the past few decades. Since UM metastatic tumor burdens are typically high when detected by changes in liver function tests or even different imaging modalities, there is no reliable and effective treatment [350, 351]. In the past,

oncologists were dependent on the measurement of liver enzymes levels in order to raise the suspicion of metastases, however a significant tumor size is sometimes needed to increase liver enzymes, therefore, sometimes patients have normal liver enzymes with diffuse hepatic metastases [352]. As a result, there is an unmet medical need to develop sensitive biomarkers to detect early metastatic UM as well as its growth patterns.

A broad variety of molecules synthesized or in the blood have been proposed as markers of cutaneous melanoma tumor progression [353]. These markers include melanin-related metabolites and enzymes (Alpha-MSH, tyrosinase), adhesion molecules (ICAM-1, PECAM-1, CD-44) and cytokines (IL-8, IL-10, IL-2R). The currently available diagnostic tests to detect cutaneous melanoma- associated molecules include LDH as introduced by the AJCC (American Joint Committee on Cancer), S-100β [354], NSE (neuron specific enolase), LASAP (lipid bound sialic acid) and melanoma-inhibitory activity (MIA) [355].

In cutaneous melanoma, a study demonstrated that serum S-100β can be an independent prognostic maker for Stage II of the disease [356, 357]. It was reported that S-100β serum level

changes can be of predictive value for a positive response to chemotherapy and immunotherapy [357], however, there is not enough information about the clinical value of S-100β in patients with UM. In addition, two serum markers reported to correlate with the presence of hepatic metastases from uveal melanoma are tumor-associated antigen known as melanoma inhibitory activity (MIA) and osteopontin (OPN) [355, 358-360].

Collagen type I as a tumor stroma-derived biomarker is important in variety of cancers since it reflects the tumor microenvironments changes, therefore, as a direct marker is a perfect target for molecular MR imaging compared to other ECM components such as elastin. Specifically, in UM, collagen type I is not only present in early stages of the disease and small micrometastasis but also an indication of tumor growth pattern difference in the liver which is indispensable for treatment choices. Furthermore, collagen targeting molecular magnetic resonance imaging demonstrates a unique application of MR technology to view biological processes at the cellular and molecular level.

Development of an MRI contrast agent to target collagen type I can be an ideal way to take advantage of combination of an imaging modality with a direct biomarker to detect UM in liver at early stage and the growth pattern differences. ProCA32.collagen1 with high binding affinity of 1.4 μM to collagen type I among agents targeting the ECM is an ideal contrast agent since it is well within the range of the natural collagen type I concertation in liver (1–20 $nmolg^{-1}$), in addition, this concentration will increase as the tumor develops or changes its pattern. ProCA32.collagen1 with high relaxivity it very sensitive to these changes for early detection and pattern distinction in UM in liver.

6.3.3 Nodular vs infiltrative growth pattern distinction using ProCA32.collagen1

Patients with UM metastasis rarely survive more than a few years after initial detection of the metastasis. The median survival time after diagnosis of metastasis in the largest published series of unselected patients with metastatic uveal melanoma was 3.6 months [361]. Cumulative actuarial survival in this series was 20% at 1 year, 13% at 2 years, 5% at 3 years, 2% at 4 years, and less than 1% at 5 years [335]. The liver is usually the first site of metastasis of UM, and is the only single organ involved in 60%–80% of UM patients[362]. The median survival of patients with liver metastasis is 2–7 months despite aggressive therapy, [363] and the clinical course of these patients is highly dependent on disease progression in the liver [364, 365].

Recognizing the different growth patterns of metastatic UM in the liver has important clinical implications. Histologically, nodular and infiltrative types exhibit differences in the host immune response: there are natural killer cells in the infiltrative form, whereas the nodular form contains cytotoxic T lymphocytes [332]. There are also discrepancies in the formation of collagen, angiogenesis, and other factors that distinguish these 2 histologic growth patterns [366]. The choice of treatment regimens in the future may be altered because of these differences. Dayani et al distinguished between infiltrative and nodular patterns of metastatic UM on hepatic angiography and noted that it can be used to predict response to hepatic arterial chemoembolization. Halenda et al[338] also noted that radioembolization was effective in treating nodular liver metastases, but not infiltrative sinusoidal metastases[334]. In that particular study, a patient had a mixture of nodular and infiltrative liver metastases demonstrated by MRI. The nodular liver metastases decreased in size with radioembolization, but the infiltrative metastases did not respond to treatment and the patient's condition ultimately progressed. Sharma et al[339] showed that patients with angiographically determined nodular tumor appearances survived longer than patients with

infiltrative lesions (overall survival, 621 vs. 114 days)[339]. Differentiating between these patterns on scans is an important consideration when determining the treatment plan for patients with metastatic UM. It is possible that the nodular pattern on imaging may represent an earlier pattern of disease that transforms into the infiltrative pattern as the tumor escapes from the portal triad. ProCA32.collagen1 is the only contrast agent developed so far with the capability of differentiating UM growth patterns in liver which is significant when choosing treatment strategies for patients to prolong the survival.

6.3.4 Transmetallation of ProCA32.Collagen and Clinical MRI Contrast Agents

The chemical instability of a Gd^{3+}-based contrast agent can lead to exchanges with other metal ions such as zinc, copper, and calcium which can, in turn, have biological consequences. These consequences include accumulation of Gd^{3+} in bones, interference with colorimetric serum determination of calcium and hence spurious hypocalcaemia, interaction with scintigraphic procedures, increased zincuria, interaction with metal-dependent biological systems such as metalloenzymes, etc. Free gadolinium is highly toxic and the ionic radius of Gd^{3+} (107.8 pm) is close to that of Ca^{2+} (114 pm) and this element is an inorganic blocker of many types of voltage-gated calcium channels at nano- to micromolar concentrations, therefore, it cab inhibit those physiological processes which depend upon Ca^{2+} influx.

Generally, there are two structurally distinct categories of gadolinium chelates exist: (a) The ‘macrocyclic’ chelates such as Gd-DOTA (Dotarem), where Gd^{3+} is ‘caged’ in the pre-organized cavity of the ligand. (b) The ‘linear’ chelates such as Gd-DTPA (Magnevist) or Gd-DTPA-BMA. The toxicity of gadolinium complexes actually depends on their ability to release free Gd^{3+} ions. Transmetallation: is a type of organometallic reaction that involves the transfer of ligands from one metal to another. Several cations such as Fe^{3+}, Cu^{2+}, Zn^{2+} or Ca^{2+} compete with

the Gd^{3+} cation and a number of other anions such as PO_4^{3-} , CO_3^{2-} , OH^- can compete with the ligands for the Gd^{3+}. Generally the stability of contrast agents has the following order: *Macrocylic ionic > Macrocylic non-ionic > linear di-ionic > linear non-ionic > cyclic-linear-charge*.

In order to further support the kinetic stability and metal selectivity of ProCA32.collagen1 for Gd^{3+} over Zn^{2+} compared to other clinical contrast agents, 55 µM and 110 µM of ProCA32.collagen1 was used along with 100 µM Gd^{3+}, 100 µM Zn^{2+} in 1.2 mM $PO4^{3-}$ buffer. For clinical contrast agents, 2.5 mM of contrast agents (Omniscan, Eovist, Mganevist and MultiHance) with 2.5 mM Zn^{2+} in 30 mM $PO4^{3-}$ was used in buffer. The relaxation rate (R_1) was measured for each contrast agent over time. To normalize the data, $R_1(t)/R_1(0)$ was calculated. Figure 3f demonstrates the relaxation rates change of clinical contrast agents (Eovist, Magnevist, Ominiscan; ProHance, MultiHance and Dotarem) and ProCA32.collagen1 (loaded with Gd^{3+} to at approximately 1:1 ratio and 1:2 ratio) in phosphate buffer supplemented with $ZnCl_2$ for different length of time. As it can be concluded form Fig. 3f, Omniscan has the highest decrease in relaxation rate after 4000 min incubation with zinc (91.2%). ProCA32.Collagen (1:1) along with Dotarem and ProHance did now show significant decrease in relaxation rate.

In addition, 250 µM of contrast agent as the final concentration was used in the human serum and incubated at 37°C for 13 days. Ponceau S solution and Coomassie brilliant blue were used for staining. As it can be seen in Fig. 8c, ProCA32.collagen1 is stable up to 10 days. These experiments further support the conclusion that ProCA32.colagen1 has significantly higher kinetic stability and metal selectivity for Gd^{3+} over Zn^{2+} than those of Omniscan, Eovist, Magnevist and MultiHance. In addition, ProCA32.collagen1 has a strong proteolytic stability, as revealed by its structural integrity for 10 days of incubation in human serum. These two experiments also showed that high concentration of Zn^{2+} is not able to compete with Gd^{3+} in ProCA32.collagen1.

6.4 Potential Application and Significance

Based on the results described in this study, ProCA32.collagen1 is capable of detecting early stage II UM tumor liver metastasis with high sensitivity which has not been achieved before by any clinical or research-based MRI contrast agent. In addition, for the first time, an MRI contrast agent is able to differentiate UM tumor growth patterns (nodular and infiltrative) in the liver resulting in important clinical consequences in terms of choosing the best treatment for UM. Detection of liver metastasis can make significant difference in patient treatment outcome and survival. In addition, noninvasive detection of tumor heterogeneity using ProCA32.collagen1 can provide important information regarding the population of different cell types (inflammatory or tumor cells).

Since of ProCA32.collagen1 has higher relaxivity values for both r_1 and r_2 compared to other contrast agents, different imaging sequences can be applied to increase the detection confidence. Furthermore, less injection dosage can be used to avoid toxicity as our results demonstrate.

6.5 Summary and Conclusion

The MRI images suggest that the contrast agent has the capability of enhancing the tumor signal in much longer times post injection (24 hours) in both T_1- and T_2-weighted images. In addition, inversion recovery technique was successfully applied for the deigned contrast agent which led to 6-fold increase in the relative contrast of the mouse implanted tumor compared to pre-injection image. Furthermore, MRI images in metastatic model (M20) studies showed the heterogeneous distribution of the contrast agent in tumors which further prove the targeting capability. Gd^{3+} biodistribution results strongly correlates with tissue staining studies. Picro-Sirius

Red staining results suggest that collagen pattern and level difference based on tumor pattern difference and the capacity of ProCA32.collagen1 in distinguishing them.

Transmetallation data suggest that ProCA32.collagen1 with (1:1) ratio of Gd^{3+} and protein has the highest kinetic stability among other clinical contrast agents. Furthermore, the contrast agent is stable in human serum up to 10 days. ProCA32.collagen1 can be considered as a promising agent in early detection of uveal melanoma metastatic liver tumor as well as distinguishing pattern difference. In addition, based on the literature, collagen has different expression levels depending on the type of the tumor, therefore, our contrast agent can be used to distinguish the originality of the metastatic tumor.

Collagen expression and changes are major diagnostic biomarker and therapeutic target for many chronic diseases including chronic liver diseases, many types of cancers and metastasis, heart failure, and pulmonary fibrosis. Uveal melanoma, the most common primary intraocular tumor, has a 40% risk of metastasizing to the liver that results in death in almost all cases. To date, there is no reliable noninvasive imaging method for early detection and staging of primary liver cancer and hepatic metastases with high sensitivity and specificity. MRI has several unique advantages for monitoring slow progression and detection of metastasis with high resolution without using radiation. There is a pressing unmet medical need to develop MRI contrast agents with desired sensitivity and collagen specificity to overcome high heterogeneous background as well as proper in vivo properties and reduced toxicity. In this study, we report the success in designing a protein-based MRI contrast agent, ProCA32.collagen1 with collagen type I targeting capability to diagnose and stage the metastasis of uveal melanoma. ProCA32.collagen1 exhibits the highest relaxivity values for r_1 and r_2 per Gd^{3+} at both 1.5 and 7.0 T and are 14-20-fold higher than clinically used contrast agents. The uniqueness of both high r_1 and r_2 relaxivity values enable

us to achieve both T_1 and T_2 imaging after a single injection of ProCA32.collagen1. More important, we can significantly improve dynamic range in detection with a 6-fold enhancement in the relative contrast for the implanted liver uveal melanoma tumor in mouse taken advantage of both relaxation property and imaging methodology. In addition, ProCA32.collagen1 is able to differentiate M15 uveal melanoma metastasized to the liver with nodular pattern from infiltrative with 14-fold increase in contrast to noise ratio (CNR) which has not been achieved using clinical contrast agent. Distinguishing different patterns of uveal melanoma has significant clinical implications in terms of choosing the most effective treatment. Based on MRI correlation with histology analysis, ProCA32.collagen1 is capable of detecting tumors as small as 0.250 mm^2 which is much smaller than not only the current detection limit of 10–20 mm but also tumors previously detected by ProCA32-P40. We have further shown that the addition of targeting moiety does not reduce its strong metal binding affinity to Gd^{3+} and 10^{11}-fold higher selectivity towards Gd^{3+} over Zn^{2+} than Eovist. The development of collagen targeting contrast agent is expected to have broad applications in detection and staging of liver metastasis from various types of cancer and probing heterogeneous microenvironment changes upon disease progression and treatment.

7 APPLICATION OF PROCA32.COLLAGEN1 IN DETCTION OF HEPATOCELLULAR CARCINOMA (HCC)

7.1 Introduction

Hepatocellular carcinoma (HCC) is the most common primary malignancy of the liver. Worldwide, approximately 500,000 new patients are diagnosed with HCC each year, often associated with poor prognosis [367]. It is the fifth most frequent neoplasm and ranks third on the list of most lethal cancers [368, 369]. The highest incidence of HCC is found in Asia and sub-

Saharan Africa. Most cases of HCC develop in a background of chronic liver damage such as cirrhosis or hepatitis [370].

Cirrhosis from any cause predisposes to hepatocellular carcinoma (HCC) and hence can be considered a premalignant condition. Indeed, the majority of patients worldwide with HCC have underlying cirrhosis [371]. With the exception of some areas of the world where hepatitis B virus (HBV) infection is endemic and the role of other oncogenic agents (ie, aflatoxin) may be important, [372] it is uncommon to find HCC in the absence of cirrhosis. On a global basis, longitudinal studies indicate that cirrhosis related to either hepatitis C virus (HCV) or hepatitis B virus (HBV) infections represent the major known risk factors for HCC [370, 373, 374].

7.1.1 HCC in Cirrhosis

HCC is a common cause of death among patients with compensated cirrhosis. European cohort studies have reported that, among persons who died of a liver- related cause, HCC was the responsible cause in 54% 6 to 70% [375] of patients with compensated cirrhosis of different etiologies and in 50% of patients with HCV-related cirrhosis [376]. Data from one of the longitudinal studies, which involved 112 cirrhotic patients with HCC detected during ultrasound surveillance, showed that tumor progression was the cause of death of 63% of patients with HCC who died during the first 4 years of surveillance (1987–1991), of 69% who died during the second 4-year period (1992–1996), and of 83% who died during the third period (1997–2001) [374].

Recent epidemiologic data indicate that, in the United States as well as in some European countries, the mortality rate from HCC is increasing [377-379]. Conversely, cirrhosis-related mortality not due to HCC declined into the early 1990s in the same areas, [380-382] although, subsequently, remained stable in the United States between 1995 and 1998 [383]. A similar trend was noted in Italy, between 1969 and 2000, where the mortality rates of cirrhosis showed a clear

decline while the mortality rates for HCC slowly increased. A possible explanation for these findings is that medical management of non-HCC complications of cirrhosis, such as prevention and treatment of variceal bleeding and management of ascites, has improved, as has the availability of alcoholism treatment, leading to longer survival of patients with cirrhosis, who in turn are at greater risk over time of developing HCC. A recent report of a decrease in the mortality rate of alcohol-related cirrhosis supports this hypothesis [384, 385].

7.1.2 Benign versus malignant hepatic nodules in HCC

According to the currently used nomenclature, there are only two types of hepatocellular nodular lesions: regenerative lesions and dysplastic or neoplastic lesions. Regenerative nodules include monoacinar regenerative nodules, multiacinar regenerative nodules, cirrhotic nodules, segmental or lobar hyperplasia, and focal nodular hyperplasia. Dysplastic or neoplastic nodules include hepatocellular adenoma, dysplastic foci, dysplastic nodules, and hepatocellular carcinoma (HCC) [386-388].

Many of these types of hepatic nodules play a role in the de novo and stepwise carcinogenesis of HCC, which comprises the following steps: regenerative nodule, low-grade dysplastic nodule, high-grade dysplastic nodule, small HCC, and large HCC (Fig. 7.1).

During the past 2 decades, MR imaging has emerged as an important imaging modality for assessing cirrhosis and its complications, such as hepatic nodules [386]. For assessment of hepatic nodules, MR imaging is more useful than any other imaging modality currently available [386].

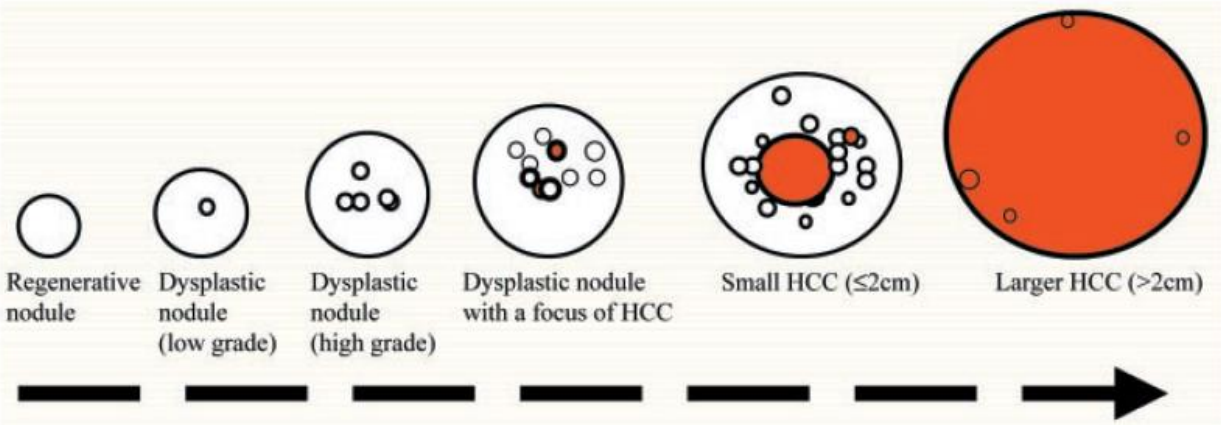

Figure 7.1 *Different steps in generation of carcinogenesis for HCC in cirrhosis[387]*.

Although arterial enhancement with delayed washout, increased T2-weighted signal intensity, delayed capsular enhancement, restricted diffusion, and tumor thrombus are typical features, not all lesions demonstrate these findings. The radiologist must be familiar with these typical imaging characteristics, and less common appearances and associated findings of HCC, and must be able to differentiate them from those of lesions that mimic HCC. Knowledge of therapeutic options and how those are related to imaging findings is imperative to assist clinicians in managing these patients [386].

Accordingly, researchers have aimed to derive target genes and drug candidates for HCC; however, the development of targeted drugs has not yet significantly improved outcomes [389, 390]. Lately, the paradigm in cancer biology has shifted from the study of the genetics of tumor cells alone to the complicated crosstalk between cancer and the tumor microenvironment (TME) [391, 392]. The TME is the cellular environment in which the tumor exists, including the surrounding blood vessels, immune cells, fibroblasts, other cells, signaling molecules, and the extracellular matrix (ECM). Recent studies have shown that the stromal cells in HCC have a dynamic and flexible function in tumor proliferation, invasion, and metastasis, and that the cells of the TME can regulate the response of cancer cells to chemotherapy [393-395]. Hepatic stellate

cells (HSCs) play critical roles in diverse aspects of liver physiology, including liver organogenesis, regeneration, and HCC. HSCs are found in the space of Disse between the sinusoidal endothelial cells and hepatic epithelial cells [396].

Hallmarks of HSC activation are reduced levels of intracellular lipid drop- lets, increased expression of α-smooth muscle actin (α-SMA) and ECM production, as well as morphological changes [397, 398]. Additionally, the interaction between HCC and activated HSCs forms a pro-angiogenic microenvironment by the overexpression of VEGF-α and matrix metallopeptidase 9 (MMP9) [399-401].

ECM-related proteins in the TME play important roles in liver function in health and disease. Abnormal ECM composition and structure in solid tumors are the major obstacles for the penetration of anticancer drugs. Among ECM proteins, collagens and specially collagen type I are the most abundant structural protein in the liver. A disproportionate concentration of collagen type I results in altered cell phenotypes and architectural distortion with abnormal blood flow in the liver. Moreover, a high collagen type I content is a key barrier for interstitial drug penetration among ECM-related proteins [402] and thereby reduces the efficacy of chemotherapeutics. Because HCC is developed from chronically damaged tissue that contains a large amount of inflammation and fibrosis, further knowledge of the crosstalk between HCC and their TME is essential for achieving a better understanding of tumor development, progression, and chemoresistance in HCC [402, 403].

7.1.3 The challenges in diagnosis of hepatocellular carcinoma

The aim of early detection plans in patients at risk of hepatocellular carcinoma (HCC) is to detect the tumor at an evolutionary phase, when a cure with long-term disease-free survival is

highly likely [404]. Accordingly, the goal is to detect and diagnose tumors when they are smaller than 2 cm in size, the so-called BCLC stage 0. Beyond this cutoff, the prevalence of satellites and/or microvascular invasion is significantly increased and treatments such as resection, transplant, and ablation will be plagued by recurrence due to dissemination prior to treatment [404].

While this goal is easy to frame, establishing accurate diagnosis in such small nodules is a major clinical challenge. Tumor markers, including alpha-fetoprotein and novel ones such as glypican or PIVKA, have no major usefulness for screening and diagnosis [404], and thus, as in most other cancer types, diagnosis would require a positive biopsy. Nevertheless, biopsy is known to have a suboptimal sensitivity (around 60–70 %) [405]. It provides a limited amount of tissue, and the fact that such small HCCs are usually well differentiated makes it difficult to confidently distinguish HCC from dysplastic or regenerative nodules. Even expert pathologists would not have a 100 % agreement without false positives and false negatives in such small malignant nodules. Immunohistochemical staining for glypican 3, heat-shock protein 90, or survivin may reinforce HCC suspicion, but they do not increase the diagnostic rate. Diagnostic signatures based on gene expression have also been proposed but have not been validated, and such molecular diagnosis is not yet in clinical practice. Even if biopsy would have 100 % sensitivity, it would not be feasible in some patients because of the location or the presence of clotting disorders.

All these comments explain the development of imaging criteria for the non-invasive diagnosis of HCC [405]. The increased arterial blood supply that characterizes HCC provides the basis for the increased contrast uptake in the arterial phase of dynamic techniques, such as computed tomography and magnetic resonance. This is a hallmark of malignancy and, if it is followed by hypointensity in the venous/delayed phases, the profile is specific for HCC [405].

This hypointense appearance of the hypervascular focal lesions known as ‘‘wash-out’’ is due to the venous supply being less prominent in HCC as compared to the surrounding liver, and, thus, the arrival of contrast through the portal vein, so that the liver intensity is enhanced as compared to the tumor. Several studies have validated such a profile as almost 100 % specific for HCC [406, 407]. Interestingly, while intrahepatic cholangiocarcinoma may display increased arterial blood supply, it does not show washout and this is key for the distinction between these two entities, which have a sharply different prognosis and treatment [5, 6]. It is important to note that intrahepatic cholangiocarcinoma (ICC) incidence is on the rise and cirrhosis is a major risk for it. Thus, differentiation between HCC and ICC is not futile. Nevertheless, as happens with biopsy, the diagnostic sensitivity of CT or MR for small HCC (~2 cm) is far from 100 %. Increased arterial blood supply appears along tumor growth and, currently, just 60–70 % of HCC\2 cm can be confidently diagnosed by imaging techniques [407].

7.1.4 Limitations of current clinical contrast agents in HCC diagnosis

All these limitations explain the need to further improve the diagnostic accuracy of imaging techniques in order to set a non-invasive diagnosis avoiding the request for a positive biopsy. The use of organ-specific contrast agents such as gadoxetic acid (GA or Eovist) or aims to fulfill this goal.

Eovist is a combined hepatobiliary (HB) and Gadolinium-chelates contrast agent, suitable for regular dynamic multiphasic studies, that offers the possibility to obtain both the conventional arterial and venous phases, but also a 20-min delayed HB phase. At this delayed time point, the hepatocytes have taken up the 50 % of the administered dose [278, 408-410]. Therefore, non-hepatocyte focal lesions and those with non-functional hepatocytes, such as most HCCs, should not accumulate contrast. This results in low signal intensity foci relative to the intensity of the liver

parenchyma in the HB phase of Eovist-enhanced MR. While this background would make Eovist-MRI an optimal technique, there are a number of issues that need active research.

Several studies suggest a potential diagnostic value [411-415], but no robust prospective study has defined its added diagnostic value in the clinical setting. Very early HCC with well-preserved hepatocyte function may show GA uptake and offer false negative results. In addition, as previously mentioned, ICC may also emerge in a cirrhotic liver, and likely this opens a potential for false positive diagnosis. Finally, the technicalities for the optimal use of GA for an adequate reading of the arterial and venous phases of MRI as done currently with gadolinium chelates are not well established. The injection rate of the small amount of contrast injected for GA-MRI may limit the proper recognition of the contrast uptake in the arterial phase and, thus, impair the use of the already validated criteria based on the recognition of arterial uptake followed by wash-out. Even wash-out recognition in such nodules may be impaired, as uptake of GA in the biliary phase may overlap with the delayed venous one. Accordingly, the injection of higher volumes or the use of different injection rates have been proposed to optimize the information offered by GA-MR.

Prior studies have evaluated the impact of injection rate and the amount of contrast injected with controversial results. Zech et al. [416] compared in an experimental study the influence of regular to double doses and different rates of injection (1–2 mL/s) on the enhancement of liver vasculature in GA-MR and Gd-DTPA. They found that the arterial enhancement in GA-MR injected at 1 mL/s was comparable to Gd-DTPA. Haradome et al. [417] reported in a retrospective study on 216 patients that fluoroscopic triggering GA-MR and slow rate injection provide proper arterial phase images. Schmid-Tannwald et al. [418]compared two injection rates (1 and 2 mL/s) for GA-MR dynamic studies in 80 patients and reported higher enhancement in the aorta in the arterial phase with the lower injection rate. Feuerlein et al. [419] compared the enhancement

characteristics of liver parenchyma, portal vein, and the portal vein to liver contrast with two HB contrast agents in 70 patients. The authors found that contrast in the arterial and portal venous phases was lower when GA was used compared to Gd-BOPTA.

It is important to note that such studies do not include patients with liver tumors. Such information is the focus of the manuscript by Chen et al. [420] published in this issue of Hepatology International. The authors describe that, in hypervascular HCCs, the enhancement in the arterial and portal phases is lower than that observed when using the conventional non-specific gadolinium. The authors found that the relative contrast difference between the liver and HCC was significantly less when using GA as compared with a nonspecific gadolinium, but, interestingly, it was increased in the portal phase. This resulted in a better definition of the hypointense lesions that may be due to the overlap of the delayed venous phase and the early HB uptake of GA by the nontumoral liver.

All these studies suggest that clinical MRI contrast agents have considerable weaknesses for the diagnosis and staging of patients with suspected or proven HCC and major clinical research is needed to develop more sensitive MRI contrast agents for the proper management of patients diagnosed with HCC. In this Chapter, our efforts to apply ProCA32.collagen1 in MR detection of HCC tumors in DEN-induced mouse model will be discussed.

7.2 Results

7.2.1 DEN-induced HCC

For these studies first, the HCC animal model was generated. For all of our studies, we employed female and male mice with C57BL/6 genetic background. Experiments involving animals were conducted in accordance with the NIH Guide for the Care and Use of Laboratory Animals and were approved by the Georgia State University IACUC. Animals were housed in a

pathogen-free animal facility under a 12 h light/dark cycle and fed a standard rodent chow and water ad libitum. In order to induce liver tumor development, 14-day-old mice were treated with a single dose of DEN (Sigma–Aldrich # N0756) given dissolved in saline at a dose of 25 mg/kg body weight by i.p. injection. Mice in one randomly pre-assigned group were killed 10 months after DEN administration for histological and biochemical analyses. Mice were randomly distributed in various groups having equal males and females.

Immediately after euthanizing, livers were removed, weighed and the numbers of visible tumors on the liver surface were counted macroscopically. The largest lobes were fixed in formalin and embedded in paraffin. Sections were stained with hematoxylin and eosin and examined microscopically.

Two mice with HCC were selected for MRI scan and after scan they were sacrificed, and livers were collected and weighted for HCC assessment (Fig. 7.2). As it can be seen from the images multiple tumors have developed in the liver which shows the large volume of the liver compared to normal liver.

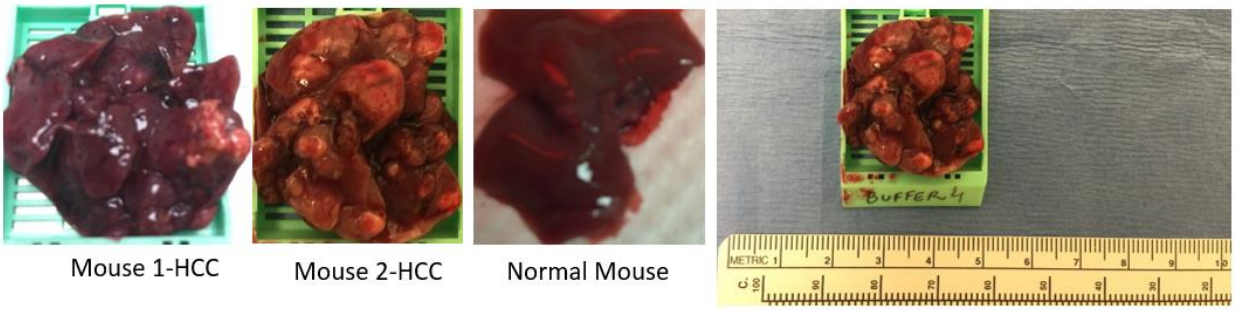

Figure 7.2 *HCC mouse livers after treatment compared to normal liver.*

7.2.2 MRI results of DEN-induced HCC mouse

The mice with HCC tumors were tail-vein injected with ProCA32.collagen1 and T2-wighted, T1-weighted, T1 map inversion recovery and T2 maps were collected before and 3 and 24 hrs post injection of ProCA32.collagen1. As Figures 7.3 to 7.6 show, after injection of ProCA32.collagen1 at both 3 and 24 hrs, there is enhancement in the tumor areas as well as cirrhotic regions.

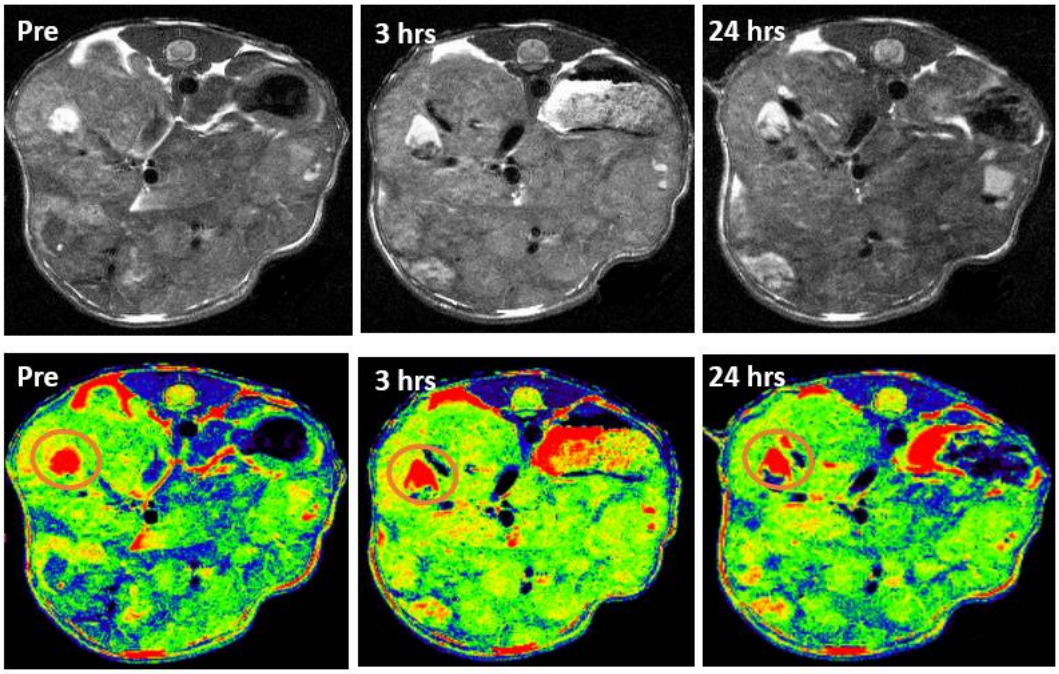

Figure 7.3 *T2-weighted images of HCC mouse post injection of ProCA32.collagen1*

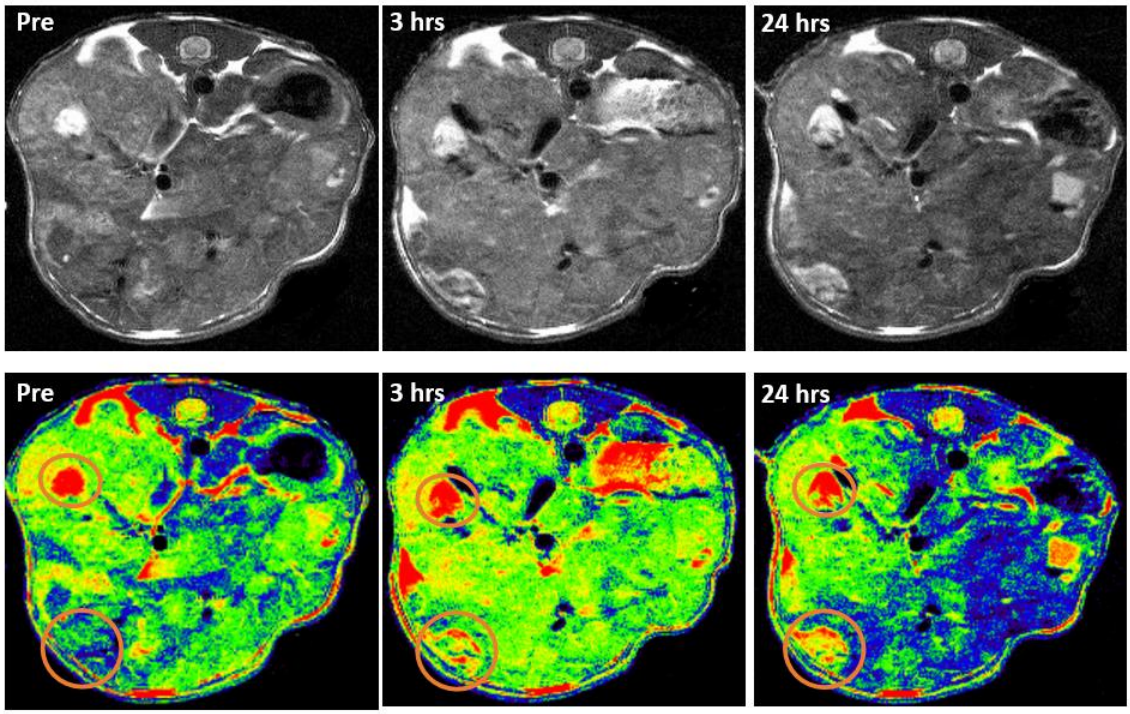

Figure 7.4 *T2-weighted images of HCC mouse post injection of ProCA32.collagen1 in a different slice of liver*

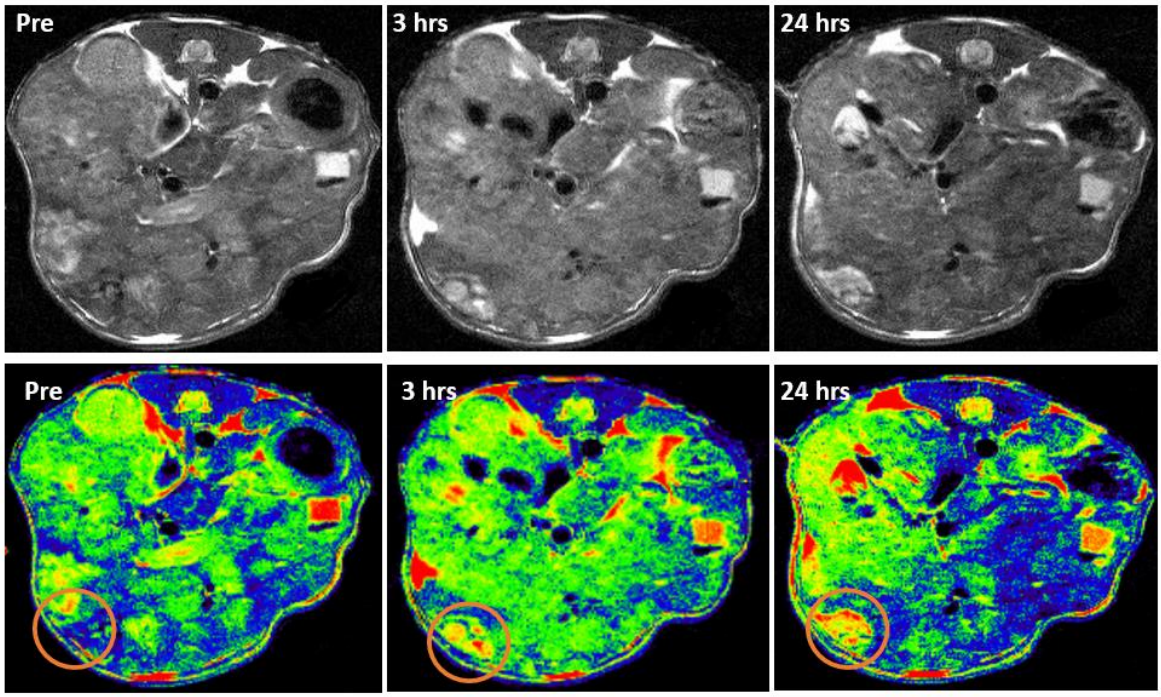

Figure 7.5 *T2-weighted MRI images in slice 12 of HCC mouse liver*

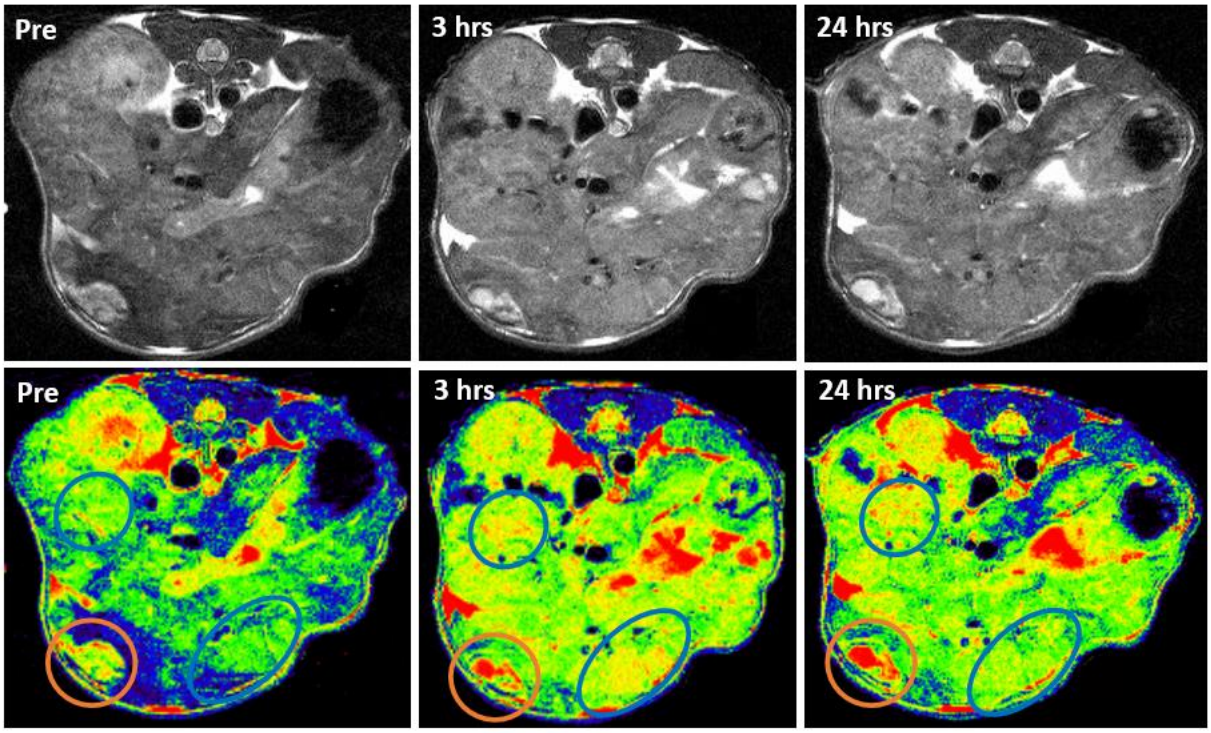

Figure 7.6 *T2-weighted MRI images in slice 13 of HCC mouse liver. Areas in orange circle shows the enhancement in tumor and areas in blue circle is showing the cirrhotic areas. ProCA32.collagen1 is able to detect both tumors and cirrhotic areas.*

Figure 7.6 is a clear demonstration of mixture of HCC and cirrhosis in the mouse liver observed by ProCA32.collagen1. In 3 hrs post injection of the contrast agent, a significant enhancement is observed in the cirrhotic areas (blue circle), and after 24 hours the contrast agent is washed out, therefore the enhancement is decreasing. Moreover, ProCA32.collagen1 can demonstrate HCC tumor 3 and 24 hrs post injection as shown by orange circle.

Further analysis of another HCC mouse (Fig. 7.7) confirms the results and show the same phenomenon.

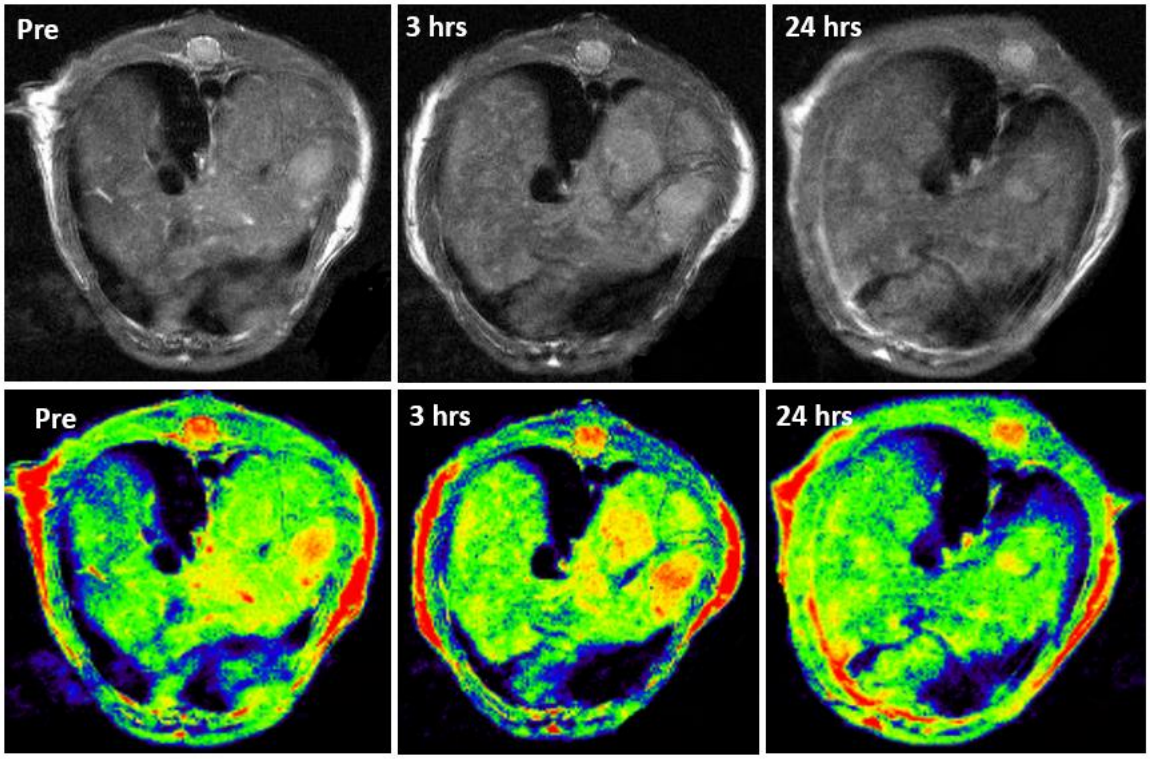

Figure 7.7 *T2-weighted MRI images of another HCC mouse liver before and 3 and 24 hrs post injection of ProCA32.collagen1*

As Fig. 7.7 demonstrates, the left segment of liver is more cirrhotic and right segment has possibly two large tumors as defined by their boundaries. After injection of ProCA32.collagen1 at 3 hrs, a significant enhancement is observed in the two large tumors as well as left segment of liver showing cirrhotic region.

Fig. 7.8 shows the R2 map analysis after injection of ProCA32.collagen1. As it is observed from the figure, T2 map results further confirm the T2-weighted results (Fig. 7.7). After quantitative analysis of T2 values, both left and right tumors in the right segment of liver showing decrease in T2 and increase in R2 (MRI image). Furthermore, left down segment of liver showing increase in R2 and decrease in T2 as indication of cirrhotic regions.

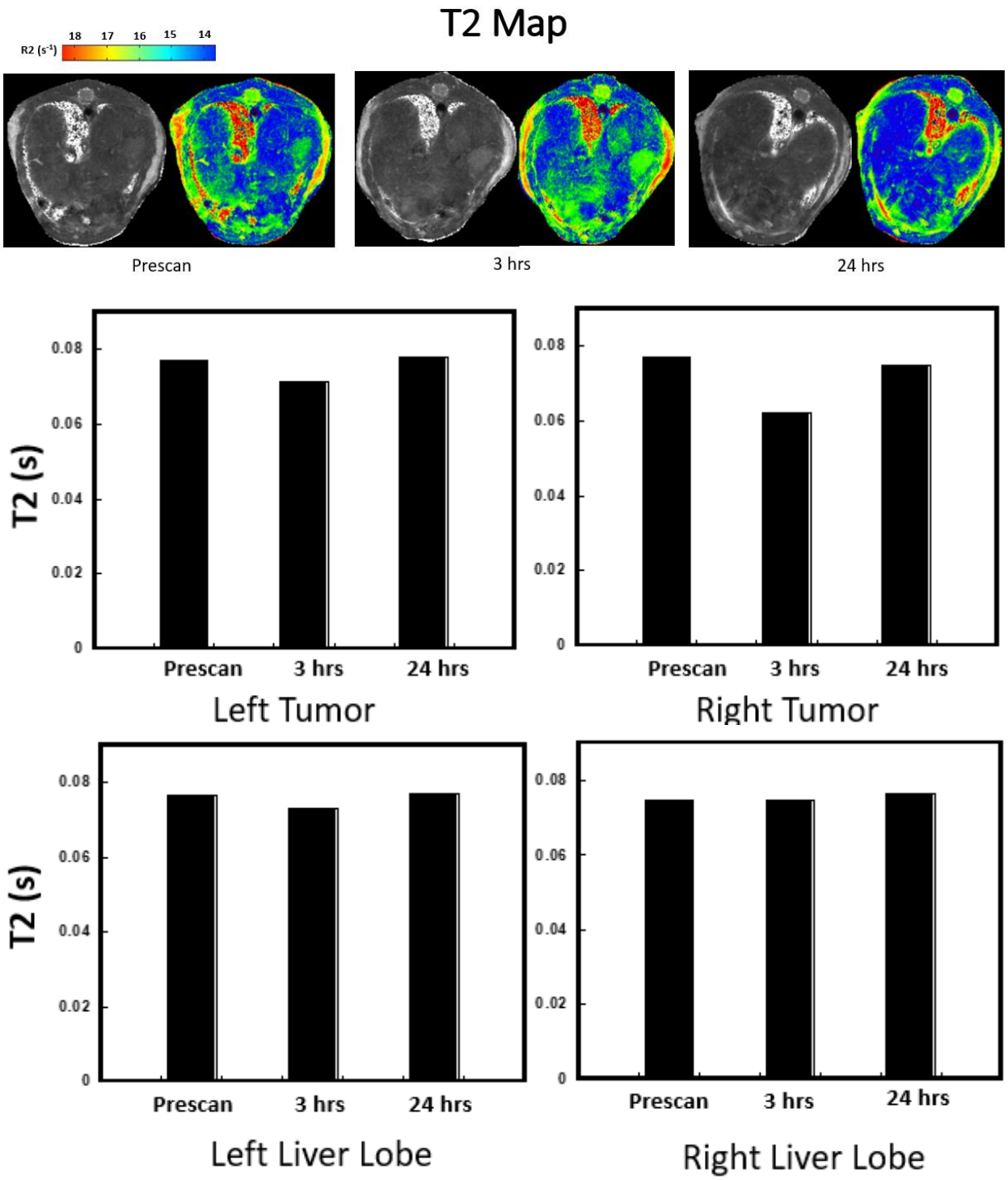

Figure 7.8 *T2 map analysis of HCC tumors and cirrhotic areas in DEN-induced HCC mouse liver. R2 map MRI images showing enhancement in tumors and quantitative analysis of T2 values showing decrease in both tumors and cirrhotic regions in the liver.*

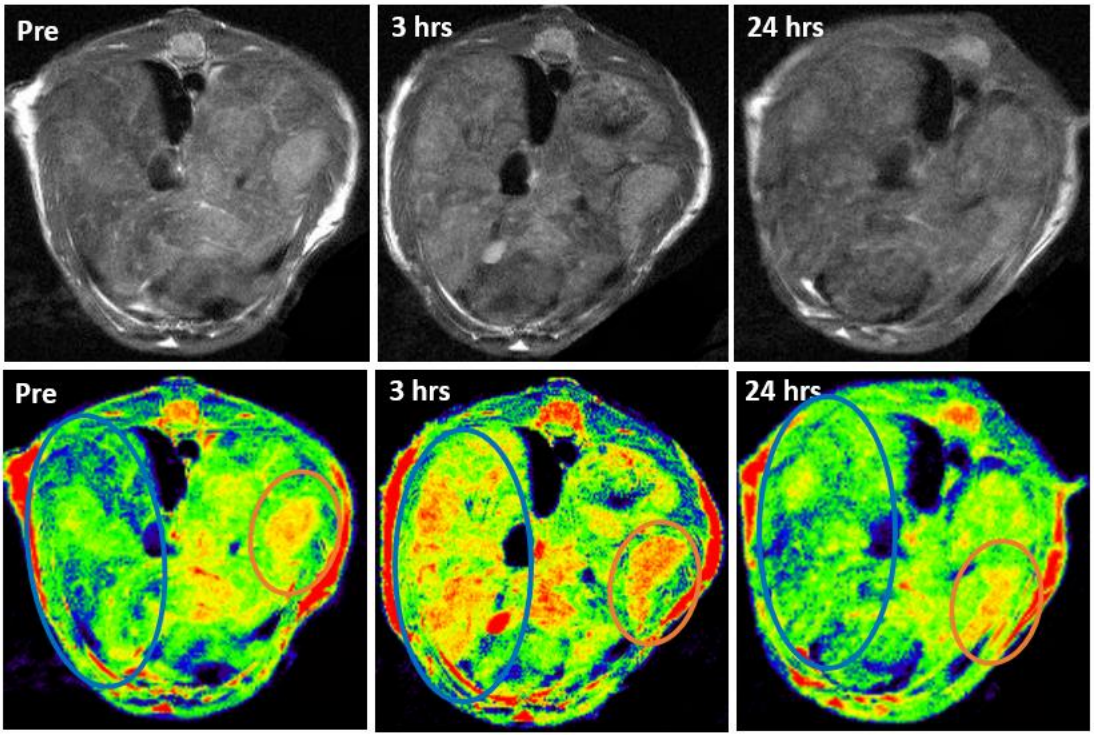

Figure 7.9 *T2-weighted MRI images of slice 2 of DEN-induced HCC mouse liver before and 3 and 24 hrs post injection of ProCA32.collagen1.*

Left segment of liver has significant enhancement 3 hrs post injection of ProCA32.collagen1 (blue circle) demonstrating cirrhotic regions and after 24 hours the contrast is washed out. Right segment of liver which was significantly enhanced after 3 hours showing HCC tumor (orange circle).

These results are consistent with results from previous HCC mouse (Fig. 7.7) which show that results are reproducible with the injection of ProCA32.collagen1. Moreover, R2 map MRI results are complimentary to T2-weighted results showing the same pattern for cirrhotic areas and tumor regions (Fig. 7.10).

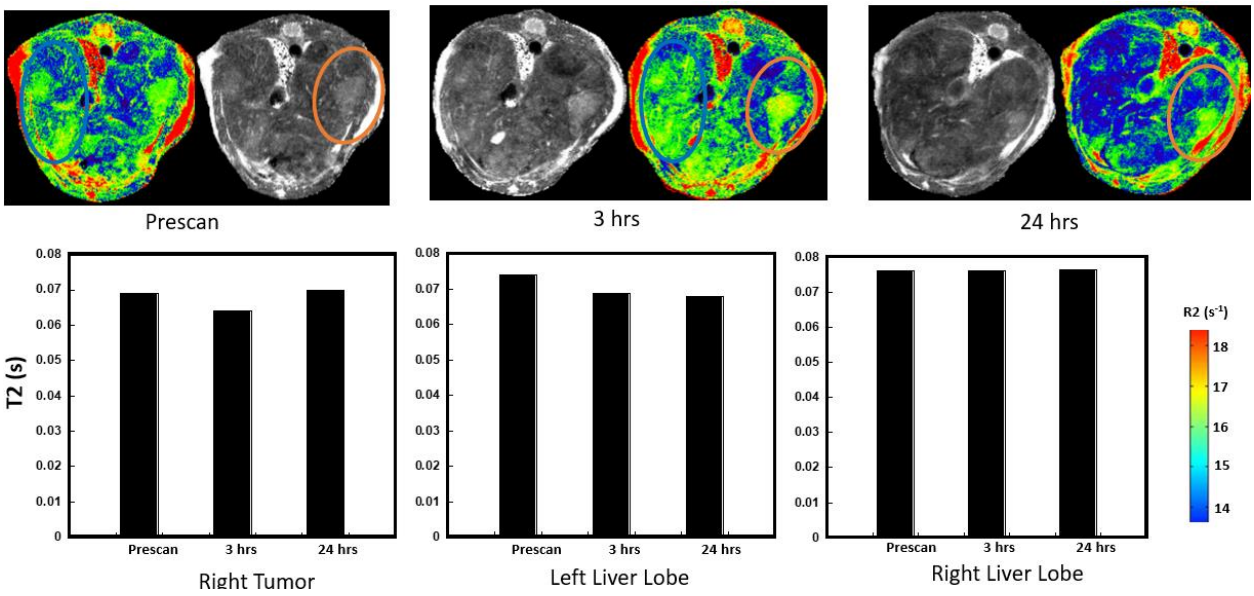

Figure 7.10 *R2 map MRI images and quantitative T2 analysis of slice 2 of DEN-induced HCC mouse liver before and 3 and 24 hrs post injection of ProCA32.collagen1.*

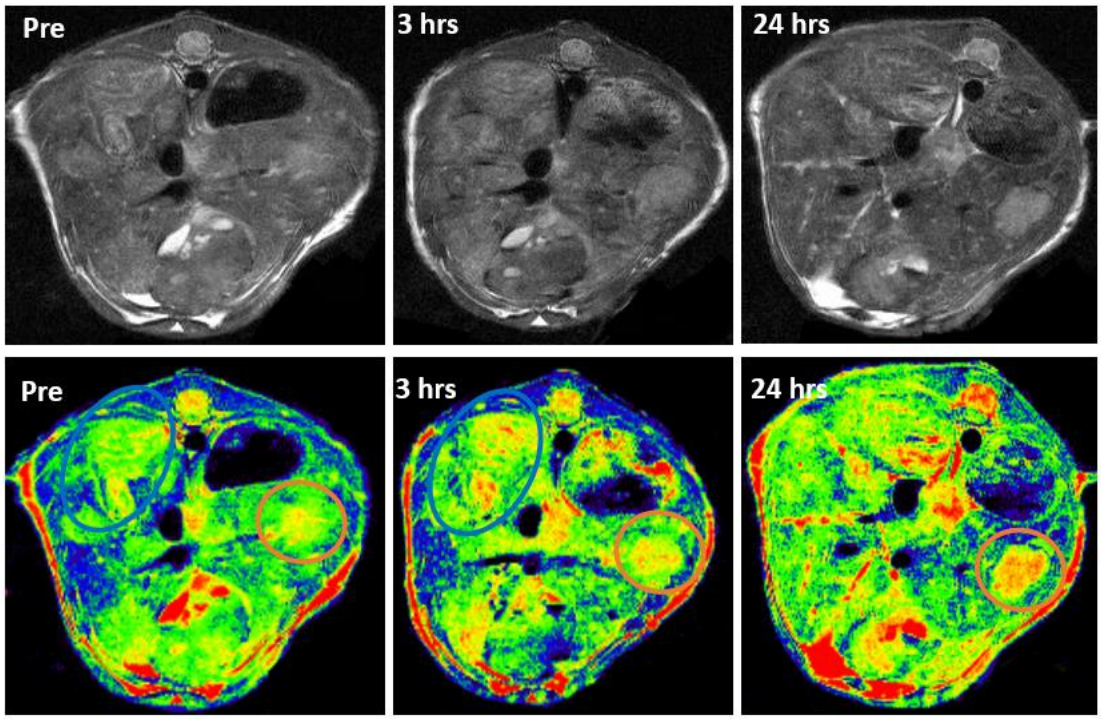

Figure 7.11 *T2-weighted MRI images of slice 4 of DEN-induced HCC mouse liver before and 3 and 24 hrs post injection of ProCA32.collagen1.*

Since our ProCA32.collagen1 has both r_1 and r_2 property, we scanned these HCC mice with multiple pulse sequence to further increase the confidence level of detection. Therefore, T1-weighted MRI was also used assess the tumor and cirrhotic regions of HCC mice.

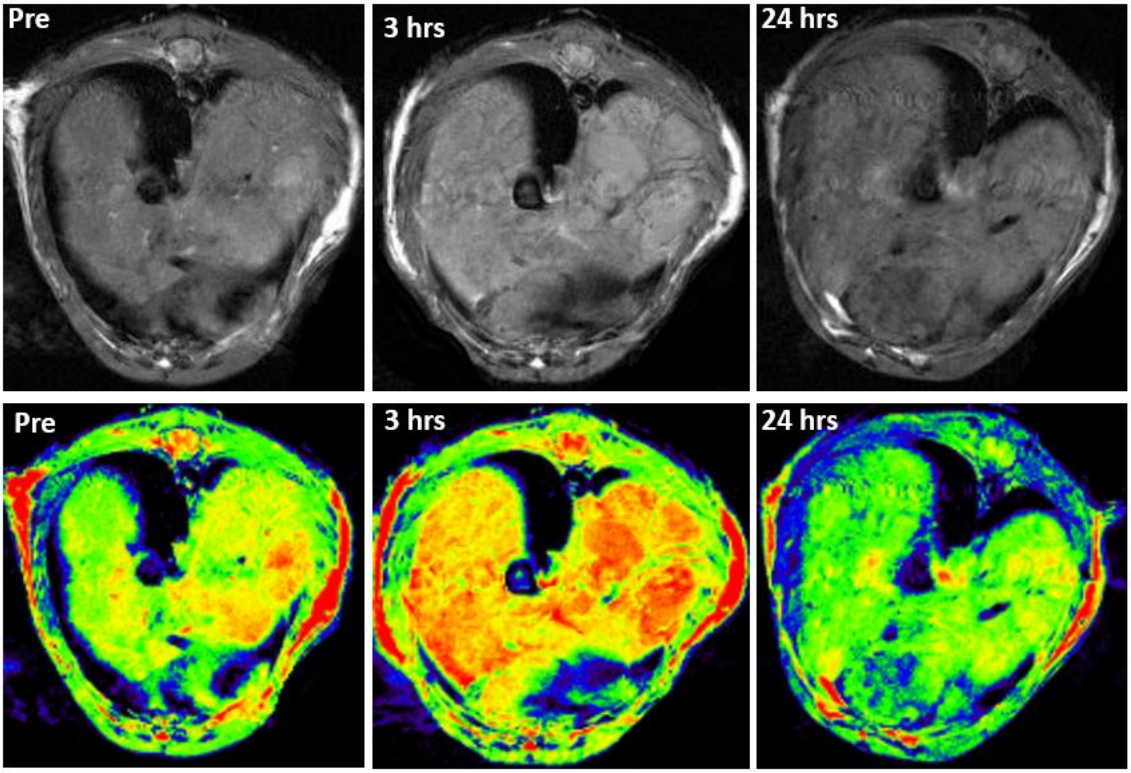

Figure 7.12 *T1-weighted MRI images of another HCC mouse liver before and 3 and 24 hrs post injection of ProCA32.collagen1.*

T1-weighted MRI images showing different regions of liver enhanced consistent with T2-weighted images in Fig. 7.7 in the same slice.

Figures 7.13 and 7.14 show the significant enhancement of liver and cirrhotic regions 3 hrs post injection of ProCA32.collagen1 in T1-weighted MRI image.

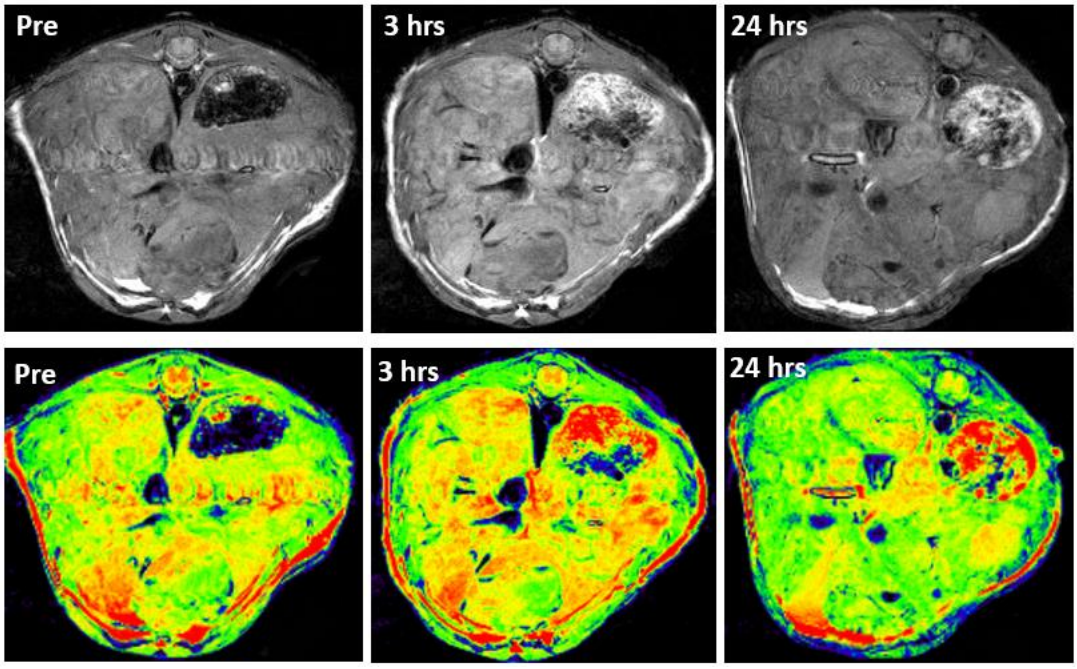

Figure 7.13 *T1-weighted MRI images of slice 4 of HCC mouse liver before and 3 and 24 hrs post injection of ProCA32.collagen1.*

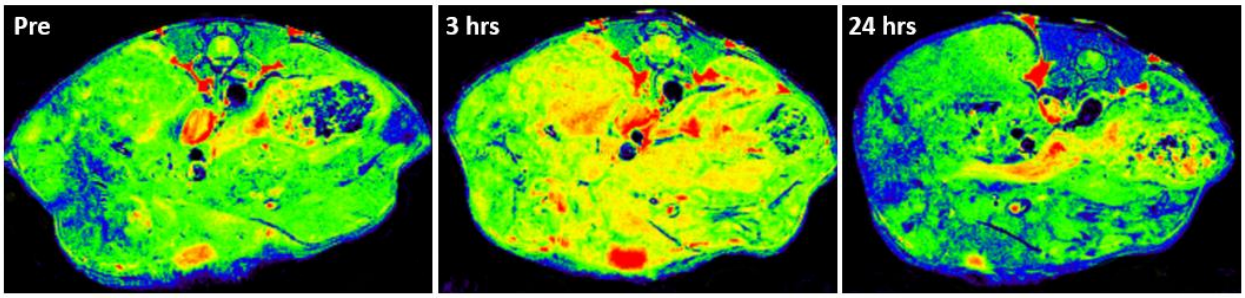

Figure 7.14 *T1-weighted MRI images of slice 5 of HCC mouse liver before and 3 and 24 hrs post injection of ProCA32.collagen1.*

7.2.3 Histology results of DEN-induced HCC mouse liver

In order to confirm the presence of tumors and collagen in HCC mouse livers, H&E and Sirius red staining were performed on paraffin embedded section of mouse liver.

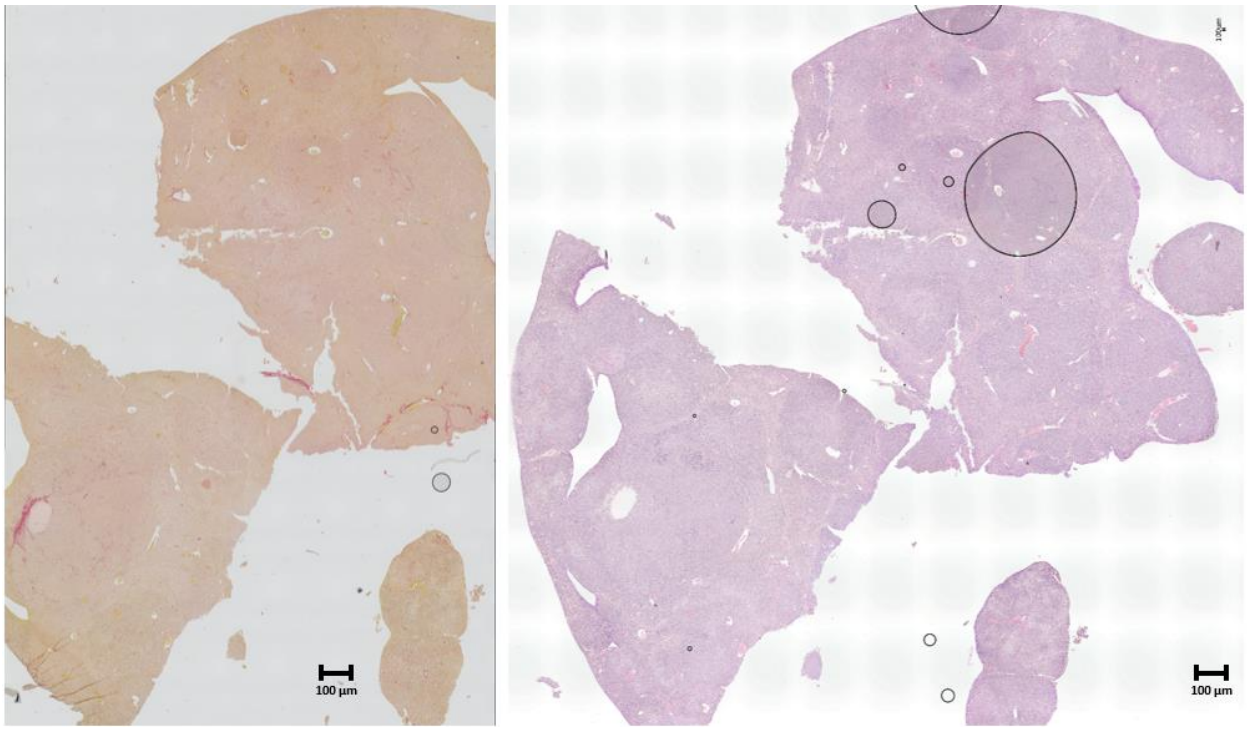

Figure 7.15 *Sirius red (left) and H&E (right) staining of mouse HCC liver. Left picture showing Sirius red staining of collagen (red) in liver and right picture demonstrating H&E. The areas with darker pink show HCC tumors as it is observed from their boundaries.*

Further analysis is required to completely correlate each specific tumor from histology with MRI and it is currently being studied.

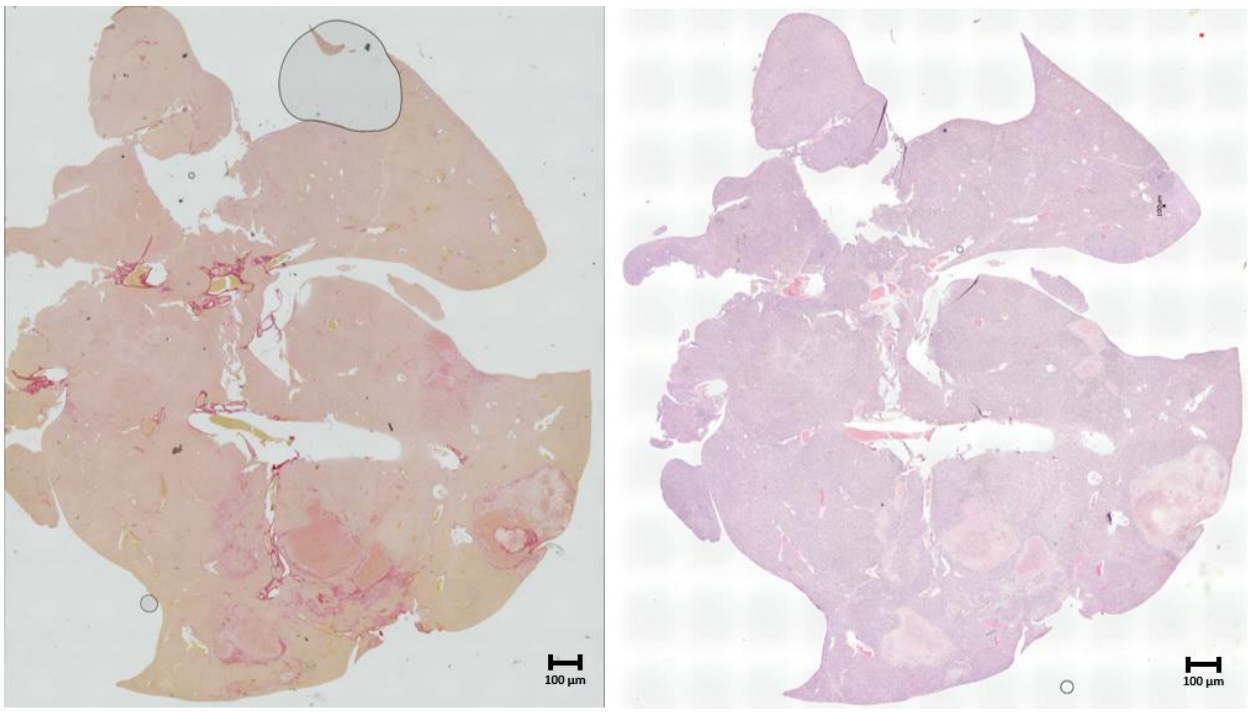

Figure 7.16 *Sirius red (left) and H&E (right) staining of mouse HCC liver.*

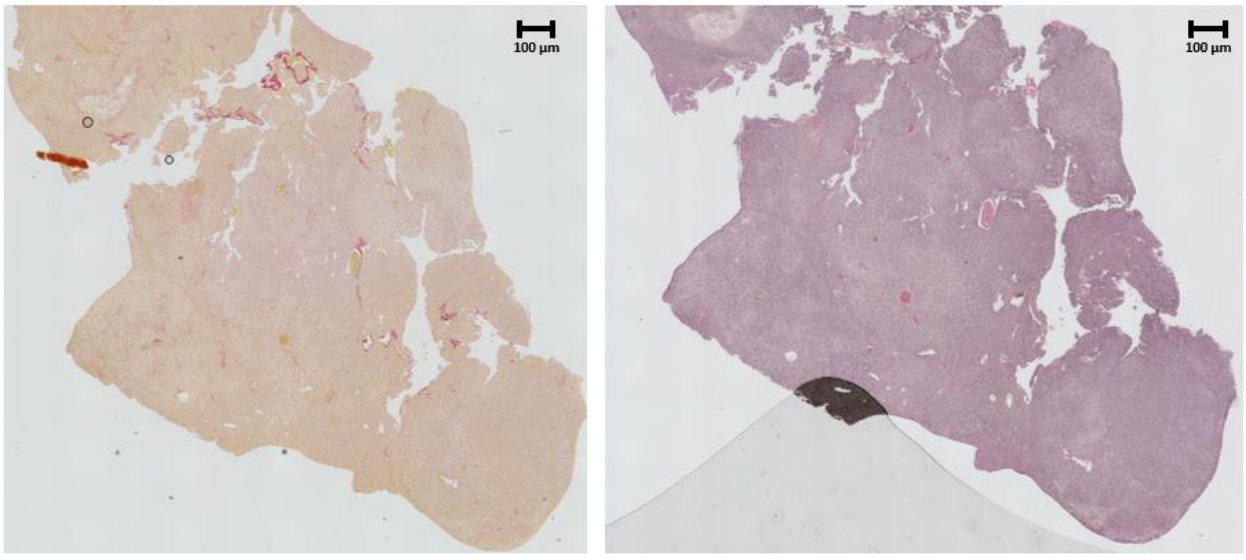

Figure 7.17 *Sirius red (left) and H&E (right) staining of mouse HCC liver.*

7.3 Summary

In summary, ProCA32.collagen1 was successfully applied in detection of DEN-induced HCC mouse model in the liver. ProCA32.collagen1 is able to enhance both cirrhotic and tumor areas in the model as confirmed by several pulse sequences. One of the advantages of using ProCA32.collagen1 in detection of HCC is that because of both r_1 and r_2 property, T1- and T2-weighted and T1 and T2 maps can be used to increase the level confidence for the detection and avoid observing artifacts in the MRI. Moreover, based on MRI images, ProCA32.collagen1 is able to show heterogeneous enhancement in both cirrhotic and tumors areas which reflect the heterogeneous collagen expression in these areas. Distinguishing collagen patterns and arrangement in HCC tumor from collagen patterns in cirrhotic areas can be a significant achievement in the clinical imaging field. These differences can shed light on how cirrhosis can progress to HCC and help with treatment strategies and even distinguishing different tumor subtypes in HCC. Further studies and correlation between MRI images and histology results are needed to achieve this goal.

8 APPLICATION OF PROCA32.COLLAGEN1 IN DETECTION OF THORACIC AORTIC ANEURYSM (TAA)

8.1 Introduction

Aortic aneurysms exhibit permanent luminal expansion of the aorta that portends rupture and usually leads to death. This disease occurs in both abdominal and thoracic aortic regions, which are termed as abdominal aortic aneurysms (AAAs) and thoracic aortic aneurysms (TAAs), respectively. Due to an incomplete understanding of molecular mechanisms and pathophysiologic processes, there is no proven medical therapy that can prevent expansion or rupture of either type of aortic aneurysms.

Patients with suspected dissection of the thoracic aorta require immediate diagnostic evaluation so that urgent therapeutic interventions can begin. Detailed information on associated findings, such as the extent of the dissection, the location of the entry site, the formation of thrombus in the false lumen, and evidence of pericardial effusion or aortic regurgitation may be helpful in selecting the best management plan and assessing the patient's prognosis [421-425]. The established diagnostic procedures, including aortography, [426, 427] contrast-enhanced x-ray computed tomography (CT), [428-433] and two-dimensional transthoracic color-flow Doppler echocardiography (TTE), [434-438] all have inherent procedural or diagnostic shortcomings. Transesophageal echocardiography (TEE) [439-441] and magnetic resonance imaging (MRI) [442, 443] are recent advances in noninvasive imaging technology that have been useful in assessing the thoracic aorta [444, 445].

The degradation of the extracellular matrix (ECM) in the medial wall in aorta is key in the formation, progression and rupture of TAA [446]. Particularly, the turnover of collagen, an essential component of the ECM, is known to be responsible for the remodeling that occurs in the adventitia. Recent studies indicate that perturbations in collagen micro-architecture and networks, probably as a result of collagen degradation and inappropriate collagen deposition, may alter vessel wall response to mechanical load and lead to vessel wall failure [447]. Therefore, imaging collagen in AAA and TAA might provide valuable information about the state of aneurysm development and the identification of AAAs and TAAs prone to severely progress or rupture.

8.1.1 Animal model of TAA and AAA

Since it is difficult to acquire patient samples and perform experiments in humans directly, research focusing on defining mechanisms of AAAs has been frequently extrapolated from animal models. A commonly used animal model is subcutaneous infusion of angiotensin II (AngII) into

mice. Compared to other surgical approaches for inducing AAAs in mice, such as intra-aortic elastase perfusion or peri-aortic application of calcium chloride that require laparotomy [448, 449], this method does not require entry into the body cavity and requires minimal surgical expertise [450, 451].

Subcutaneous infusion of AngII through osmotic pumps to induce AAAs and TAAS was initially reported in low density-lipoprotein (LDL) receptor -/-mice fed a saturated fat-enriched diet [450], and subsequently in apo E -/- mice fed a normal laboratory diet [451]. Many recent studies have also demonstrated that AngII induces AAAs in normolipidemic mice [452-454]. The approach of infusing AngII has been applied to induce AAAs and explore molecular mechanisms as well as development of potential therapeutic strategies [455] since this model recapitulates many features observed in human AAAs. For example, risk factors of human AAAs such as smoking, aging, and male gender also augment AngII-induced AAAs in mice [456, 457]. The association of hypercholesterolemia with AAAs in humans requires clarification. However, it has been consistent that hypercholesterolemia augments AngII-induced AAAs in mice [458, 459]. Pathologies of AngII-induced AAAs in mice are highly heterogenous and are characterized by profound macrophage infiltration, collagen degradation, thrombotic formation and resolution, and neovascularization [460]. In contrast to the most common infrarenal aortic location of AAAs in humans, AngII-induced AAAs in mice occur in the suprarenal aortic region. Another ubiquitous feature of AngII-induced AAAs is the transmural medial break, leading to transmural thrombosis. It is unclear whether transmural elastin rupture occurs in humans since pathological development of AAAs in humans has not been exclusively studied due to lack of aneurysmal tissues from earlier stages. AngII infusion into mice also leads to profound expansion of the thoracic aortic region, that is predominantly restricted to the ascending aorta which is the most common region for TAAs

in humans [461, 462]. Similar to AngII-induced AAAs, TAAs induced during AngII infusion also recapitulate many features of human TAAs [463]. However, in contrast to AngII-induced AAAs, AngII-induced TAAs are not associated with hypercholesterolemia and do not have gender differences. The overall goal of subcutaneous AngII infusion into mice is to study pathological features and molecular mechanisms of AAAs and TAAs.

In this Chapter, we first explored the use of multi-sequence high-field MRI to study the development of TAA in the animal model with subcutaneous infusion of angiotensin II (AngII) into mice. Then, we applied our recently developed protein-based collagen targeted MRI contrast agent, ProCA32.collagen1 with collagen-targeting capability to identify presence of collagen in the aneurysmal wall in aorta with molecular MRI.

8.2 Results

8.2.1 MRI procedure for cardiac gating

The fundamental challenges of cardiac MRI imaging is that movement of the heart throughout the cardiac cycle and the movement of the lungs during the respiratory cycle produce motion artifacts in the image. Respiratory motion can be alleviated with breath holding during imaging. The problem of heart motion can be solved with the use of ECG gated imaging. ECG gating allows for stop motion imaging by acquiring data only during a specified portion of the cardiac cycle, typically during diastole when the heart is not moving. The R wave of the ECG is used as a reference point with data acquisition being initiated following a given delay after the R wave. Images are created from data collected over a series of cardiac cycles (R to R intervals) (Fig. 8.1 and 8.2) [464].

ECG electrodes are placed over the mouse's chest right under the skin in both hands (Fig. 8.1) using either a three or four lead configuration. Lead are positioned such to accentuate the R

wave and minimized the T wave. If the procedure is being used in humans, patients with a prominent T wave often prove difficult to image as misgating can occur from triggering off the T wave rather than the R wave. Artifacts also occur when there are differences in the length of the R to R interval, such as occurs in cardiac dysrhythmias. ECG gating may be impaired in people with a low ECG signal. A low ECG signal results from geometries that decrease signal to the ECG leads, such as in barrel chested patients with COPD. Large pericardial effusion can also decrease the ECG signal. A common gating artifact, known as the magnetohydrodynamic effect, occurs when ions within the blood are transported through a magnetic field, inducing a voltage and distorting the ECG recording. This artifact can often be overcome by vectorcardiogram gating (VCG), which can distinguish electrical activity of the heart from ions in the blood. In cases where ECG gating is unsuccessful, pulse triggering can be employed using a pulse oximeter with the systolic upstroke as the trigger for the pulse sequence. This technique is not very successful in patients with a delayed pulse upstroke relative to heart contraction [464].

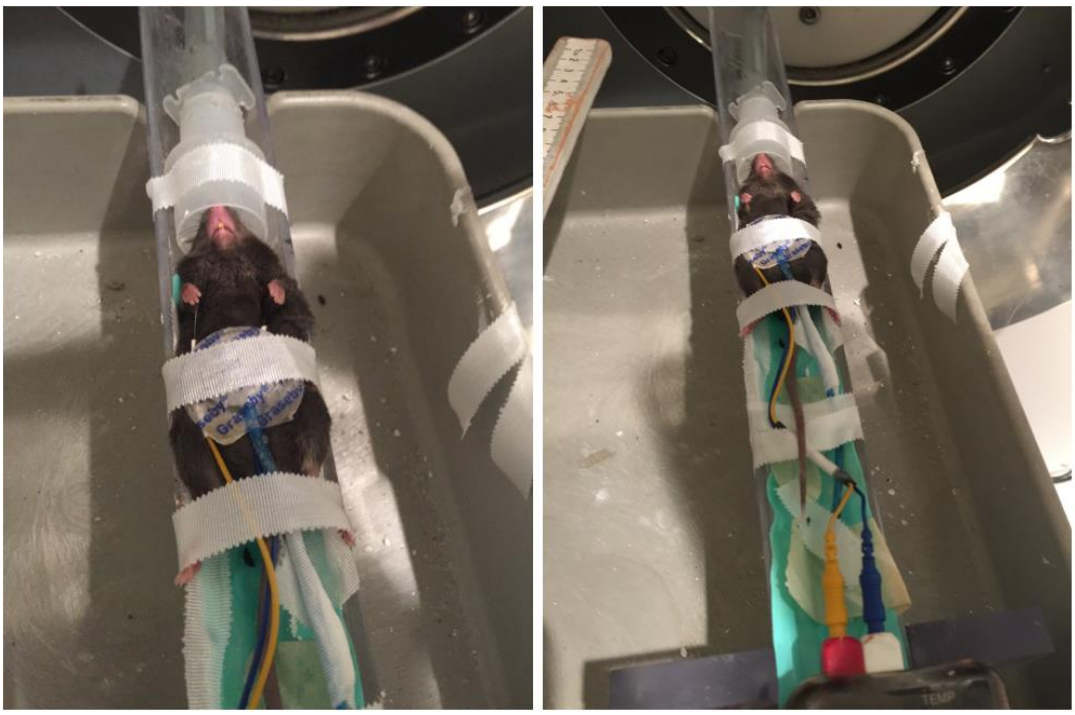

Figure 8.1 *ECG gating procedure in mouse with TAA*

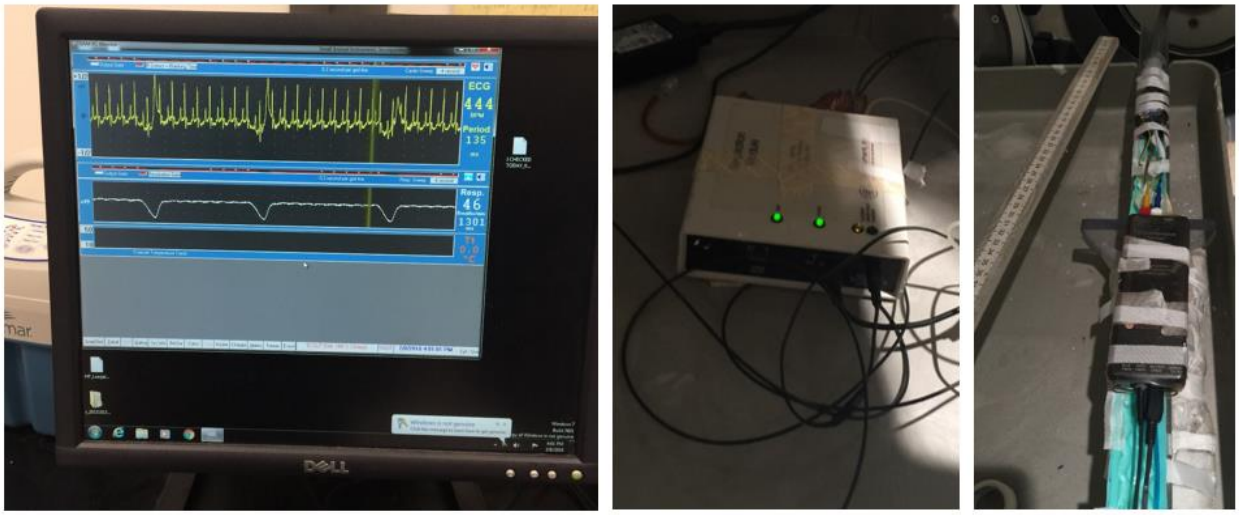

Figure 8.2 *Cardiac and respiratory gating diagrams and module in mouse with TAA*

As it is observed in Fig. 8.2, there are two diagrams conducting the gating in 7.0 T MRI, one indicating the ECG gating by monitoring the mouse beat per minute (BPM) number and the

other one that is monitoring the mouse respiratory by breath per minute number. The MRI is signal is collected in between these signals.

8.2.2 MRI pulse sequence

For MRI scan of heart, several pulse sequences were used. Black blood T1-weighted and black blood proton density are one of the most common pulse sequences used for heart imaging as they show blood vessels as dark images. In black blood T1-weighted, TR of 13.82 ms and TE of 3.11 ms were used. For black blood proton density which has both T1 and T2 property, TR of 250 ms and TE of 7 ms were used. For both of the pulse sequences, a total of 7 slices were collected with matrix size of 128×128, FOV= 35 mm with no gap.

Dark Blood MR is vascular imaging strategy wherein the signal from flowing blood is suppressed (rendering it "black") rather than enhanced as it is in conventional Bright Blood MRI techniques. Rapidly flowing or turbulent blood has a naturally low signal because of phase-dispersion and time-of-flight signal losses. These effects may be further accentuated by application of flow-spoiling gradients, saturation bands, and/or inversion pulses. The well-recognized vascular "flow voids" seen on routine MR imaging represent a crude form of dark-blood MRI.

8.2.3 MRI images of mouse with TAA

After performing the ECG and respiratory gating and using the mentioned pulse sequences, MRI images of TAA and control mice were collected before and 16 and 24 hours post injection of ProCA32.collagen1. Several slices of MRI were collected focused on the aortic arch or thorax-I as shown in Fig. 8.3. Figure 8.4 shows the whole field of view of MRI which has the aorta shown in black hole at the center of the image (red circle).

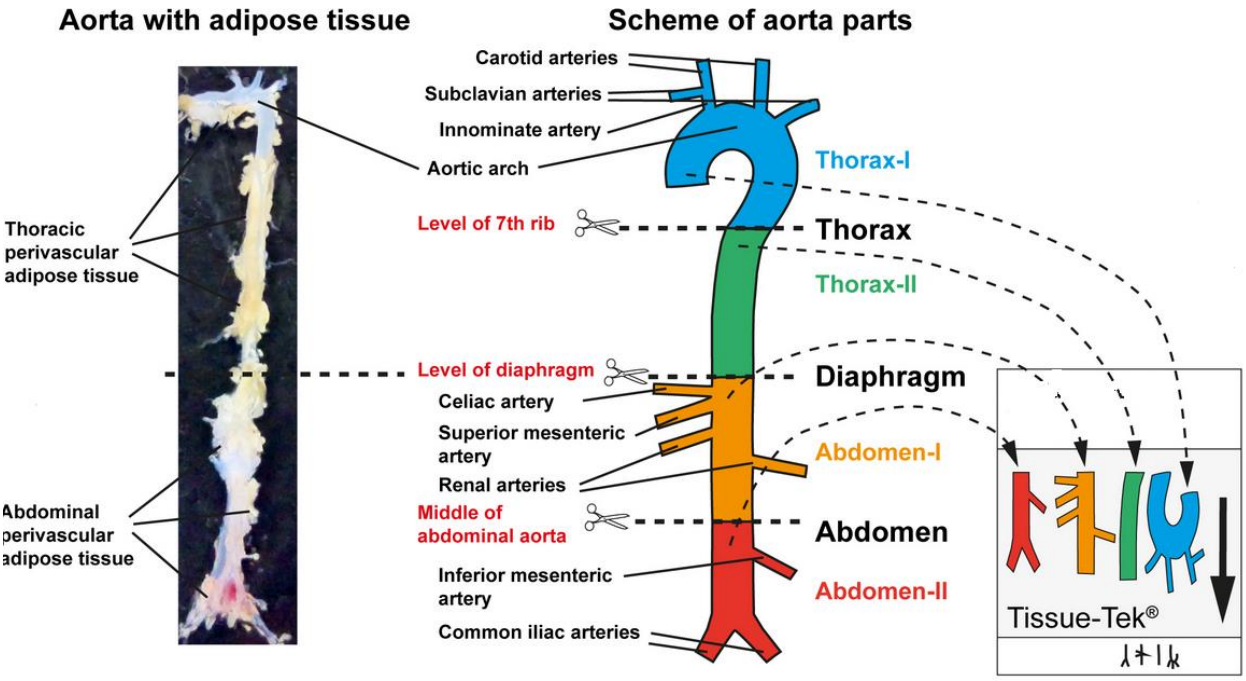

Figure 8.3 *Graphic image of different sections of aorta*

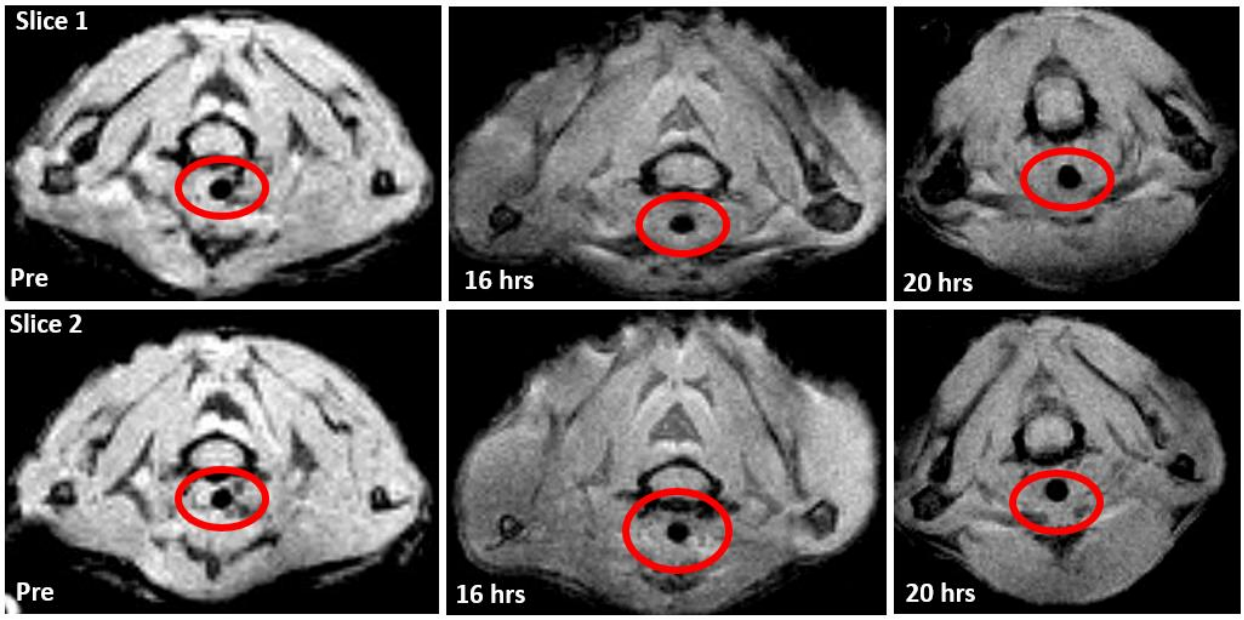

Figure 8.4 *Black blood T1-weighted images of TAA mouse before and post injection of ProCA32.collagen1.*

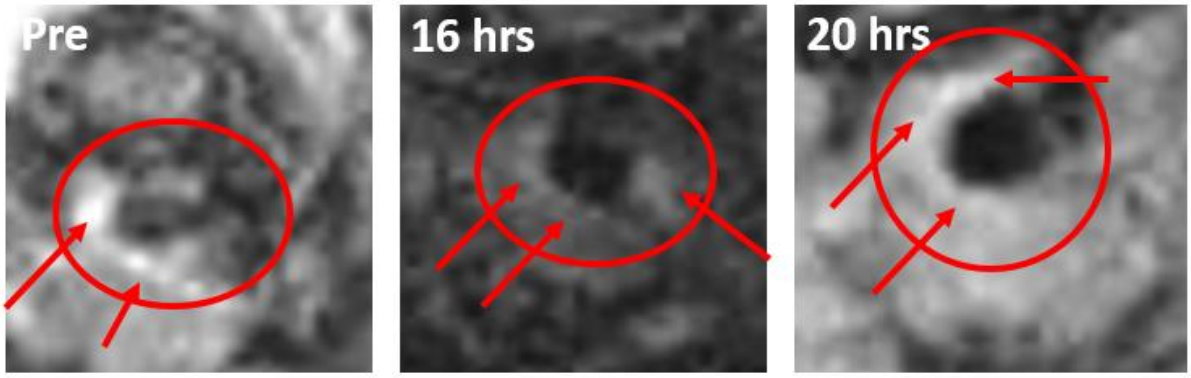

Figure 8.5 *MRI images of black blood proton density-weighted of TAA-1 mouse before and post injection of ProCA32.collagen1.*

The black hole encircled in red in all images represent the aorta in the thorax region and the white area surrounding the aorta shown by red arrows is collagen surrounding the wall of aorta.

Figure 8.5 shows the focused images on the aorta region before and 16 and 20 hrs post injection of ProCA32.collagen1 in mouse with TAA in black blood proton density-weighted images.

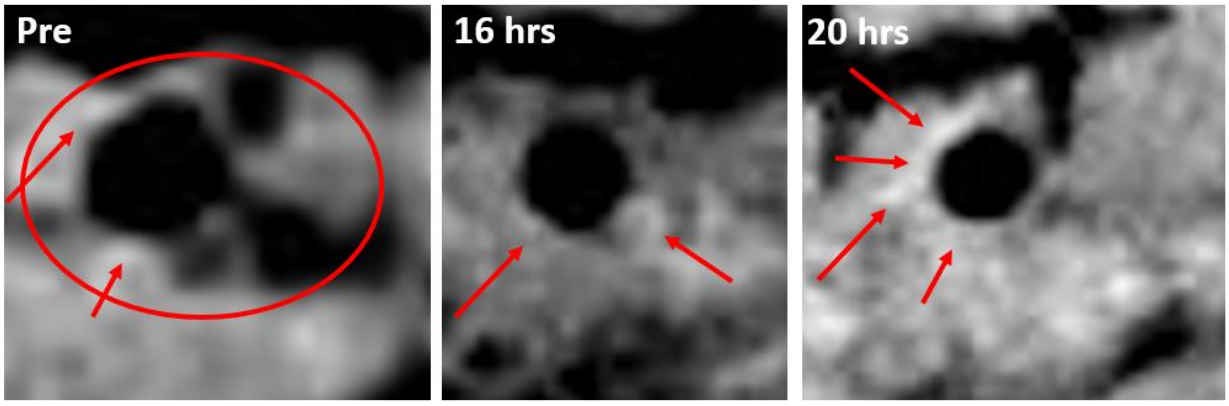

Figure 8.6 *MRI images of black blood T1-weighted of TAA-1 mouse before and post injection of ProCA32.collagen1.*

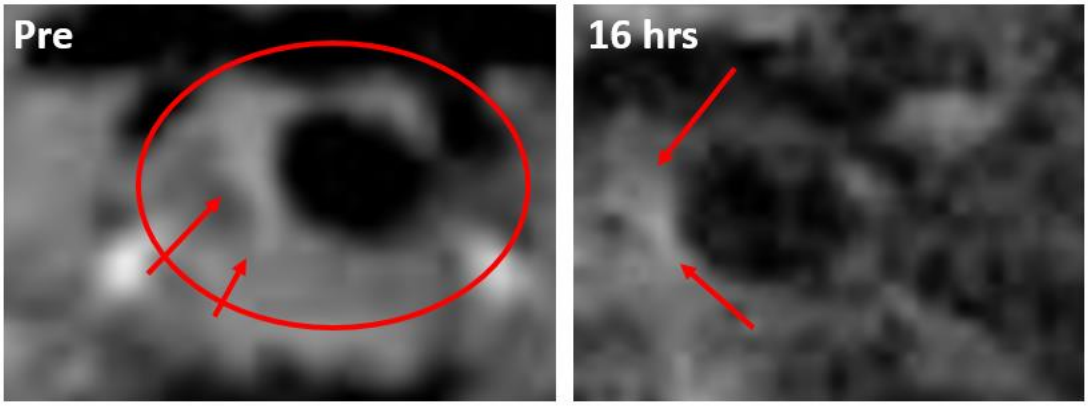

Figure 8.7 *MRI images of black blood proton density-weighted of normal mouse before and post injection of ProCA32.collagen1.*

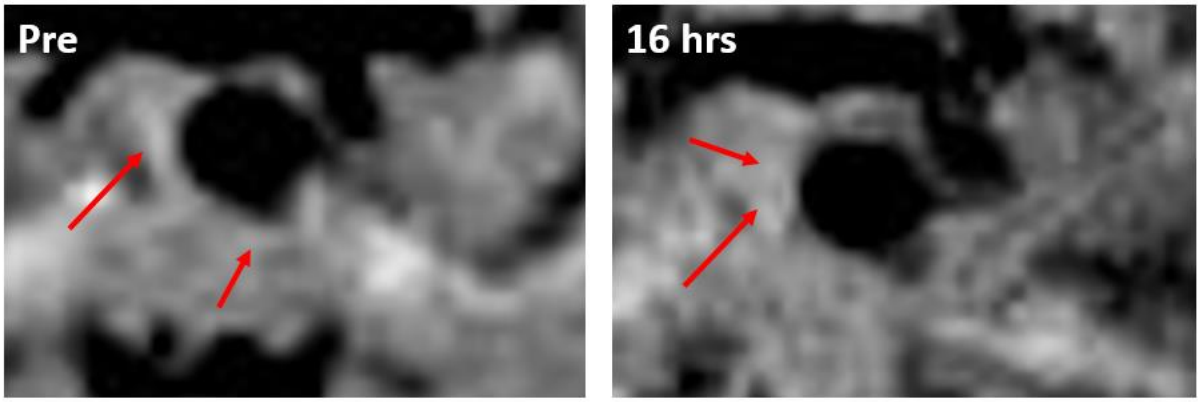

Figure 8.8 *MRI images of black blood T1-weighted of normal mouse before and post injection of ProCA32.collagen1.*

As it is observed from the above figures, white regions surrounding the aorta is enhanced 20 hrs post injection of ProCA32.collagen1 which might be an indication of collagens surrounding the aorta.

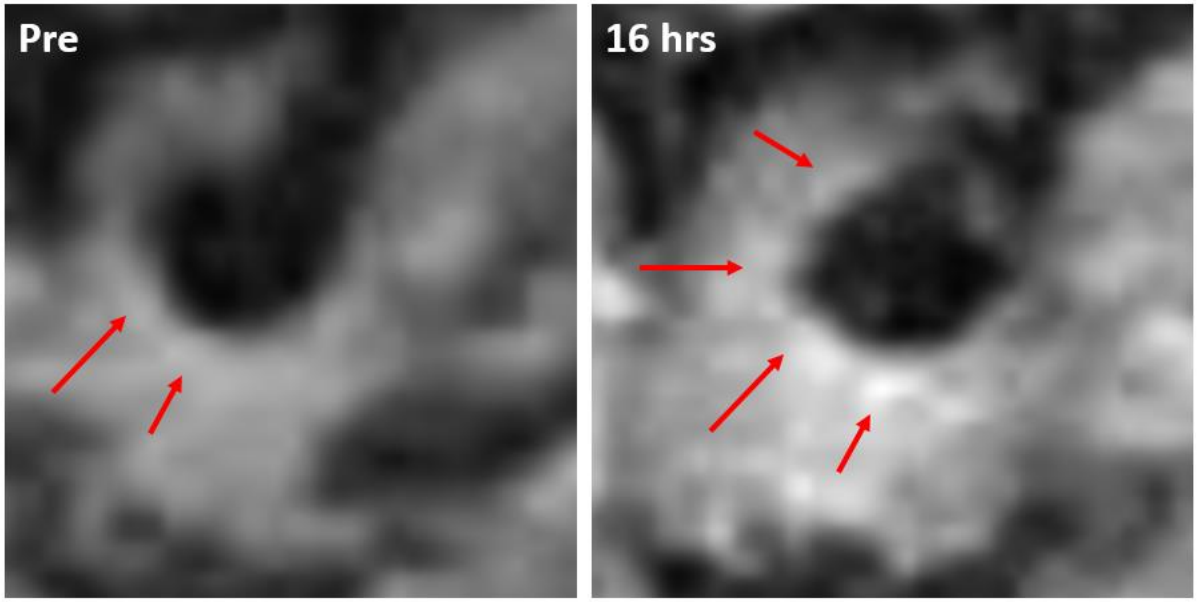

Figure 8.9 *MRI images of black blood proton density-weighted of TAA-2 mouse before and post injection of ProCA32.collagen1.*

As Fig. 8.9 demonstrates, clearly there is an enhancement in proton density MRI images 16 hrs post injection of ProCA32.collagen1 which is possibly due to presence of collagen outside of aorta walls.

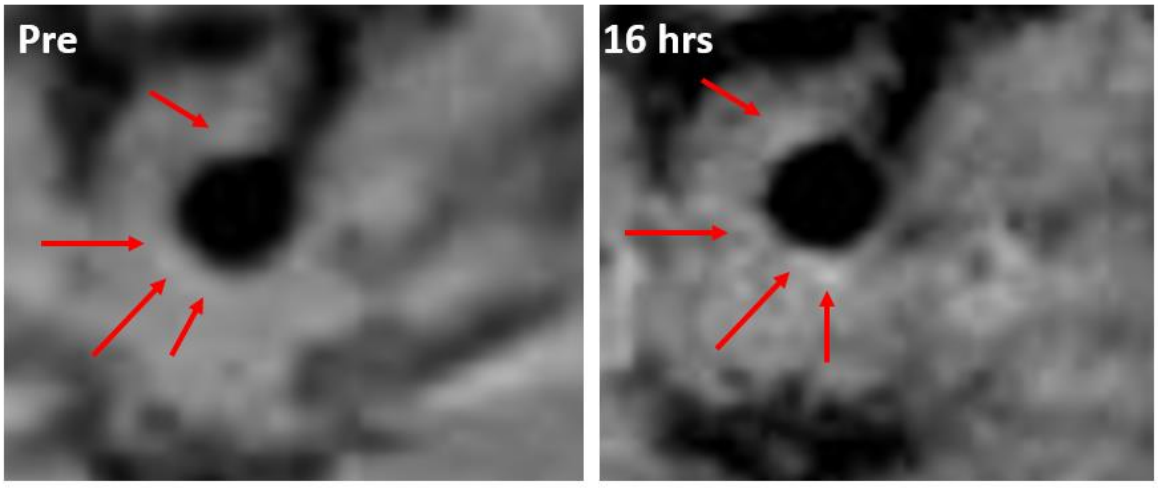

Figure 8.10 *MRI images of black blood T1-weighted of TAA-2 mouse before and post injection of ProCA32.collagen1.*

Figures 8.9 and 8.10 are showing black blood MRI images of another TAA mouse which shows the areas of enhancement aroud16 hours post injection of ProCA32.collagen1. This might be an indication of presence of collagen around the aorta walls.

8.2.4 Histology results of TAA and normal mice

After MRI data collection, the mice were sacrificed and whole aorta was collected as shown in Fig. 8.11 and then they were sliced in paraffin embedded sections.

Figure 8.11 *Aortic images (ex vivo) from mice infused with AngII (TAA) and normal mouse (control). The area pointed with red arrow is where the MRI images where collected.*

Trichrome Stains (Masson) was used to study the presence of collagen fibers in the aorta walls. This procedure is intended for use in the study of connective tissue, muscle and collagen fibers. Trichrome Stain reagents are for ‘‘In Vitro Diagnostic Use’’. Trichrome stains are used

primarily for distinguishing collagen from muscle tissue. In general, they consist of nuclear, collagenous and cytoplasmic dyes in mordants such as phosphotungstic or phosphomolybdic acid. The procedure described here is using aniline blue as a collagen stain instead of a green dye. Tissue sections are treated with Bouin's solution to intensify the final coloration. Nuclei are stained with Weigert's iron hematoxylin, and cytoplasm and muscle are then stained with Beibrich scarlet-acid fuchsin. After treatment with phosphotungstic and phosphomolybdic acid, collagen is demonstrated by staining with aniline blue. Rinsing in acetic acid after staining renders the shades of color more delicate and transparent.

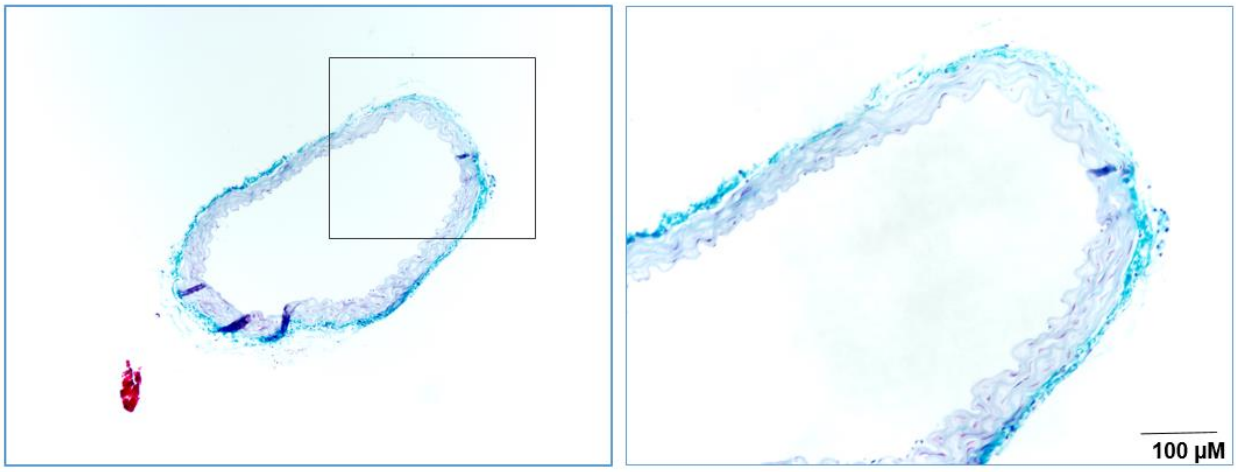

Figure 8.12 *Masson's trichrome stain of aorta in normal mouse.*

In the slide, nuclei are shown in black, cytoplasm is shown in red, muscle fibers are shown in red and collagen fibers are shown in blue.

Fig. 8.12 is showing the control mouse have some collagen fibers (blue) surrounding the muscle of aorta. Masson's trichrome stain was also performed for two TAA mice. The results are shown in Fig. 8.13 and 8.14.

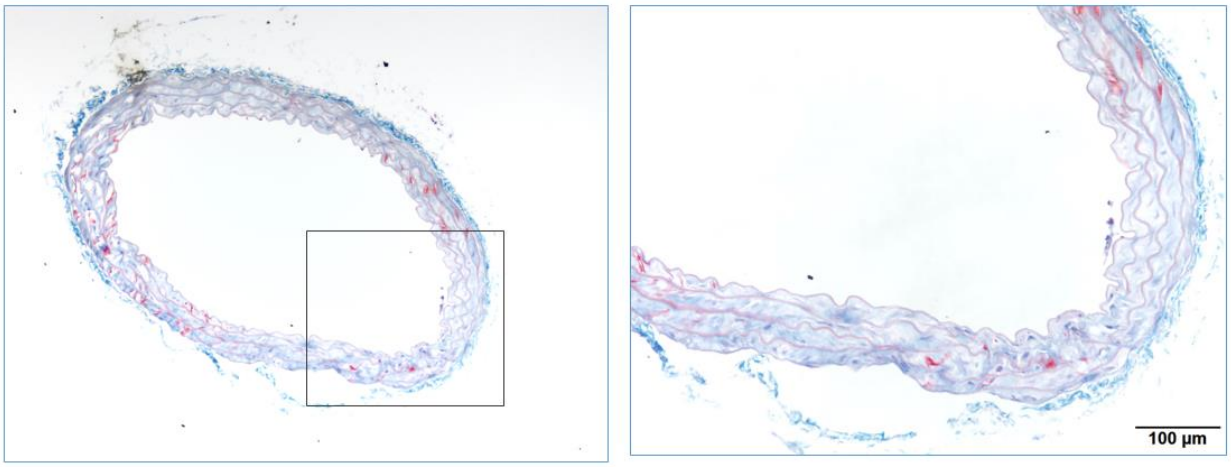

TAA 1

Figure 8.13 *Masson's trichrome stain of aorta in TAA-1 mouse.*

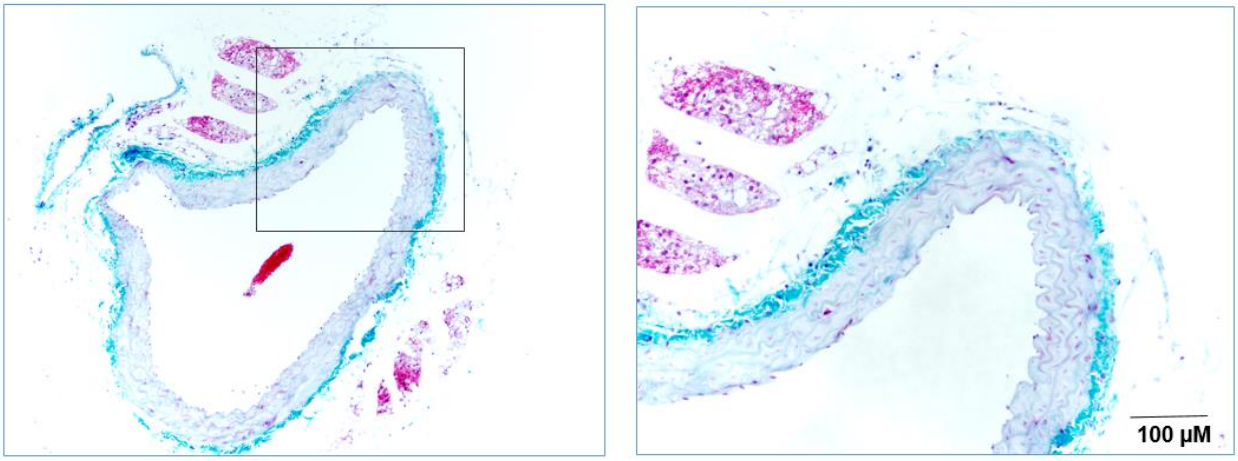

TAA 2

Figure 8.14 *Masson's trichrome stain of aorta in TAA-2 mouse.*

As shown in Fig. 8.14, the amount of collagen fibers is relatively higher compared to TAA-1 mouse and control mouse which confirms the enhancement in Figures 8.9 and 8.10.

8.3 Summary

In conclusion, ProCA32.collagen1 was used to image collagen fibers surrounding aorta wall in both normal and two Ang II mice with TAA. Black blood T1-weighted and proton density-weighted MRI images were used to suppress the bright signal from the blood vessels to facilitate the visualization of aorta and its surroundings. Based on literature, collagen should appear as a bright signal in black blood pulse sequences. MRI images before and 16 and 20 hrs post injection of ProCA32.collagen1 demonstrate signal enhancement post injection around the aorta wall. Furthermore, based on histology analysis, TAA-2 mouse has more collagen fibers (blue) as shown by Masson's trichrome stain. Therefore, it can be concluded that ProCA32.collagen1 is capable of imaging collagen in mouse with thoracic aortic aneurism. It is worth mentioning that, TAA and AAA models in a much later stage will have significant collagen expression and fibrosis which will be used in our future studies.

9 APPLICATION OF PROCA32.COLLAGEN1 IN DETECTION OF NONALCOHOLIC FATTY LIVER DISEASE (NAFLD)

9.1 Introduction

Nonalcoholic fatty liver disease (NAFLD) is a condition in which excess fat is stored in the liver. This buildup of fat is not caused by heavy alcohol use. When heavy alcohol use causes fat to build up in the liver, this condition is called alcoholic liver disease. Two types of NAFLD are simple fatty liver and nonalcoholic steatohepatitis (NASH). Simple fatty liver and NASH are two separate conditions. People typically develop one type of NAFLD or the other, although sometimes people with one form are later diagnosed with the other form of NAFLD.

Non-alcoholic fatty liver disease (NAFLD), defined as excess accumulation of fat in the liver, has become the most common cause for chronic liver disease in the Western world and is

estimated to impact at least 30% of Americans [465, 466] or Chinese [467] with the prevalence appearing to rise in recent years [468, 469]. Non-alcoholic steatohepatitis (NASH) is a subset of NAFLD, estimated to affect 2–5% of Americans, in which increased liver fat is accompanied by cellular injury, inflammatory infiltrate and, subsequently, liver fibrosis, which can progress to cirrhosis with it associated complications [470].

Nonalcoholic fatty liver disease is characterized by hepatic steatosis, without a history of excessive alcohol use, in the absence of other known liver diseases [471-474]. Nonalcoholic fatty liver disease is categorized into 2 subtypes: nonalcoholic fatty liver (NAFL), which is usually nonprogressive, and NASH, which is often progressive and can lead to cirrhosis and HCC [475]. Nonalcoholic fatty liver and NASH have traditionally been considered 2 separate clinical entities, rather than 2 points on a disease continuum [476]. Recent studies evaluating sequential liver biopsies are challenging this notion [477] .A systematic review and meta-analysis of paired biopsy studies found that both patients with NAFL and NASH have the potential to develop progressive liver disease [478]. The fibrosis progression rate from stage 0 to stage 1 for NAFL vs NASH is 14 years vs 7 years, providing suggestive evidence that NAFL, NASH, and fibrosis progression are a continuum rather than separate diagnoses [478].

Patients with NAFL and mild lobular inflammation, without ballooning, had an increased risk of disease progression as compared with those without inflammation. Another retrospective study evaluated serial liver biopsies in 108 patients and found no significant difference in the proportion of fibrosis progression between patients with NAFL and those with NASH at index biopsy (37% vs 43%; P=.65). Similarly, a recent study analyzing paired liver biopsies over time found that even patients with bland steatosis can progress to NASH, especially in the setting of metabolic risk factors [479].

For reasons that are not completely clear, NAFLD is more common in men than women and precise estimates of incidence rates for NAFLD are uncertain (because of difficulties with establishing a precise diagnosis during sequential follow-up) current incidence rates are approximately 20/10,000 person-years, peaking in the sixth decade of life. Current population-based prevalence of NAFLD is approximately 30–40% in men and 15–20% in women and is even higher in people with type 2 diabetes mellitus (T2DM), occurring in up to 70% of this group of patients [480].

Establishing an accurate diagnosis of NASH is of major clinical importance. A histologic diagnosis of NASH is associated with cardiovascular disease and more rapid progression of liver disease. To accurately distinguish NASH from NAFL requires liver biopsy. Nonalcoholic fatty liver is defined as bland steatosis with minimal or no inflammation, whereas NASH is characterized by macrovesicular steatosis, ballooning, and mixed lobular inflammation with or without zone 3 perisinusoidal fibrosis [481, 482].

Although fatty liver by itself is associated with other features of the metabolic syndrome such as obesity, diabetes mellitus type 2, hypertension and dyslipidemia, increased liver-related mortality is essentially limited to patients with NASH [483].

Increased triglyceride deposition in the liver reflects an input/output imbalance of hepatic free fatty acid (FFA) metabolism. In obesity-associated NAFLD, there is an increase of FFA delivery to the liver, especially during the fed state, due to adipose tissue insulin resistance [484, 485]. In addition, de novo lipogenesis is increased, [486] driven by the hyperinsulinemia as well as excess availability of carbohydrates. Compensatory increase in very low-density lipoprotein (VLDL) secretion is not sufficient to overcome the excess formation of triglycerides [487] while it is unclear whether β-oxidation is increased or decreased in these subjects [488].

The accumulated triglycerides in steatosis appear to be relatively inert with benign outcome; hepatocellular injury is driven by lipotoxicity from FFAs and their derivatives, [489] as well as overloading of mitochondrial capacity. This initial metabolic stress activates multiple cell stress pathways, including generation of reactive oxygen species, endoplasmic reticulum stress and apoptosis. Injury signals from stressed or dying hepatocytes, lipids and chemokines activate an immune response, including recruitment and activation of variety of immune cells, further increasing cellular injury. Key mediators are the Kupffer cells and macrophages, which are further activated by bacterial products from the gut microbiome. Hepatocellular injury and immune cell activity converge to activate hepatic stellate cells, causing a change in their phenotype and deposition of collagen, resulting in increased fibrosis and hepatic architectural distortion.

Although the injury patterns are common and conserved, there is variability between patients with NAFLD in the degree of activation of each individual pathway, likely accounting for the heterogeneity of clinical phenotypes and severity. This may be secondary to different external stimuli (ie, dietary composition), genetic components and modulation by the gut microbiome, among other factors.

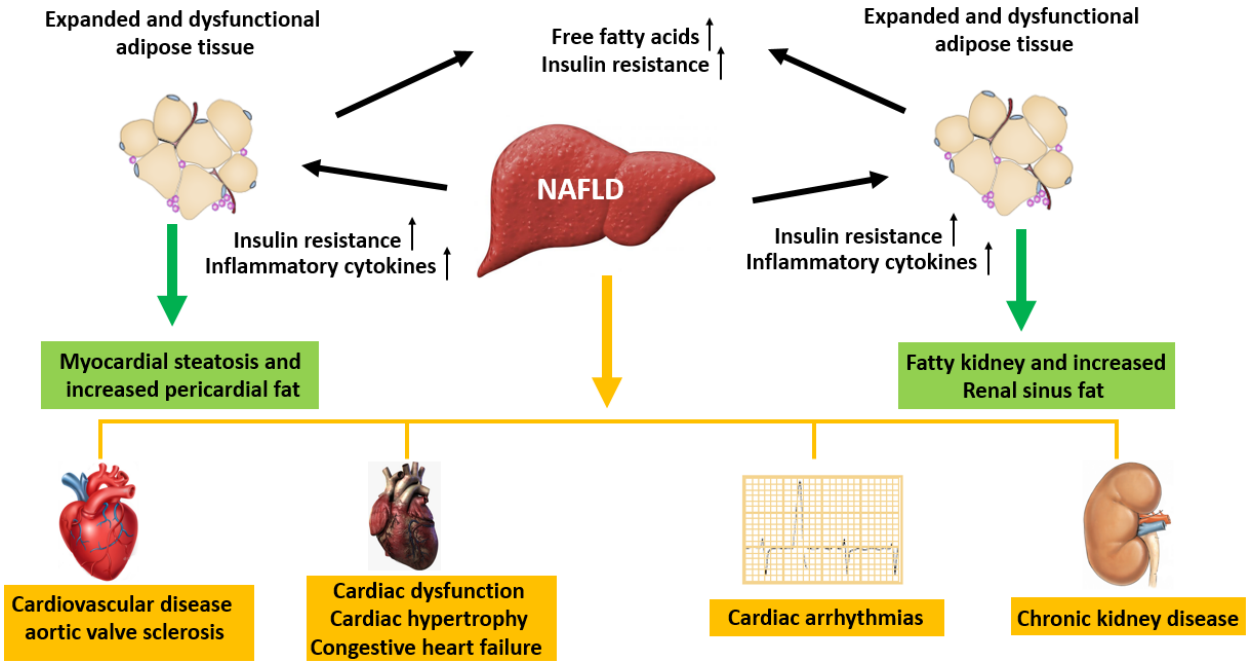

Figure 9.1 *Schematic representation of the putative mechanisms underlying the contribution of NAFLD to the increased risk of cardiovascular and kidney chronic diseases.*

Although there are no Food and Drug Administration-approved medications for NASH, there are several medications that have shown benefits in clinical trials. Prompt diagnosis, timely referrals, and effective treatments are necessary to improve the long-term outcomes of patients with NAFLD and NASH in the setting of primary care and general gastroenterology practices[490].

NAFLD affects a substantial proportion of the population worldwide. Only a minority of subjects who have the condition develop liver-related complications. Predicting which patients will develop progressive disease is problematic. Currently, there is no available noninvasive test demonstrated to be simple, reproducible, and valid for disease staging in patients with NAFLD. Liver biopsy remains the gold standard investigation to distinguish between patients with NASH and those without NASH or bland steatosis, and to determine disease prognosis based on fibrosis staging [491].

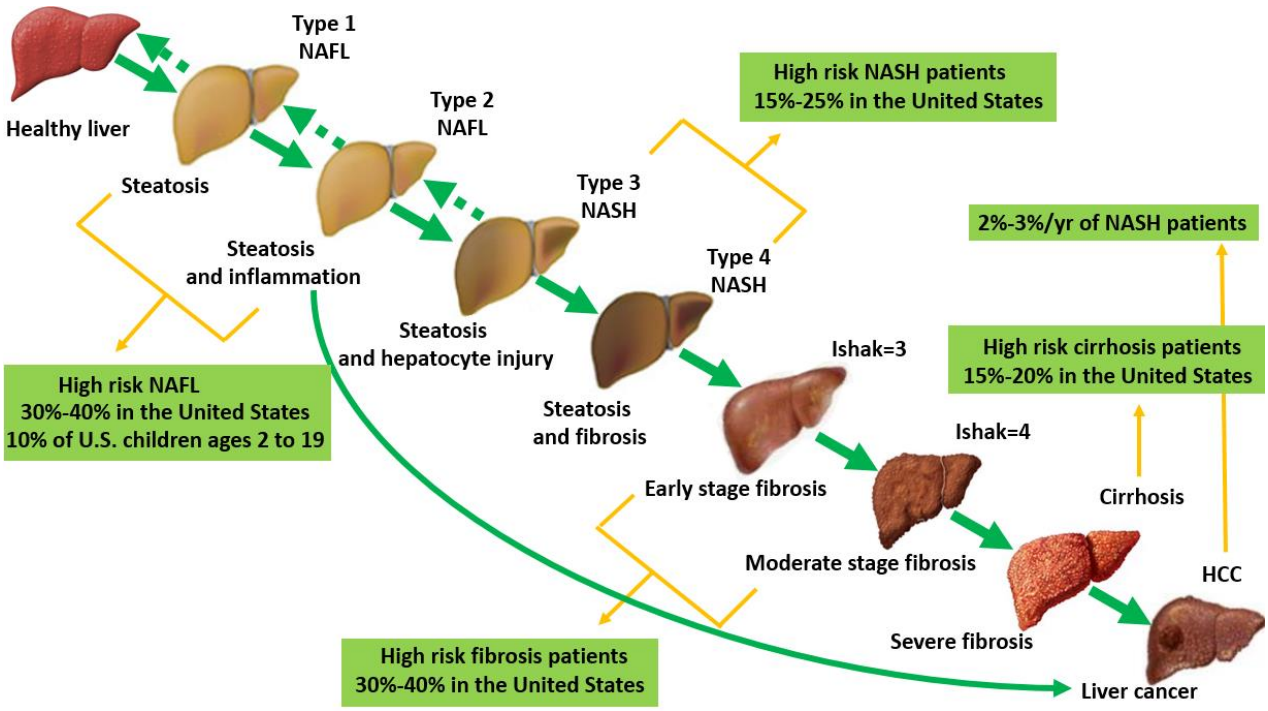

Figure 9.2 *Epidemiology of NAFLD.*

In this chapter, our efforts in extending the application of ProCA32.collagen1 in early detection of NASH will be discussed. Furthermore, liver cirrhosis induced by NASH diet has been imaged with ProCA32.collagen1. Based on our results, we have demonstrated that ProCA32.collagen1 can detect liver fibrosis even at a much earlier stage of nonalcoholic steatohepatitis where liver has a mixture of steatosis and fibrosis. Based on histology analysis, ProCA32.collagen1 can detect Ishak stage 1 of 6 or 1A Mild in NASH/CRN scoring systems.

9.2 Results

9.2.1 NASH animal model

Two different groups of mice (n=4 in each group) on NASH diet were chosen for our studies in detection of NASH in NAFLD mice. First group, they had a liver-specific Comparative Gene Identification-58 (CGI-58) knocked out (LivKO) and second group were wild type (WT) mice. Both groups were fed with a western diet (D12079B) and fructose in drinking water (42g/L) starting from 6-week old. They were also fed with ASO with dose of 25g/kg per injection. IP injection was done twice a week. Fructose in drinking water was autoclaved and changed twice a week. They were on western diet all the time.

9.2.2 Analysis of LivKO group

ProCA32.collagen1 was injected through tail vein and MRI images of mouse livers of LivKO group were collected before and 3 and 24 hrs post injection of the contrast agent. Then the mice were sacrificed and their livers were collected and examined for histology analysis.

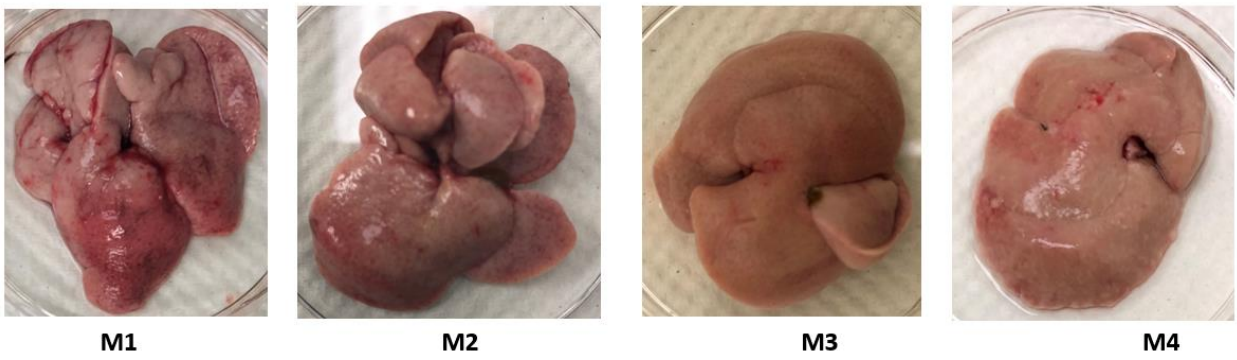

Figure 9.3 *Liver images of four LivKO mice with severe NASH and fibrosis.*

As it is seen from Fig. 9.3, livers are fatty and weights are much larger than normal livers. The liver weights were ranging from 5.0-5.9 grams.

9.2.3 MRI results of LivKO mice

Similar to our previous MRI experiments, several pulse sequences were used to image LiveKO mice livers. Heavy T2-wrighted, T1 weighted, T1 map, and T2 map sequences were collected for all four mice and quantitative analysis was performed on the liver signal. Figures 9.4 to 9.7 demonstrates the heavy T2-weighted MRI images of liver before and 3 and 24 hrs post injection of ProCA32.collagen1.

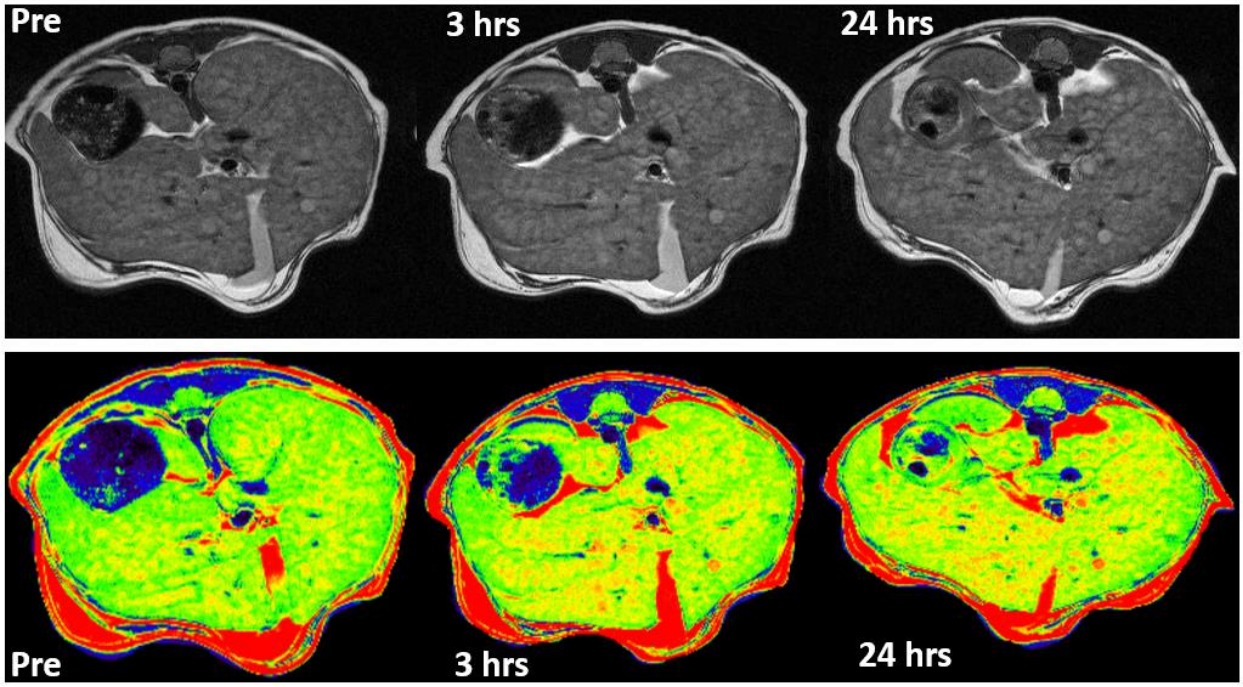

Figure 9.4 *Heavy T2-weighted MRI images of mouse 1 with significant fibrosis due to fatty liver before and 3 and 24 hrs post injection of ProCA32.collagen1.*

Regions shown in green, yellow and red are livers which show significant enhancement after injection of the contrast agent.

MRI images are shown in both gray scale and color map to illustrate the amount of increase in the liver after injection of ProCA32.collagen1. The regions in the border of the images are fat that show a high intensity signal under MRI (red color).

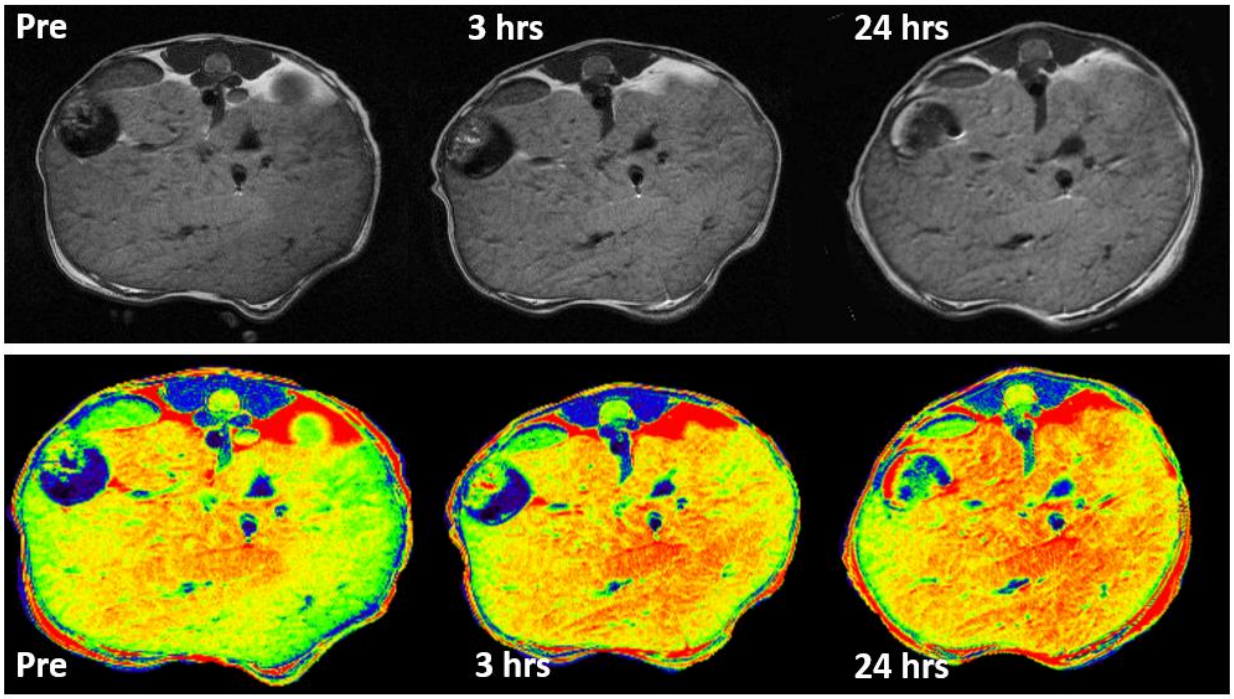

Figure 9.5 *Heavy T2-weighted MRI images of mouse 2 with significant fibrosis due to fatty liver before and 3 and 24 hrs post injection of ProCA32.collagen1.*

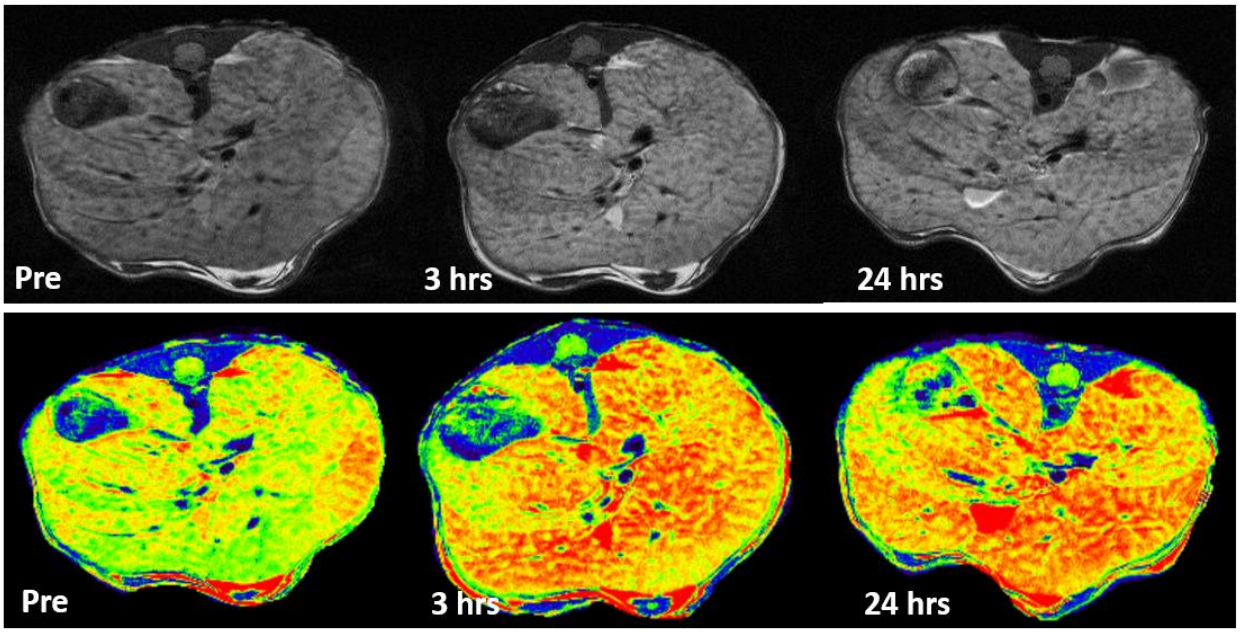

Figure 9.6 *Heavy T2-weighted MRI images of mouse 3 with significant fibrosis due to fatty liver before and 3 and 24 hrs post injection of ProCA32.collagen1.*

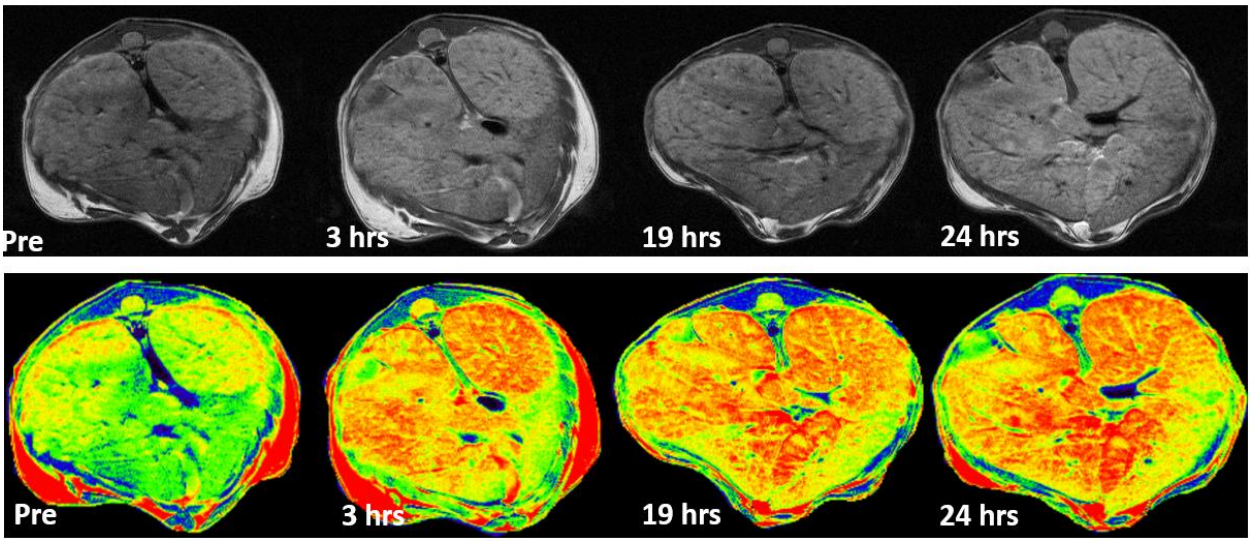

Figure 9.7 *Heavy T2-weighted MRI images of mouse 4 with significant fibrosis due to fatty liver before and 3, 19 and 24 hrs post injection of ProCA32.collagen1.*

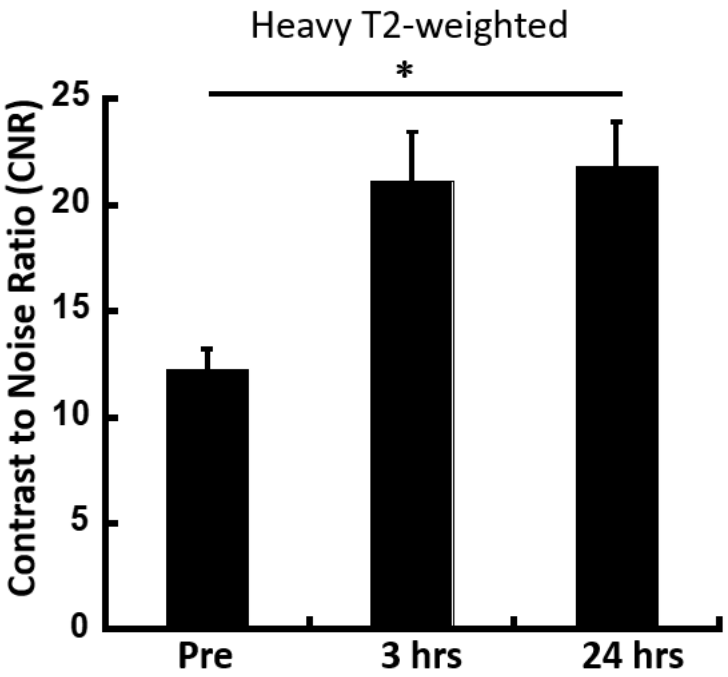

Figure 9.8 *Contrast to noise ratio (CNR) analysis of fibrotic livers pre- and 3 and 24 hrs post injection of ProCA32.collagen1.*

*A significant increase in CNR of livers was observed post injection of ProCA32.collagen1. The value almost doubled after the injection (n=4, * $P < 0.05$, student's t-test).*

9.2.4 Analysis of WT group

ProCA32.collagen1 was injected through tail vein and MRI images of mouse livers of WT group were collected before and 3 and 24 hrs post injection of the contrast agent. Then the mice were sacrificed and their livers were collected and examined for histology analysis.

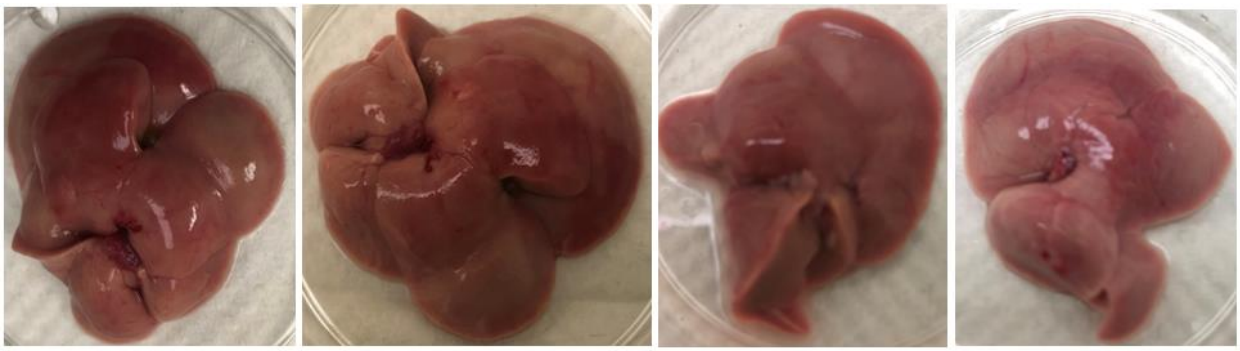

Figure 9.9 *Liver images of four WT mice with mild NASH and fibrosis.*

As it is seen from Fig. 9.9, livers are fatty and weights are larger than normal livers. The liver weights were ranging from 2.1-3.4 grams which are lighter than KO mice which is an indication of milder NASH and fibrosis.

9.2.5 Comparison of heavy T2-weighted MRI results of WT and KO groups

In order to study the ability of ProCA32.collagen1 in distinguishing between different stages of fatty liver, heavy T2-weighted MRI images of KO and WT mice were collected and compared before and 3 and 24 hrs post injection of the contrast agent. Contrast to noise ratio (CNR) analysis was also used to show the MRI signal enhancement different between livers after injection of ProCA32.collagen1. The results can be observed in Fig 9.10. As it is observed, CNR of both WT and KO mice increased 3 hrs post injection of the contrast agent, however, this increase is much higher for KO mice which might be an indication of portal hypertension existence in this group. In 24 hrs, the targeting ability of the contrast agent is visible as the KO mice with severe

NASH and fibrosis have larger CNR compared to WT mice. Moreover, CNR of WT mice has increased significantly compared to CNR at 3 hrs which confirms the targeting capability of ProCA32.collagen1.

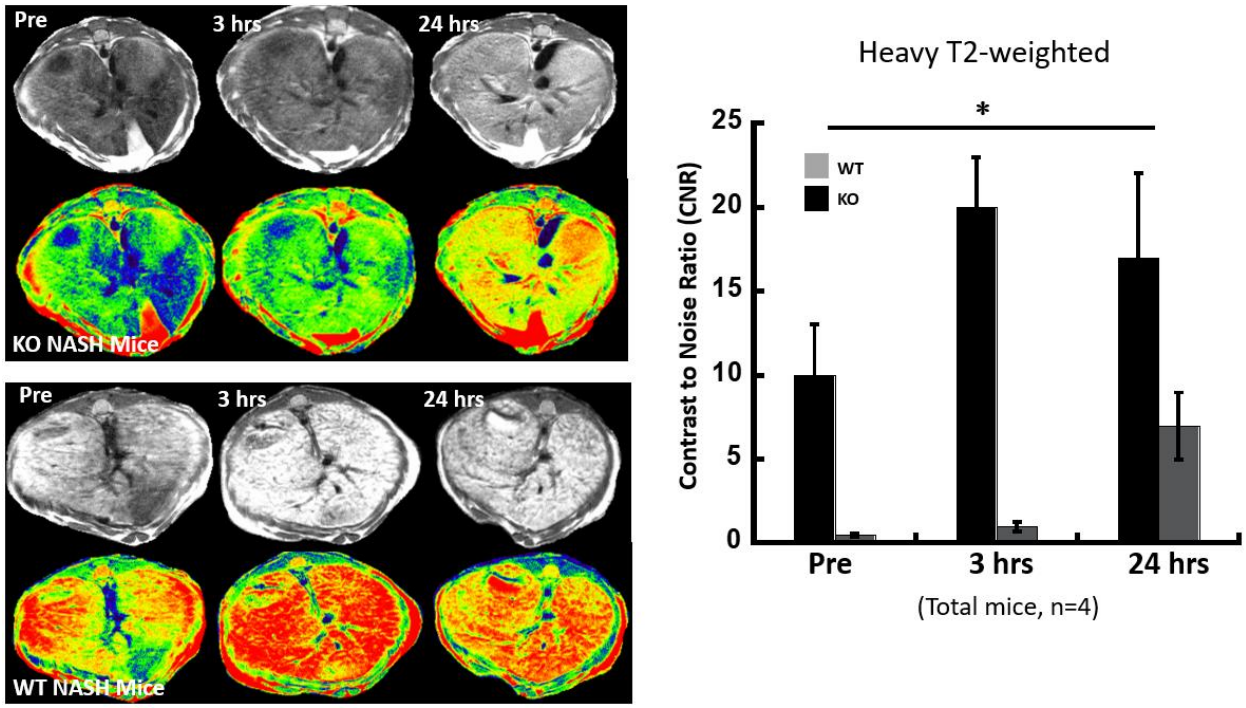

Figure 9.10 *Heavy T2-weighted MRI images of WT and KO livers before and 3 and 24 hrs after injection of ProCA32.collagen1 along with CNR their corresponding CNR.*

CNR of both WT and KO mice increased 3 hrs post injection of the contrast agent, however, this increase is much higher for KO mice which might be an indication of portal hypertension existence in this group. In 24 hrs, the targeting ability of the contrast agent is visible as the KO mice with severe NASH and fibrosis have larger CNR compared to WT mice. Moreover, CNR of WT mice has increased significantly compared to CNR at 3 hrs which confirms the targeting capability of ProCA32.collagen1.

9.2.6 Comparison of R1 map MRI results of WT and KO groups

Since ProCA32.collagen1 has both r_1 and r_2 properties, T1 map MRI images of mouse livers from these two groups were also scanned to further confirm the results observed by heavy T2-wighted images. Using MATLAB software, T1 map data were processed and analyzed (Fig. 9.11). Consistent with results in Chapter 5 where late stage liver cirrhosis (Ishak=5) and portal hypertension was detected in TAA/alcohol-induced mice, R1 has significantly increased at 3 hrs for KO group which has severe fatty liver. In addition, targeting process of ProCA32.collagen1 was observed in 24 hrs time point.

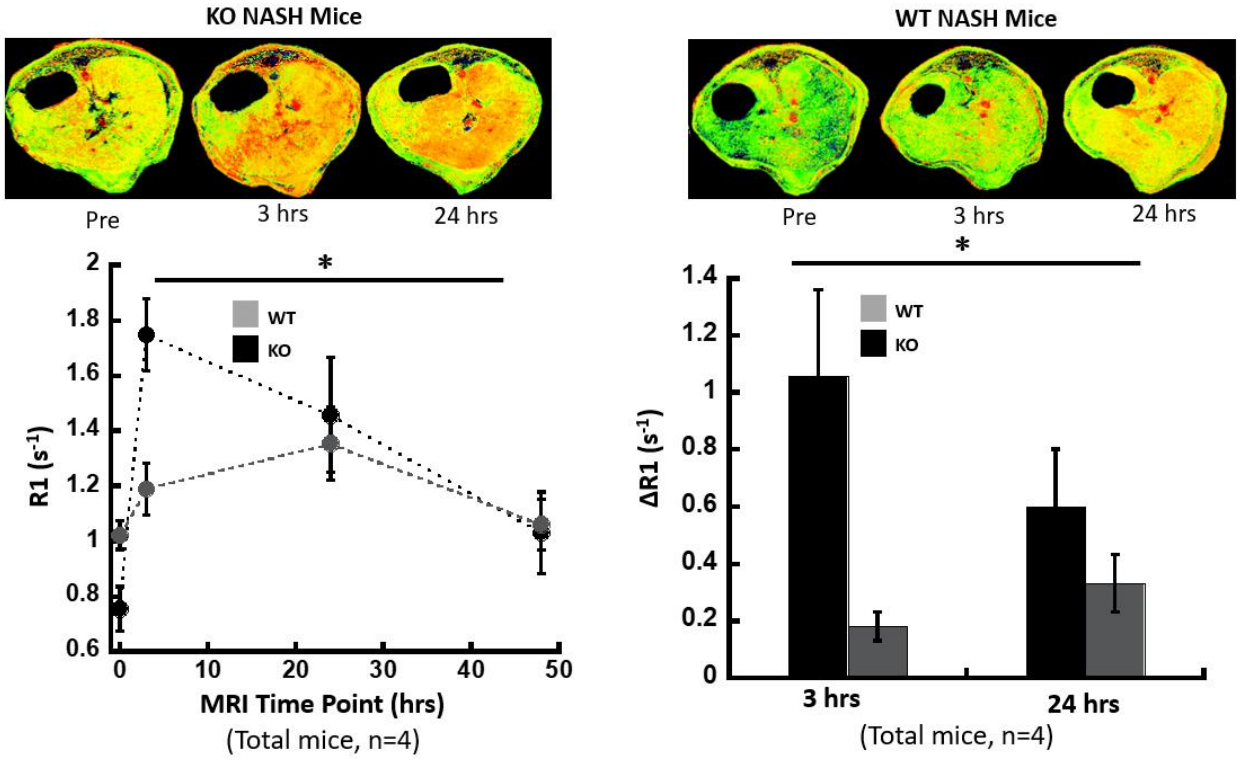

Figure 9.11 *R1 map analysis of KO and WT Mice with fatty liver before and after injection of ProCA32.collagen1.*

R1 of both WT and KO mice increased 3 hrs post injection of the contrast agent, however, this increase is much higher for KO mice which might be an indication of portal hypertension existence in this group. In 24 hrs, the targeting ability of the contrast agent is visible as the KO mice with

severe NASH and fibrosis have larger R1 compared to WT mice. Moreover, CNR of WT mice has increased significantly compared to CNR at 3 hrs which confirms the targeting capability of ProCA32.collagen1. Moreover, ΔR1 analysis shows the highest enhancement for KO mice at 3 hrs and targeting at 24 hrs.

9.2.7 Histology results of NASH mice

After MRI analysis, detailed histology consisting of Sirius red stain for collagen and hematoxylin and eosin (H&E) for fat cells were performed to confirm the stage of fatty liver for these two groups. As the results demonstrate in Fig. 9.12 and 9.13, there is a distinctive difference in liver structure among WT and KO groups showing the WT mice have mild fatty liver and KO mice have sever fatty liver disease.

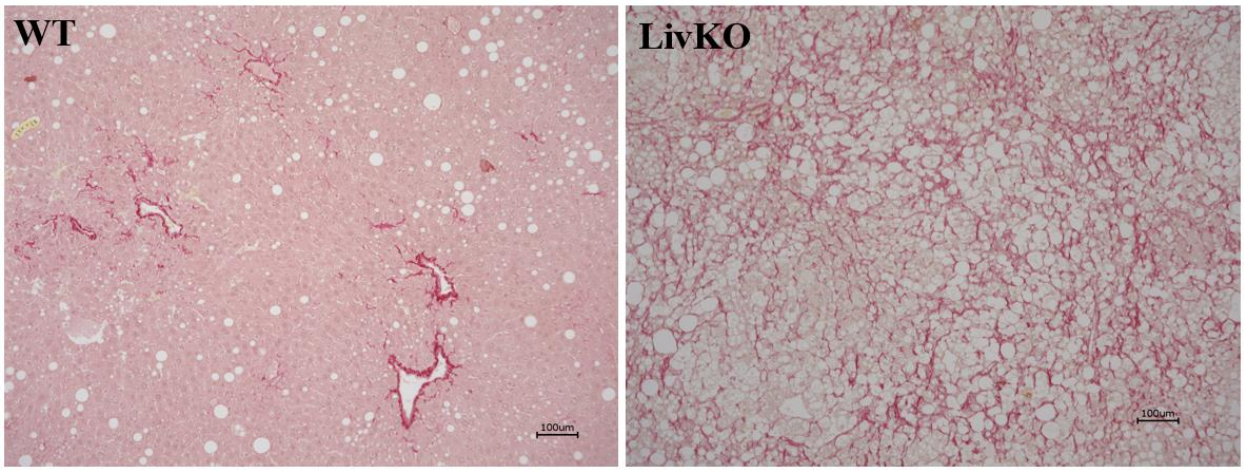

Figure 9.12 *Sirius red staining collagen (red) of fatty mouse liver in KO and WT groups. Collagen networks in red color can be observed for both KO and WT groups, however, in KO mice much higher collagen levels can be observed which is an indication of the severity of fatty liver compared to WT which has milder fatty liver.*

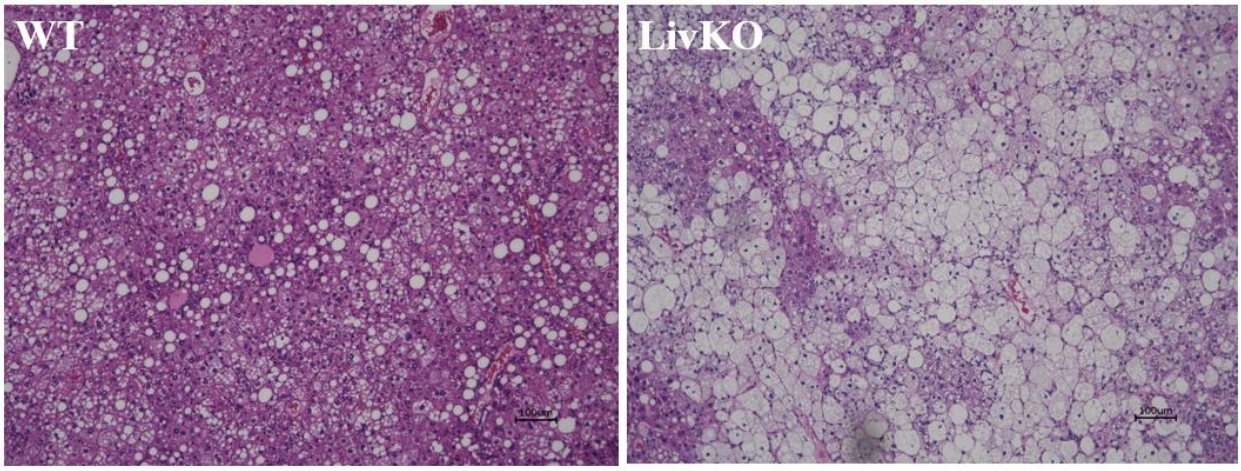

Figure 9.13 *Hematoxylin and eosin (H&E) staining of fatty mouse liver in KO and WT groups. Microvesicular steatosis can be observed in both images, however KO mice has much higher degree of steatosis.*

9.3 Summary

ProCA32.collagen1 has proved that it has the capacity to detect early stage fatty liver disease and distinguish late stage from early stage NASH using both r_1 and r_2 property with high confidence. Moreover, at 3 hrs time point, ProCA32.collagen1 is able to show the vascular structural changes during late stage of NASH white at 24 hrs time point, the targeting capability occurs. Both R1 map and CNR analysis exhibit the higher enhancement in KO group liver compared to WT mice. Sirius red and H&E staining both confirmed the early stage of NASH in WT mice and late stage of NASH in KO mice.

10 MAJOR FINDINGS AND FUTURE DIRECTION

To achieve “Precision Diagnostics” in molecular imaging of chronic liver and heart diseases, first, we need to identify and validate biomarkers of early disease which may likely to be different than those of late stage disease. Second, we need to develop new high throughput methods

to develop imaging agents targeted to these new biomarkers. Third, we need to develop more sensitive, high-resolution imaging technologies that can multiplex signals.

Monitoring different disease biomarkers in patients with invasive methods such as biopsy has so many disadvantages such as its invasiveness, high costs and sampling error, intra/interobserver variability, hospitalization in 1–5% of cases, mortality in 0.01–0.1% of cases, lack of accuracy due to substantial sampling error, cost associated morbidity, pain and bruising at the biopsy site, prolonged bleeding, infection of the biopsy site, and pneumothorax and hemothorax. For instance, there is a 33% error in diagnosis of liver cirrhosis which severely affect the patient outcomes. With its unique capacity to generate reproducible and non-invasive assessment of biological/disease processes of different organs at various time points, molecular imaging of disease biomarkers using MRI can be an important and ideal diagnostic tool to facilitate the understanding of the disease, monitoring disease progression and drug treatment and activity during preclinical and clinical application. However, one of the major limitations of MRI is lack of sensitive contrast agents with targeting capability.

Disease biomarkers, are important indicators of disease formation and progression. Disease biomarkers have been extensively applied in the disease diagnosis for the identification of disease, prediction of disease progression and follow the effects of drug treatment. Image and quantify these biomarkers provides valuable information for the disease evaluation and treatment. Although huge progress has been made during the past few decades, immunohistochemistry after biopsy is still the major approach to evaluate biomarkers. Unfortunately, biopsy is an invasive technique; patient suffers huge pain during this process. Moreover, only limited samples can be collected by biopsy which could easily lead to false positive and false negative results. Therefore, non-invasive

imaging techniques, which enables image the biomarker in the whole disease tissue, are in urgent need for the disease diagnosis, especially cancer diagnosis and evaluation.

Collagen type I is an appealing target for molecular imaging of a variety of diseases such as liver fibrosis, liver metastasis, breast cancer, pancreatic cancer and aortic aneurysms. In organ fibrosis and different cancers, collagen accumulation as well as its concentration increases by the disease progression. In addition, collagen type I is an extracellular protein which makes it accessible for any agent. Collagen type I meets the criteria for an ideal biomarker since its concentration can increase with disease progression to provide a quantitative level for disease stage (Early vs Late). In addition, its extracellular location can make it readily accessible by the probe. Collagen has different patterns which can reflect the disease cause and stage as well as providing information on the disease microenvironment to reflect the mechanism. Collagen type I is also responsive to treatment (Monitoring treatment) and it is specific in determining the disease state.

In order to address major barriers in the field of clinical diagnostics, we have developed a collagen type I-targeted MR contrast agent, ProCA32.collagen1 to act as an agent to image chronic heart and liver diseases. We have successfully applied the contrast agent in a variety of mouse models with liver and heart disease.

As discussed in Chapter 1, there is pressing need to develop more sensitive imaging agents for early diagnosis of different chronic liver and heart diseases. We have shown in Chapter 4 that ProCA32.collagen1 has improved sensitivity and targeting capability and superior biophysical characteristics compared to other previously developed contrast agents in our lab and clinically available contrast agents.

The contrast agent has very high relaxivity at both 1.4 T (clinical magnetic field) and 7.0 T compared to all clinically used contrast agents and majority of research-based agents. It has very

good Gd^{3+} binding affinity as well as high selectivity in the presence of other physiological metal ions such as Ca^{2+} and Zn^{2+}. ProCA32.collagen1 has shown no signs of toxicity and has improved safety properties. It is very stable in serum and has strong resistance against transmetallation. ProCA32.collagen1 has low injection dosage given its high relaxivity as well as good collagen type I binding affinity, the highest reported for a collagen-targeted MRI contrast agent (Figure 10.1). ProCA32.collagen1 has better collagen I affinity compared to EP-3533 (K_d = 1.4 μM) which is a research-based contrast agent based three Magnevists.

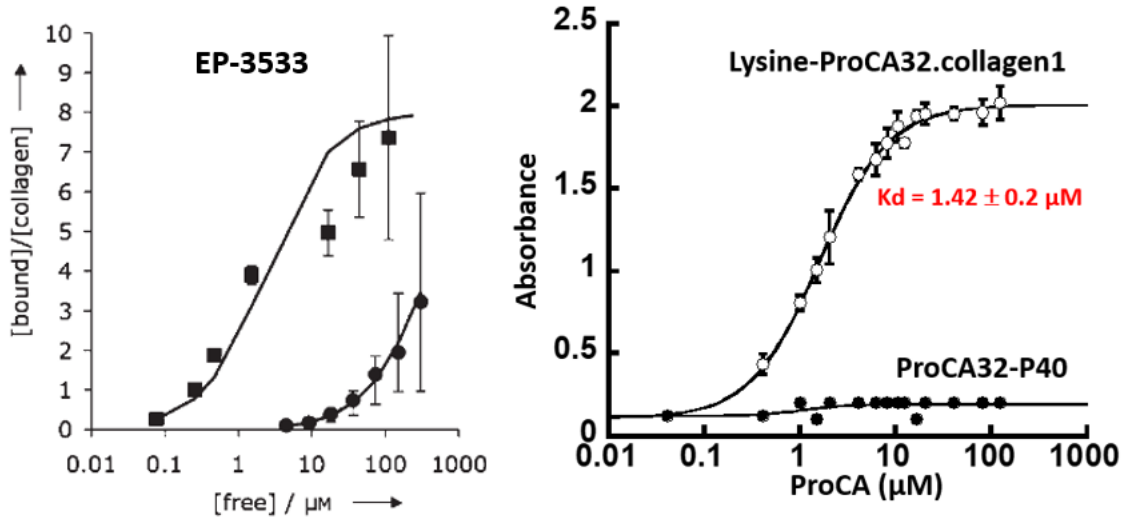

Figure 10.1 *Collagen type I binding affinity comparison between ProCA32.collagen1 and EP3533.*

In Chapter 5 and 9, we have successfully applied ProCA32.collagen1 in early detection of alcohol induced mouse liver fibrosis and nonalcoholic steatohepatitis using both r_1 and r_2 property. ProCA32.collagen1 enables the first robust detection of early stage (Ishak stage 3 of 6) liver fibrosis and nonalcoholic steatohepatitis (Ishak stage 1 of 6 or 1A Mild) in animal models via dual contrast modes. ProCA32.collagen1 also provides the first non-invasive mapping of intrahepatic angiogenesis associated with vascular distortion during late-stage cirrhosis and heterogeneity via dynamic molecular imaging (DMI).

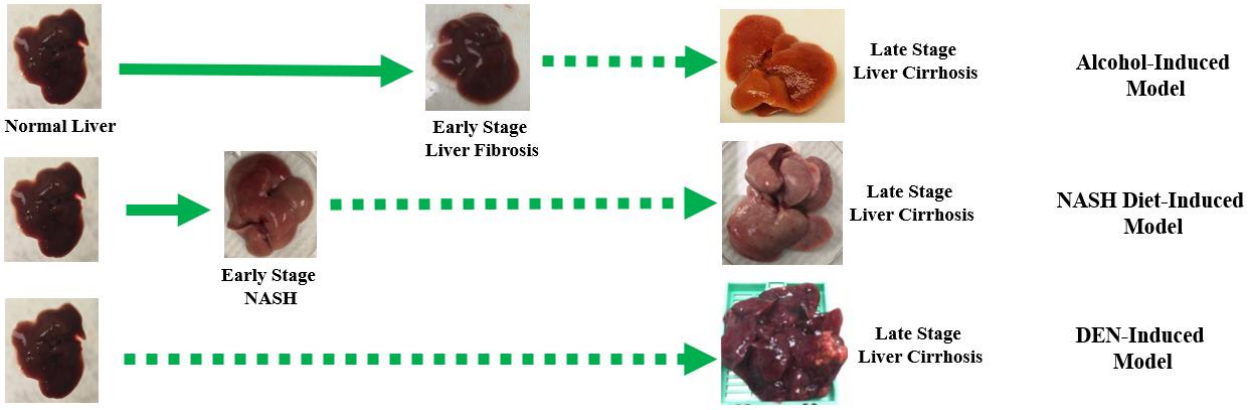

Figure 10.2 *Animal Models of Liver Fibrosis.*

In Chapter 6, ProCA32.collagen1 was successfully used for early detection of human uveal melanoma tumors metastasis to mouse liver. ProCA32.collagen1 can detect UM tumors in liver in both implanted and metastatic mouse models. ProCA32.collagen1 can demonstrate tumor heterogeneity in metastatic model with 14-fold increase in contrast to nose ratio and has improved sensitivity compared to non-targeted agent (ProCA32-P40) and Eovist which could not detect any tumors. The contrast agent is able to show both UM patterns in liver (Nodular and Infiltrative). Based on MRI correlation with histology analysis, ProCA32.collagen1 is capable of detecting tumors as small as 0.250 mm^2 which is much smaller than not only the current detection limit of 10–20 mm but also tumors previously detected by ProCA32-P40. The dynamic range in detection was significantly improved with a 6-fold enhancement in the relative contrast for the implanted liver uveal melanoma tumor in mouse taken advantage of both relaxation property and imaging methodology

In Chapter 7, we have used ProCA32.collagen1 in detection of hepatocellular carcinoma (HCC) in liver in DEN-induced mouse model. ProCA32.collagen1 has shown promising results in distinguishing cirrhotic regions in liver from HCC tumors, and finally, in Chapter 8, we have described our attempt in extending the application of ProCA32.collagen1 in imaging collagen in

mouse model of thoracic and abdominal aortic aneurysm (TAA/AAA) with subcutaneous infusion of angiotensin II (AngII) from implanted osmotic pump.

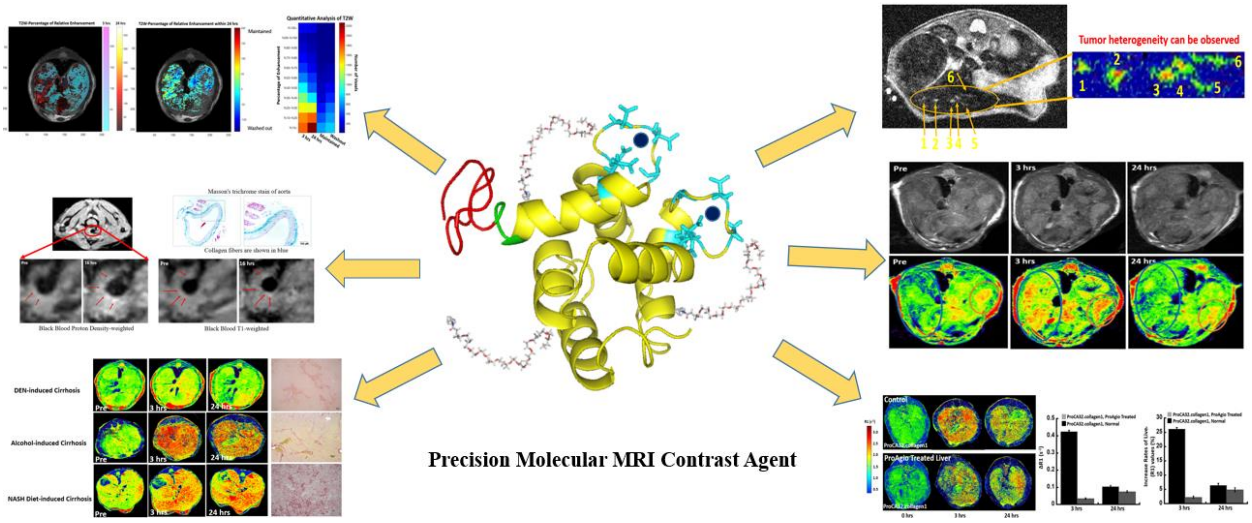

Figure 10.3 *Summary of application of ProCA32.collagen1in diagnosis of chronic diseases.*

Overall, by developing ProCA32.collagen1, we have tried to address several challenges in clinical diagnostics field and facilitate precision diagnostics. We have addressed early diagnosis to facilitate treatment or reversal of the disease. We have successfully imaged disease heterogeneity by monitoring spatial and temporal changes of biomarker (Collagen) to facilitate biopsy. We were also able to monitor drug treatment in liver fibrosis. The development of collagen targeting contrast agent is expected to have broad applications in detection and staging of various chronic diseases and probing heterogeneous microenvironment changes upon disease progression and treatment in different organs. This work will have broad applications in early diagnosis of chronic diseases as shown in Figure 10.2.

REFERENCES

1. Kirchin, M.A. and V.M. Runge, *Contrast agents for magnetic resonance imaging: safety update.* Top Magn Reson Imaging, 2003. **14**(5): p. 426-35.
2. Cheng, L.L., et al., *Correlation of high-resolution magic angle spinning proton magnetic resonance spectroscopy with histopathology of intact human brain tumor specimens.* Cancer Res, 1998. **58**(9): p. 1825-32.
3. Jones, R.A., et al., *Magnetic resonance imaging evaluation of renal structure and function related to disease: technical review of image acquisition, postprocessing, and mathematical modeling steps.* J Magn Reson Imaging, 2011. **33**(6): p. 1270-83.
4. Wang, Z., M.Y. Su, and O. Nalcioglu, *Applications of dynamic contrast enhanced MRI in oncology: measurement of tumor oxygen tension.* Technol Cancer Res Treat, 2002. **1**(1): p. 29-38.
5. Meade, T.J., A.K. Taylor, and S.R. Bull, *New magnetic resonance contrast agents as biochemical reporters.* Curr Opin Neurobiol, 2003. **13**(5): p. 597-602.
6. Caravan, P., *Strategies for increasing the sensitivity of gadolinium based MRI contrast agents.* Chem Soc Rev, 2006. **35**(6): p. 512-23.
7. Major, J.L. and T.J. Meade, *Bioresponsive, cell-penetrating, and multimeric MR contrast agents.* Acc Chem Res, 2009. **42**(7): p. 893-903.
8. Weinmann, H.J., et al., *Tissue-specific MR contrast agents.* Eur J Radiol, 2003. **46**(1): p. 33-44.
9. Kirsch, J.E., *Basic principles of magnetic resonance contrast agents.* Top Magn Reson Imaging, 1991. **3**(2): p. 1-18.

10. Wolf, G.L. and J.T. Halavaara, *Basic principles of MR contrast agents.* Magn Reson Imaging Clin N Am, 1996. **4**(1): p. 1-10.

11. Aime, S. and P. Caravan, *Biodistribution of gadolinium-based contrast agents, including gadolinium deposition.* J Magn Reson Imaging, 2009. **30**(6): p. 1259-67.

12. Nonat, A., et al., *Gadolinium(III) complexes of 1,4,7-triazacyclononane based picolinate ligands: simultaneous optimization of water exchange kinetics and electronic relaxation.* Dalton Trans, 2009(38): p. 8033-46.

13. Robinson, P.J., *Imaging liver metastases: current limitations and future prospects.* Br J Radiol, 2000. **73**(867): p. 234-41.

14. Afdhal, N.H. and D. Nunes, *Evaluation of liver fibrosis: a concise review.* Am J Gastroenterol, 2004. **99**(6): p. 1160-74.

15. Weiss, C.R., S.G. Nour, and J.S. Lewin, *MR-guided biopsy: a review of current techniques and applications.* J Magn Reson Imaging, 2008. **27**(2): p. 311-25.

16. Joffe, P., H.S. Thomsen, and M. Meusel, *Pharmacokinetics of gadodiamide injection in patients with severe renal insufficiency and patients undergoing hemodialysis or continuous ambulatory peritoneal dialysis.* Acad Radiol, 1998. **5**(7): p. 491-502.

17. Koenig, S.H. and K.E. Kellar, *Blood-pool contrast agents for MRI: a critical evaluation.* Acad Radiol, 1998. **5 Suppl 1**: p. S200-5; discussion S226-7.

18. Watrin-Pinzano, A., et al., *Quantitative dynamic contrast enhanced MRI of experimental synovitis in the rabbit knee: comparison of macromolecular blood pool agents vs. Gadolinium-DOTA.* Biomed Mater Eng, 2008. **18**(4-5): p. 261-72.

19. Wedeking, P., et al., *Quantitative dependence of MR signal intensity on tissue concentration of Gd(HP-DO3A) in the nephrectomized rat.* Magn Reson Imaging, 1992. **10**(1): p. 97-108.

20. Sadowski, E.A., et al., *Nephrogenic systemic fibrosis: risk factors and incidence estimation.* Radiology, 2007. **243**(1): p. 148-57.

21. Gibby, W.A., K.A. Gibby, and W.A. Gibby, *Comparison of Gd DTPA-BMA (Omniscan) versus Gd HP-DO3A (ProHance) retention in human bone tissue by inductively coupled plasma atomic emission spectroscopy.* Invest Radiol, 2004. **39**(3): p. 138-42.

22. Thomsen, H.S., S.K. Morcos, and P. Dawson, *Is there a causal relation between the administration of gadolinium based contrast media and the development of nephrogenic systemic fibrosis (NSF)?* Clin Radiol, 2006. **61**(11): p. 905-6.

23. Prince, M.R., et al., *Nephrogenic systemic fibrosis and its impact on abdominal imaging.* Radiographics, 2009. **29**(6): p. 1565-74.

24. Villaraza, A.J., A. Bumb, and M.W. Brechbiel, *Macromolecules, dendrimers, and nanomaterials in magnetic resonance imaging: the interplay between size, function, and pharmacokinetics.* Chem Rev, 2010. **110**(5): p. 2921-59.

25. Laurent, S., L.V. Elst, and R.N. Muller, *Comparative study of the physicochemical properties of six clinical low molecular weight gadolinium contrast agents.* Contrast Media Mol Imaging, 2006. **1**(3): p. 128-37.

26. Bellin, M.F., *MR contrast agents, the old and the new.* Eur J Radiol, 2006. **60**(3): p. 314-23.

27. Cacheris, W.P., S.C. Quay, and S.M. Rocklage, *The relationship between thermodynamics and the toxicity of gadolinium complexes.* Magn Reson Imaging, 1990. **8**(4): p. 467-81.

28. Tweedle, M.F., P. Wedeking, and K. Kumar, *Biodistribution of radiolabeled, formulated gadopentetate, gadoteridol, gadoterate, and gadodiamide in mice and rats.* Invest Radiol, 1995. **30**(6): p. 372-80.

29. Lauffer, R.B., et al., *MS-325: albumin-targeted contrast agent for MR angiography.* Radiology, 1998. **207**(2): p. 529-38.

30. Caravan, P., *Protein-targeted gadolinium-based magnetic resonance imaging (MRI) contrast agents: design and mechanism of action.* Acc Chem Res, 2009. **42**(7): p. 851-62.

31. Choi, H.S., et al., *Renal clearance of quantum dots.* Nat Biotechnol, 2007. **25**(10): p. 1165-70.

32. Goel, A., et al., *Genetically engineered tetravalent single-chain Fv of the pancarcinoma monoclonal antibody CC49: improved biodistribution and potential for therapeutic application.* Cancer Res, 2000. **60**(24): p. 6964-71.

33. Olmsted, S.S., et al., *Diffusion of macromolecules and virus-like particles in human cervical mucus.* Biophys J, 2001. **81**(4): p. 1930-7.

34. Lund, U., et al., *Glomerular filtration rate dependence of sieving of albumin and some neutral proteins in rat kidneys.* Am J Physiol Renal Physiol, 2003. **284**(6): p. F1226-34.

35. Wedeking, P., K. Kumar, and M.F. Tweedle, *Dissociation of gadolinium chelates in mice: relationship to chemical characteristics.* Magn Reson Imaging, 1992. **10**(4): p. 641-8.

36. Rohrer, M., et al., *Comparison of magnetic properties of MRI contrast media solutions at different magnetic field strengths.* Invest Radiol, 2005. **40**(11): p. 715-24.

37. Powell, D.H. and M.D. Hiatt, *Auditory and visual recall of forward and backward digit spans.* Percept Mot Skills, 1996. **82**(3 Pt 2): p. 1099-103.

38. Casali, C., et al., *Evaluation of Gd-DOTA-labeled dextran polymer as an intravascular MR contrast agent for myocardial perfusion.* Acad Radiol, 1998. **5 Suppl 1**: p. S214-8.

39. Port, M., et al., *Physicochemical and biological evaluation of P792, a rapid-clearance blood-pool agent for magnetic resonance imaging.* Invest Radiol, 2001. **36**(8): p. 445-54.

40. Port, M., et al., *P792: a rapid clearance blood pool agent for magnetic resonance imaging: preliminary results.* MAGMA, 2001. **12**(2-3): p. 121-7.

41. Fulton, D.A., et al., *Efficient relaxivity enhancement in dendritic gadolinium complexes: effective motional coupling in medium molecular weight conjugates.* Chem Commun (Camb), 2005(4): p. 474-6.

42. Ranganathan, R.S., et al., *Polymethylated DOTA ligands. 1. Synthesis of rigidified ligands and studies on the effects of alkyl substitution on acid-base properties and conformational mobility.* Inorg Chem, 2002. **41**(25): p. 6846-55.

43. Ranganathan, R.S., et al., *Polymethylated DOTA ligands. 2. Synthesis of rigidified lanthanide chelates and studies on the effect of alkyl substitution on conformational mobility and relaxivity.* Inorg Chem, 2002. **41**(25): p. 6856-66.

44. Zech, S.G., et al., *Probing the water coordination of protein-targeted MRI contrast agents by pulsed ENDOR spectroscopy.* Chemphyschem, 2005. **6**(12): p. 2570-7.

45. Francesconi, L.C., et al., *Technetium-99m N,N'-bis(2-mercapto-2-methylpropyl)-2-aminobenzylamine: technetium-99m complexes of a novel bis(aminoethanethiol) ligand.* J Med Chem, 1994. **37**(20): p. 3282-8.

46. Raymond, K.N. and V.C. Pierre, *Next generation, high relaxivity gadolinium MRI agents.* Bioconjug Chem, 2005. **16**(1): p. 3-8.

47. Caravan, P., et al., *Gadolinium(III) Chelates as MRI Contrast Agents: Structure, Dynamics, and Applications.* Chem Rev, 1999. **99**(9): p. 2293-352.

48. Toth, E., Helm, L., Merbach, A. E. , *Relaxivity of gadolinium(III) complexes: theory and mechanism*. 2001: New York.

49. Vincent-Viry, M., et al., *Lack of a genetic polymorphism in the glucuronidation of fenofibric acid.* Pharmacogenetics, 1995. **5**(1): p. 50-2.

50. Troughton, J.S., et al., *Synthesis and evaluation of a high relaxivity manganese(II)-based MRI contrast agent.* Inorg Chem, 2004. **43**(20): p. 6313-23.

51. Zhou, X., et al., *On the philosophy of optimizing contrast agents. An analysis of 1H NMRD profiles and ESR lineshapes of the Gd(III)complex MS-325+HSA.* J Magn Reson, 2004. **167**(1): p. 147-60.

52. Shoup, D. and A. Szabo, *Role of diffusion in ligand binding to macromolecules and cell-bound receptors.* Biophys J, 1982. **40**(1): p. 33-9.

53. Astashkin, A.V., et al., *Pulsed EPR investigations of systems modeling molybdenum enzymes: hyperfine and quadrupole parameters of oxo-17O in [Mo 17O(SPh)4]*. J Am Chem Soc, 2005. **127**(47): p. 16713-22.

54. Nicolle, G.M., et al., *The impact of rigidity and water exchange on the relaxivity of a dendritic MRI contrast agent.* Chemistry, 2002. **8**(5): p. 1040-8.

55. Sherry, A.D. and Y. Wu, *The importance of water exchange rates in the design of responsive agents for MRI.* Curr Opin Chem Biol, 2013. **17**(2): p. 167-74.

56. Bonnet, C.S., et al., *Outer-sphere investigation of MRI relaxation contrast agents. Example of a cyclodecapeptide gadolinium complex with second-sphere water.* J Phys Chem B, 2010. **114**(26): p. 8770-81.

57. Jacques, V., et al., *High-relaxivity magnetic resonance imaging contrast agents. Part 2. Optimization of inner- and second-sphere relaxivity.* Invest Radiol, 2010. **45**(10): p. 613-24.

58. Aime, S., et al., *Ternary Gd(III)L-HSA adducts: evidence for the replacement of inner-sphere water molecules by coordinating groups of the protein. Implications for the design of contrast agents for MRI.* J Biol Inorg Chem, 2000. **5**(4): p. 488-97.

59. Caravan, P., et al., *Influence of molecular parameters and increasing magnetic field strength on relaxivity of gadolinium- and manganese-based T1 contrast agents.* Contrast Media Mol Imaging, 2009. **4**(2): p. 89-100.

60. Lohrke, J., et al., *25 Years of Contrast-Enhanced MRI: Developments, Current Challenges and Future Perspectives.* Adv Ther, 2016. **33**(1): p. 1-28.

61. Cheng, Z., D.L. Thorek, and A. Tsourkas, *Gadolinium-conjugated dendrimer nanoclusters as a tumor-targeted T1 magnetic resonance imaging contrast agent.* Angew Chem Int Ed Engl, 2010. **49**(2): p. 346-50.

62. Gianolio, E., et al., *Relaxometric investigations and MRI evaluation of a liposome-loaded pH-responsive gadolinium(III) complex.* Inorg Chem, 2012. **51**(13): p. 7210-7.

63. Flacke, S., et al., *Novel MRI contrast agent for molecular imaging of fibrin: implications for detecting vulnerable plaques.* Circulation, 2001. **104**(11): p. 1280-5.

64. Datta, A., et al., *High relaxivity gadolinium hydroxypyridonate-viral capsid conjugates: nanosized MRI contrast agents.* J Am Chem Soc, 2008. **130**(8): p. 2546-52.

65. Richard, C., et al., *Noncovalent functionalization of carbon nanotubes with amphiphilic gd3+ chelates: toward powerful t1 and t2 MRI contrast agents.* Nano Lett, 2008. **8**(1): p. 232-6.

66. Caravan, P., et al., *Gadolinium-binding helix-turn-helix peptides: DNA-dependent MRI contrast agents.* Chem Commun (Camb), 2003(20): p. 2574-5.

67. Lauffer, R.B. and T.J. Brady, *Preparation and water relaxation properties of proteins labeled with paramagnetic metal chelates.* Magn Reson Imaging, 1985. **3**(1): p. 11-6.

68. Wikstrom, M.G., et al., *Contrast-enhanced MRI of tumors. Comparison of Gd-DTPA and a macromolecular agent.* Invest Radiol, 1989. **24**(8): p. 609-15.

69. Brasch, R., et al., *Assessing tumor angiogenesis using macromolecular MR imaging contrast media.* J Magn Reson Imaging, 1997. **7**(1): p. 68-74.

70. Karfeld-Sulzer, L.S., et al., *Multivalent protein polymer MRI contrast agents: controlling relaxivity via modulation of amino acid sequence.* Biomacromolecules, 2010. **11**(6): p. 1429-36.

71. Matsumoto, Y. and A. Jasanoff, *Metalloprotein-based MRI probes.* FEBS Lett, 2013. **587**(8): p. 1021-9.

72. Chen, Y., et al., *Role of calcium in metalloenzymes: effects of calcium removal on the axial ligation geometry and magnetic properties of the catalytic diheme center in MauG.* Biochemistry, 2012. **51**(8): p. 1586-97.

73. Shapiro, M.G., et al., *Directed evolution of a magnetic resonance imaging contrast agent for noninvasive imaging of dopamine.* Nat Biotechnol, 2010. **28**(3): p. 264-70.

74. Qiao, J., et al., *Molecular imaging of EGFR/HER2 cancer biomarkers by protein MRI contrast agents.* J Biol Inorg Chem, 2014. **19**(2): p. 259-70.

75. Sana, B., C.L. Poh, and S. Lim, *A manganese-ferritin nanocomposite as an ultrasensitive T2 contrast agent.* Chem Commun (Camb), 2012. **48**(6): p. 862-4.

76. Sana, B., et al., *Iron-based ferritin nanocore as a contrast agent.* Biointerphases, 2010. **5**(3): p. FA48-52.

77. Bar-Shir, A., et al., *Human protamine-1 as an MRI reporter gene based on chemical exchange.* ACS Chem Biol, 2014. **9**(1): p. 134-8.

78. Xue, S., et al., *Design of a novel class of protein-based magnetic resonance imaging contrast agents for the molecular imaging of cancer biomarkers.* Wiley Interdiscip Rev Nanomed Nanobiotechnol, 2013. **5**(2): p. 163-79.

79. Yang, J.J., et al., *Rational design of protein-based MRI contrast agents.* J Am Chem Soc, 2008. **130**(29): p. 9260-7.

80. Qiao, J., et al., *HER2 targeted molecular MR imaging using a de novo designed protein contrast agent.* PLoS One, 2011. **6**(3): p. e18103.

81. Pasut, G. and F.M. Veronese, *PEGylation for improving the effectiveness of therapeutic biomolecules.* Drugs Today (Barc), 2009. **45**(9): p. 687-95.

82. Pasut, G. and F.M. Veronese, *PEG conjugates in clinical development or use as anticancer agents: an overview.* Adv Drug Deliv Rev, 2009. **61**(13): p. 1177-88.

83. Xue, S., et al., *Protein MRI contrast agent with unprecedented metal selectivity and sensitivity for liver cancer imaging.* Proc Natl Acad Sci U S A, 2015. **112**(21): p. 6607-12.

84. Li, S., et al., *PEGylation of protein-based MRI contrast agents improves relaxivities and biocompatibilities.* J Inorg Biochem, 2012. **107**(1): p. 111-8.

85. Pidcock, E. and G.R. Moore, *Structural characteristics of protein binding sites for calcium and lanthanide ions.* J Biol Inorg Chem, 2001. **6**(5-6): p. 479-89.

86. Yang, W., et al., *The effects of Ca2+ binding on the dynamic properties of a designed Ca2+-binding protein.* Biochemistry, 2005. **44**(23): p. 8267-73.

87. Yang, W., et al., *Design of a calcium-binding protein with desired structure in a cell adhesion molecule.* J Am Chem Soc, 2005. **127**(7): p. 2085-93.

88. Moats, R.A., Fraser, S.E., Meade, T.J., *A "smart" magnetic resonance imaging agent that reports on specific enzymatic activity.* Angew Chem Int Edit, 1997. **37**(7): p. 726–728.

89. Louie, A.Y., et al., *In vivo visualization of gene expression using magnetic resonance imaging.* Nat Biotechnol, 2000. **18**(3): p. 321-5.

90. Caravan, P., et al., *The Gd(3+) complex of a fatty acid analogue of DOTP binds to multiple albumin sites with variable water relaxivities.* Inorg Chem, 2001. **40**(26): p. 6580-7.

91. Vander Elst, L., et al., *Stereospecific binding of MRI contrast agents to human serum albumin: the case of Gd-(S)-EOB-DTPA (Eovist) and its (R) isomer.* J Biol Inorg Chem, 2001. **6**(2): p. 196-200.

92. Esqueda, A.C., et al., *A new gadolinium-based MRI zinc sensor.* J Am Chem Soc, 2009. **131**(32): p. 11387-91.

93. Zhang, Z., et al., *Multilocus binding increases the relaxivity of protein-bound MRI contrast agents.* Angew Chem Int Ed Engl, 2005. **44**(41): p. 6766-9.

94. Thompson, M.K., et al., *Hetero-tripodal hydroxypyridonate gadolinium complexes: syntheses, relaxometric properties, water exchange dynamics, and human serum albumin binding.* Inorg Chem, 2004. **43**(26): p. 8577-86.

95. Werner, E.J., et al., *Highly soluble tris-hydroxypyridonate Gd(III) complexes with increased hydration number, fast water exchange, slow electronic relaxation, and high relaxivity.* J Am Chem Soc, 2007. **129**(7): p. 1870-1.

96. Foster, T.E., et al., *Platelet-rich plasma: from basic science to clinical applications.* Am J Sports Med, 2009. **37**(11): p. 2259-72.

97. Ohgushi, H., *[Basic science and clinical applications of mesenchymal stem cells]*. Seikagaku, 2009. **81**(2): p. 99-104.

98. Wilkins, A.L., et al., *Metal-binding studies for a de novo designed calcium-binding protein.* Protein Eng, 2002. **15**(7): p. 571-4.

99. Yang, W., et al., *Structural analysis, identification, and design of calcium-binding sites in proteins.* Proteins, 2002. **47**(3): p. 344-56.

100. Dudev, T., et al., *First-second shell interactions in metal binding sites in proteins: a PDB survey and DFT/CDM calculations.* J Am Chem Soc, 2003. **125**(10): p. 3168-80.

101. Wang, X., et al., *Analysis and prediction of calcium-binding pockets from apo-protein structures exhibiting calcium-induced localized conformational changes.* Protein Sci, 2010. **19**(6): p. 1180-90.

102. Wang, X., et al., *Towards predicting Ca2+-binding sites with different coordination numbers in proteins with atomic resolution.* Proteins, 2009. **75**(4): p. 787-98.

103. Kirberger, M. and J.J. Yang, *Structural differences between Pb2+- and Ca2+-binding sites in proteins: implications with respect to toxicity.* J Inorg Biochem, 2008. **102**(10): p. 1901-9.

104. Kirberger, M., et al., *Statistical analysis of structural characteristics of protein Ca2+-binding sites.* J Biol Inorg Chem, 2008. **13**(7): p. 1169-81.

105. Deng, H., et al., *Predicting calcium-binding sites in proteins - a graph theory and geometry approach.* Proteins, 2006. **64**(1): p. 34-42.

106. Carroll, A., et al., *Amyloid fibril formation by a domain of rat cell adhesion molecule.* Cell Biochem Biophys, 2006. **44**(2): p. 241-9.

107. Gore, J.C., et al., *Magnetic resonance in the era of molecular imaging of cancer.* Magn Reson Imaging, 2011. **29**(5): p. 587-600.

108. Zhu, W., et al., *PAMAM dendrimer-based contrast agents for MR imaging of Her-2/neu receptors by a three-step pretargeting approach.* Magn Reson Med, 2008. **59**(4): p. 679-85.

109. Caravan, P., et al., *Collagen-targeted MRI contrast agent for molecular imaging of fibrosis.* Angew Chem Int Ed Engl, 2007. **46**(43): p. 8171-3.

110. Polasek, M., et al., *Molecular MR imaging of liver fibrosis: a feasibility study using rat and mouse models.* J Hepatol, 2012. **57**(3): p. 549-55.

111. Spuentrup, E., et al., *Molecular magnetic resonance imaging of myocardial perfusion with EP-3600, a collagen-specific contrast agent: initial feasibility study in a swine model.* Circulation, 2009. **119**(13): p. 1768-75.

112. Burtea, C., et al., *Magnetic resonance molecular imaging of vascular cell adhesion molecule-1 expression in inflammatory lesions using a peptide-vectorized paramagnetic imaging probe.* J Med Chem, 2009. **52**(15): p. 4725-42.

113. De Leon-Rodriguez, L.M., et al., *MRI detection of VEGFR2 in vivo using a low molecular weight peptoid-(Gd)8-dendron for targeting.* J Am Chem Soc, 2010. **132**(37): p. 12829-31.

114. Schmieder, A.H., et al., *Molecular MR imaging of melanoma angiogenesis with alphanubeta3-targeted paramagnetic nanoparticles.* Magn Reson Med, 2005. **53**(3): p. 621-7.

115. Winter, P.M., et al., *Molecular imaging of angiogenesis in nascent Vx-2 rabbit tumors using a novel alpha(nu)beta3-targeted nanoparticle and 1.5 tesla magnetic resonance imaging.* Cancer Res, 2003. **63**(18): p. 5838-43.

116. Winter, P.M., et al., *Molecular imaging of angiogenesis in early-stage atherosclerosis with alpha(v)beta3-integrin-targeted nanoparticles.* Circulation, 2003. **108**(18): p. 2270-4.

117. Ouimet, T., et al., *Molecular and cellular targets of the MRI contrast agent P947 for atherosclerosis imaging.* Mol Pharm, 2012. **9**(4): p. 850-61.

118. Boles, K.S., et al., *MR angiogenesis imaging with Robo4- vs. alphaVbeta3-targeted nanoparticles in a B16/F10 mouse melanoma model.* FASEB J, 2010. **24**(11): p. 4262-70.

119. Artemov, D., et al., *Magnetic resonance molecular imaging of the HER-2/neu receptor.* Cancer Res, 2003. **63**(11): p. 2723-7.

120. Caravan, P., et al., *A lysine walk to high relaxivity collagen-targeted MRI contrast agents.* Chem Commun (Camb), 2009(4): p. 430-2.

121. Farrar, C.T., et al., *3D molecular MR imaging of liver fibrosis and response to rapamycin therapy in a bile duct ligation rat model.* J Hepatol, 2015. **63**(3): p. 689-96.

122. Caravan, P., et al., *Molecular magnetic resonance imaging of pulmonary fibrosis in mice.* Am J Respir Cell Mol Biol, 2013. **49**(6): p. 1120-6.

123. Zhang, Y.; Available from: https://zhanglab.ccmb.med.umich.edu/I-TASSER/.

124. Huebsch, N. and D.J. Mooney, *Inspiration and application in the evolution of biomaterials.* Nature, 2009. **462**(7272): p. 426-32.

125. Azzarito, V., et al., *Inhibition of alpha-helix-mediated protein-protein interactions using designed molecules.* Nat Chem, 2013. **5**(3): p. 161-73.

126. Little, L.E., et al., *Exploiting bacterial peptide display technology to engineer biomaterials for neural stem cell culture.* Biomaterials, 2011. **32**(6): p. 1484-94.

127. Tashiro, K., et al., *A synthetic peptide containing the IKVAV sequence from the A chain of laminin mediates cell attachment, migration, and neurite outgrowth.* J Biol Chem, 1989. **264**(27): p. 16174-82.

128. Neffe, A.T. and B. Meyer, *A peptidomimetic HIV-entry inhibitor directed against the CD4 binding site of the viral glycoprotein gp120.* Angew Chem Int Ed Engl, 2004. **43**(22): p. 2937-40.

129. Collier, J.H. and T. Segura, *Evolving the use of peptides as components of biomaterials.* Biomaterials, 2011. **32**(18): p. 4198-204.

130. DeForest, C.A., B.D. Polizzotti, and K.S. Anseth, *Sequential click reactions for synthesizing and patterning three-dimensional cell microenvironments.* Nat Mater, 2009. **8**(8): p. 659-64.

131. Ouasti, S., et al., *Network connectivity, mechanical properties and cell adhesion for hyaluronic acid/PEG hydrogels.* Biomaterials, 2011. **32**(27): p. 6456-70.

132. Ouasti, S., et al., *The CD44/integrins interplay and the significance of receptor binding and re-presentation in the uptake of RGD-functionalized hyaluronic acid.* Biomaterials, 2012. **33**(4): p. 1120-34.

133. Zaki, N.M., A. Nasti, and N. Tirelli, *Nanocarriers for cytoplasmic delivery: cellular uptake and intracellular fate of chitosan and hyaluronic acid-coated chitosan nanoparticles in a phagocytic cell model.* Macromol Biosci, 2011. **11**(12): p. 1747-60.

134. Zaki, N.M. and N. Tirelli, *Assessment of nanomaterials cytotoxicity and internalization.* Methods Mol Biol, 2011. **695**: p. 243-59.

135. Federico, S., et al., *Design of Decorin-Based Peptides That Bind to Collagen I and their Potential as Adhesion Moieties in Biomaterials.* Angew Chem Int Ed Engl, 2015. **54**(37): p. 10980-4.

136. Krishnan, A.S., et al., *Detection of cell death in tumors by using MR imaging and a gadolinium-based targeted contrast agent.* Radiology, 2008. **246**(3): p. 854-62.

137. Erdogan, S., et al., *Enhanced tumor MR imaging with gadolinium-loaded polychelating polymer-containing tumor-targeted liposomes.* J Magn Reson Imaging, 2008. **27**(3): p. 574-80.

138. Amirbekian, V., et al., *Detecting and assessing macrophages in vivo to evaluate atherosclerosis noninvasively using molecular MRI.* Proc Natl Acad Sci U S A, 2007. **104**(3): p. 961-6.

139. Vaccaro, M., et al., *Structural and relaxometric characterization of peptide aggregates containing gadolinium complexes as potential selective contrast agents in MRI.* Chemphyschem, 2007. **8**(17): p. 2526-38.

140. Kandimalla, K.K., et al., *Pharmacokinetics and amyloid plaque targeting ability of a novel peptide-based magnetic resonance contrast agent in wild-type and Alzheimer's disease transgenic mice.* J Pharmacol Exp Ther, 2007. **322**(2): p. 541-9.

141. De Leon-Rodriguez, L.M., et al., *Solid-phase synthesis of DOTA-peptides.* Chemistry, 2004. **10**(5): p. 1149-55.

142. De Leon-Rodriguez, L.M., et al., *Magnetic resonance imaging detects a specific peptide-protein binding event.* J Am Chem Soc, 2002. **124**(14): p. 3514-5.

143. De Leon-Rodriguez, L.M., et al., *Responsive MRI agents for sensing metabolism in vivo.* Acc Chem Res, 2009. **42**(7): p. 948-57.

144. Weinmann, H.J., et al., *Characteristics of gadolinium-DTPA complex: a potential NMR contrast agent.* AJR Am J Roentgenol, 1984. **142**(3): p. 619-24.

145. Brown, E.M., et al., *Cloning and characterization of an extracellular Ca(2+)-sensing receptor from bovine parathyroid.* Nature, 1993. **366**(6455): p. 575-80.

146. Ogurusu, T., S. Wakabayashi, and M. Shigekawa, *Functional characterization of lanthanide binding sites in the sarcoplasmic reticulum Ca(2+)-ATPase: do lanthanide ions bind to the calcium transport site?* Biochemistry, 1991. **30**(41): p. 9966-73.

147. Biagi, B.A. and J.J. Enyeart, *Gadolinium blocks low- and high-threshold calcium currents in pituitary cells.* Am J Physiol, 1990. **259**(3 Pt 1): p. C515-20.

148. Idee, J.M., et al., *Clinical and biological consequences of transmetallation induced by contrast agents for magnetic resonance imaging: a review.* Fundam Clin Pharmacol, 2006. **20**(6): p. 563-76.

149. Ye, Z., et al., *Polydisulfide manganese(II) complexes as non-gadolinium biodegradable macromolecular MRI contrast agents.* J Magn Reson Imaging, 2012. **35**(3): p. 737-44.

150. Tweedle, M.F., *The ProHance story: the making of a novel MRI contrast agent.* Eur Radiol, 1997. **7 Suppl 5**: p. 225-30.

151. *NIST Critically Selected Stability Constants of Metal Complexes: Version 8.0*. 2017; Available from: https://www.nist.gov/srd/nist46.

152. Yanyi, C., et al., *Calciomics: prediction and analysis of EF-hand calcium binding proteins by protein engineering.* Sci China Chem, 2010. **53**(1): p. 52-60.

153. Zhou, Y., et al., *Probing Ca2+-binding capability of viral proteins with the EF-hand motif by grafting approach.* Methods Mol Biol, 2013. **963**: p. 37-53.

154. Sherry, A.D., P. Caravan, and R.E. Lenkinski, *Primer on gadolinium chemistry.* J Magn Reson Imaging, 2009. **30**(6): p. 1240-8.

155. Fang, M., et al., *Collagen as a double-edged sword in tumor progression.* Tumour Biol, 2014. **35**(4): p. 2871-82.

156. De Jong, W.H., et al., *Particle size-dependent organ distribution of gold nanoparticles after intravenous administration.* Biomaterials, 2008. **29**(12): p. 1912-9.

157. Frenzel, T., et al., *Stability of gadolinium-based magnetic resonance imaging contrast agents in human serum at 37 degrees C.* Invest Radiol, 2008. **43**(12): p. 817-28.

158. White, G.W., W.A. Gibby, and M.F. Tweedle, *Comparison of Gd(DTPA-BMA) (Omniscan) versus Gd(HP-DO3A) (ProHance) relative to gadolinium retention in human*

bone tissue by inductively coupled plasma mass spectroscopy. Invest Radiol, 2006. **41**(3): p. 272-8.

159. Thakral, C. and J.L. Abraham, *Nephrogenic systemic fibrosis: histology and gadolinium detection.* Radiol Clin North Am, 2009. **47**(5): p. 841-53, vi-vii.

160. Thakral, C. and J.L. Abraham, *Gadolinium-induced nephrogenic systemic fibrosis is associated with insoluble Gd deposits in tissues: in vivo transmetallation confirmed by microanalysis.* J Cutan Pathol, 2009. **36**(12): p. 1244-54.

161. Motola, D.L., et al., *Noninvasive Biomarkers of Liver Fibrosis: Clinical Applications and Future Directions.* Curr Pathobiol Rep, 2014. **2**(4): p. 245-256.

162. Nunn, A.D., K.E. Linder, and M.F. Tweedle, *Can receptors be imaged with MRI agents?* Q J Nucl Med, 1997. **41**(2): p. 155-62.

163. Delli Castelli, D., et al., *In vivo MRI multicontrast kinetic analysis of the uptake and intracellular trafficking of paramagnetically labeled liposomes.* J Control Release, 2010. **144**(3): p. 271-9.

164. Kok, M.B., et al., *Cellular compartmentalization of internalized paramagnetic liposomes strongly influences both T1 and T2 relaxivity.* Magn Reson Med, 2009. **61**(5): p. 1022-32.

165. Kok, M.B., G.J. Strijkers, and K. Nicolay, *Dynamic changes in 1H-MR relaxometric properties of cell-internalized paramagnetic liposomes, as studied over a five-day period.* Contrast Media Mol Imaging, 2011. **6**(2): p. 69-76.

166. Artemov, D., Z.M. Bhujwalla, and J.W. Bulte, *Magnetic resonance imaging of cell surface receptors using targeted contrast agents.* Curr Pharm Biotechnol, 2004. **5**(6): p. 485-94.

167. Glunde, K., et al., *Magnetic resonance spectroscopy in metabolic and molecular imaging and diagnosis of cancer.* Chem Rev, 2010. **110**(5): p. 3043-59.

168. Yoo, B. and M.D. Pagel, *An overview of responsive MRI contrast agents for molecular imaging.* Front Biosci, 2008. **13**: p. 1733-52.

169. Zhang, X., et al., *18F-labeled bombesin analogs for targeting GRP receptor-expressing prostate cancer.* J Nucl Med, 2006. **47**(3): p. 492-501.

170. Lu, P., et al., *Extracellular matrix degradation and remodeling in development and disease.* Cold Spring Harb Perspect Biol, 2011. **3**(12).

171. Brodsky, B. and A.V. Persikov, *Molecular structure of the collagen triple helix.* Adv Protein Chem, 2005. **70**: p. 301-39.

172. Polasek, M., et al., *Molecular MR imaging of fibrosis in a mouse model of pancreatic cancer.* Sci Rep, 2017. **7**(1): p. 8114.

173. Henzl, M.T. and J.S. Graham, *Conformational stabilities of the rat alpha- and beta-parvalbumins.* FEBS Lett, 1999. **442**(2-3): p. 241-5.

174. Dithmar, S., D. Rusciano, and H.E. Grossniklaus, *A new technique for implantation of tissue culture melanoma cells in a murine model of metastatic ocular melanoma.* Melanoma Res, 2000. **10**(1): p. 2-8.

175. Yang, H., S. Dithmar, and H.E. Grossniklaus, *Interferon alpha 2b decreases hepatic micrometastasis in a murine model of ocular melanoma by activation of intrinsic hepatic natural killer cells.* Invest Ophthalmol Vis Sci, 2004. **45**(7): p. 2056-64.

176. Grynkiewicz, G., M. Poenie, and R.Y. Tsien, *A new generation of Ca2+ indicators with greatly improved fluorescence properties.* J Biol Chem, 1985. **260**(6): p. 3440-50.

177. Pu, F., et al., *Prostate-specific membrane antigen targeted protein contrast agents for molecular imaging of prostate cancer by MRI.* Nanoscale, 2016. **8**(25): p. 12668-82.

178. Ishak, K., et al., *Histological grading and staging of chronic hepatitis.* J Hepatol, 1995. **22**(6): p. 696-9.

179. Standish, R.A., et al., *An appraisal of the histopathological assessment of liver fibrosis.* Gut, 2006. **55**(4): p. 569-78.

180. Sudnick, D.R. and W.D. Horrocks, Jr., *Lanthanide ion probes of structure in biology. Environmentally sensitive fine structure in laser-induced terbium(III) luminescence.* Biochim Biophys Acta, 1979. **578**(1): p. 135-44.

181. Afshar-Oromieh, A., et al., *Comparison of PET/CT and PET/MRI hybrid systems using a 68Ga-labelled PSMA ligand for the diagnosis of recurrent prostate cancer: initial experience.* Eur J Nucl Med Mol Imaging, 2014. **41**(5): p. 887-97.

182. Afshar-Oromieh, A., et al., *Comparison of (6)(8)Ga-DOTATOC-PET/CT and PET/MRI hybrid systems in patients with cranial meningioma: Initial results.* Neuro Oncol, 2015. **17**(2): p. 312-9.

183. Geraldes, C.F., et al., *Preparation, physico-chemical characterization, and relaxometry studies of various gadolinium(III)-DTPA-bis(amide) derivatives as potential magnetic resonance contrast agents.* Magn Reson Imaging, 1995. **13**(3): p. 401-20.

184. Ye, Y., et al., *Probing site-specific calmodulin calcium and lanthanide affinity by grafting.* J Am Chem Soc, 2005. **127**(11): p. 3743-50.

185. Frydrychowicz, A., et al., *Hepatobiliary MR imaging with gadolinium-based contrast agents.* J Magn Reson Imaging, 2012. **35**(3): p. 492-511.

186. Swaminathan, S., et al., *Cardiac and vascular metal deposition with high mortality in nephrogenic systemic fibrosis.* Kidney Int, 2008. **73**(12): p. 1413-8.

187. Singh, M., et al., *A follow-up of four cases of nephrogenic systemic fibrosis: is gadolinium the specific trigger?* Br J Dermatol, 2008. **158**(6): p. 1358-62.

188. Boyd, A.S., S. Sanyal, and J.L. Abraham, *Gadolinium is not deposited in the skin of patients with normal renal function after exposure to gadolinium-based contrast agents.* J Am Acad Dermatol, 2008. **59**(2): p. 356-8.

189. Wiginton, C.D., et al., *Gadolinium-based contrast exposure, nephrogenic systemic fibrosis, and gadolinium detection in tissue.* AJR Am J Roentgenol, 2008. **190**(4): p. 1060-8.

190. Abraham, J.L., et al., *Dermal inorganic gadolinium concentrations: evidence for in vivo transmetallation and long-term persistence in nephrogenic systemic fibrosis.* Br J Dermatol, 2008. **158**(2): p. 273-80.

191. Khurana, A., J.F. Greene, Jr., and W.A. High, *Quantification of gadolinium in nephrogenic systemic fibrosis: re-examination of a reported cohort with analysis of clinical factors.* J Am Acad Dermatol, 2008. **59**(2): p. 218-24.

192. Kay, J., et al., *Case records of the Massachusetts General Hospital. Case 6-2008. A 46-year-old woman with renal failure and stiffness of the joints and skin.* N Engl J Med, 2008. **358**(8): p. 827-38.

193. White, D.H., et al., *The thermodynamics of complexation of lanthanide (III) DTPA-bisamide complexes and their implication for stability and solution structure.* Invest Radiol, 1991. **26 Suppl 1**: p. S226-8; discussion S232-5.

194. Wedeking, P., K. Kumar, and M.F. Tweedle, *Dose-dependent biodistribution of [153Gd]Gd(acetate)n in mice.* Nucl Med Biol, 1993. **20**(5): p. 679-91.

195. Muhler, A. and H.J. Weinmann, *Biodistribution and excretion of 153Gd-labeled gadolinium ethoxybenzyl diethylenetriamine pentaacetic acid following repeated intravenous administration to rats.* Acad Radiol, 1995. **2**(4): p. 313-8.

196. Parmelee, D.J., et al., *Preclinical evaluation of the pharmacokinetics, biodistribution, and elimination of MS-325, a blood pool agent for magnetic resonance imaging.* Invest Radiol, 1997. **32**(12): p. 741-7.

197. Spinazzi, A., et al., *Multihance clinical pharmacology: biodistribution and MR enhancement of the liver.* Acad Radiol, 1998. **5 Suppl 1**: p. S86-9; discussion S93-4.

198. Sieber, M.A., et al., *Gadolinium-based contrast agents and their potential role in the pathogenesis of nephrogenic systemic fibrosis: the role of excess ligand.* J Magn Reson Imaging, 2008. **27**(5): p. 955-62.

199. Sieber, M.A., et al., *Preclinical investigation to compare different gadolinium-based contrast agents regarding their propensity to release gadolinium in vivo and to trigger nephrogenic systemic fibrosis-like lesions.* Eur Radiol, 2008. **18**(10): p. 2164-73.

200. Sieber, M.A., et al., *A preclinical study to investigate the development of nephrogenic systemic fibrosis: a possible role for gadolinium-based contrast media.* Invest Radiol, 2008. **43**(1): p. 65-75.

201. Henzl, M.T., *Characterization of parvalbumin and polcalcin divalent ion binding by isothermal titration calorimetry.* Methods Enzymol, 2009. **455**: p. 259-97.

202. Laurent, S., et al., *How to measure the transmetallation of a gadolinium complex.* Contrast Media Mol Imaging, 2010. **5**(6): p. 305-8.

203. Tenni, R., et al., *Interaction of decorin with CNBr peptides from collagens I and II. Evidence for multiple binding sites and essential lysyl residues in collagen.* Eur J Biochem, 2002. **269**(5): p. 1428-37.

204. McDonald, R.J., et al., *Gadolinium Deposition in Human Brain Tissues after Contrast-enhanced MR Imaging in Adult Patients without Intracranial Abnormalities.* Radiology, 2017. **285**(2): p. 546-554.

205. Gulani, V., et al., *Gadolinium deposition in the brain: summary of evidence and recommendations.* Lancet Neurol, 2017. **16**(7): p. 564-570.

206. Khawaja, A.Z., et al., *Revisiting the risks of MRI with Gadolinium based contrast agents-review of literature and guidelines.* Insights Imaging, 2015. **6**(5): p. 553-8.

207. Wynn, T.A., *Cellular and molecular mechanisms of fibrosis.* J Pathol, 2008. **214**(2): p. 199-210.

208. Border, W.A. and N.A. Noble, *Transforming growth factor beta in tissue fibrosis.* N Engl J Med, 1994. **331**(19): p. 1286-92.

209. Friedman, S.L., et al., *Therapy for fibrotic diseases: nearing the starting line.* Sci Transl Med, 2013. **5**(167): p. 167sr1.

210. Koyama, Y. and D.A. Brenner, *Liver inflammation and fibrosis.* J Clin Invest, 2017. **127**(1): p. 55-64.

211. Murray, L.A., *Editorial: The Cell Types of Fibrosis.* Front Pharmacol, 2015. **6**: p. 311.

212. Marcellin, P., et al., *Regression of cirrhosis during treatment with tenofovir disoproxil fumarate for chronic hepatitis B: a 5-year open-label follow-up study.* Lancet, 2013. **381**(9865): p. 468-75.

213. Cox, T.R. and J.T. Erler, *Molecular pathways: connecting fibrosis and solid tumor metastasis.* Clin Cancer Res, 2014. **20**(14): p. 3637-43.

214. McDonald, L.T. and A.C. LaRue, *Hematopoietic stem cell derived carcinoma-associated fibroblasts: a novel origin.* Int J Clin Exp Pathol, 2012. **5**(9): p. 863-73.

215. van den Berg, P.J., et al., *Preclinical detection of liver fibrosis using dual-modality photoacoustic/ultrasound system.* Biomed Opt Express, 2016. **7**(12): p. 5081-5091.

216. Tung, J.C., et al., *Tumor mechanics and metabolic dysfunction.* Free Radic Biol Med, 2015. **79**: p. 269-80.

217. Bachem, M.G., et al., *Pancreatic carcinoma cells induce fibrosis by stimulating proliferation and matrix synthesis of stellate cells.* Gastroenterology, 2005. **128**(4): p. 907-21.

218. Fazel, Y., et al., *Epidemiology and natural history of non-alcoholic fatty liver disease.* Metabolism, 2016. **65**(8): p. 1017-25.

219. Manning, D.S. and N.H. Afdhal, *Diagnosis and quantitation of fibrosis.* Gastroenterology, 2008. **134**(6): p. 1670-81.

220. Chen, D.L., et al., *PET imaging approaches for inflammatory lung diseases: Current concepts and future directions.* Eur J Radiol, 2017. **86**: p. 371-376.

221. Jellis, C., et al., *Assessment of nonischemic myocardial fibrosis.* J Am Coll Cardiol, 2010. **56**(2): p. 89-97.

222. Qayyum, A., et al., *Evaluation of diffuse liver steatosis by ultrasound, computed tomography, and magnetic resonance imaging: which modality is best?* Clin Imaging, 2009. **33**(2): p. 110-5.

223. Canto, M.I., et al., *Frequent detection of pancreatic lesions in asymptomatic high-risk individuals.* Gastroenterology, 2012. **142**(4): p. 796-804; quiz e14-5.

224. Giannico, G. and A.B. Fogo, *Lupus nephritis: is the kidney biopsy currently necessary in the management of lupus nephritis?* Clin J Am Soc Nephrol, 2013. **8**(1): p. 138-45.

225. Farris, A.B., et al., *Morphometric and visual evaluation of fibrosis in renal biopsies.* J Am Soc Nephrol, 2011. **22**(1): p. 176-86.

226. Fryer, E., et al., *How often do our liver core biopsies reach current definitions of adequacy?* J Clin Pathol, 2013. **66**(12): p. 1087-9.

227. Popov, Y. and D. Schuppan, *Targeting liver fibrosis: strategies for development and validation of antifibrotic therapies.* Hepatology, 2009. **50**(4): p. 1294-306.

228. Gerlag, D.M. and P.P. Tak, *How useful are synovial biopsies for the diagnosis of rheumatic diseases?* Nat Clin Pract Rheumatol, 2007. **3**(5): p. 248-9.

229. Mahadevan, D. and D.D. Von Hoff, *Tumor-stroma interactions in pancreatic ductal adenocarcinoma.* Mol Cancer Ther, 2007. **6**(4): p. 1186-97.

230. Ueno, H., et al., *Clinicopathological significance of the 'keloid-like' collagen and myxoid stroma in advanced rectal cancer.* Histopathology, 2002. **40**(4): p. 327-34.

231. Park, J.H., et al., *The relationship between tumour stroma percentage, the tumour microenvironment and survival in patients with primary operable colorectal cancer.* Ann Oncol, 2014. **25**(3): p. 644-51.

232. Park, J.H., et al., *Evaluation of a tumor microenvironment-based prognostic score in primary operable colorectal cancer.* Clin Cancer Res, 2015. **21**(4): p. 882-8.

233. Bijlsma, M.F. and H.W. van Laarhoven, *The conflicting roles of tumor stroma in pancreatic cancer and their contribution to the failure of clinical trials: a systematic review and critical appraisal.* Cancer Metastasis Rev, 2015. **34**(1): p. 97-114.

234. Neesse, A., et al., *Stromal biology and therapy in pancreatic cancer.* Gut, 2011. **60**(6): p. 861-8.

235. Wang, L.M., et al., *The prognostic role of desmoplastic stroma in pancreatic ductal adenocarcinoma.* Oncotarget, 2016. **7**(4): p. 4183-94.

236. Ueno, H., et al., *Histologic categorization of desmoplastic reaction: its relevance to the colorectal cancer microenvironment and prognosis.* Ann Surg Oncol, 2015. **22**(5): p. 1504-12.

237. Rousselet, M.C., et al., *Sources of variability in histological scoring of chronic viral hepatitis.* Hepatology, 2005. **41**(2): p. 257-64.

238. Myers, R.P., A. Fong, and A.A. Shaheen, *Utilization rates, complications and costs of percutaneous liver biopsy: a population-based study including 4275 biopsies.* Liver Int, 2008. **28**(5): p. 705-12.

239. Rotman, Y. and A.J. Sanyal, *Current and upcoming pharmacotherapy for non-alcoholic fatty liver disease.* Gut, 2017. **66**(1): p. 180-190.

240. Gerlinger, M., et al., *Intratumor heterogeneity and branched evolution revealed by multiregion sequencing.* N Engl J Med, 2012. **366**(10): p. 883-892.

241. Robertson, E.G. and G. Baxter, *Tumour seeding following percutaneous needle biopsy: the real story!* Clin Radiol, 2011. **66**(11): p. 1007-14.

242. Diaz, L.A., Jr. and A. Bardelli, *Liquid biopsies: genotyping circulating tumor DNA.* J Clin Oncol, 2014. **32**(6): p. 579-86.

243. Crowley, E., et al., *Liquid biopsy: monitoring cancer-genetics in the blood.* Nat Rev Clin Oncol, 2013. **10**(8): p. 472-84.

244. Alix-Panabieres, C. and K. Pantel, *Clinical Applications of Circulating Tumor Cells and Circulating Tumor DNA as Liquid Biopsy.* Cancer Discov, 2016. **6**(5): p. 479-91.

245. European Association for Study of, L. and H. Asociacion Latinoamericana para el Estudio del, *EASL-ALEH Clinical Practice Guidelines: Non-invasive tests for evaluation of liver disease severity and prognosis.* J Hepatol, 2015. **63**(1): p. 237-64.

246. Xie, Q., et al., *The performance of enhanced liver fibrosis (ELF) test for the staging of liver fibrosis: a meta-analysis.* PLoS One, 2014. **9**(4): p. e92772.

247. Shiha, G., et al., *Asian-Pacific Association for the Study of the Liver (APASL) consensus guidelines on invasive and non-invasive assessment of hepatic fibrosis: a 2016 update.* Hepatol Int, 2017. **11**(1): p. 1-30.

248. Sangwaiya, M.J., et al., *Latest developments in the imaging of fibrotic liver disease.* Acta Radiol, 2014. **55**(7): p. 802-13.

249. Genovese, F., et al., *The extracellular matrix in the kidney: a source of novel non-invasive biomarkers of kidney fibrosis?* Fibrogenesis Tissue Repair, 2014. **7**(1): p. 4.

250. Blachier, M., et al., *The burden of liver disease in Europe: a review of available epidemiological data.* J Hepatol, 2013. **58**(3): p. 593-608.

251. Rehm, J., A.V. Samokhvalov, and K.D. Shield, *Global burden of alcoholic liver diseases.* J Hepatol, 2013. **59**(1): p. 160-8.

252. Younossi, Z.M., et al., *Global epidemiology of nonalcoholic fatty liver disease-Meta-analytic assessment of prevalence, incidence, and outcomes.* Hepatology, 2016. **64**(1): p. 73-84.

253. Estes, C., et al., *Modeling the epidemic of nonalcoholic fatty liver disease demonstrates an exponential increase in burden of disease.* Hepatology, 2018. **67**(1): p. 123-133.

254. Mokdad, A.A., et al., *Liver cirrhosis mortality in 187 countries between 1980 and 2010: a systematic analysis.* BMC Med, 2014. **12**: p. 145.

255. Dulai, P.S., et al., *Increased risk of mortality by fibrosis stage in nonalcoholic fatty liver disease: Systematic review and meta-analysis.* Hepatology, 2017. **65**(5): p. 1557-1565.

256. Angulo, P., et al., *Liver Fibrosis, but No Other Histologic Features, Is Associated With Long-term Outcomes of Patients With Nonalcoholic Fatty Liver Disease.* Gastroenterology, 2015. **149**(2): p. 389-97 e10.

257. European Association for the Study of the, L., D. European Association for the Study of, and O. European Association for the Study of, *EASL-EASD-EASO Clinical Practice Guidelines for the Management of Non-Alcoholic Fatty Liver Disease.* Obes Facts, 2016. **9**(2): p. 65-90.

258. Choong, C.C., S.K. Venkatesh, and E.P. Siew, *Accuracy of routine clinical ultrasound for staging of liver fibrosis.* J Clin Imaging Sci, 2012. **2**: p. 58.

259. Smith, A.D., et al., *Liver Surface Nodularity Quantification from Routine CT Images as a Biomarker for Detection and Evaluation of Cirrhosis.* Radiology, 2016. **280**(3): p. 771-81.

260. Van Beers, B.E., J.L. Daire, and P. Garteiser, *New imaging techniques for liver diseases.* J Hepatol, 2015. **62**(3): p. 690-700.

261. Sandrin, L., et al., *Transient elastography: a new noninvasive method for assessment of hepatic fibrosis.* Ultrasound Med Biol, 2003. **29**(12): p. 1705-13.

262. Foucher, J., et al., *Diagnosis of cirrhosis by transient elastography (FibroScan): a prospective study.* Gut, 2006. **55**(3): p. 403-8.

263. Castera, L., X. Forns, and A. Alberti, *Non-invasive evaluation of liver fibrosis using transient elastography.* J Hepatol, 2008. **48**(5): p. 835-47.

264. Myers, R.P., et al., *Feasibility and diagnostic performance of the FibroScan XL probe for liver stiffness measurement in overweight and obese patients.* Hepatology, 2012. **55**(1): p. 199-208.

265. Mueller, S. and L. Sandrin, *Liver stiffness: a novel parameter for the diagnosis of liver disease.* Hepat Med, 2010. **2**: p. 49-67.

266. Liu, J., et al., *Liver Shear-Wave Velocity and Serum Fibrosis Markers to Diagnose Hepatic Fibrosis in Patients with Chronic Viral Hepatitis B.* Korean J Radiol, 2016. **17**(3): p. 396-404.

267. Feng, Y.H., et al., *Shear wave elastography results correlate with liver fibrosis histology and liver function reserve.* World J Gastroenterol, 2016. **22**(17): p. 4338-44.

268. Loomba, R., et al., *Magnetic resonance elastography predicts advanced fibrosis in patients with nonalcoholic fatty liver disease: a prospective study.* Hepatology, 2014. **60**(6): p. 1920-8.

269. Imajo, K., et al., *Magnetic Resonance Imaging More Accurately Classifies Steatosis and Fibrosis in Patients With Nonalcoholic Fatty Liver Disease Than Transient Elastography.* Gastroenterology, 2016. **150**(3): p. 626-637 e7.

270. Park, C.C., et al., *Magnetic Resonance Elastography vs Transient Elastography in Detection of Fibrosis and Noninvasive Measurement of Steatosis in Patients With Biopsy-*

Proven Nonalcoholic Fatty Liver Disease. Gastroenterology, 2017. **152**(3): p. 598-607 e2.

271. Chen, J., et al., *Early detection of nonalcoholic steatohepatitis in patients with nonalcoholic fatty liver disease by using MR elastography.* Radiology, 2011. **259**(3): p. 749-56.

272. Venkatesh, S.K., et al., *Magnetic resonance elastography for the detection and staging of liver fibrosis in chronic hepatitis B.* Eur Radiol, 2014. **24**(1): p. 70-8.

273. Venkatesh, S.K., et al., *Magnetic resonance elastography of liver in healthy Asians: normal liver stiffness quantification and reproducibility assessment.* J Magn Reson Imaging, 2014. **39**(1): p. 1-8.

274. Dyvorne, H.A., et al., *Prospective comparison of magnetic resonance imaging to transient elastography and serum markers for liver fibrosis detection.* Liver Int, 2016. **36**(5): p. 659-66.

275. Xu, G., et al., *The functional pitch of an organ: quantification of tissue texture with photoacoustic spectrum analysis.* Radiology, 2014. **271**(1): p. 248-54.

276. Lei, H., et al., *Characterizing intestinal inflammation and fibrosis in Crohn's disease by photoacoustic imaging: feasibility study.* Biomed Opt Express, 2016. **7**(7): p. 2837-48.

277. Knieling, F., et al., *Multispectral Optoacoustic Tomography for Assessment of Crohn's Disease Activity.* N Engl J Med, 2017. **376**(13): p. 1292-1294.

278. Vogl, T.J., et al., *Liver tumors: comparison of MR imaging with Gd-EOB-DTPA and Gd-DTPA.* Radiology, 1996. **200**(1): p. 59-67.

279. Hammerstingl, R., et al., *Diagnostic efficacy of gadoxetic acid (Primovist)-enhanced MRI and spiral CT for a therapeutic strategy: comparison with intraoperative and histopathologic findings in focal liver lesions.* Eur Radiol, 2008. **18**(3): p. 457-67.

280. Van Beers, B.E., C.M. Pastor, and H.K. Hussain, *Primovist, Eovist: what to expect?* J Hepatol, 2012. **57**(2): p. 421-9.

281. Feier, D., et al., *Liver fibrosis: histopathologic and biochemical influences on diagnostic efficacy of hepatobiliary contrast-enhanced MR imaging in staging.* Radiology, 2013. **269**(2): p. 460-8.

282. Ehling, J., et al., *Elastin-based molecular MRI of liver fibrosis.* Hepatology, 2013. **58**(4): p. 1517-8.

283. Fuchs, B.C., et al., *Molecular MRI of collagen to diagnose and stage liver fibrosis.* J Hepatol, 2013. **59**(5): p. 992-8.

284. Li, F., et al., *Molecular imaging of hepatic stellate cell activity by visualization of hepatic integrin alphavbeta3 expression with SPECT in rat.* Hepatology, 2011. **54**(3): p. 1020-30.

285. Kuijpers, B.H., et al., *Preparation and evaluation of glycosylated arginine-glycine-aspartate (RGD) derivatives for integrin targeting.* Bioconjug Chem, 2007. **18**(6): p. 1847-54.

286. Patsenker, E., et al., *Pharmacological inhibition of integrin alphavbeta3 aggravates experimental liver fibrosis and suppresses hepatic angiogenesis.* Hepatology, 2009. **50**(5): p. 1501-11.

287. Hatori, A., et al., *Utility of Translocator Protein (18 kDa) as a Molecular Imaging Biomarker to Monitor the Progression of Liver Fibrosis.* Sci Rep, 2015. **5**: p. 17327.

288. Li, D., et al., *Targeting activated hepatic stellate cells (aHSCs) for liver fibrosis imaging.* EJNMMI Res, 2015. **5**(1): p. 71.

289. Beljaars, L., et al., *The preferential homing of a platelet derived growth factor receptor-recognizing macromolecule to fibroblast-like cells in fibrotic tissue.* Biochem Pharmacol, 2003. **66**(7): p. 1307-17.

290. Friedman, S.L., *Hepatic fibrosis -- overview.* Toxicology, 2008. **254**(3): p. 120-9.

291. Kenneth D. Kochanek, S.L.M., Jiaquan Xu, Betzaida Tejada-Vera, *Deaths: Final Data for 2014.* National Vital Statistics Reports, Centers for Disease Control and Prevention 2016. **65**.

292. Friedman, S.L., *Mechanisms of hepatic fibrogenesis.* Gastroenterology, 2008. **134**(6): p. 1655-69.

293. Lu, J., et al., *NRBF2 regulates autophagy and prevents liver injury by modulating Atg14L-linked phosphatidylinositol-3 kinase III activity.* Nat Commun, 2014. **5**: p. 3920.

294. Wang, Y., et al., *Assessment of chronic hepatitis and fibrosis: comparison of MR elastography and diffusion-weighted imaging.* AJR Am J Roentgenol, 2011. **196**(3): p. 553-61.

295. Kim, H.J., et al., *Hirschsprung disease and hypoganglionosis in adults: radiologic findings and differentiation.* Radiology, 2008. **247**(2): p. 428-34.

296. Tschirch, F.T., et al., *Contrast-enhanced MR cholangiography with Gd-EOB-DTPA in patients with liver cirrhosis: visualization of the biliary ducts in comparison with patients with normal liver parenchyma.* Eur Radiol, 2008. **18**(8): p. 1577-86.

297. Tamada, T., et al., *Gd-EOB-DTPA-enhanced MR imaging: evaluation of hepatic enhancement effects in normal and cirrhotic livers.* Eur J Radiol, 2011. **80**(3): p. e311-6.

298. Namasivayam, S., D.R. Martin, and S. Saini, *Imaging of liver metastases: MRI.* Cancer Imaging, 2007. **7**: p. 2-9.

299. Hanaoka, K., et al., *The detection limit of a Gd3+-based T1 agent is substantially reduced when targeted to a protein microdomain.* Magn Reson Imaging, 2008. **26**(5): p. 608-17.

300. Albiin, N., *MRI of Focal Liver Lesions.* Curr Med Imaging Rev, 2012. **8**(2): p. 107-116.

301. Maniam, S. and J. Szklaruk, *Magnetic resonance imaging: Review of imaging techniques and overview of liver imaging.* World J Radiol, 2010. **2**(8): p. 309-22.

302. Ersoy, H. and F.J. Rybicki, *Biochemical safety profiles of gadolinium-based extracellular contrast agents and nephrogenic systemic fibrosis.* J Magn Reson Imaging, 2007. **26**(5): p. 1190-7.

303. Maharaj, B., et al., *Sampling variability and its influence on the diagnostic yield of percutaneous needle biopsy of the liver.* Lancet, 1986. **1**(8480): p. 523-5.

304. Abdi, W., J.C. Millan, and E. Mezey, *Sampling variability on percutaneous liver biopsy.* Arch Intern Med, 1979. **139**(6): p. 667-9.

305. Regev, A., et al., *Sampling error and intraobserver variation in liver biopsy in patients with chronic HCV infection.* Am J Gastroenterol, 2002. **97**(10): p. 2614-8.

306. Venkatesh, S.K., et al., *Magnetic resonance elastography: beyond liver fibrosis-a case-based pictorial review.* Abdom Radiol (NY), 2017.

307. Dodd, G.D., 3rd, et al., *Spectrum of imaging findings of the liver in end-stage cirrhosis: Part II, focal abnormalities.* AJR Am J Roentgenol, 1999. **173**(5): p. 1185-92.

308. Dodd, G.D., 3rd, et al., *Spectrum of imaging findings of the liver in end-stage cirrhosis: part I, gross morphology and diffuse abnormalities.* AJR Am J Roentgenol, 1999. **173**(4): p. 1031-6.

309. Ismail, M.H. and M. Pinzani, *Reversal of liver fibrosis.* Saudi J Gastroenterol, 2009. **15**(1): p. 72-9.

310. Jung, Y.K. and H.J. Yim, *Reversal of liver cirrhosis: current evidence and expectations.* Korean J Intern Med, 2017. **32**(2): p. 213-228.

311. Banerjee, R., et al., *Multiparametric magnetic resonance for the non-invasive diagnosis of liver disease.* J Hepatol, 2014. **60**(1): p. 69-77.

312. Papastergiou, V., E. Tsochatzis, and A.K. Burroughs, *Non-invasive assessment of liver fibrosis.* Ann Gastroenterol, 2012. **25**(3): p. 218-231.

313. Neuman, R.E. and M.A. Logan, *The determination of collagen and elastin in tissues.* J Biol Chem, 1950. **186**(2): p. 549-56.

314. Kolodziej, A.F., et al., *Peptide optimization and conjugation strategies in the development of molecularly targeted magnetic resonance imaging contrast agents.* Methods Mol Biol, 2014. **1088**: p. 185-211.

315. Helm, P.A., et al., *Postinfarction myocardial scarring in mice: molecular MR imaging with use of a collagen-targeting contrast agent.* Radiology, 2008. **247**(3): p. 788-96.

316. Pu, F., et al., *GRPR-targeted Protein Contrast Agents for Molecular Imaging of Receptor Expression in Cancers by MRI.* Sci Rep, 2015. **5**: p. 16214.

317. Elpek, G.O., *Angiogenesis and liver fibrosis.* World J Hepatol, 2015. **7**(3): p. 377-91.

318. Bocca, C., et al., *Angiogenesis and Fibrogenesis in Chronic Liver Diseases.* Cell Mol Gastroenterol Hepatol, 2015. **1**(5): p. 477-488.

319. Fernandez, M., et al., *Angiogenesis in liver disease.* J Hepatol, 2009. **50**(3): p. 604-20.

320. Thabut, D. and V. Shah, *Intrahepatic angiogenesis and sinusoidal remodeling in chronic liver disease: new targets for the treatment of portal hypertension?* J Hepatol, 2010. **53**(5): p. 976-80.

321. Zhang, W., et al., *Dynamic Contrast-Enhanced Magnetic Resonance Imaging with Gd-EOB-DTPA for the Evaluation of Liver Fibrosis Induced by Carbon Tetrachloride in Rats.* PLoS One, 2015. **10**(6): p. e0129621.

322. Zhou, L., et al., *Liver dynamic contrast-enhanced MRI for staging liver fibrosis in a piglet model.* J Magn Reson Imaging, 2014. **39**(4): p. 872-8.

323. Chen, B.B., et al., *Dynamic contrast-enhanced magnetic resonance imaging with Gd-EOB-DTPA for the evaluation of liver fibrosis in chronic hepatitis patients.* Eur Radiol, 2012. **22**(1): p. 171-80.

324. Schuppan, D. and N.H. Afdhal, *Liver cirrhosis.* Lancet, 2008. **371**(9615): p. 838-51.

325. Park, S., et al., *Differential Roles of Angiogenesis in the Induction of Fibrogenesis and the Resolution of Fibrosis in Liver.* Biol Pharm Bull, 2015. **38**(7): p. 980-5.

326. *EMA's final opinion confirms restrictions on use of linear gadolinium agents in body scans.* European Medicines Agency, 2017.

327. Eckhardt, B.L., et al., *Strategies for the discovery and development of therapies for metastatic breast cancer.* Nat Rev Drug Discov, 2012. **11**(6): p. 479-97.

328. Van den Eynden, G.G., et al., *The multifaceted role of the microenvironment in liver metastasis: biology and clinical implications.* Cancer Res, 2013. **73**(7): p. 2031-43.

329. Singh, A.D., M.E. Turell, and A.K. Topham, *Uveal melanoma: trends in incidence, treatment, and survival.* Ophthalmology, 2011. **118**(9): p. 1881-5.

330. McLaughlin, C.C., et al., *Incidence of noncutaneous melanomas in the U.S.* Cancer, 2005. **103**(5): p. 1000-7.

331. Spagnolo, F., G. Caltabiano, and P. Queirolo, *Uveal melanoma.* Cancer Treat Rev, 2012. **38**(5): p. 549-53.

332. Grossniklaus, H.E., et al., *Metastatic ocular melanoma to the liver exhibits infiltrative and nodular growth patterns.* Hum Pathol, 2016. **57**: p. 165-175.

333. Singh, A.D. and E.C. Borden, *Metastatic uveal melanoma.* Ophthalmol Clin North Am, 2005. **18**(1): p. 143-50, ix.

334. Halenda, K.M., et al., *Reduction of Nodular Growth Pattern of Metastatic Uveal Melanoma after Radioembolization of Hepatic Metastases.* Ocul Oncol Pathol, 2016. **2**(3): p. 160-5.

335. Augsburger, J.J., Z.M. Correa, and A.H. Shaikh, *Effectiveness of treatments for metastatic uveal melanoma.* Am J Ophthalmol, 2009. **148**(1): p. 119-27.

336. Grossniklaus, H.E., *Progression of ocular melanoma metastasis to the liver: the 2012 Zimmerman lecture.* JAMA Ophthalmol, 2013. **131**(4): p. 462-9.

337. Liao, A., et al., *Radiologic and Histopathologic Correlation of Different Growth Patterns of Metastatic Uveal Melanoma to the Liver.* Ophthalmology, 2017.

338. Dayani, P.N., et al., *Hepatic metastasis from uveal melanoma: angiographic pattern predictive of survival after hepatic arterial chemoembolization.* Arch Ophthalmol, 2009. **127**(5): p. 628-32.

339. Sharma, K.V., et al., *Hepatic arterial chemoembolization for management of metastatic melanoma.* AJR Am J Roentgenol, 2008. **190**(1): p. 99-104.

340. Cardenas-Rodriguez, J., et al., *A reference agent model for DCE MRI can be used to quantify the relative vascular permeability of two MRI contrast agents.* Magn Reson Imaging, 2013. **31**(6): p. 900-10.

341. Yankeelov, T.E., R.G. Abramson, and C.C. Quarles, *Quantitative multimodality imaging in cancer research and therapy.* Nat Rev Clin Oncol, 2014. **11**(11): p. 670-80.

342. Mehlen, P. and A. Puisieux, *Metastasis: a question of life or death.* Nat Rev Cancer, 2006. **6**(6): p. 449-58.

343. Zhou, Z., et al., *MRI detection of breast cancer micrometastases with a fibronectin-targeting contrast agent.* Nat Commun, 2015. **6**: p. 7984.

344. Quail, D.F. and J.A. Joyce, *Microenvironmental regulation of tumor progression and metastasis.* Nat Med, 2013. **19**(11): p. 1423-37.

345. Reticker-Flynn, N.E., et al., *A combinatorial extracellular matrix platform identifies cell-extracellular matrix interactions that correlate with metastasis.* Nat Commun, 2012. **3**: p. 1122.

346. Choi, J., et al., *Engineered collagen hydrogels for the sustained release of biomolecules and imaging agents: promoting the growth of human gingival cells.* Int J Nanomedicine, 2014. **9**: p. 5189-201.

347. Jin, H.E., R. Farr, and S.W. Lee, *Collagen mimetic peptide engineered M13 bacteriophage for collagen targeting and imaging in cancer.* Biomaterials, 2014. **35**(33): p. 9236-45.

348. Damato, B., *Developments in the management of uveal melanoma.* Clin Exp Ophthalmol, 2004. **32**(6): p. 639-47.

349. Mudhar, H.S., et al., *A critical appraisal of the prognostic and predictive factors for uveal malignant melanoma.* Histopathology, 2004. **45**(1): p. 1-12.

350. Kaiserman, I., R. Amer, and J. Pe'er, *Liver function tests in metastatic uveal melanoma.* Am J Ophthalmol, 2004. **137**(2): p. 236-43.

351. Toivonen, P., et al., *Microcirculation and tumor-infiltrating macrophages in choroidal and ciliary body melanoma and corresponding metastases.* Invest Ophthalmol Vis Sci, 2004. **45**(1): p. 1-6.

352. Donoso, L.A., et al., *Metastatic uveal melanoma: diffuse hepatic metastasis in a patient with concurrent normal serum liver enzyme levels and liver scan.* Arch Ophthalmol, 1985. **103**(6): p. 758.

353. Hannsson L, H.A., Bonfrer JMG, Duffy J, Einarsson R., *Tumor markers in malignant melanoma – EGTM (European Group on Tumor Markers) Guidelines.* Tumor Biology, 2006. **27**: p. 35-S1.

354. Bonfrer, J.M., et al., *The luminescence immunoassay S-100: a sensitive test to measure circulating S-100B: its prognostic value in malignant melanoma.* Br J Cancer, 1998. **77**(12): p. 2210-4.

355. Bosserhoff, A.K., et al., *Melanoma-inhibiting activity, a novel serum marker for progression of malignant melanoma.* Cancer Res, 1997. **57**(15): p. 3149-53.

356. Hauschild, A., *[Meeting report of the 39th Annual Conference of the American Society of Clinical Oncology (ASCO), 5/31-6/3/2003, Chicago, USA]*. Hautarzt, 2003. **54**(10): p. 999-1002.

357. Hauschild, A., et al., *S100B protein detection in serum is a significant prognostic factor in metastatic melanoma.* Oncology, 1999. **56**(4): p. 338-44.

358. Tuck, A.B., et al., *Osteopontin expression in a group of lymph node negative breast cancer patients.* Int J Cancer, 1998. **79**(5): p. 502-8.

359. Kadkol, S.S., et al., *Osteopontin expression and serum levels in metastatic uveal melanoma: a pilot study.* Invest Ophthalmol Vis Sci, 2006. **47**(3): p. 802-6.

360. Rittling, S.R. and A.F. Chambers, *Role of osteopontin in tumour progression.* Br J Cancer, 2004. **90**(10): p. 1877-81.

361. Diener-West, M., et al., *Development of metastatic disease after enrollment in the COMS trials for treatment of choroidal melanoma: Collaborative Ocular Melanoma Study Group Report No. 26.* Arch Ophthalmol, 2005. **123**(12): p. 1639-43.

362. Rietschel, P., et al., *Variates of survival in metastatic uveal melanoma.* J Clin Oncol, 2005. **23**(31): p. 8076-80.

363. Barbazetto, I.A., et al., *Treatment of choroidal melanoma using photodynamic therapy.* Am J Ophthalmol, 2003. **135**(6): p. 898-9.

364. Woodman, S.E., *Metastatic uveal melanoma: biology and emerging treatments.* Cancer J, 2012. **18**(2): p. 148-52.

365. Pereira, P.R., et al., *Current and emerging treatment options for uveal melanoma.* Clin Ophthalmol, 2013. **7**: p. 1669-82.

366. Yang, H. and H.E. Grossniklaus, *Constitutive overexpression of pigment epithelium-derived factor inhibition of ocular melanoma growth and metastasis.* Invest Ophthalmol Vis Sci, 2010. **51**(1): p. 28-34.

367. Motola-Kuba, D., et al., *Hepatocellular carcinoma. An overview.* Ann Hepatol, 2006. **5**(1): p. 16-24.

368. Parkin, D.M., et al., *Estimating the world cancer burden: Globocan 2000.* Int J Cancer, 2001. **94**(2): p. 153-6.

369. Parkin, D.M., *Global cancer statistics in the year 2000.* Lancet Oncol, 2001. **2**(9): p. 533-43.

370. Tsukuma, H., et al., *Risk factors for hepatocellular carcinoma among patients with chronic liver disease.* N Engl J Med, 1993. **328**(25): p. 1797-801.

371. Simonetti, R.G., et al., *Hepatocellular carcinoma. A worldwide problem and the major risk factors.* Dig Dis Sci, 1991. **36**(7): p. 962-72.

372. Kew, M.C., *Hepatocellular carcinoma with and without cirrhosis. A comparison in southern African blacks.* Gastroenterology, 1989. **97**(1): p. 136-9.

373. Chen, T.H., et al., *Ultrasound screening and risk factors for death from hepatocellular carcinoma in a high risk group in Taiwan.* Int J Cancer, 2002. **98**(2): p. 257-61.

374. Sangiovanni, A., et al., *Increased survival of cirrhotic patients with a hepatocellular carcinoma detected during surveillance.* Gastroenterology, 2004. **126**(4): p. 1005-14.

375. Benvegnu, L., et al., *Natural history of compensated viral cirrhosis: a prospective study on the incidence and hierarchy of major complications.* Gut, 2004. **53**(5): p. 744-9.

376. Fattovich, G., et al., *Effect of hepatitis B and C virus infections on the natural history of compensated cirrhosis: a cohort study of 297 patients.* Am J Gastroenterol, 2002. **97**(11): p. 2886-95.

377. Deuffic, S., et al., *Trends in primary liver cancer.* Lancet, 1998. **351**(9097): p. 214-5.

378. El-Serag, H.B. and A.C. Mason, *Rising incidence of hepatocellular carcinoma in the United States.* N Engl J Med, 1999. **340**(10): p. 745-50.

379. La Vecchia, C., et al., *Trends in mortality from primary liver cancer in Europe.* Eur J Cancer, 2000. **36**(7): p. 909-15.

380. Corrao, G., et al., *Trends of liver cirrhosis mortality in Europe, 1970-1989: age-period-cohort analysis and changing alcohol consumption.* Int J Epidemiol, 1997. **26**(1): p. 100-9.

381. Roizen, R., W.C. Kerr, and K.M. Fillmore, *Cirrhosis mortality and per capita consumption of distilled spirits, United States, 1949-94: trend analysis.* BMJ, 1999. **319**(7211): p. 666-70.

382. Roizen, R., W.C. Kerr, and K.M. Fillmore, *Cirrhosis mortality and per capita consumption of distilled spirits, United States, 1949-1994: trend analysis.* West J Med, 1999. **171**(2): p. 83-7.

383. Vong, S. and B.P. Bell, *Chronic liver disease mortality in the United States, 1990-1998.* Hepatology, 2004. **39**(2): p. 476-83.

384. Alter, M.J., et al., *The prevalence of hepatitis C virus infection in the United States, 1988 through 1994.* N Engl J Med, 1999. **341**(8): p. 556-62.

385. Fattovich, G., et al., *Hepatocellular carcinoma in cirrhosis: incidence and risk factors.* Gastroenterology, 2004. **127**(5 Suppl 1): p. S35-50.

386. Hussain, S.M., R.C. Semelka, and D.G. Mitchell, *MR imaging of hepatocellular carcinoma.* Magn Reson Imaging Clin N Am, 2002. **10**(1): p. 31-52, v.

387. Choi, B.I., K. Takayasu, and M.C. Han, *Small hepatocellular carcinomas and associated nodular lesions of the liver: pathology, pathogenesis, and imaging findings.* AJR Am J Roentgenol, 1993. **160**(6): p. 1177-87.

388. Mitchell, D.G., *Liver I: Currently available gadolinium chelates.* Magn Reson Imaging Clin N Am, 1996. **4**(1): p. 37-51.

389. Scudellari, M., *Drug development: try and try again.* Nature, 2014. **516**(7529): p. S4-6.

390. Villanueva, A. and J.M. Llovet, *Second-line therapies in hepatocellular carcinoma: emergence of resistance to sorafenib.* Clin Cancer Res, 2012. **18**(7): p. 1824-6.

391. Meads, M.B., R.A. Gatenby, and W.S. Dalton, *Environment-mediated drug resistance: a major contributor to minimal residual disease.* Nat Rev Cancer, 2009. **9**(9): p. 665-74.

392. Llovet, J.M., et al., *Advances in targeted therapies for hepatocellular carcinoma in the genomic era.* Nat Rev Clin Oncol, 2015. **12**(8): p. 436.

393. Tredan, O., et al., *Drug resistance and the solid tumor microenvironment.* J Natl Cancer Inst, 2007. **99**(19): p. 1441-54.

394. Wu, S.D., et al., *Role of the microenvironment in hepatocellular carcinoma development and progression.* Cancer Treat Rev, 2012. **38**(3): p. 218-25.

395. Heindl, A., et al., *Similarity and diversity of the tumor microenvironment in multiple metastases: critical implications for overall and progression-free survival of high-grade serous ovarian cancer.* Oncotarget, 2016. **7**(44): p. 71123-71135.

396. Yin, C., et al., *Hepatic stellate cells in liver development, regeneration, and cancer.* J Clin Invest, 2013. **123**(5): p. 1902-10.

397. Carpino, G., et al., *Alpha-SMA expression in hepatic stellate cells and quantitative analysis of hepatic fibrosis in cirrhosis and in recurrent chronic hepatitis after liver transplantation.* Dig Liver Dis, 2005. **37**(5): p. 349-56.

398. Sokolovic, A., et al., *Insulin-like growth factor binding protein 5 enhances survival of LX2 human hepatic stellate cells.* Fibrogenesis Tissue Repair, 2010. **3**: p. 3.

399. Friedman, S.L., *Hepatic stellate cells: protean, multifunctional, and enigmatic cells of the liver.* Physiol Rev, 2008. **88**(1): p. 125-72.

400. Santamato, A., et al., *Hepatic stellate cells stimulate HCC cell migration via laminin-5 production.* Clin Sci (Lond), 2011. **121**(4): p. 159-68.

401. Amann, T., et al., *Activated hepatic stellate cells promote tumorigenicity of hepatocellular carcinoma.* Cancer Sci, 2009. **100**(4): p. 646-53.

402. Choi, J., et al., *Intraperitoneal immunotherapy for metastatic ovarian carcinoma: Resistance of intratumoral collagen to antibody penetration.* Clin Cancer Res, 2006. **12**(6): p. 1906-12.

403. Erikson, A., et al., *Physical and chemical modifications of collagen gels: impact on diffusion.* Biopolymers, 2008. **89**(2): p. 135-43.

404. Bruix, J., M. Sherman, and D. American Association for the Study of Liver, *Management of hepatocellular carcinoma: an update.* Hepatology, 2011. **53**(3): p. 1020-2.

405. Forner, A., et al., *Diagnosis of hepatic nodules 20 mm or smaller in cirrhosis: Prospective validation of the noninvasive diagnostic criteria for hepatocellular carcinoma.* Hepatology, 2008. **47**(1): p. 97-104.

406. Sangiovanni, A., et al., *The diagnostic and economic impact of contrast imaging techniques in the diagnosis of small hepatocellular carcinoma in cirrhosis.* Gut, 2010. **59**(5): p. 638-44.

407. Rimola, J., et al., *Non-invasive diagnosis of hepatocellular carcinoma </= 2 cm in cirrhosis. Diagnostic accuracy assessing fat, capsule and signal intensity at dynamic MRI.* J Hepatol, 2012. **56**(6): p. 1317-23.

408. Schuhmann-Giampieri, G., et al., *Preclinical evaluation of Gd-EOB-DTPA as a contrast agent in MR imaging of the hepatobiliary system.* Radiology, 1992. **183**(1): p. 59-64.

409. Frericks, B.B., et al., *Qualitative and quantitative evaluation of hepatocellular carcinoma and cirrhotic liver enhancement using Gd-EOB-DTPA.* AJR Am J Roentgenol, 2009. **193**(4): p. 1053-60.

410. Ayuso, C., J. Rimola, and A. Garcia-Criado, *Imaging of HCC.* Abdom Imaging, 2012. **37**(2): p. 215-30.

411. Golfieri, R., et al., *Contribution of the hepatobiliary phase of Gd-EOB-DTPA-enhanced MRI to Dynamic MRI in the detection of hypovascular small (</= 2 cm) HCC in cirrhosis.* Eur Radiol, 2011. **21**(6): p. 1233-42.

412. Granito, A., et al., *Impact of gadoxetic acid (Gd-EOB-DTPA)-enhanced magnetic resonance on the non-invasive diagnosis of small hepatocellular carcinoma: a prospective study.* Aliment Pharmacol Ther, 2013. **37**(3): p. 355-63.

413. Golfieri, R., et al., *Which is the best MRI marker of malignancy for atypical cirrhotic nodules: hypointensity in hepatobiliary phase alone or combined with other features? Classification after Gd-EOB-DTPA administration.* J Magn Reson Imaging, 2012. **36**(3): p. 648-57.

414. Bartolozzi, C., et al., *Contrast-enhanced magnetic resonance imaging of 102 nodules in cirrhosis: correlation with histological findings on explanted livers.* Abdom Imaging, 2013. **38**(2): p. 290-6.

415. Bashir, M.R., et al., *Hepatocellular carcinoma in a North American population: does hepatobiliary MR imaging with Gd-EOB-DTPA improve sensitivity and confidence for diagnosis?* J Magn Reson Imaging, 2013. **37**(2): p. 398-406.

416. Zech, C.J., et al., *Vascular enhancement in early dynamic liver MR imaging in an animal model: comparison of two injection regimen and two different doses Gd-EOB-DTPA (gadoxetic acid) with standard Gd-DTPA.* Invest Radiol, 2009. **44**(6): p. 305-10.

417. Haradome, H., et al., *Can MR fluoroscopic triggering technique and slow rate injection provide appropriate arterial phase images with reducing artifacts on gadoxetic acid-DTPA (Gd-EOB-DTPA)-enhanced hepatic MR imaging?* J Magn Reson Imaging, 2010. **32**(2): p. 334-40.

418. Schmid-Tannwald, C., et al., *Optimization of the dynamic, Gd-EOB-DTPA-enhanced MRI of the liver: the effect of the injection rate.* Acta Radiol, 2012. **53**(9): p. 961-5.

419. Feuerlein, S., et al., *Hepatocellular MR contrast agents: enhancement characteristics of liver parenchyma and portal vein after administration of gadoxetic acid in comparison to gadobenate dimeglumine.* Eur J Radiol, 2012. **81**(9): p. 2037-41.

420. Chen, C.Z., et al., *Hepatocellular carcinoma 20 mm or smaller in cirrhosis patients: early magnetic resonance enhancement by gadoxetic acid compared with gadopentetate dimeglumine.* Hepatol Int, 2014. **8**(1): p. 104-11.

421. Wong, K.K., et al., *Computational medical imaging and hemodynamics framework for functional analysis and assessment of cardiovascular structures.* Biomed Eng Online, 2017. **16**(1): p. 35.

422. Ray, H.M., et al., *Predictors of intervention and mortality in patients with uncomplicated acute type B aortic dissection.* J Vasc Surg, 2016. **64**(6): p. 1560-1568.

423. Gupta, R. and R. Munoz, *Evaluation and Management of Chest Pain in the Elderly.* Emerg Med Clin North Am, 2016. **34**(3): p. 523-42.

424. Wong, K.K., et al., *Medical image diagnostics based on computer-aided flow analysis using magnetic resonance images.* Comput Med Imaging Graph, 2012. **36**(7): p. 527-41.

425. Parsa, C.J. and G.C. Hughes, *Surgical options to contend with thoracic aortic pathology.* Semin Roentgenol, 2009. **44**(1): p. 29-51.

426. Sato, F., et al., *Newly diagnosed acute aortic dissection: characteristics, treatment modifications, and outcomes.* Int Heart J, 2005. **46**(6): p. 1083-98.

427. Vernhet, H., et al., *Abdominal CT angiography before surgery as a predictor of postoperative death in acute aortic dissection.* AJR Am J Roentgenol, 2004. **182**(4): p. 875-9.

428. Godwin, J.D., et al., *Evaluation of dissections and aneurysms of the thoracic aorta by conventional and dynamic CT scanning.* Radiology, 1980. **136**(1): p. 125-33.

429. Vasile, N., et al., *Computed tomography of thoracic aortic dissection: accuracy and pitfalls.* J Comput Assist Tomogr, 1986. **10**(2): p. 211-5.

430. Iliceto, S., et al., *Diagnosis of aneurysm of the thoracic aorta. Comparison between two non invasive techniques: two-dimensional echocardiography and computed tomography.* Eur Heart J, 1984. **5**(7): p. 545-55.

431. Godwin, J.D., R.S. Breiman, and J.M. Speckman, *Problems and pitfalls in the evaluation of thoracic aortic dissection by computed tomography.* J Comput Assist Tomogr, 1982. **6**(4): p. 750-6.

432. Thorsen, M.K., et al., *Dissecting aortic aneurysms: accuracy of computed tomographic diagnosis.* Radiology, 1983. **148**(3): p. 773-7.

433. Singh, H., E. Fitzgerald, and M.S. Ruttley, *Computed tomography: the investigation of choice for aortic dissection?* Br Heart J, 1986. **56**(2): p. 171-5.

434. Mintz, G.S., et al., *Two dimensional echocardiographic recognition of the descending thoracic aorta.* Am J Cardiol, 1979. **44**(2): p. 232-8.

435. Kasper, W., et al., *Diagnosis of dissecting aortic aneurysm with suprasternal echocardiography.* Am J Cardiol, 1978. **42**(2): p. 291-4.

436. Victor, M.F., et al., *Two dimensional echocardiographic diagnosis of aortic dissection.* Am J Cardiol, 1981. **48**(6): p. 1155-9.

437. Mathew, T. and N.C. Nanda, *Two-dimensional and Doppler echocardiographic evaluation of aortic aneurysm and dissection.* Am J Cardiol, 1984. **54**(3): p. 379-85.

438. Iliceto, S., et al., *Color Doppler evaluation of aortic dissection.* Circulation, 1987. **75**(4): p. 748-55.

439. Borner, N., et al., *Diagnosis of aortic dissection by transesophageal echocardiography.* Am J Cardiol, 1984. **54**(8): p. 1157-8.

440. Erbel, R., et al., *Echocardiography in diagnosis of aortic dissection.* Lancet, 1989. **1**(8636): p. 457-61.

441. Ballal, R.S., et al., *Usefulness of transesophageal echocardiography in assessment of aortic dissection.* Circulation, 1991. **84**(5): p. 1903-14.

442. Geisinger, M.A., et al., *Thoracic aortic dissections: magnetic resonance imaging.* Radiology, 1985. **155**(2): p. 407-12.

443. Dinsmore, R.E., et al., *MRI of dissection of the aorta: recognition of the intimal tear and differential flow velocities.* AJR Am J Roentgenol, 1986. **146**(6): p. 1286-8.

444. Goldman, A.P., et al., *The complementary role of magnetic resonance imaging, Doppler echocardiography, and computed tomography in the diagnosis of dissecting thoracic aneurysms.* Am Heart J, 1986. **111**(5): p. 970-81.

445. Dinsmore, R.E., et al., *Magnetic resonance imaging of thoracic aortic aneurysms: comparison with other imaging methods.* AJR Am J Roentgenol, 1986. **146**(2): p. 309-14.

446. Hellenthal, F.A., et al., *Biomarkers of abdominal aortic aneurysm progression. Part 2: inflammation.* Nat Rev Cardiol, 2009. **6**(8): p. 543-52.

447. Abdul-Hussien, H., et al., *Collagen degradation in the abdominal aneurysm: a conspiracy of matrix metalloproteinase and cysteine collagenases.* Am J Pathol, 2007. **170**(3): p. 809-17.

448. Pyo, R., et al., *Targeted gene disruption of matrix metalloproteinase-9 (gelatinase B) suppresses development of experimental abdominal aortic aneurysms.* J Clin Invest, 2000. **105**(11): p. 1641-9.

449. Chiou, A.C., B. Chiu, and W.H. Pearce, *Murine aortic aneurysm produced by periarterial application of calcium chloride.* J Surg Res, 2001. **99**(2): p. 371-6.

450. Daugherty, A. and L. Cassis, *Chronic angiotensin II infusion promotes atherogenesis in low density lipoprotein receptor -/- mice.* Ann N Y Acad Sci, 1999. **892**: p. 108-18.

451. Daugherty, A., M.W. Manning, and L.A. Cassis, *Angiotensin II promotes atherosclerotic lesions and aneurysms in apolipoprotein E-deficient mice.* J Clin Invest, 2000. **105**(11): p. 1605-12.

452. Deng, G.G., et al., *Urokinase-type plasminogen activator plays a critical role in angiotensin II-induced abdominal aortic aneurysm.* Circ Res, 2003. **92**(5): p. 510-7.

453. King, V.L., et al., *Selective cyclooxygenase-2 inhibition with celecoxib decreases angiotensin II-induced abdominal aortic aneurysm formation in mice.* Arterioscler Thromb Vasc Biol, 2006. **26**(5): p. 1137-43.

454. Uchida, H.A., et al., *Urokinase-type plasminogen activator deficiency in bone marrow-derived cells augments rupture of angiotensin II-induced abdominal aortic aneurysms.* Arterioscler Thromb Vasc Biol, 2011. **31**(12): p. 2845-52.

455. Krishna, S.M., et al., *A peptide antagonist of thrombospondin-1 promotes abdominal aortic aneurysm progression in the angiotensin II-infused apolipoprotein-E-deficient mouse.* Arterioscler Thromb Vasc Biol, 2015. **35**(2): p. 389-98.

456. Norman, P.E. and J.A. Curci, *Understanding the effects of tobacco smoke on the pathogenesis of aortic aneurysm.* Arterioscler Thromb Vasc Biol, 2013. **33**(7): p. 1473-7.

457. Daugherty, A. and J.T. Powell, *Recent highlights of ATVB: aneurysms.* Arterioscler Thromb Vasc Biol, 2014. **34**(4): p. 691-4.

458. Liu, J., A. Daugherty, and H. Lu, *Angiotensin II and Abdominal Aortic Aneurysms: An update.* Curr Pharm Des, 2015. **21**(28): p. 4035-48.

459. Saraff, K., et al., *Aortic dissection precedes formation of aneurysms and atherosclerosis in angiotensin II-infused, apolipoprotein E-deficient mice.* Arterioscler Thromb Vasc Biol, 2003. **23**(9): p. 1621-6.

460. Daugherty, A., L.A. Cassis, and H. Lu, *Complex pathologies of angiotensin II-induced abdominal aortic aneurysms.* J Zhejiang Univ Sci B, 2011. **12**(8): p. 624-8.

461. Daugherty, A., et al., *Angiotensin II infusion promotes ascending aortic aneurysms: attenuation by CCR2 deficiency in apoE-/- mice.* Clin Sci (Lond), 2010. **118**(11): p. 681-9.

462. Davis, F.M., et al., *Smooth muscle cell deletion of low-density lipoprotein receptor-related protein 1 augments angiotensin II-induced superior mesenteric arterial and ascending aortic aneurysms.* Arterioscler Thromb Vasc Biol, 2015. **35**(1): p. 155-62.

463. Rateri, D.L., et al., *Angiotensin II induces region-specific medial disruption during evolution of ascending aortic aneurysms.* Am J Pathol, 2014. **184**(9): p. 2586-95.

464. Lanzer, P., et al., *ECG-synchronized cardiac MR imaging: method and evaluation.* Radiology, 1985. **155**(3): p. 681-6.

465. Browning, J.D., et al., *Prevalence of hepatic steatosis in an urban population in the United States: impact of ethnicity.* Hepatology, 2004. **40**(6): p. 1387-95.

466. Williams, C.D., et al., *Prevalence of nonalcoholic fatty liver disease and nonalcoholic steatohepatitis among a largely middle-aged population utilizing ultrasound and liver biopsy: a prospective study.* Gastroenterology, 2011. **140**(1): p. 124-31.

467. Wong, V.W., et al., *Prevalence of non-alcoholic fatty liver disease and advanced fibrosis in Hong Kong Chinese: a population study using proton-magnetic resonance spectroscopy and transient elastography.* Gut, 2012. **61**(3): p. 409-15.

468. Kanwal, F., et al., *Trends in the Burden of Nonalcoholic Fatty Liver Disease in a United States Cohort of Veterans.* Clin Gastroenterol Hepatol, 2016. **14**(2): p. 301-8 e1-2.

469. Younossi, Z.M., et al., *Changes in the prevalence of the most common causes of chronic liver diseases in the United States from 1988 to 2008.* Clin Gastroenterol Hepatol, 2011. **9**(6): p. 524-530 e1; quiz e60.

470. Angulo, P., *Nonalcoholic fatty liver disease.* N Engl J Med, 2002. **346**(16): p. 1221-31.

471. Vernon, G., A. Baranova, and Z.M. Younossi, *Systematic review: the epidemiology and natural history of non-alcoholic fatty liver disease and non-alcoholic steatohepatitis in adults.* Aliment Pharmacol Ther, 2011. **34**(3): p. 274-85.

472. Chalasani, N., et al., *The diagnosis and management of non-alcoholic fatty liver disease: practice Guideline by the American Association for the Study of Liver Diseases,*

American College of Gastroenterology, and the American Gastroenterological Association. Hepatology, 2012. **55**(6): p. 2005-23.

473. Chalasani, N., et al., *The diagnosis and management of non-alcoholic fatty liver disease: Practice guideline by the American Association for the Study of Liver Diseases, American College of Gastroenterology, and the American Gastroenterological Association.* Am J Gastroenterol, 2012. **107**(6): p. 811-26.

474. Chalasani, N., et al., *The diagnosis and management of non-alcoholic fatty liver disease: practice guideline by the American Gastroenterological Association, American Association for the Study of Liver Diseases, and American College of Gastroenterology.* Gastroenterology, 2012. **142**(7): p. 1592-609.

475. Fraser, A., M.P. Longnecker, and D.A. Lawlor, *Prevalence of elevated alanine aminotransferase among US adolescents and associated factors: NHANES 1999-2004.* Gastroenterology, 2007. **133**(6): p. 1814-20.

476. Teli, M.R., et al., *The natural history of nonalcoholic fatty liver: a follow-up study.* Hepatology, 1995. **22**(6): p. 1714-9.

477. McPherson, S., et al., *Evidence of NAFLD progression from steatosis to fibrosing-steatohepatitis using paired biopsies: implications for prognosis and clinical management.* J Hepatol, 2015. **62**(5): p. 1148-55.

478. Singh, S., et al., *Fibrosis progression in nonalcoholic fatty liver vs nonalcoholic steatohepatitis: a systematic review and meta-analysis of paired-biopsy studies.* Clin Gastroenterol Hepatol, 2015. **13**(4): p. 643-54 e1-9; quiz e39-40.

479. Pais, R., et al., *A systematic review of follow-up biopsies reveals disease progression in patients with non-alcoholic fatty liver.* J Hepatol, 2013. **59**(3): p. 550-6.

480. Byrne, C.D. and G. Targher, *NAFLD: a multisystem disease.* J Hepatol, 2015. **62**(1 Suppl): p. S47-64.

481. Arulanandan, A., et al., *Association Between Quantity of Liver Fat and Cardiovascular Risk in Patients With Nonalcoholic Fatty Liver Disease Independent of Nonalcoholic Steatohepatitis.* Clin Gastroenterol Hepatol, 2015. **13**(8): p. 1513-20 e1.

482. Yeh, M.M. and E.M. Brunt, *Pathological features of fatty liver disease.* Gastroenterology, 2014. **147**(4): p. 754-64.

483. Ekstedt, M., et al., *Fibrosis stage is the strongest predictor for disease-specific mortality in NAFLD after up to 33 years of follow-up.* Hepatology, 2015. **61**(5): p. 1547-54.

484. Sanyal, A.J., et al., *Nonalcoholic steatohepatitis: association of insulin resistance and mitochondrial abnormalities.* Gastroenterology, 2001. **120**(5): p. 1183-92.

485. Donnelly, K.L., et al., *Sources of fatty acids stored in liver and secreted via lipoproteins in patients with nonalcoholic fatty liver disease.* J Clin Invest, 2005. **115**(5): p. 1343-51.

486. Lambert, J.E., et al., *Increased de novo lipogenesis is a distinct characteristic of individuals with nonalcoholic fatty liver disease.* Gastroenterology, 2014. **146**(3): p. 726-35.

487. Fabbrini, E., et al., *Alterations in adipose tissue and hepatic lipid kinetics in obese men and women with nonalcoholic fatty liver disease.* Gastroenterology, 2008. **134**(2): p. 424-31.

488. Fabbrini, E., S. Sullivan, and S. Klein, *Obesity and nonalcoholic fatty liver disease: biochemical, metabolic, and clinical implications.* Hepatology, 2010. **51**(2): p. 679-89.

489. Neuschwander-Tetri, B.A., *Hepatic lipotoxicity and the pathogenesis of nonalcoholic steatohepatitis: the central role of nontriglyceride fatty acid metabolites.* Hepatology, 2010. **52**(2): p. 774-88.

490. Spengler, E.K. and R. Loomba, *Recommendations for Diagnosis, Referral for Liver Biopsy, and Treatment of Nonalcoholic Fatty Liver Disease and Nonalcoholic Steatohepatitis.* Mayo Clin Proc, 2015. **90**(9): p. 1233-46.

491. Grandison, G.A. and P. Angulo, *Can NASH be diagnosed, graded, and staged noninvasively?* Clin Liver Dis, 2012. **16**(3): p. 567-85.

492. Zhang, Y., et al., *Ca(2+) dissociation from the C-terminal EF-hand pair in calmodulin: a steered molecular dynamics study.* FEBS Lett, 2008. **582**(9): p. 1355-61.

493. Yang, T. and B.W. Poovaiah, *Calcium/calmodulin-mediated signal network in plants.* Trends Plant Sci, 2003. **8**(10): p. 505-12.

494. Huang, Y., et al., *Identification and dissection of Ca(2+)-binding sites in the extracellular domain of Ca(2+)-sensing receptor.* J Biol Chem, 2007. **282**(26): p. 19000-10.

495. Saucerman, J.J. and D.M. Bers, *Calmodulin binding proteins provide domains of local Ca2+ signaling in cardiac myocytes.* J Mol Cell Cardiol, 2012. **52**(2): p. 312-6.

496. Retamal, M.A., et al., *Opening of connexin 43 hemichannels is increased by lowering intracellular redox potential.* Proc Natl Acad Sci U S A, 2007. **104**(20): p. 8322-7.

497. Saez, J.C., et al., *Connexin-based gap junction hemichannels: gating mechanisms.* Biochim Biophys Acta, 2005. **1711**(2): p. 215-24.

498. Kar, R., et al., *Biological role of connexin intercellular channels and hemichannels.* Arch Biochem Biophys, 2012. **524**(1): p. 2-15.

499. Peracchia, C., *Chemical gating of gap junction channels; roles of calcium, pH and calmodulin.* Biochim Biophys Acta, 2004. **1662**(1-2): p. 61-80.

500. Neyton, J. and A. Trautmann, *Physiological modulation of gap junction permeability.* J Exp Biol, 1986. **124**: p. 993-114.

501. Reaume, A.G., et al., *Cardiac malformation in neonatal mice lacking connexin43.* Science, 1995. **267**(5205): p. 1831-4.

502. Lai-Cheong, J.E., K. Arita, and J.A. McGrath, *Genetic diseases of junctions.* J Invest Dermatol, 2007. **127**(12): p. 2713-25.

503. Bootman, M.D. and M.J. Berridge, *The elemental principles of calcium signaling.* Cell, 1995. **83**(5): p. 675-8.

504. Berridge, M.J., M.D. Bootman, and H.L. Roderick, *Calcium signalling: dynamics, homeostasis and remodelling.* Nat Rev Mol Cell Biol, 2003. **4**(7): p. 517-29.

505. Berridge, M.J., P. Lipp, and M.D. Bootman, *The versatility and universality of calcium signalling.* Nat Rev Mol Cell Biol, 2000. **1**(1): p. 11-21.

506. Haiech, J., S.B. Moulhaye, and M.C. Kilhoffer, *The EF-Handome: combining comparative genomic study using FamDBtool, a new bioinformatics tool, and the network of expertise of the European Calcium Society.* Biochim Biophys Acta, 2004. **1742**(1-3): p. 179-83.

APPENDICES

Appendix A. Identification of Calmodulin Binding Domain in Cx43 Gap Junction Protein

Appendix A.1. Introduction

Cellular communication is an important aspect in maintaining homeostasis within multicellular organisms. Processes such as hormone signaling, neural transmission, and cell-tocell adhesion have provided animals with a wide variety of communication mechanisms that operate with very high specificity. In addition to these mechanisms of cellular communication, individual cells also contain numerous protein channels that allow communication with the extracellular environment. In fact, membrane proteins can pass a large number of ions and metabolites across the cell membrane in very short time periods. With such numerous possibilities of cellular communication, it may appear that the direct connection between the intracellular environments of two adjacent cells provided by gap junctions would be redundant [492].

Multicellular organisms require various means of cellular communication to respond to internal and environmental stimuli. One method of communication is through the use of gap junctions, which allow the exchange of ions, nutrients and small metabolites from one cell to neighboring cells [493]. Gap junctions consist of the intercellular channels that mediate the cell-to cell transfer of small molecules, including metabolites, second messengers, and ions, in mammalian cells [494]. Gap junctions are composed of two hemichannels (termed connexons) with each composed of six connexin (Cx) 3 subunits. The connexon from one cell joins in mirror symmetry with another connexon of the opposing cell. Currently, at least 20 connexin genes have been identified in the human genome, with connexin 43 (Cx43) the most ubiquitous connexin [495].

Connexins (Cx) are proteins encoded by a multigene family that typically form cell-cell channels. To date, 21 Cx genes have been identified in the human genome and most of their Cx orthologues have been described in other vertebrate species. The assembly of connexins into gap junction channels (GJC) occurs in two main stages. Connexins first oligomerize into hexameric hemichannels (HC) in the Golgi apparatus, from where they are transported to the cell surface in vesicles and they fuse to the plasma membrane in an exocytotic process [496].

The number of HCs delivered to the plasma membrane can be represent only the 4-15% of total Cx protein [497]. Subsequently, hemichannels presented by adjacent cells make contact and dock to form a complete intercellular channel. During the docking process, the channel interior becomes isolated from the extracellular environment and the newly formed channel opens, allowing the direct exchange of ions, second messengers and metabolites between the interior of the two cells. New intercellular channels aggregate to form plaque-like structures, while older channels are endocytosed as double-membrane gap junction structures by one of the two contributing cells, indicating that the hemichannels remain docked during gap junction degradation. It was previously thought that hemichannels remained closed until docking during channel formation. However, the opening of undocked hemichannels has been demonstrated in solitary Xenopus oocytes expressing the lens Cx46 [498] and in isolated horizontal cells of the catfish retina [499]. Twenty years later, there is now evidence that HCs composed of different connexins can be electrically and chemically activated [500], and in native cells these HCs can mediate the rapid flow of ions across the cell membrane to regulate ionic homeostasis, and to facilitate the release of ATP, NAD+, glutamate or prostaglandins involved in autocrine/paracrine signaling [501], as well as the transfer of nitric oxide [502].

Both Ca^{2+} and H^{+} play a role in chemical gating of gap junction channels, but, with the possible exception of Cx46 hemichannels, neither of them is likely to induce gating by a direct interaction with connexins. Some evidence suggests that low pHi affects gating via an increase in $[Ca^{2+}]$; in turn, Ca^{2+} is likely to induce gating by activation of CaM, which may act directly as a gating particle. Each Cx43 monomer consists of four highly conserved transmembrane segments, a short N-terminal cytoplasmic region, one intracellular and two extracellular loops, and a C-terminal tail. Variability in sequence homology across different connexin types is greatest in the intracellular loop and C terminus. Efforts to map the potential CaM-binding sites in Cx43 have led to conflicting results [503].

This protein family is related with many diseases, like skin disease, tooth, and heart diseases (Figure 3). The first inherited abnormality of a gap junction protein was reported in 1993 with mutations in Cx32 in individuals with X-linked charcot-marie-tooth disease [504]. Then in 1997, mutations in Cx26 were identified in case of deafness [505], a finding that led to the significant discovery that mutations in Cx26 are in fact a common cause for several forms of deafness. Later, mutations have been discovered in seven Cxs: Cx30, 30.3, 31, 40 43, 46 and 50 to be related with different diseases. Among them, four connexins are associated with skin diseases, Cx26, Cx30, Cx30.3, Cx31. Cx46 and 50 have been shown to underlie cases of cataract.

Gap junctions play an important role in maintaining cell and tissue function and homeostasis, and loss of function of connexin43 mutations has been linked to several serious human diseases. Cx43 is the most abundantly expressed human connexin. Recently, a CaM binding site was assigned to the second half of the cytoplasmic loop (CL) domain of Cx43, Cx44, and Cx50 and confirmed using surface plasmon resonance, circular dichroism, fluorescence spectroscopy, and nuclear magnetic resonance. Gap junctions have been shown to be regulated by

[Ca^{2+}] and also mediated by CaM interacting directly with the connexin proteins. Zhou et al. indicated that the 136–158 amino acids of Cx43 bind with CaM with 1:1 stoichiometry in a Ca^{2+}-dependent manner [506].

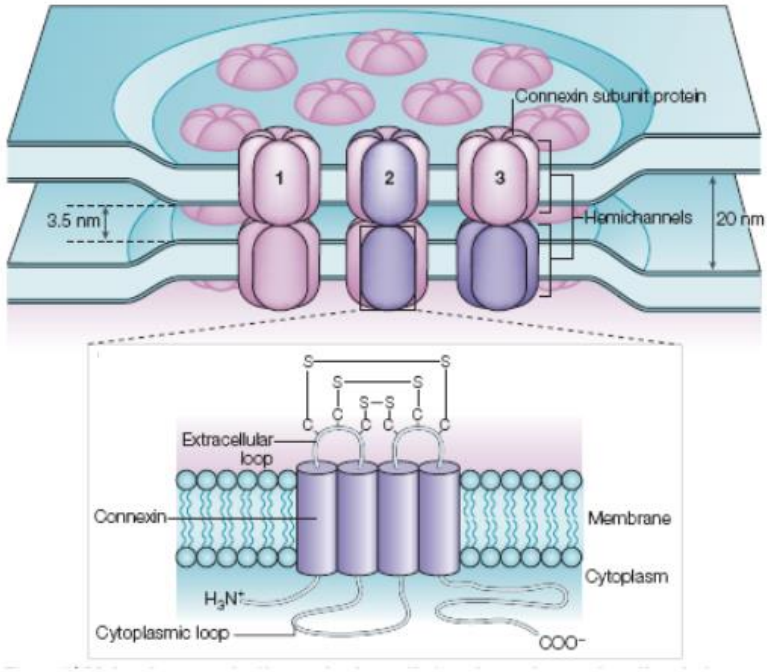

Appendix 1. *Molecular organization and schematic topology of a gap-junctional plaque*

Recently, CaM binding sites have been identified on the cytoplasmic loop (CL) of at least three Cxs in the α family. It has been shown that the Ca^{2+} regulation of Cx43 gap junctions is blocked by CaM inhibitors. It is proposed that the carboxyl-terminal part of the Cx43 in the cytoplasmic loop (Cx43136–158) domain is essential in regulation of Cx43 gap junction by CaM in a Ca^{2+}-dependent manner and eventually closure of Cx43 gap junction. The Cx43 CaM binding domain follows the 1–5-10 CaM-binding mode subclass with hydrophobic residues at positions 1, 5, and 10 which is similar to the CAMBD of Ca^{2+}/CaM-dependent kinase II (CaMKII). Ca^{2+}-bound CaM induces a conformational change in cytoplasmic loop of Cx43 or a combination of both steric hindrance mechanisms cause the closure of the channel. Furthermore, it has been shown that, the

addition of CaMKII inhibits CaM-Cx43 cytoplasmic loop interaction which causes a subsequent transition of the channel from close to open state.

Connexin43, which is a CaM target protein, is a membrane protein. Therefore, it is difficult to study the complex due to the challenges associated with the membrane proteins such as; difficulty in expression and purification, low solubility and conformational flexibility. Therefore, the intracellular regions of Cxs are largely "invisible" in the reported X-ray structures. Thus, the molecular mechanisms for CaM regulation of Cx43 are not well established.

In this section, we have described a strategy to further study the binding between CaM and Connexin43 and possible role of transmembrane residues in CaM binding to Cx43 (Figure 5). In this approach, two fusion proteins with the sequences of Cx43(99-154) and Cx43(88-164) were designed and expressed. A peptide that contains the entire intercellular loop (Cx43, 99-154) was designed to study the interaction of CaM with the entire loop. Another peptide that contains the entire intercellular loop and also parts of the transmembrane domains (Cx43, 88-164) was designed to study the importance of the transmembrane domain to the interaction of CaM with intercellular loop. Initial studies between D-CaM and the two proteins suggest that there is an interaction between Cx43(88-164) + Fusion protein, however, the peptides are not purified yet. In order to purify the peptides TEV protease and thrombin used as enzymes to cleave the rest of the protein and produce only sequences of Cx43 (99-154) and Cx43 (88-164). Different cleavage conditions were used to test whether TEV protease can cleave the protein or not.

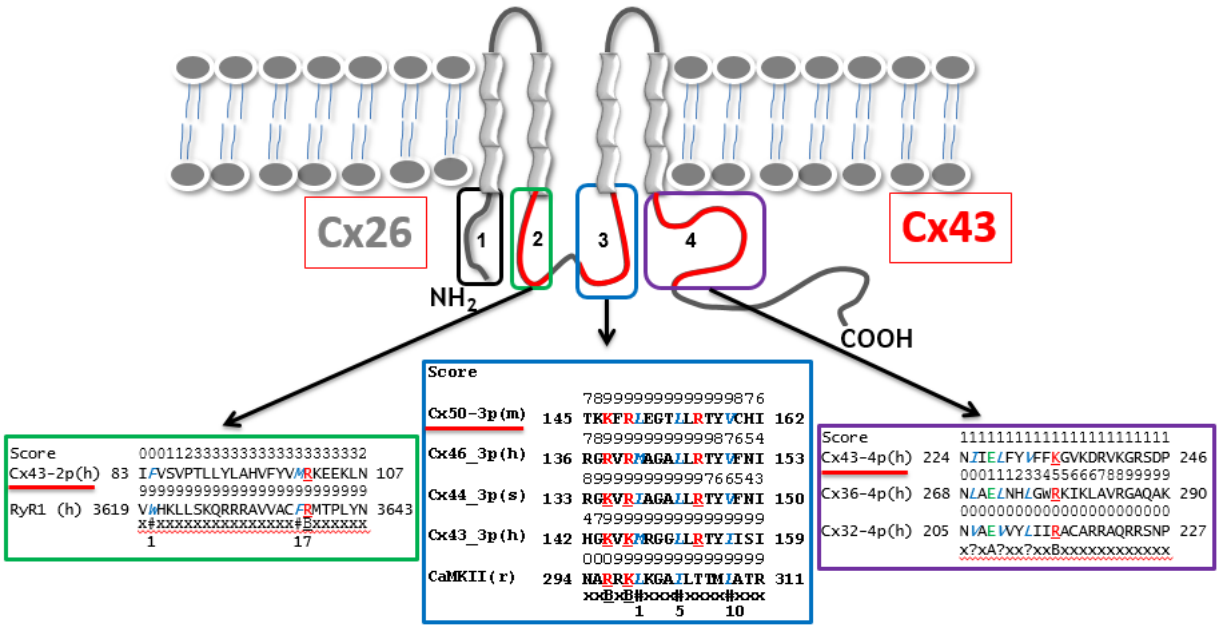

Appendix 2 *CaM binding sites in gap junction.*

Appendix A.2. Expression and purification of His-tagged Cx43 (99-154)

The vector carrying the sequence of thioredoxin protein fused at N-terminal which contains a histag before the sequence of the Cx43 (99-154) was transformed into BL21(DE3) Green E-coli cell strain. M9 medium was used for the expression of the protein. (Carbenicillin was used instead of ampicillin because of better stability). First the protein was expressed in small scale (200 mL) and the bacterium was grown over night at 37°C, 200 rpm. Then the solution was induced into 2L of M9 medium and the bacteria was allowed to grow at 37°C until its optical density reached 0.6-0.8, then 200 µL of IPTG was added for over expression of the protein and then the temperature was immediately decreased to 28°C and it was allowed to grow over night. Then in the morning the cell debris was collected. Figure 13 shows the full sequence map of Cx43(99-154) with fusion protein and TEV cleavage site. Figure 14 demonstrates SDS-page results for expression of Cx43(99-154).

Appendix 3 *Mechanism of Cx43 purification with TEV protease.*

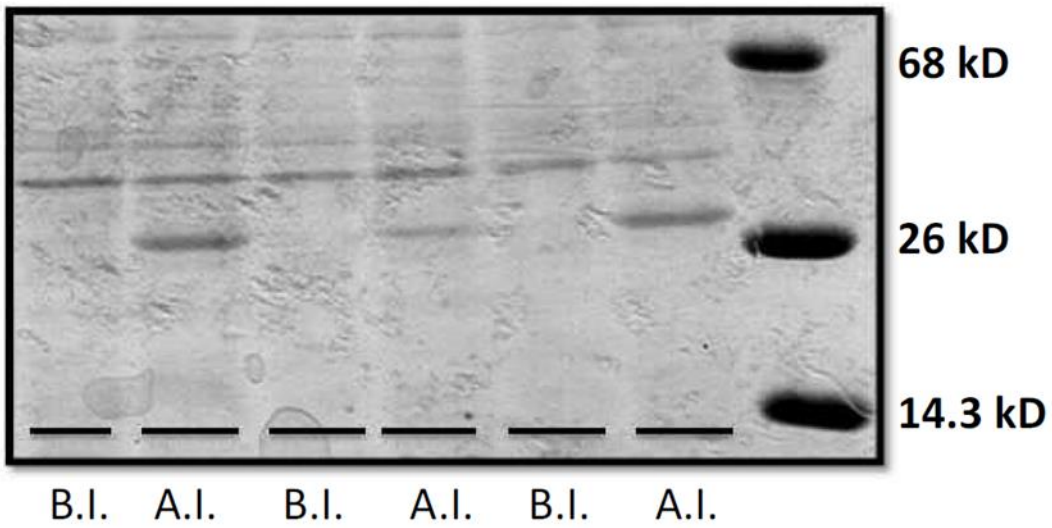

Appendix 4 *SDS-page results for expression of Cx43(99-154).*

After centrifuge and collecting the cell debris, the following buffer was used: 25 mM HEPES, 500mM NaCl, 1% sarkosyl, pH=7.2, and after that 5 to 10 mL of the buffer was added and then Lysozyme was added to the final concentration of 150 µg/mL and the solution was incubated for 30 min at 37°C. Then it was sonicated 3 times for 30 seconds, and 5 min rest between each sonication, and then it was centrifuged. The same buffer was used to wash the cell debris for the second time. For the third time 2M of Urea, 20 mM Tris-HCl, 0.5 M NaCl, and 2% Triton X-100 (pH=8) was used to wash and lysate the cell debris and denature the protein in order to make it more soluble. Finally, after centrifuge and collecting the cell debris, it was washed with 6 M Guanidine hydrochloride, 1 mM 2-mercaptoethanol, 20 mM Tris-HCl, 0.5 M NaCl, 5 mM

Imidazole (5 mL), and then let it stir for 1 hour at room temperature, and then it was centrifuged at 4°C, 7000 rpm, 20 min. The reason for washing with this buffer is again to make the protein more soluble by denaturing it. Only 5 mL of the last buffer was used to wash the cell debris for FPLC injection.

Appendix A.3. FPLC Purification of Cx43 (99-154) using His-tag Column

First the column was washed with EDTA to remove any positively charged ions. Then, FPLC column was charged with Nickel ions, so that the desired protein which has six consecutive histidine residues can bind to the column. Then the column was washed with high concentration of Urea (20 mM Tras-HCl, 0.5 M NaCl, 20 mM imidazole, 1mM 2-mercaptoethanol, 6 M of Urea) to unfold the protein and then it was washed with 0M of Urea (20 mM Tras-HCl, 0.5 M NaCl, 20 mM imidazole, 1mM 2-mercaptoethanol, 0 M of Urea) to refold the protein back again. In order to equilibrate the column, the buffer with high concentration of guanidine (6M) was used to wash the column. Since imidazole forms a strong complex with nickel, finally high concentration of imidazole was used to elute the protein out of the column. These two buffers were used for the purification in the FPLC column. The buffer which has lower concentration of imidazole was used to equilibrate the column (Buffer A: 20 mM Tras-HCl, 0.5 M NaCl, 20 mM imidazole, 1mM 2-mercaptoethanol, pH=8.0). (Buffer B: 20 mM Tras-HCl, 0.5 M NaCl, 500 mM imidazole, 1mM 2-mercaptoethanol, pH=8.0). After elution, a large peak came out from the column and samples were taken from the peak fractions for SDS-page to confirm that the protein is pure. As it is shown in Appendix 5, fractions 28 to 41 contain single band which confirms they contain our protein based on the molecular size.

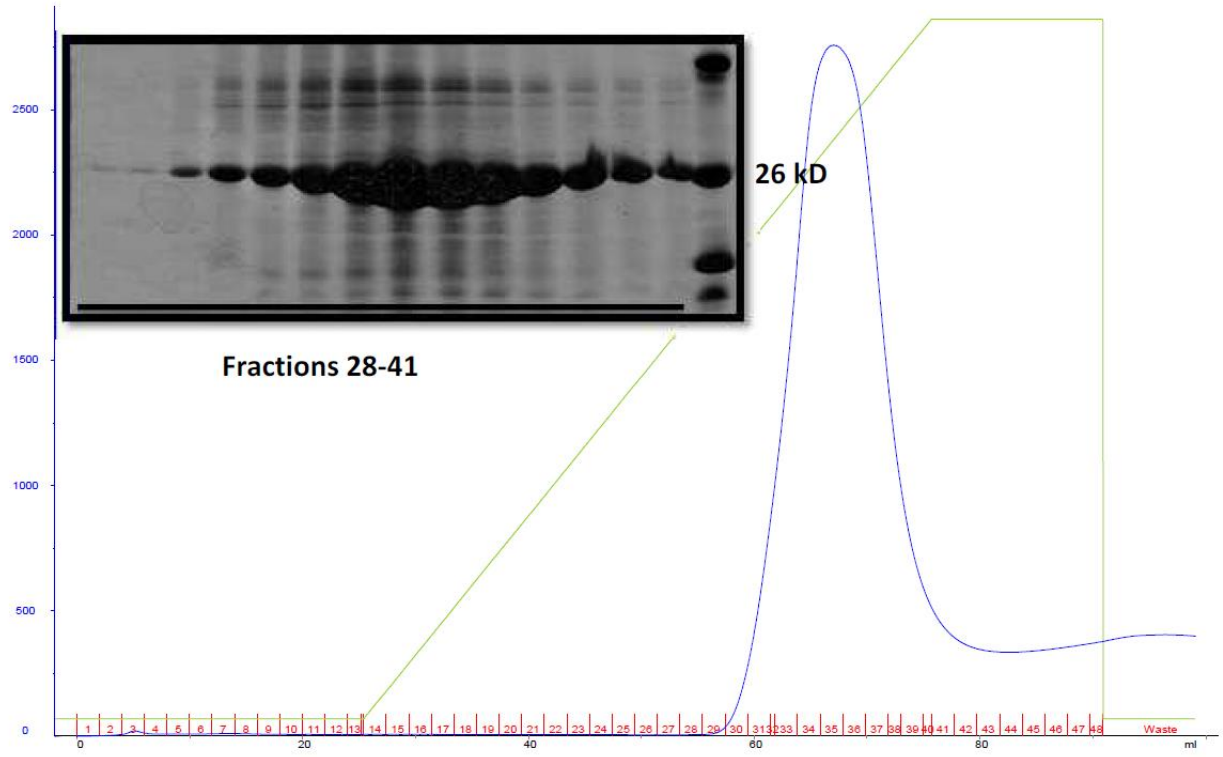

Appendix 5 *Purification of Cx43(99-154) with Fusion Protein.*

The column was washed with high concentration of Urea (20 mM Tras-HCl, 0.5 M NaCl, 20 mM imidazole, 1mM 2-mercaptoethanol, 6 M of Urea) to unfold the protein and then washed with 0M of Urea (20 mMTras-HCl, 0.5 M NaCl, 20 mM imidazole, 1mM 2-mercaptoethanol, 0 M of Urea) to refold the protein back again. After the purification, in order to remove the imidazole, desalting column was used and the protein solution was passed through the column, and then the protein was dialyzed against 10 mM Tris in pH of 8.0. After that the concentration and yield of the protein was calculated. Appendix 6 indicates the FPLC results for desalting column, and Appendix 7 corresponds to concentration and yield of the protein.

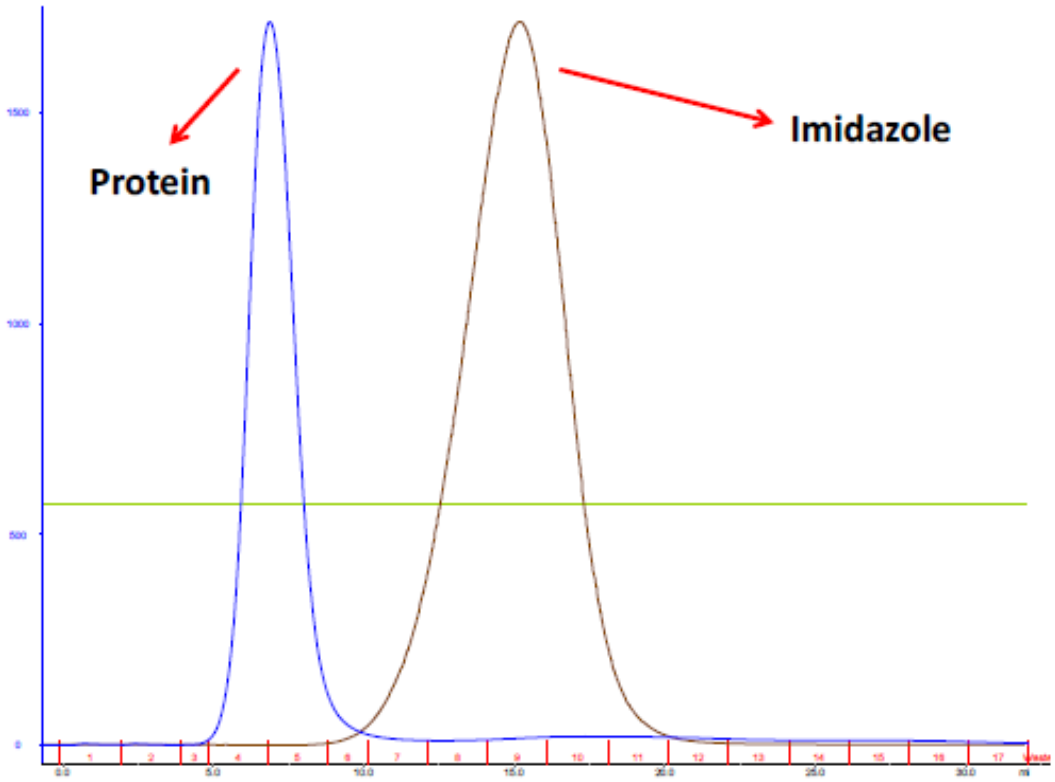

Appendix 6 *Imidazole removal from the protein using desalting column.*

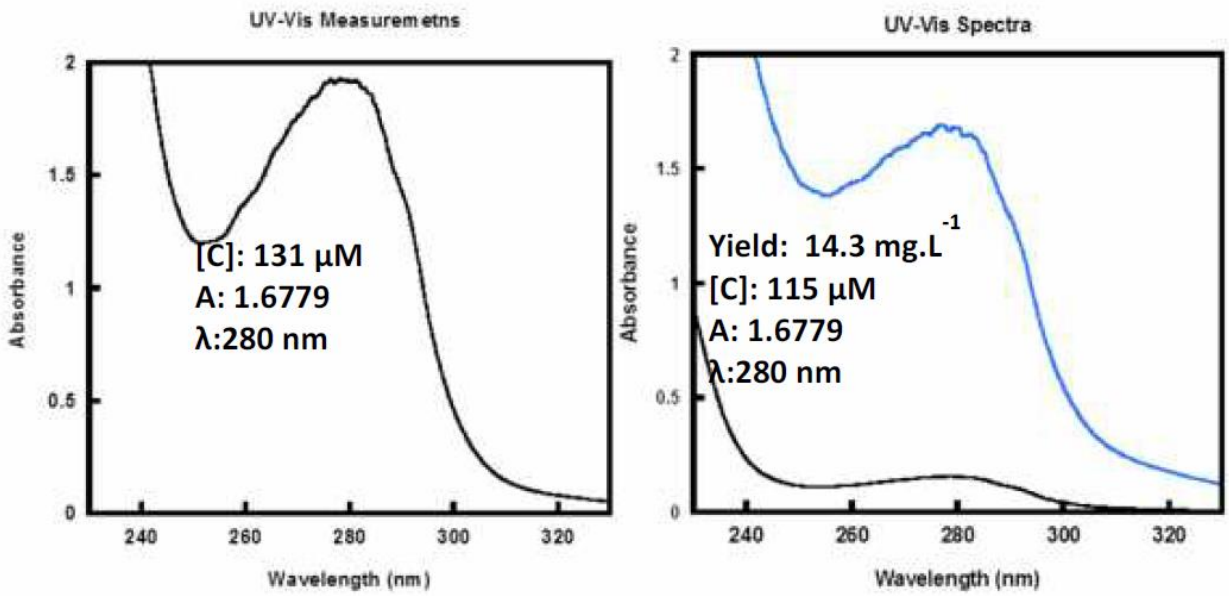

Appendix 7 *Cx43 (99-154) concentration calculation based on UV absorbance.*

Appendix A.4. Testing TEV Protease Cleavage Conditions with Purified Cx43(99-154) with fusion protein

After the protein was purified, in order to see whether direct addition of the enzyme cleaves the protein or not, different amounts of the enzyme were directly added to the purified protein. For this purpose, two sets of experiments were designed. First, the factor of time was changed, and second, the amount of the enzyme was changed. Appendix 8 summarizes these two sets of experiments.

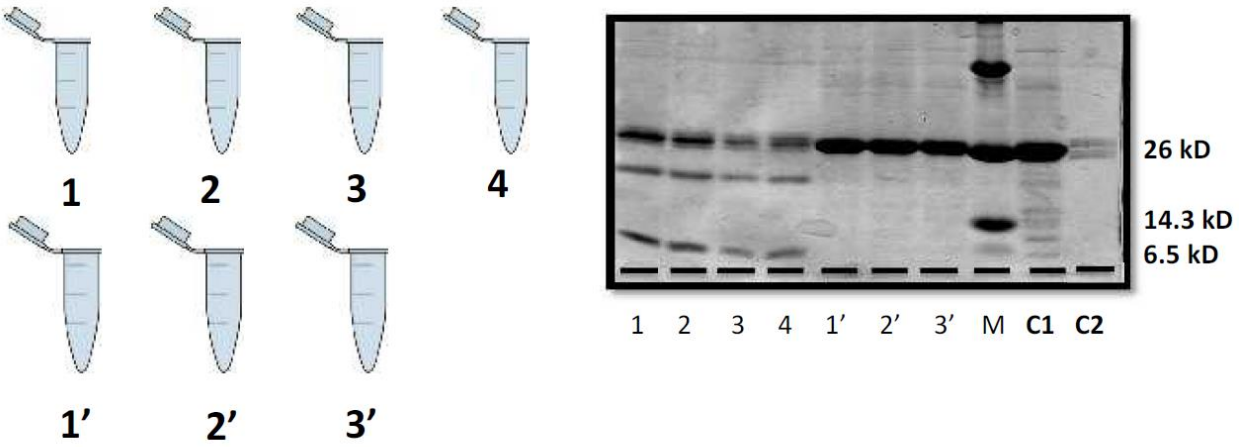

	1	**2**	**3**	**4**	**1'**	**2'**	**3'**
Protein:	10 µL	10	10	10	10	10	10
Buffer:	5 µL	5	5	5	5	5	5
Enzyme:	**10 µL**	**15**	**20**	**25**	10	10	10

Appendix 8 *SDS-page results for testing different cleavage conditions of TEV protease, C1 and C2 correspond to protein and the enzyme, respectively.*

For experiment set No.1 (1 to 4), the amount of the enzyme was changed and the time was kept constant at 4°C overnight for 2 days. As you can see, the more enzyme is added the more cleavage of the protein occurs and it results in two products: 1. Fusion protein with histag which is 16.9 kD and 2. The peptide fragment which is 6.5 kD and corresponds to Cx43 (99-154), therefore, it can be concluded that amount of the enzyme plays a role in the cleavage. In experiment

set No.2 (1’ to 3’), only the time was changed to 2h, 4h and 6h at room temperature. Based on SDS-page results, no cleavage occurred during the tested times. We can conclude that if the cleavage occurs at room temperature, TEV protease will degrade and autolysis happens which result in a dramatic reduction in the enzyme activity, therefore no cleavage will carry out. Appendix 9 shows the cleavage products of Cx43(99-154) with fusion protein.

Appendix 9 *The cleavage products of Cx43(99-154) with fusion protein.*

Appendix A.5. New method for Purification of Cx43 (99-154)

After adding the pure enzyme to pure fusion protein, everything that is in the solution has histidine tag except our desired peptide, therefore, we have come up with a new purification protocol. In this procedure, after letting the cleavage reaction complete, nickel beads were added to the mixture, and they were mixed with the solution for 2 hours at 4°C, then the mixture was

centrifuged and the supernatant was separated from the beads. Theoretically, the peptide should be in the supernatant and the enzyme, cleaved fusion protein, and uncleaved protein will bind to nickel beads. After performing the mentioned experiment, the Cx43 (99-154) was successfully purified from the mixture. Figure 20 shows the experiment steps for purification of Cx43 (99-154) peptide.

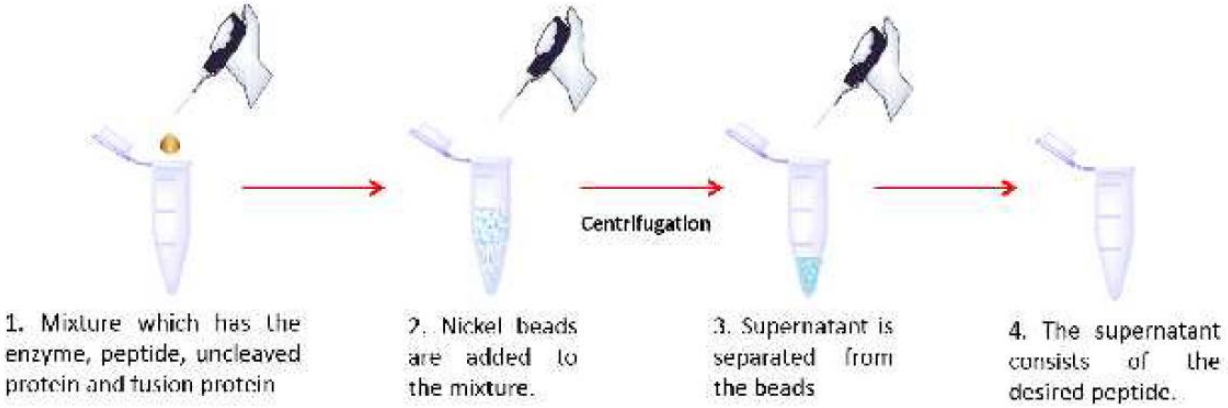

Appendix 10 *The enzyme, uncleaved protein, and cleaved fusion protein have histidine tag therefore, nickel beads can be used to separate the peptide from the mixture after cleavage.*

After obtaining the supernatant, SDS-page was run to make sure the peptide is pure. Appendix 11 shows the pure peptide after cleavage with molecular weight of 6.5 kDa.

The final concentration of peptide was calculated to be 993 μM with the final yield is 4 mg L^{-1}.

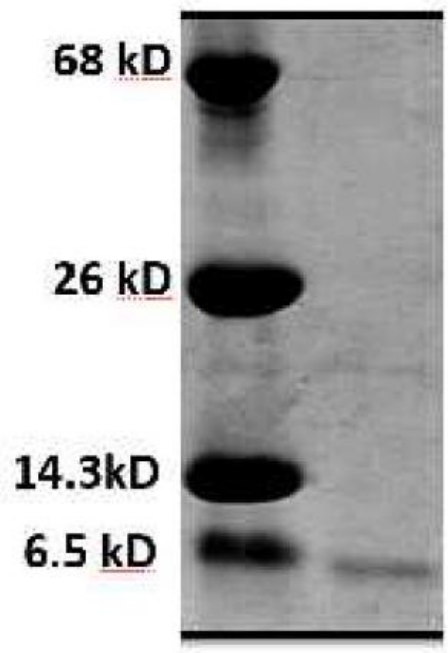

Appendix 11 *Pure Cx43 (99-154) after Purification.*

Appendix A.6. Monitoring the Interaction between Cx43 (99-154) and Calmodulin

After obtaining the pure peptide, steady-state and anisotropy fluorescence spectroscopy was used to monitor the interaction between CaM and Cx43 (99-154) peptide. For this purpose, in steady state fluorescence spectroscopy, 4 μM of dansylated CaM was used, and the signal of dansyl chloride was monitored during the interaction. Different volumes of the peptide were titrated to CaM. The titration was continued until the total concentration of the peptide in the solution reached 30 μM. After adding different volumes of the peptide no increase in the signal was observed suggesting there is no interaction between the peptide and dansyl CaM. To further prove there is no interaction, fluorescence anisotropy was used. Fluorescence anisotropy can be used to measure the binding constants and kinetics of reactions that cause a change in the rotational time of the molecules. If the fluorophore is bound to a small molecule, the rate at which it tumbles can decrease significantly when it is bound tightly to a large protein. If the fluorophore is attached to

the larger protein in a binding pair, the difference in polarization between bound and unbound states will be smaller (because the unbound protein will already be fairly stable and tumble slowly to begin with) and the measurement will be less accurate. The degree of binding is calculated by using the difference in anisotropy of the partially bound, free and fully bound (large excess of protein) states measured by titrating the two binding partners. After performing the experiment, again no interaction was observed proving our previous steady state fluorescence experiment. Appendix 12. Illustrates the mentioned experiment.

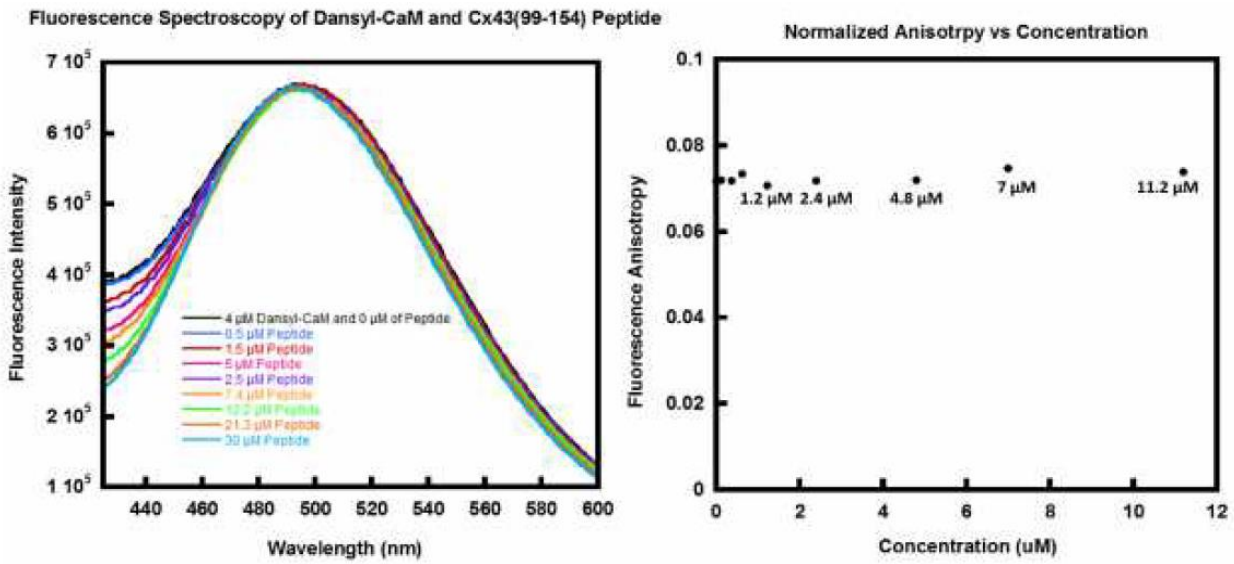

Appendix 12 *Fluorescence Steady State and Anisotropy of Dansyl-CaM and Cx43(99-154).*

Appendix A.7. Purification of Cx43 (88-163) Peptide

Using the same procedure discussed in section 2.12, another peptide with transmembrane residues was purified. This peptide consists of the same resides that Cx43 (99-154) peptide had with additional transmembrane residues at both ends. Figure 23 demonstrates the SDS-page results for purification of Cx43 (88-163) peptide.

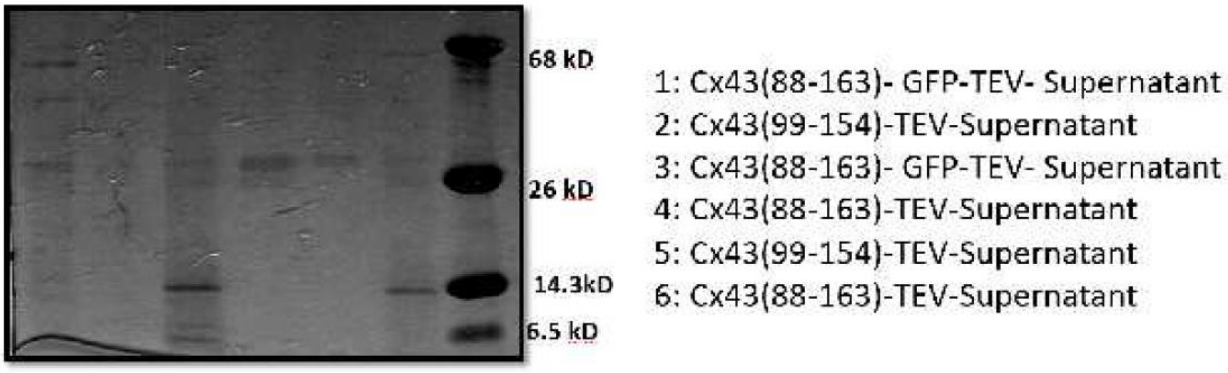

Appendix 13 *The purified Cx43 (88-163) peptide.*

After obtaining the other peptide, a preliminary study was performed using steady-state fluorescence spectroscopy. As you can see in figure 24b, after titrating the peptide to dansyl-CaM, an increase and blue shift was observed which suggests the possible binding of CaM to Cx43(88-163) peptide. Appendix 14 illustrates the interaction and comparison between the two peptides and their interaction with Dansyl-CaM.

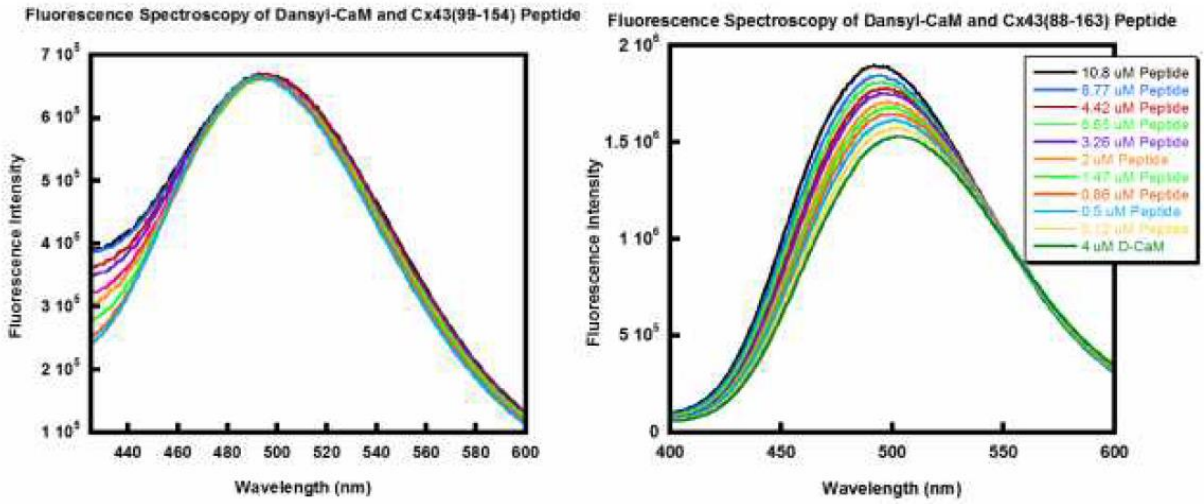

Appendix 14 *Comparison between the interactions of two peptides with dansyl-CaM.*

Appendix A.8. Summary and conclusion

Based on the new purification technique that we used, two peptides one consisting of the whole loop of Cx43 (99-154) and another one which has loop with transmembrane residues were successfully purified. Fluorescence steady-state and anisotropy were used to monitor the interaction between Cx43 (99-154) and Cx43 (88-164) peptides with dansyl-CaM. Based on the preliminary results, Cx43 (88-163) binds to dansyl CaM, however, Cx43(99-154) does not show any increase or blue shift in the signal of dansyl-CaM which suggests there is not interaction between them.